"Numerical investigation of the set-up around the shaft of a driven pile in clay"

de Chaunac, Henri

Abstract

The context of this thesis is the installation of driven piles in clay. Pile driving is an installation method which consists of repeatedly striking the pile head with a mass until desired embedment is attained. Driving brings severe distortions to the soil which has to accommodate for the penetrating pile. At the end of installation, the soil is left in a distressed state, which progressively tends to equilibrium with time, leading to a change in pile capacity. This phenomenon referred to as pile set-up. The objective of this thesis was to implement a numerical model which could account for pile installation and subsequent set-up in clayey soils. Focus was placed on behaviour round the pile shaft. The particularity the developed model is that it accounts for the cycles of shaft-soil shearing occurring during driving. Supported by experimental evidence, the original model developed in this work outlines the following conclusions: • During installation, total stress at pile wall dec...

Document type : *Thèse (Dissertation)*

UCL
Université
catholique
de Louvain

Numerical investigation of the set-up around the shaft of a driven pile in clay

Henri de Chaunac

A thesis submitted to the Université catholique de Louvain
in partial fulfilment of the requirements for the degree of
Doctor in Engineering Sciences of the Ecole polytechnique de Louvain

December 2015

Supervisor:
Alain Holeyman (Université catholique de Louvain)

Members of the Jury:
Eric Deleersnijder (Université catholique de Louvain), president
Richard Jardine (Imperial College London), co-advisor
Alain Puech (Fugro GeoConsulting France), co-advisor
Daniel Verástegui (Université catholique de Louvain)

Abstract

The context of this thesis is the installation of driven piles in clay. Pile driving is an installation method which consists of repeatedly striking the pile head with a mass until desired embedment is attained. Driving brings severe distortions to the soil which has to accommodate for the penetrating pile. At the end of installation, the soil is left in a distressed state, which progressively tends to equilibrium with time, leading to a change in pile capacity. This phenomenon referred to as pile set-up.

The objective of this thesis was to implement a numerical model which could account for pile installation and subsequent set-up in clayey soils. Focus was placed on behaviour around the pile shaft. The particularity the developed model is that it accounts for the cycles of shaft-soil shearing occurring during driving.

This work is divided in eight chapters. The first and last one are the introduction and conclusion, respectively. Chapters 2 and 3 present a literature survey of experimental and numerical pile installation models, respectively. Chapters 4 and 5 each describe a part of the numerical tool developed. Chapter 6 explores the simulation results and Chapter 7 compares the simulation results with an experimental pile installation at the Bothkennar site.

Supported by experimental evidence, the original model developed in this work outlines the following conclusions:

(i) During installation, total stress at pile wall decreases with vertical distance from pile toe (the h/R effect) due to (a) stress relief away from the pile toe and (b) fatigue from the accumulation of driving blows;

(ii) After installation, the radial distribution of pore pressure presents a peak a few radii away from the pile shaft. The value of this peak increases with overconsolidation ratio (OCR) while the pore pressure at the pile wall decreases with OCR;

(iii) The shape of pore pressure distribution after installation leads to a short term minimum in radial effective stress (therefore in pile capacity) during set-up.

Furthermore, the model yielded the following additional conclusions, which were outside of the scope of the available experimental data:

(i) The soil effective stress response during installation and set-up is mainly governed by overconsolidation ratio, rather than soil strength or stiffness;

(ii) There is a critical hammer velocity for which the soil offers maximum adherence to the pile;

(iii) Although shaft capacity after set-up was comparable for the open-ended and the closed-ended piles, open-ended set-up time was four times shorter.

Résumé

Ce travail s'intéresse aux pieux battus dans l'argile. Un pieu battu est un pieu préfabriqué que l'on installe grâce à une répétition de coups portés sur sa tête. Durant le battage, le sol est forcé de laisser place au pieu. De ce fait, à la fin de l'installation, le sol qui entoure le pieu est dans un état fortement perturbé. Avec le temps, cet état tend vers l'équilibre et cela entraîne un changement de la capacité portante du pieu. Ce phénomène est appelé cicatrisation ou "set-up" en anglais.

L'objectif de cette thèse était d'implémenter un modèle numérique dont le but était d'évaluer les effets d'installation et le set-up des pieux battus dans l'argile. L'accent a été mis sur le comportement du fût et la particularité de l'approche choisie est de tenir compte des cycles de cisaillement entre le fût et le sol pendant le battage.

Ce travail est divisé en huit chapitres. Le premier et le dernier en sont respectivement l'introduction et la conclusion. Les chapitres 2 et 3 présentent un compte rendu de la littérature concernant les pieux battus dans l'argile, expérimentalement et numériquement, respectivement. Les chapitres 4 et 5 décrivent l'outil numérique développé dans cette thèse. Le chapitre 6 expose les résultats des simulations entreprises et le chapitre 7 compare une simulation à un essai expérimental sur le site de Bothkennar.

Le modèle développé dans cette thèse a permis de formuler les conclusions suivantes, qui confirment les conclusions établies suites à des essais expérimentaux :

(i) Pendant l'installation, la contrainte radiale totale le long du fût décroit avec la distance verticale par rapport à la pointe du pieu (l'effet h/R). Ceci peut être expliqué par (a) le transfert de charge qui s'applique au sol situé près de la pointe et (b) la fatigue due à l'accumulation des coups de battage ;

(ii) A la fin de l'installation, la distribution radiale de pression interstitielle présente un pic à quelques rayons du fût. Ce pic croît avec le degré de surconsolidation (OCR) alors que la valeur de pression interstitielle au fût décroît avec l'OCR ;

(iii) La forme de la distribution radiale de pression interstitielle à la fin de l'installation implique que la contrainte radiale effective le long du fût atteint un minimum pendant le set-up. Ceci implique un minimum de la capacité portante.

Le modèle a également permis de conduire aux conclusions suivantes, qui étaient en dehors de la portée des essais expérimentaux :

(i) Pendant l'installation et le set-up, la réponse du sol en termes de contraintes effectives est principalement contrôlée par le degré de surconsolidation, plutôt que la résistance ou la raideur du sol ;

(ii) Il existe une vitesse critique du marteau de battage pour laquelle le sol offre une adhérence maximale au fût ;

(iii) La valeur de la capacité portante après set-up est comparable pour un pieu ouvert et un pieu fermé, mais le temps nécessaire pour atteindre cette valeur est quatre fois moindre pour le pieu ouvert.

Acknowledgements

The research described in this thesis was carried out during the period September 2011 to December 2015 and was made possible by a Research Assistantship and a grant from the FonDyTest Project.

I am indebted to my supervisor, Alain Holeyman, for his guidance and encouragement during these years. Many ideas of this thesis would not have taken shape without his original thinking and numerous suggestions. I would like to thank Richard Jardine (Imperial College London) and Alain Puech (Fugro GeoConsulting France) who accepted to be advisors to this thesis. Over the years, their incisive comments helped me model this thesis.

I would like to thank geotechnical engineers, worldwide, who responded to my questions. I am particularly grateful to David Mašín (Charles University) for his helpful comments about hypoplasticity and to César Sagaseta (Universidad de Cantabria) for the interesting conversations we had about the Strain Path Method. I am also grateful to Philippe Reiffsteck (Terrasol) for his knowledge and kind help regarding Flanders clay calibration and Arnold Verruijt (Delft University of Technology) for his guidance through my battle with coupled consolidation analysis.

I am appreciative to Eric Deleersnijder and Daniel Verástegui for accepting to be in my thesis jury.

Thanks to all my colleagues in the Department. Particular thanks to Malek Allani and Sami Hamdi for our stimulating exchanges about soil mechanics, Luc Yung and Stephane Gorski, the laboratory technicians, and the secretaries, Viviane Delmarcelle, Marie-Rose Decelle, and Claire Lagasse de Locht for their daily good mood. Thanks to all of those who remain unnamed, but not forgotten.

Finally, I would like to thank my family and close friends for their constant encouragement.

Contents

Notations and conventions

The subscript (x, y, z) is used for a general Cartesian system. The cylindrical coordinate system is defined by (r, θ, z) and the spherical coordinate system by (r, θ, ϕ). The acceleration, velocity and displacement components are respectively denoted by letters a_α, v_α and u_α, α being a subscript defining the component direction.

Without loss of generality, in a Cartesian coordinate system (x, y, z), the normal stresses are σ_x, σ_y, and σ_z; the shear stresses are τ_{xy}, τ_{xz}, and τ_{yz}. Effective stress is noted with an prime symbol ($'$). The normal strains are ε_x, ε_y, and ε_z; and the engineering shear strains are γ_{xy}, γ_{xz}, and γ_{yz}. Roscoe's variables are: p', q, ε_v and ε_q. Small increments are preceded by δ. The principal stresses and strains are designated by the subscripts (1, 2, 3), where the subscripts (1, 2, 3) do not signify any particular sequence of relative magnitudes (so they can be used as orthogonal Cartesian axes to define a three-dimensional space; see Appendix B).The major, intermediate, and minor principal effective stresses are respectively σ'_{I}, σ'_{II}, and σ'_{III}.

Adopting the usual sign convention of soil mechanics, compressive normal strains and stresses are positive. Shear strains and stresses follow this convention, as explained in Appendix C.

The upper dot ($\dot{}$) represents the material derivative (in an Eulerian representation).

Vectors are underlined (e.g. $\underline{a}$), second order tensors or matrices are embolden (*e.g.* $\mathbf{D}$ or $\boldsymbol{\sigma}'$), and fourth order tensors are slanted (*e.g.* $\mathscr{M}$). $\mathbf{I} = I_{ij}$ is the second order unit tensor and $\mathscr{I} = I_{ijkl} = \frac{1}{2}(I_{ik}I_{jl} + I_{il}I_{jk})$ is the fourth order unit tensor.

Terminology and barbarisms used in this work are defined in Appendix A.

Notation

The following list contains the definition of symbols used in this thesis. Although there is some duplication, I hope that this will not cause any confusion.

A_E	Pile embedded shaft area,
a_0	Dimensionless frequency,
a_α	Skeleton acceleration in the α direction,
c'	Soil effective cohesion,

c	Compressive wave velocity in the pile,
c_b	Absorbing boundary dashpot coefficient,
c_h	Coefficient of horizontal consolidation,
c_s	Shear wave velocity of the soil,
c_v	Coefficient of vertical consolidation,
D	Pile outer diameter,
$\mathbf{D}$	Rate of deformation tensor (or strain rate tensor),
E_{pm}	Pressuremeter modulus,
e	Soil voids ratio ($= V_v/V_s$),
f_d	Pyknotropy factor (hypoplasticity),
f_s	Average shaft shear stress between instrument clusters,
f_s	Barotropy factor (hypoplasticity),
G	Shear modulus,
G'	Soil shear modulus (effective stress),
G_0	Small strain soil shear modulus,
G_s	Specific gravity,
H	$= \sigma_r - u_{w0}$,
h	Vertical distance from pile toe (upward positive),
K'	Effective soil bulk modulus,
K	Coefficient of earth pressure around a pile ($= \sigma'_r/\sigma'_{z0}$),
K_0	Coefficient of earth pressure at rest ($= \sigma'_{h0}/\sigma'_{z0}$),
K_{0nc}	Value of K_0 for normally consolidated soil (OCR = 1),
k_b	Absorbing boundary spring coefficient,
k_r	Horizontal permeability,
k_z	Vertical complex stiffness,
L	Pile length,
L_E	Pile embedment,
LI	Liquidity index,
M	Shape factor for the modified Cam clay ellipse (slope of the csl in the $p' : q$ plane) where subscripts 'c', 'e', and 'ps' correspond to triaxial compression, triaxial extension, and plane strain, respectively,
M'	One dimensional compression modulus (oedometric compression modulus),
m_v	One dimensional coefficient of volume compressibility ($= 1/M'$),
N^*	Intercept of the iso-ncl at $p' = 1$ kPa in the $v : \ln p'$ compression plane,
N^*	Intercept of the iso-ncl at $p' = 1$ kPa in the $\ln v : \ln p'$ compression plane (hypoplasticity),
n	Soil porosity, when saturated, n is in fact the water (fluid phase) porosity (in contrast with the skeleton porosity),
n_p	Overconsolidation ratio defined for the modified Cam clay model ($= p'_y/p'_0$),
OCR	Apparent overconsolidation ratio ($= \sigma'_{vy}/\sigma'_{v0}$),
OCR*	Overconsolidation ratio definition for the hypoplastic model ($= p'_c/p'_0$),

PI	Plasticity index,
p'	Mean effective stress,
p'_{cs}	Intersection, in the compression plane ($v : \ln p'$ or $\ln v : \ln p'$), of the url passing through the current stress and the csl,
p^*_{cs}	Horizontal projection, in the compression plane ($v : \ln p'$ or $\ln v : \ln p'$), of the current stress on the csl,
p'_e	Hvorslev's equivalent mean effective stress, *i.e.* the horizontal projection, in the compression plane ($v : \ln p'$ or $\ln v : \ln p'$), of the current stress on the iso-ncl,
p'_y	Preconsolidation (or yield) mean effective stress,
p_L	Pressuremeter limit pressure,
Q_s	Pile shaft capacity,
q	Distortional stress,
q_b	Pile toe resistance,
q_c	Cone penetration resistance,
$q_{c,net}$	Net cone resistance ($= q_t - \sigma_{v0}$),
q_t	Corrected total cone resistance ($= q_c + (1-\alpha)u_2$),
R	Pile outer radius,
R^*	Open-ended pile equivalent radius ($= \sqrt{R^2-(R-t)^2}$),
R_p	Radius of the plastic zone,
r	Radial position,
r'	Radial position with respect to the pile shaft ($= r - R$),
s_u	Undrained shear strength,
T^*	Dimensionless time used during consolidation (subscripts '1', '2'... are used to denote variations),
t	Pile wall thickness,
t	Time,
u_2	Pore pressure measured at the piezocone shoulder,
u_α	Skeleton displacement in the α direction,
u_w	Pore water pressure,
$u_{z,p}$	Pile vertical displacement,
V	Normalised penetration velocity ($= v_{z,p} D/c_v$),
v	Soil specific volume ($= 1 + e$),
v_λ	Intercept of the K_0-ncl at $p' = 1$ kPa in the $\ln v : \ln p'$ compression plane (hypoplasticity),
$\mathbf{v}$	Skeleton velocity (vector),
$\mathbf{v}_w$	Pore water velocity (vector),
v_α	Skeleton velocity in the α direction,
$v_{w,\alpha}$	Pore water velocity in the α direction,
$v_{z,p}$	Pile vertical velocity,
W	Work,
$\mathbf{W}$	Spin tensor,
w	Water content,
z	Vertical position (downward positive),

z_0 Initial vertical position,

α Ratio of internal to external cross-sectional areas of a cone penetrometer,
Γ Intercept of the csl at $p' = 1\,\text{kPa}$ in the $v : \ln p'$ compression plane,
Γ^* Intercept of the csl at $p' = 1\,\text{kPa}$ in the $\ln v : \ln p'$ compression plane (hypoplasticity),
γ Soil unit weight,
γ Shear strain in the vertical plane (positive for pile loading, following the convention defined in Eq. 5.3, p. 95),
γ_s Unit weight of the skeleton,
γ_w Unit weight of water,
Δu_w Excess pore water pressure,
δ Small increment,
δ Interface angle of friction at the pile shaft ($= \arctan(\tau/\sigma'_n)$),
η Stress ratio ($= q/p'$),
θ Lode angle,
κ Slope of the url in the $v : \ln p$ compression plane,
κ^* Initial slope of the url in the $\ln v : \ln p'$ compression plane (hypoplasticity),
λ Lamé's first parameter,
λ Slope of the ncl in the $v : \ln p'$ compression plane,
λ^* Slope of the ncl in the $\ln v : \ln p'$ compression plane (hypoplasticity),
ν Poisson ratio,
ρ Soil (skeleton and water) bulk density,
ρ_d Soil dry bulk density,
ρ_s Skeleton (grains) bulk density,
ρ_w Water bulk density,
σ'_n Effective stress acting normal to the shear plane,
τ Local shear stress in the vertical plane (positive for pile loading, following the convention defined in Eq. 5.3, p. 95),
τ_{av} Depth average shaft stress ($= Q_s/A_E$),
ϕ' Effective stress friction angle,
ϕ'_{cs} Critical state effective stress friction angle,
ω Angular frequency,
∇ Del/Nabla operator.

Superscripts

$'$ Effective stress quantity,
n Time in the finite difference discretisation,
T Transpose of the matrix.

Subscripts

0	*In situ* conditions or initial state,
b	Outer boundary of the model,
c	Post-equalisation state,
cs	Critical state value,
i	Immediately after installation,
y	Yield value (apparent preconsolidation value).

Abbreviations

ALE	Arbitrary Lagrangian Eulerian,
CEL	Coupled Eulerian Lagrangian,
CEM	Cavity Expansion Method,
csl	Critical state line,
iso-ncl	Isotropic normal compression line,
MCC	Modified Cam clay,
ncl	Normal compression line,
OCR	Apparent overconsolidation ratio,
PIV	Particle image velocimetry,
RITSS	Remeshing and Interpolation Technique with Small Strain,
SPM	Strain Path Method,
SRD	Soil Resistance to Driving,
url	Unloading reloading line.

Chapter 1

Introduction

Since the beginning of the twentieth century, petroleum gained increasing importance in key economic sectors. Hydrocarbon production has surpassed coal during the 1950s and today, more than half the energy needs of the planet are met by oil and gas (BP, 2015).

Fig. 1.1 illustrates the increase in worldwide oil production. Except a for few relapses, production has grown each year since the 1950s, reaching 89 millions Barrels per day in 2014. Gas production followed the same trend, topping at 30 millions of Barrels of Oil Equivalent per day[1] in 2014.

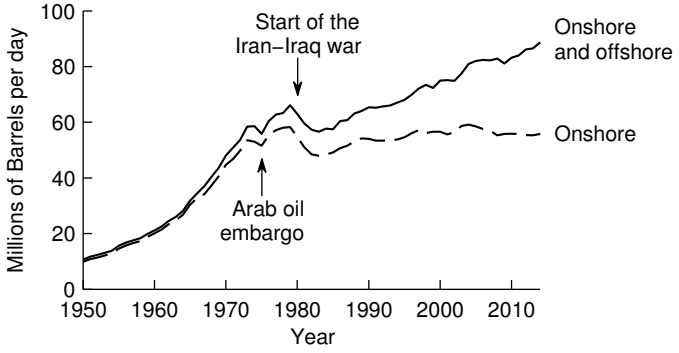

Figure 1.1 Worldwide oil production (data from Ferentinos, 2013; ENI, 2014; BP, 2015).

Drilling for oil is carried out either onshore or offshore. Although onshore oil represents over 65% of the total production, it has stagnated during the last 20 years while the growth in oil production has been mainly filled by offshore supply (Fig. 1.1).

The development of offshore oil began in 1947 in the Gulf of Mexico (Chakrabarti et al., 2005). Since, the offshore industry has seen many innovative structures, fixed and floating, placed in progressively deeper waters and in more challenging and

[1] 1 Barrel of oil = 0·159 m^3.

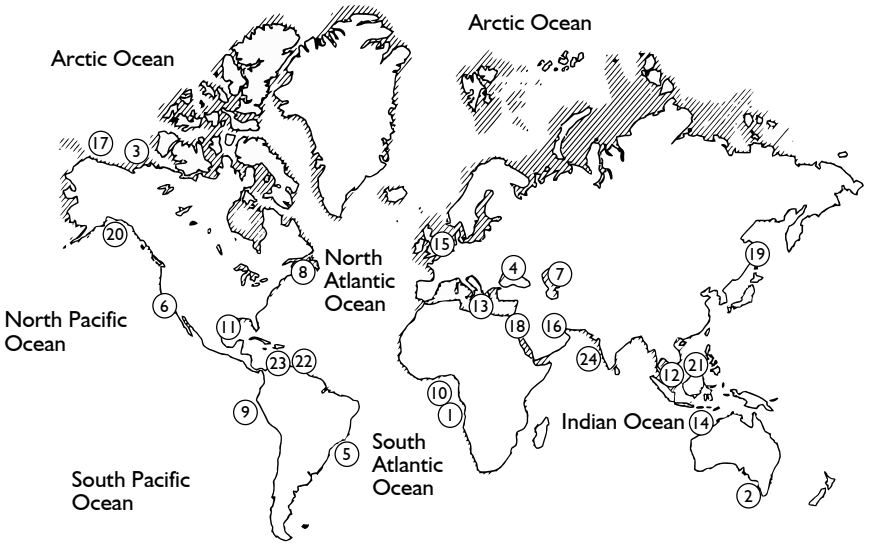

1	Angola	9	Ecuador and Peru	17	Prudhoe Bay
2	Bass Strait	10	Gulf of Guinea	18	Red Sea
3	Beaufort Sea	11	Gulf of Mexico	19	Sakhalin
4	Black Sea	12	Gulf of Thailand	20	South Alaska
5	Brazil	13	Mediterranean	21	South China Sea
6	California	14	North West Shelf	22	Trinidad and Tobago
7	Caspian Sea	15	North Sea	23	Venezuela
8	Atlantic Canada	16	Persian Gulf	24	West India

Figure 1.2 Major regions of offshore oil and gas drilling activity (after McClelland, 1974 and Dean, 2010; continental shelves are indicated by the shaded areas).

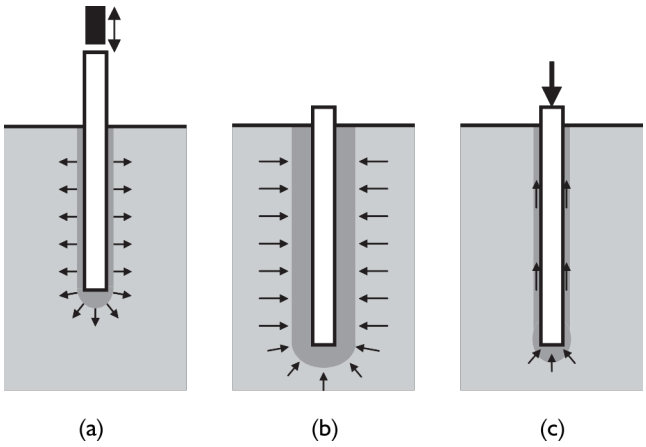

Figure 1.3 Three main stages in the life of a driven pile: (a) installation, (b) equalisation, and (c) loading (Randolph, 2003).

hostile environments. Today, there are more than 10 000 platforms worldwide (Chakrabarti et al., 2005). Fig. 1.2 shows the main offshore oil and gas producing areas of the world. Alongside the Gulf of Mexico, other major areas include the Persian Gulf, the Red Sea, the North Sea, and the Gulf of Guinea (Sandrea and Sandrea, 2007).

In recent years, another type of offshore structure has been on the rise: wind power. Installed in very shallow water (depths of less than 50 m; EWEA, 2015), there are over 2500 offshore wind turbines installed worldwide (EWEA, 2015), of which more than 91% can be found in European waters (equating to 8 GW of installed power), mainly in the North Sea (GWEC, 2015).

Each of these structures, in shallow or deep waters, needs to be anchored to the seabed, which is in most cases done with piled foundations. This lays the context of the research presented herein, *i.e.* why I followed a stream of people who studied offshore piles.

The following paragraphs present what happens during and after the installation of an offshore pile, what questions are still raised about it and how my research answers some of them.

The most common type of offshore pile is the open-ended steel pile which is driven into the ground by a hammer which repeatedly strikes a large mass on the pile head (Poulos, 1988; Randolph and Gourvenec, 2011). A driven pile is installed by displacing, rather than removing, the soil (Fig. 1.3a). The severe soil distortions imposed by the penetrating pile induce a change in the soil stress state around the pile. Once the pile has been driven to the required embedment, installation is stopped and the pile is left to 'rest' before it is eventually loaded, fulfilling its purpose (Fig. 1.3b and c).

Typically, offshore steel open-ended piles have an outer diameter (D) ranging from 1 to 2·5 m and a length (L) ranging from 40 to 150 m. Ratios of diameter to wall

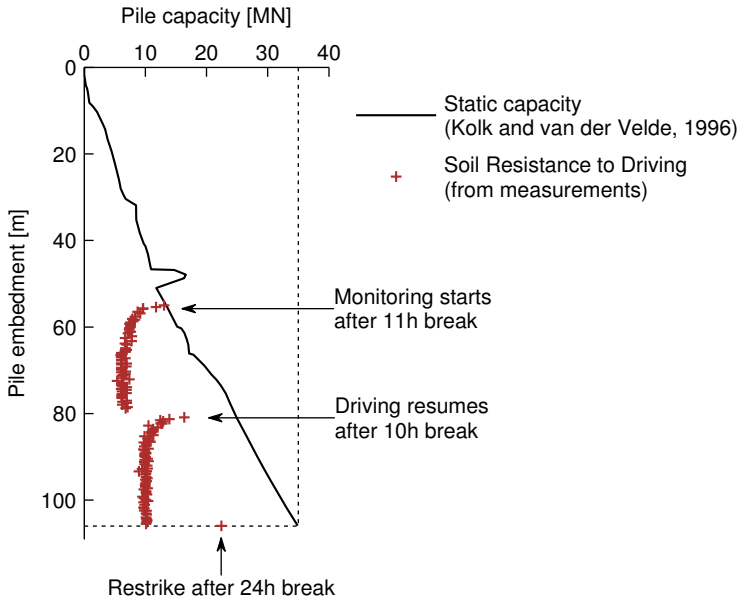

Figure 1.4 Static capacity and Soil Resistance to Driving of a pile driven in a soft clay (Gulf of Thailand; data courtesy of Fugro).

thickness (D/t) are between 20 and 60 (Dean, 2010). Design loads reaching 50 MN per pile (5000 tons) are common practice. Long piles are spliced in several sections which are driven and welded together on site (Cathie, 2012). As the piles are open-ended, most of the pile capacity stems from shaft friction (τ_f) while toe resistance (q_b) plays only a minor part.

In clays, two surprising phenomena are observed during pile installation and equalisation, which are illustrated by the following example. A pile is installed in a soft clay in the Gulf of Thailand. The pile is required to develop an axial static capacity of 35 MN. After studying local geology and performing relevant geotechnical site investigations, the required pile length to develop 35 MN is estimated to be 105 m (Fig. 1.4; Kolk and van der Velde, 1996).

Following its design, the pile is built in four sections, shipped on site and driven. During driving, monitoring of the pile allows one to estimate the axial pile capacity that would prevail under *static* loading conditions during each blow (Dean, 2010). This value is named the Soil Resistance to Driving (SRD) and is shown in Fig. 1.4 for the last two sections of the pile, where it can be compared to the computed static capacity. As the driving progresses, the Soil Resistance to Driving decreases even though the penetration depth increases: the soil around the pile weakens after each driving blow. On the other hand, when driving is resumed after a break, the Soil Resistance to Driving has increased: the soil around the pile has 'healed' leading to an increase in pile capacity over time; a phenomenon referred to as 'set-up' or

'freeze.'

This characteristic of increase in soil strength, *i.e.* set-up, is one of the most important considerations in planning a successful offshore pile installation (Vijayvergiya et al., 1977). Underestimation of soil set-up might result in unforeseen pile driving refusal. On the other hand, when easy driving is experienced near the design penetration because of the degradation of soil strength (as in the example of Fig. 1.4), the installation engineer might erroneously decide to drive the pile deeper than its design penetration. Both cases of ill-judgement would result in additional expensive offshore operations such as replacing the hammer or even jetting or drilling for the former and mobilization of additional pile materials for the latter.

Set-up is quantified by the set-up factor: the ratio of pile capacity after equalisation to the pile capacity at the end of driving. Set-up is most marked for clay soils for which the set-up factor can range from 1 to 6 (Poulos, 1988; Rausche et al., 2004) but is also displayed in chalk (Vijayvergiya et al., 1977) and sand (Jardine et al., 2006). A set-up factor inferior to 1 is sometimes found after driving in soils that are strongly dilatant such as heavily overconsolidated clays and silts (Randolph and Gourvenec, 2011), a case which is named 'set-down' or 'relaxation.'

In clays, soil degradation during driving and set-up during equalisation are mainly related to the generation and dissipation of excess pore pressure (Δu_w) around the pile. These pore pressures changes, alongside with an increase in total radial stress (σ_r), induce a change in the radial effective stress (σ'_r) acting on the pile wall. The latter governs the unit skin friction (τ_f) through the Coulomb friction law: $\tau_f \approx 0{\cdot}8\sigma'_r \tan\delta$ where δ is the angle of friction developed at the pile-soil interface (Jardine et al., 2005). As the present work focuses on the shaft behaviour of the pile, the set-up factor in this thesis is defined in terms of unit skin friction, which, assuming that δ is constant, is defined as:

$$\text{set-up factor} = \frac{\sigma'_{rc}}{\sigma'_{ri}}, \tag{1.1}$$

where σ'_{rc} and σ'_{ri} are the radial effective stresses after equalisation and installation, respectively.

The aim of this thesis is to understand, explain, and numerically predict soil set-up around the shaft of a driven pile. The thesis is divided in eight chapters, the content of which is summarised hereunder:

Chapter 2 reviews selected results of instrumented pile installations in clays. Twelve field locations, alongside with four laboratory studies, are presented. Measured values of stress and pore pressure on the pile toe, pile shaft, and in the soil during installation and equalisation are compiled and compared. Trends are outlined from which mechanisms are inferred.

Chapter 3 presents a literature review of previous simulation attempts of modelling pile installation and equalisation. Over the years, a limited number of rational methods have emerged; these are exposed and compared.

At the end of Chapter 3, the approach used in this work to model pile installation and equalisation is justified, based on the literature review of Chapters 2 and 3. The main novelty of the presented approach is to take into account the cycles of shaft-soil shearing occurring during driving.

Chapters 4 and 5 present the numerical tool developed. Chapter 4 describes the constitutive law chosen, which models the clay effective stress behaviour. Chapter 5 presents the pile driving model: a numerical model the aim of which is to predict the soil state around the shaft of a driven pile, during and after installation.

Chapter 6 explores the pile driving model capabilities and compares its output to the trends from the experimental results of Chapter 2. Chapter 6 also compares an open- and closed-ended installation and studies the influence of several constitutive parameters.

Chapter 7 compares the pile driving model result to a experimental pile installation in Bothkennar clay.

Finaly, *Chapter 8* offers a short summary of the conclusions from each chapter and presents perspectives for future research.

Chapter 2

Literature review: field and laboratory experiments

Over the last 50 years, tens of field and laboratory experiments have been conducted in order to comprehend the installation effects of offshore driven piles in clay. The ideal field experiment would involve accurate measurements of stress and pore pressure during and after the driving of an offshore pile, on the pile shaft and in the surrounding soil. That is unfortunately very difficult to obtain for three reasons.

First of all, the field experiments involve piles installed onshore because it is a much less hostile environment than offshore. In most cases however, the test sites are selected for having similar soil conditions to the one encountered offshore.

In field experiments, the timespan of a driving blow (Fig. 2.1a) prevents any measurements to be made *during* the pile movement. Furthermore, the violence of a hammer blow often implies that pile wall sensors are destroyed at the end of installation. Thus, the only measurements that can be made around a driven pile are soil measurements. Therefore, the majority of the field research of displacement piles uses jacked piles, which allows the pile sensors to survive the installation but also to measure stresses *during* penetration. As for scale models, the wave reflections on the boundary of the model and the scale effect compromise the possibility of driving a pile.

Thirdly, instrumenting an open-ended pile requires to have a thick pile wall, so that the instruments can be placed within. This is usually cost prohibitive.

Therefore, the available field experiments involve onshore jacked closed-ended piles, instead of offshore driven open-ended piles.

The physical quantities measured on the pile shaft are:

- Pore pressure u_w (saturated semi-conductor or strain-gauged transducers);
- Radial total stress σ_r (strain-gauged surface stress transducer);
- Shear stress τ (strain-gauged surface stress transducer or axial load cells),

and in the soil surrounding the pile:

- Pore pressure u_w (piezometer or transducer);

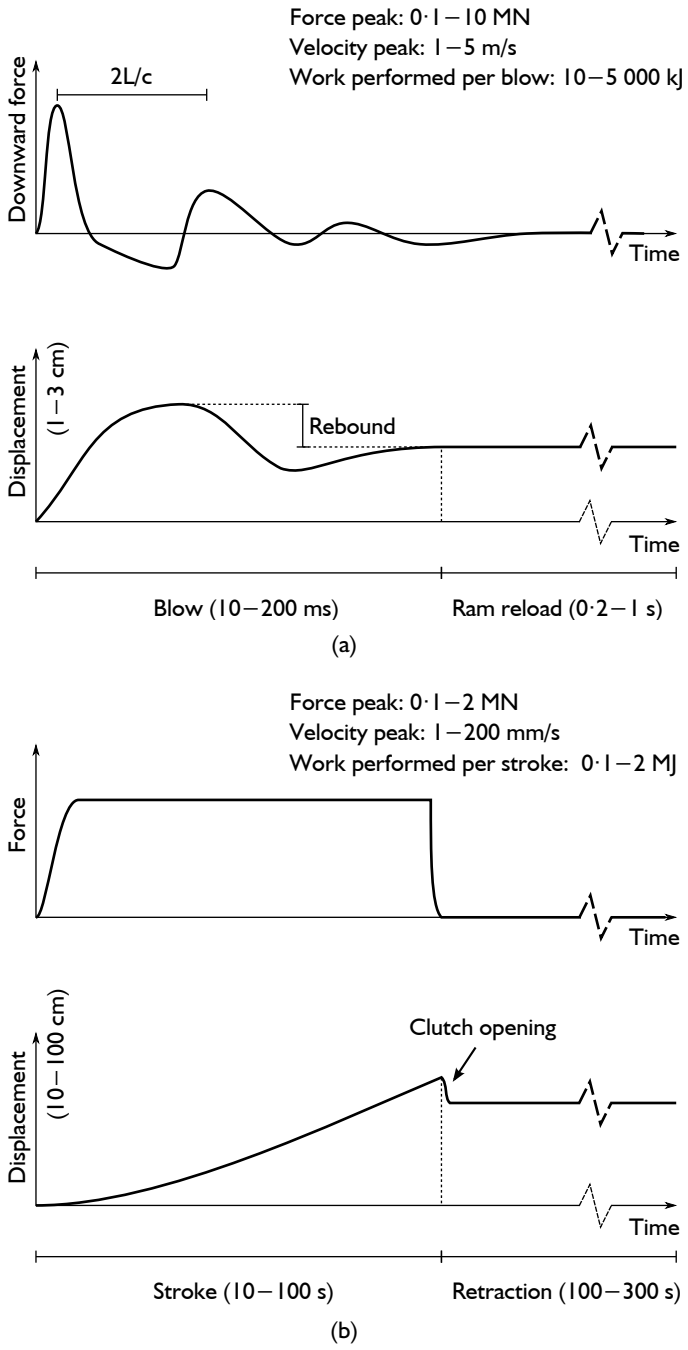

Figure 2.1 One event of the pile installation sequence by (a) driving and (b) jacking.

- Radial displacement u_r (inclinometer in field experiments; photographic inspection, X-ray, or particle image velocimetry [PIV] in laboratory experiments);
- Vertical displacement u_z (only through laboratory experiment with photographic inspection, X-ray, or PIV analysis).

Two stages of the life of a displacement pile are investigated in this chapter: installation and subsequent equalisation. During installation, the pile encounters a repetition of driving blows/jacking strokes (during which the pile is moving) interspersed by pauses, allowing for the ram to reload/the jack to retract (during which the pile is stationary). One event of this pile installation sequence is depicted in Fig. 2.1a and b for driving and jacking, respectively. After the last blow/stroke, the *equalisation* stage begins: the pile sits at its desired embedment, but the soil around is still under high stress and strain gradients, which tends towards an equilibrium over time. Equalisation is also called *set-up* or *(re)consolidation*, as the principal phenomena occurring is the dissipation of excess pore pressure created during the driving. As an illustration, Fig. 2.2 depicts a typical measurement result in an overconsolidated clay: the total radial stress and pore pressure measured at the pile shaft versus time, at the end of the last pause between the jacks, followed by the last jack stroke and subsequent equalisation.

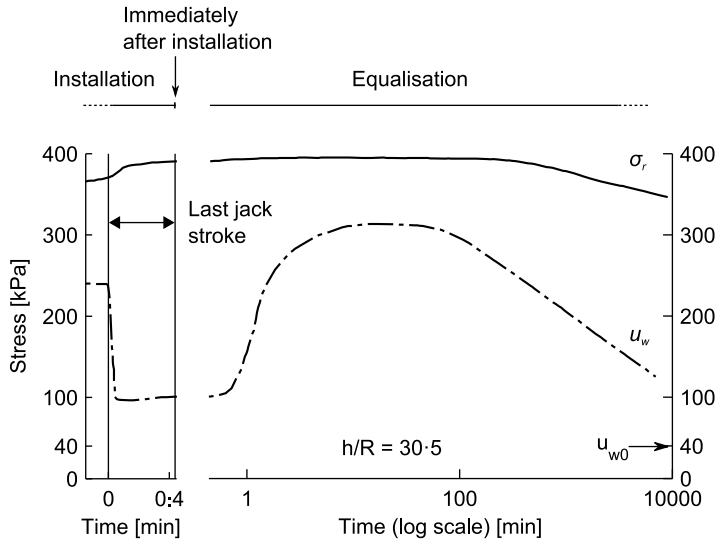

Figure 2.2 Illustration of the installation and equalisation stages using total radial stress and pore pressure measurements at the shaft of a jacked pile (data from Lehane and Jardine, 1994b, in stiff overconsolidated Cowden clay).

This chapter is divided into five sections. The first section lists the research groups investigated. The three following sections report the observations withdrawn from the selected literature: Section 2.2 includes observations reported *during* the

actual movement of the pile, Section 2.3 presents measurements obtained when the pile is stationary, immediately after the end of driving and Section 2.4 covers the equalisation phase. Finally, Section 2.5 concludes this chapter.

2.1 Selected database of displacement pile installations in clay

The gathered database of displacement pile installations in clay was selected from the literature because the following criteria were met:

- The speed of penetration was fast enough for it to be considered undrained;
- The clay characteristics were established with reasonable reliability;
- The installation procedure, as well as the measurement gear, were described with care and precision;
- The published measurements were accessible;
- The results were rationally criticised by the authors.

The measurements database presented comprises seven research groups of field experiments and four of laboratory studies, respectively described in Sections 2.1.1 and 2.1.2.

2.1.1 Field experiments

This section, with Tables 2.3 and 2.4 (pp. 14–15), describes the field experiments data of the seven selected research groups. Among these seven: the first four report measurements at the pile wall, the fifth proposes measurements both on and around the pile, and the last two focus on measurements in the soil around the pile.

Imperial College The Imperial College instrumented pile (ICP) is a cone-ended test pile which has three or four instrumented sections. Each cluster of instruments contains one axial load cell measuring the axial load, two diametrically opposite pore pressure probes and one surface stress transducer measuring radial total stress, local shear stress and temperature. Four different clay installation sites were investigated: Canons Park (London clay), Cowden, Bothkennar, and Pentre.

The Canons Park test site comprises London clay, a stiff highly overconsolidated clay of high plasticity (Bond and Jardine, 1991). Two 7 m long ICPs were used to perform four installations. The piles were jacked in a series of 225 mm long jack pushes at rates varying from 1·3 to 8·3 mm/s.

Lehane and Jardine (1994b) used four ICPs to investigate displacement pile behaviour in Cowden till, a stiff glacial soil. The jacking penetration rate was 8·3 mm/s.

The third site investigated by Imperial College is located at Bothkennar, where the soil is composed of a soft cemented organic sensitive lightly overconsolidated clay (Lehane and Jardine, 1994a). Again, four ICPs where jacked at 8·3 mm/s.

At the Pentre test site, Chow (1996) performed seven installations of a longer 21 m ICP. Pentre clay-silt combines the index properties of a silty clay with a uniform silt-sized grading, laminated macro-fabric, high permeability and fast consolidation characteristics. Its clay particles are aggregated into silt size packs that can be broken down by large shearing, making Pentre clay-silt behave differently than other low plasticity clays (Jardine et al., 2012). High permeability meant that partial drainage between the jacks was unavoidable. Length of the jack strokes were varied (0·025 to 1·5 m), as was rate of jacking (11 to 30 mm/s) and the length of equalisation period (15 hours to 3 days).

Massachusetts Institute of Technology The Piezo-Lateral Stress (PLS) cell was introduced by the MIT in 1978. It consist of an instrumented cone-ended model pile fitted with one level of sensors. The PLS cell sensors position is aimed at capturing data that has minimum influence from the pile toe, as it is located at least at 40 radii from it ($h/R > 40$). Nine PLS cell jackings were performed between 1980 and 1984, at typical penetration speeds of 20 mm/s, at two sites: Empire, Louisiana (Azzouz and Lutz, 1986) and Saugus, Massachusetts (Azzouz and Morrison, 1988).

From Azzouz and Lutz (1986), I present the results of the first layer of Empire clay ('zone 1' in their Paper), located between 35 and 50 m from ground level, whose characteristics are very uniform. In this layer, Empire clay is a plastic lightly overconsolidated clay.

In Saugus (Azzouz and Morrison, 1988), measurements were limited to the Boston Blue clay layer (which is located at depths below 23 m), also because of its homogeneity. The Boston Blue clay at this depth is a sensitive lightly overconsolidated marine illitic clay. I fetched some additional Boston Blue clay characteristics from Ladd et al. (1980).

Oxford University The *in situ* model pile (IMP) is a closed- or open-ended tubular 1·14 m long instrumented device that is attached to a pile toe. Coop (1987) and Coop and Wroth (1989) report the use of the IMP in four test sites; three of which are presented here: Madingley (Gault clay), Canons Park (London clay), and Huntspill. The data presented in this report stems from closed-ended tests only, where the pile was jacked at 3·8 mm/s (45 cm stroke).

The Gault clay present at Madingley is a stiff, heavily overconsolidated clay. Six successful IMP soundings were performed at this site.

The Canons Park test site, which has been hereinabove mentioned, comprises the heavily overconsolidated London clay. One IMP penetration was made at this location.

Huntspill's soil is a soft normally consolidated silty clay, although agricultural drainage has given rise to an overconsolidated crust. Two successful tests were made at this site.

Federal University of Rio de Janeiro Soares and Dias (1989) installed a large diameter closed-ended pile jacked (5 mm/s) in soft gray Rio de Janeiro clay. The pile contained

two instrumented clusters at the shaft and one at the pile toe.

Norwegian Geotechnical Institute Between 1980 and 1984, the NGI built two flat closed-ended 5·15 m long instrumented piles (Karlsrud and Haugen, 1985; Karlsrud, 2012). The two piles were jacked respectively one and 16 times in Haga, a test site containing an homogeneous (to a depth of 4·5 m) marine firm sensitive leached clay oversonsolidated primarily as a result of the removal of 6 m of overburden at the test site. Despite being overconsolidated, the Haga clay displays characteristics of lightly overconsolidated clays, e.g. a high liquidity index and a contractant response when sheared (Lehane, 1992). The piles had at least four instrumented clusters containing earth pressure cells, pore pressure cells, and sometimes, strain gauges. Prior to the first pile installation, six free field piezometers were installed alongside to the first pile, 2·6 m below ground surface where the apparent overconsolidation ratio was 5.

The Norwegian Geotechnical Institute performed field installations on four other sites: Pentre and Tilbrook in the U.K. and Onsøy and Lierstranda in Norway. Although made with much precision and care, the total stress measurements were under recorded (Chow, 1996; Jardine et al., 2012) and there was a large scatter around the pore pressure measurements (Karlsrud, 2012). Furthermore, the clays encountered in Onsøy and Lierstranda displayed singular characteristics such as very high set-up and were categorised as 'problematic soils' (Jardine et al., 2012) For all these reasons I chose not to include these measurements in this chapter.

Université Laval Roy et al. (1981) and Konrad and Roy (1987) jacked respectively six and one closed-ended piles in the soft sensitive Champlain clay in Saint-Alban. Installation rates varied between 0·3, 0·6, and 2·3 mm/s. Roy and Lemieux (1986) subsequently used two remaining piles to study their long term behaviour.

Berkeley Pestana et al. (2002) drove a closed-ended steel pile in Young Bay Mud, while measuring the excess pore pressure and horizontal deformation at three distinct radial distances from the pile shaft and at several depths. Piezometers were used to measure pore pressure and inclinometers to compute horizontal deformation. A pre-augered 5 m deep section was drilled prior to installation and the pile was driven in three 12·2 m sections (Hunt et al., 2000).

The site soil profile is composed of two Yound Bay Mud layers, a soft plastic sensitive marine clay, interrupted by a thin sandy layer at a depth of 15·5 m. In a companion paper, Hunt et al. (2002) reports soil characteristics before and after driving from soil samples collected close to the pile.

Table 2.1 Consistency scale used in Table 2.3 (from Atkinson, 2007).

Consistency	*Undrained strength* s_{u0} *[kPa]*
Very soft	< 20
Soft	20–40
Firm	40–75
Stiff	75-150
Hard	> 150

Table 2.2 Plasticity scale used in Table 2.3 (from Burmister, 1949, cited by Das, 2006).

Classification	*PI*
Non plastic	0
Slightly plastic	1–5
Low plasticity	5–10
Intermediate plasticity	10–20
High plasticity	20–40
Very high plasticity	> 40

Table 2.3 Field experiments database – soil description.

Clay	*Consis-tency*	*OCR*	*PI [%]*	*LI*	*Sensi-tivity*	*Reference(s)*
Imperial College						
London	Stiff	50–20	35–45	0	1*	Bond and Jardine (1991)
Cowden	Stiff	10–2	19	—0·2	1*	Lehane and Jardine (1994b)
Bothkennar	Soft	1·7	25–50	0·5-0·9	5	Lehane and Jardine (1994a)
Pentre	Soft to firm	3–1·6	10–23	0·7-0·2	0·7–3·1	Chow (1996)
Massachusetts Institute of Technology						
Empire	Soft to stiff	1·7	60	0·3	2 ± 1	Azzouz and Lutz (1986)
Boston Blue	Soft	1·2	21	1	7 ± 2	Azzouz and Morrison (1988)
Federal University of Rio de Janeiro						
Rio de Janeiro	Very soft	2·5–1·7	60	1·6	N.A.	Soares and Dias (1989)
Oxford University						
Gault	Stiff	10–5	48	0	N.A.	Coop and Wroth (1989)
London	Stiff	50–20	45	0	1*	Coop (1987)
Huntspill	Soft	3–1	35	1	N.A.	Coop and Wroth (1989)
Nowegian Geotechnical Institute						
Haga	Firm	17–3	15	1	4–6	Karlsrud and Haugen (1985); Karlsrud (2012)
Université Laval						
Champlain	Soft	2·2	27–11	2·3	14–22	Roy et al. (1981); Konrad and Roy (1987)
Berkeley						
Young Bay	Soft	1·3	40	0·9	N.A.	Pestana et al. (2002)

NOTES: The soil consistency scale is reproduced in Table 2.1; N.A.: not available.

* Described as 'insensitive' in Lehane and Jardine (1994a).

Table 2.4 Field experiments database - piles description.

Clay	*Name*	*D (mm)*	L_E *(m)*	*Sensor(s) h/R*	*Note(s)*	*# tests*	Data collected
Imperial College							
London	ICP	102	4·1–6·2	5, 30, 53*	J-C$^{60°}$	4	(u_w, σ_r, τ) on pile shaft
Cowden	ICP	102	3·6 or 6·4	"	J-C$^{60°}$	4	"
Bothkennar	ICP	102	3·2 or 6	"	J-C$^{60°}$	4	"
Pentre	ICP	102	14–19	5, 30, 53, 75†	J-C$^{60°}$	7	"
Massachusetts Institute of Technology							
Empire	PLS	38·4	50, 77	95	J-C$^{60°}$	2	"
Boston Blue	PLS	38·4	26–39	49	J-C$^{60°}$	6	(u_w, σ_r, τ) on pile shaft
Federal University of Rio de Janeiro							
Rio de Janeiro		220	7	0‡, 13·8, 25	J-C$^{60°}$	1	(u_w, σ_r) on pile shaft
Oxford University							
Gault	IMP	80	6·5–8	0§, 4, 20	J-C	6	(u_w, σ_r, τ) on pile shaft
London	IMP	80	5	"	J-C	1	"
Huntspill	IMP	80	6 and 9	"	J-C	2	"
Nowegian Geotechnical Institute							
Haga		153	5	5·2, 22·9, 42·5, 60·8	J-C	17	(u_w, σ_r) on pile shaft
Université Laval							
Champlain		219	7·6	1·2, 15·4, 29·2, 42·8	J-C	7	u_w on pile shaft and soil
Berkeley							
Young Bay		610	35·7	–	D-C	1	(u_w, u_r) in soil

NOTES: D: pile diameter; R: pile radius; L_E: pile embedment; h: vertical distance from pile toe; J: jacked, D: driven; C: closed-ended; C$^{60°}$: 60° cone closed-ended.

* Location of the u_w sensors; σ_r and τ sensors were at $h/R = 8$, 28 and 50;

† Location of the u_w sensors; σ_r and τ sensors were at $h/R = 8$, 27, 50 and 72;

‡ At the pile toe, pore pressure and toe resistance were measured;

§ At pile toe, only pore pressure was measured.

2.1.2 Laboratory experiments

Four laboratory experiments are presented hereunder and in Table 2.5. During field experiments, even slow jacking speeds induces an undrained penetration.[1] For laboratory studies however, the small radii of the model piles implies that slow penetration rates can result in significant drainage occurring during penetration. Therefore, the normalised penetration velocity is introduced (Randolph and Hope, 2004):

$$V = \frac{v_{z,p} D}{c_h}, \tag{2.1}$$

where $v_{z,p}$ is the pile penetration velocity, D is the pile diameter, and c_h is the horizontal consolidation coefficient. Normalised velocities exceeding 30 are likely to be undrained (as explained in the upcoming Section 2.2f, p. 20; Randolph and Gourvenec, 2011). Table 2.5 shows the normalised velocities for each of the investigated laboratory study.[2]

Randolph, Steenfelt and Wroth (1979) jacked, in a single 3 s motion, one flat closed-ended 16 mm diameter pile in a semi-circular cylinder of speswhite kaolin (300 mm in diameter and $\sim$ 400 mm high). The semi-cylinder plane surface was a transparent perspex plate. Previous to the pile installation, the clay resting against the plane surface was marked with grid lines using a felt-tip pen. Photographs were taken before and after installation, from which soil displacement was computed: assuming that all the particles in a particular line parallel to the pile axis undergo a similar displacement path, the movement of any such particle was tracked, analysing the end-of-installation photograph taken, by considering different particles on the same vertical grid line but at different positions relative to the pile toe.

Steenfelt et al. (1981) jacked, in a single motion of $\sim$ 8 s, four 19 mm diameter conical closed-ended piles in a cylindrical sample of speswhite kaolin (250 mm in diameter and 600 mm high). Displacement measured by placing lead shots in the clay sample. There were 2 $\times$ 12 rows $\times$ 13 radii of 2 mm diameter lead shots placed.

Lehane and Gill (2004) jacked, in approximately 70 pushes, a 12·7 mm diameter flat closed-ended model pile in transparent soil. Two identical experiments were performed. The soil consisted of a mixture of amorphous fumed silica (mean diameter 0·014 μm) and de-aired fluid, both of which had a matching refractive index. Soil movements were recorded by tracking twelve 'targets' (black 2 μm diameter spherical beads) within the transparent soil using a 'videoextensometer' (Messphysik, 1996, cited by Lehane and Gill, 2004). The glass chamber containing the experiment was 800 mm deep with dimensions in plan of 160 $\times$ 280 mm.

Ni et al. (2010) jacked, in a single 114 s motion, four 8 mm diameter flat closed-ended piles in a parallelepiped sample of transparent soil (100 mm long and wide,

[1] It should be noted that Chow (1996), in moderate permeability Pentre clay–silt, did come across partially drained installation.

[2] As consolidation is dominated by radial water flow (this is reported in Section 2.4a, p. 32), the horizontal coefficient of consolidation (c_h) has been chosen instead of the usual vertical one (c_v) (Chung et al., 2006). Nevertheless, when c_h was not available, c_v was used.

Table 2.5 Laboratory experiments database.

Reference	*Soil*	*D (mm)*	L_E/R	*V*	*Technology*
Randolph, Steenfelt and Wroth (1979)	Kaolin	16	88	3000 >	Felt-tip pen
Steenfelt et al. (1981)	Kaolin	19	46	800 >	X-rays
Lehane and Gill (2004)	Transparent	12·7	57*	27	Video-extenso-meter
Ni et al. (2010)	Transparent	8	10	6	PIV

* This is the average normalised velocity.

and 160–200 mm high) saturated with a blend of two mineral oils. Displacement was measured using light-reflecting target particles and a PIV software (White et al., 2003) on images taken of the soil sample while being illuminated by a vertical light sheet of uniform intensity.

2.2 Pile installation – Moving pile

This section covers the field and laboratory measurements made *during* the actual movement of the pile. Excluded from this section are measurements made while the pile was stationary during installation, *e.g.* during the jack retraction. This section is divided, as are the next two ones, into subsections relating the measurements made: (a) pore pressure, (b) radial total stress, (c) radial effective stress, (d) shear stress, (e) displacement, and (f) other observations.

Research teams that published data during the movement of the pile are Imperial College and Oxford University for the field experiments (which cover measurements of pore pressure, total radial stress and shear stress on the shaft of a jacked pile), and Randolph, Steenfelt and Wroth (1979) and Lehane and Gill (2004) for the laboratory studies (which report soil displacement measurements around a jacked model pile).

This section and the following two sections are trying to relate the observations to the critical state theory (Fig. 2.3): a lightly overconsolidated soil stands on the wet side of the critical state line (csl) and tends to contract when being sheared. This implies a reduction in effective mean stress and, if the total stress is constant, a rise of excess pore pressure (Δu_w). An overconsolidated soil on the other hand stands on the dry side of critical and exhibits contrary behaviour in terms of stress. Nevertheless, the (radial) effective stress must be apprehended with care because it is computed from pore pressure and total stress measurements. This can be harmful when pore pressure and total stress are in the same range, which implies that small errors in the measurements (*e.g.* 1%) can lead to significant errors in the computed effective stress (hundreds of %; Azzouz and Morrison, 1988).

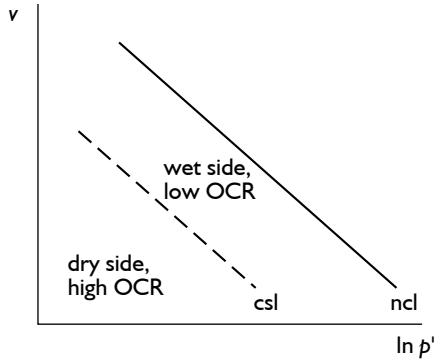

Figure 2.3 Normal compression line (ncl) and critical state line (csl); the latter separates the 'wet' and 'dry' sides of critical, equivalent to lightly and heavily overconsolidated states for clays, respectively (after Schofield and Wroth, 1968).

(a) Pore pressure

On the shaft of a jacked pile, pore pressure (u_w) recorded while the pile was moving was always less than the stationary value measured during the installation pause periods. At the beginning of a jacking stage, pore pressure reduced (negative excess pore pressure Δu_w) and remained at a lower value as the pile penetrated the ground (Fig. 2.2).

This was observed regardless of the overconsolidation ratio or any other soil characteristics when two criteria were met: (1) Pile movement was fast enough to imply undrained conditions and (2) The pore pressure sensor was entering *presheared* soil (*i.e.* soil that had been sheared in a previous jacking stage, in contrast with *virgin* soil).

When entering a virgin material (at undrained rates), the excess pore pressure during movement on the pile shaft was positive in the lightly overconsolidated Pentre clay-silt and Boston Blue clay (Chow, 1996; Azzouz and Morrison, 1988). London, Cowden, and Bothkennar clays do not share this trend: there was pore pressure reduction during pile movement regardless of the virgin or non virgin soil state, implying that the soil had already been presheared by the heavy distortion brought by the toe insertion.

Values of pore pressures (u_w) during pile movement were always positive in the lightly overconsolidated Bothkennar clay, but were negative close to the pile toe in Cowden till and negative along the entire shaft in the very heavily overconsolidated London clay (Lehane and Jardine, 1994a).

It should be noted that during movement, pore pressure measurements made on opposite sides of the pile often differed, sometimes by as much as 200 kPa (Coop, 1987; Lehane and Jardine, 1994b; Chow, 1996). After dissipation the measurements returned to within ±10 kPa of ambient conditions. These variations in readings may be due to irregularities on the pile surface, differences in probe response times,

lateral variations in soil conditions, or eccentric loading (Chow, 1996).

(b) Radial total stress

As illustrated in Fig. 2.2, during pile movement, the total radial stress (σ_r) at any pile shaft sensor showed a slight increase. The first observation is that the variation of σ_r is much smaller than the pore pressure variation.

To understand what this variation shows, two points must be made. First of all, there is negligible variation of total radial stress between the jacking stages (assuming they are short enough) (Bond and Jardine, 1991). Therefore, during installation, all the changes in σ_r occur during pile movement. Secondly, it will be shown, in Section 2.3c, that the radial total stress at a particular soil horizon falls as the pile advances.

Having these two facts in mind, one can distinguish between two effects explaining the variation of total radial stress during pile movement: (1) the shaft-soil shearing induces a change in σ_r and (2) the increase in penetration depth induces an increase in σ_r.

Fig. 2.2 shows a slight increase in total radial stress during pile movement. This increase is due to the fact that during the stroke, the pile advances 220 mm down and the overburden total radial stress increases with depth. In the light of all those facts, it can be concluded that the pile movement induces a *decrease* in total radial stress (σ_r) for a particular soil horizon. Although Fig. 2.2 shows measurements made in an overconsolidated clay, the above conclusion is also accurate for lightly overconsolidated clays (Lehane and Jardine, 1994a).

Values of the total radial stress during installation on pile shaft were seen, by Lehane and Jardine (1994a), to lie between the initial undisturbed horizontal stress (σ_{r0}) and the limit pressure measured in self-boring pressuremeter tests (p_L).

(c) Radial effective stress

From the pore pressure and total stress measurements, the radial effective stress (σ'_r) can be computed. It is important to bear in mind that effective stress is computed, especially when pore pressure and total stress are in the same range, which could lead to loss of significance errors.

During the pile movement, the pore water pressure decreases considerably, compared to the variation of total radial stress. Therefore σ'_r increases during pile movement, implying a dilatant behaviour (corresponding to a state on the dry side of csl) of the soil in contact with the pile.

(d) Shear stress

Shaft shear stress can be measured and computed three different ways:

(i) The depth average shaft stress $\tau_{av} = Q_s/A_E$ where Q_s is the shaft load and A_E the embedded shaft area;

(ii) The average shear stress f_s measured between two instrument clusters (containing axial load cells); and

(iii) The local shear stress τ from a surface stress transducer.

Likewise toe resistance, in the Bothkennar and Pentre lightly overconsolidated clays, long jack strokes (50 cm and above) brought the average shear stress τ_{av} to reduce from a maximum at the start of the jack stroke to a minimum at the end (Lehane and Jardine, 1994a; Chow, 1996). For short 2·5 cm jack strokes (which are closer to the set encountered after each driving blow), no reduction in τ_{av} was visible over each individual stroke (Fig. 2.4). However, τ_{av} reduced overall during a series of short strokes. In the overconsolidated Cowden till and Gault clay, τ_{av} was seen to increase during each jack stroke.

The change of τ_{av} as jacking progresses concurs with the change in Soil Resistance to Driving during the first few blows of driving (depicted in Fig. 1.4, p. 4).

The f_s response resembled the τ_{av} one (Chow, 1996) and the surface stress transducer readings (τ) showed the same trends, only with a higher degree of variation.

This behaviour cannot be explained by the critical state soil mechanics framework (Fig. 2.3) which, for a particular void ratio, would predict the same ultimate shear strength for each and every jack stroke. This point is highlighted in Section 4.5.3c, p 87.

(e) Displacement

Soil displacement measurements *during* the pile push cannot, to my knowledge, be achieved during field installation. Therefore only laboratory testing can offer an insight into displacement patterns around the pile during installation.

Fig. 2.5 depicts the soil trajectories during pile movement from two laboratory model pile installations performed by Randolph, Steenfelt and Wroth (1979) and Lehane and Gill (2004). Although the latter experiment cannot be considered undrained ($V_{av} = 6$, see Table 2.5), it is presented for lack of better comparison. The following observations can be noted: (1) A vertical component of movement is caused by a pressure bulb ahead of the pile toe; (2) Negligible vertical displacement occur at a radial distance of $3R$ from pile centreline, where radial displacement is the predominant mode of deformation; (3) A soil particle begins to move when the pile toe is approximately 5 radii above the particle location.

As the installation progresses, further vertical soil movement happens due to the pure shearing imposed by the pile shaft. Unfortunately, the displacement paths during shaft-soil shearing have not been precisely recorded. In the next section, the final displacement (due to the toe insertion and the shaft-soil shearing) is presented.

(f) Other observations

Cycles During a hammer blow, upward displacement waves reflected from the pile shaft or toe create a rebound during the pile penetration (Fig. 2.1a). This rebound

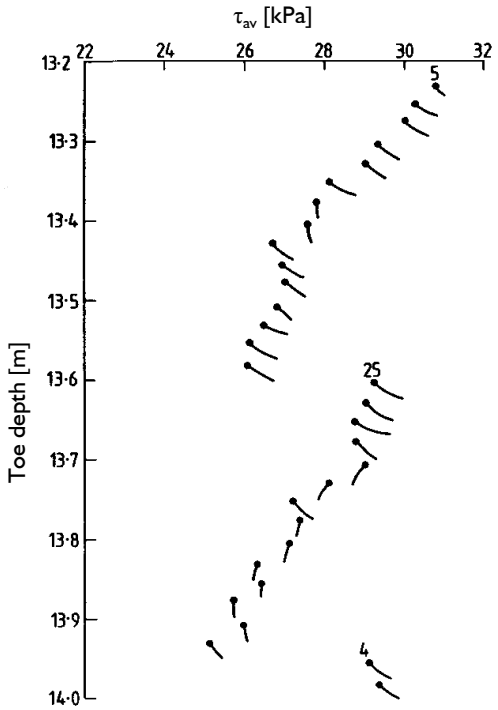

Figure 2.4 Average shaft shear stresses (τ_{av}) during jacking in Pentre clay-silt. Each line represents a 2·5 cm jack stroke and numbers denote pause period, in minutes, before each jacking stage (only pauses greater than 2 minutes are written) (Chow, 1996).

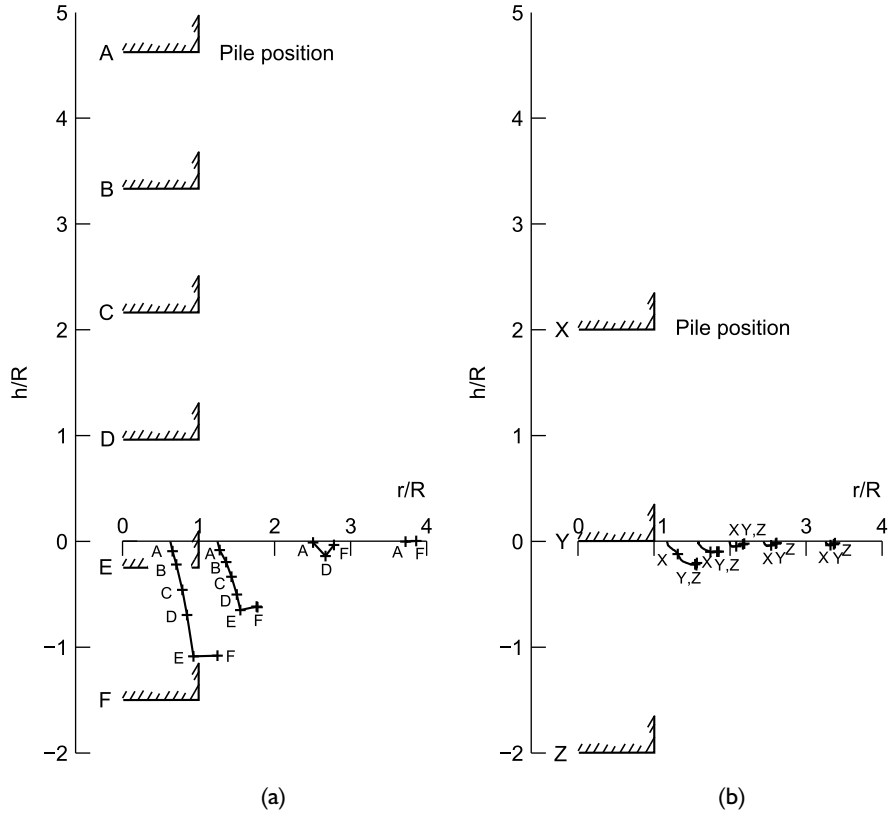

Figure 2.5 Soil trajectories during laboratory pile jacking in (a) spestone kaolin clay and (b) transparent soil (data respectively from Randolph, Steenfelt and Wroth, 1979 and Lehane and Gill, 2004).

induces a strain path reversal (*i.e.* a strain cycle). For a jacked pile, following the stroke of the jack, the jack clutch is opened which allows the pile to pull out of the soil. Albeit to a lesser extent, this also induces a strain cycle. Unfortunately, the cyclic effect of the pile push has not been come across in the literature.

Rate effects In low permeability soils, the rate of penetration is of utmost importance for the pile response during installation. The importance of rate dependence of clays was first appreciated by Taylor (1942), since which extensive research has been realised. The following paragraphs offer a very brief review of rate effects on the cone resistance of a piezocone, instead of the shaft friction, because the latter is harder to measure. Therefore, investigations of rate effect on shaft friction are rare (Litkouthi and Poskitt, 1980). Nevertheless, similar rate effects are expected between shaft and toe (Litkouthi and Poskitt, 1980), in the same way that the same rate effects can be observed between the cone resistance and triaxial or simple shear testing (Kulhawy and Mayne, 1980; Robinson and Brown, 2013).

In order to illustrate the rate effects, Fig. 2.6a depicts the net cone resistance of a piezocone $q_{c,net}$ relative to the normalised penetration velocity (V, introduced in Eq. 2.1) from three laboratory experiments not described in Section 2.1.2. Fig. 2.6b depicts the normalised excess pore pressure measured behind the advancing cone (u_2) versus V. Randolph and Hope (2004) performed a model piezocone installation in a 100 g centrifuge test in kaolin clay. Kim et al. (2008) installed two piezocones *in situ* in silty clay in Indiana. Litkouthi and Poskitt (1980) performed a model pile installation in a 25·4 cm high London clay sample during which pore pressure was not measured. Therefore Litkouthi and Poskitt (1980)'s data is presented in term of q_c rather than $q_{c,net}$ which, being normalised, can be compared to the other two experiments thanks to the fact that soil properties are reasonably constant through the short sample height (Litkouthi and Poskitt, 1980). Furthermore, in the absence of specific data, a coefficient of consolidation c_h of $2\,m^2$/year was chosen to compute V for Litkouthi and Poskitt (1980)'s data.

Alongside the experimental data of Fig. 2.6a is depicted a 'backbone' (or transition) curve introduced by Randolph and Hope (2004):

$$\frac{q}{q_{ref}} = \left(1 + \frac{b}{1 + c\,V^d}\right)\left(1 + \frac{\lambda}{\ln 10}\left[\sinh^{-1}\frac{V}{V_0} - \sinh^{-1}\frac{V}{V_{ref}}\right]\right),$$

where parameters $b = 3$, $c = 0.5$, $d = 1$, $\lambda = 0.2$, $V_0 = 10$, and $V_{ref} = 100$ control the shape of the backbone curve.

Three stages can be inferred from Fig. 2.6a. For very low penetration speeds ($V < 0{\cdot}3$), the installation process is fully drained: the penetration rate is slow enough for the pore pressures generated to fully dissipate as soon as they are created. However, the low permeability of clayey soils precludes this drained stage to be ever come across *in situ*, even during static pile loading (Quinn et al., 2012). For these low penetration speeds, a shear strength plateau is expected to exist, as depicted by the dotted extension of the backbone curve in Fig. 2.6a.

As the rate of cone penetration increases, a transition from drained to undrained behaviour occurs. The consolidation becomes only partial as some pore pressure is

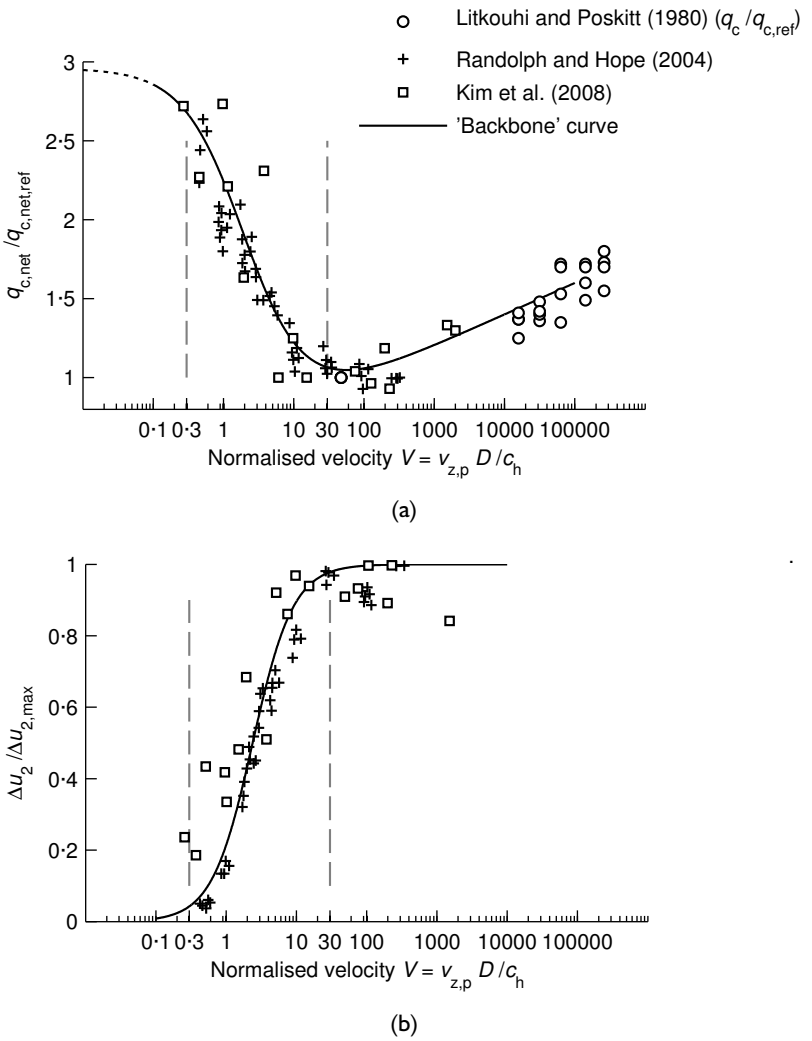

Figure 2.6 (a) Cone resistance and (b) Excess pore pressure behind the shoulder versus normalised penetration velocity *V*.

generated while the cone advances through the soil (Fig. 2.6b). This transition zone sees the cone resistance decrease to a minimum attained when the the penetration process becomes fully undrained. The transition between drained to undrained penetration occurs between V values of 0·1 to 30 (Randolph and Hope, 2004; Kim et al., 2008).

Above V values of 30 the penetration process is fully undrained. At this point, the cone resistance trend is reversed as it increases with increasing V. The experimental data presented on Fig. 2.6a depicts an increase in cone resistance of 20% for each log cycle increase in V. The physical processes behind this increase in resistance is associated with the adsorbed water in the electrostatic double layer that surrounds clay minerals. Relative movement between particles takes place within this water which, due to strong molecular forces, gives rise to a viscous resistance (Litkouthi and Poskitt, 1980). This behaviour is referred to as a viscous, damping, or even 'dynamic' effect. Rate effects are generally accepted to fall in a framework described by Tatsuoka (2007).

Although the normalised velocities of the jacked piles reported in this section cover 2½ orders of magnitude (V ranging from 10^3 to 5×10^5 for the field tests), the range of penetration speeds for each individual field test was too narrow to outline any rate effects.

Finally, it should be noted that the high velocities encountered during driving blows (see Fig. 2.1, p. 8) are in excess of 10^7. These values are outside the scope of any measurement.

The literature review of viscous effects of soil behaviour before failure is somewhat mitigated. Some experiments report that small strain soil stiffness G_0 is independent of rate (Brown et al., 2006) but recent experimental evidence shows the contrary, where G_0 is seen to decrease with increasing shearing rate (Robinson and Brown, 2013).

2.3 Pile installation – Immediately after installation

This section presents the data measured *immediately* after installation of the pile, not allowing any time for the equalisation stage to commence. This precision is particularly important for shaft measurements which vary considerably in the first few minutes after installation (this is discussed in Section 2.4) but soil measurements are less sensible to this pattern. The subscript 'i' is used to denote quantities measured immediately after installation.

(a) Pore pressure

Fig. 2.7 depicts the excess pore pressure at the end of installation (Δu_{wi}), measured at 20 cm from pile shaft from four vertical locations. Above the pile toe ($h > 0$), excess pore pressure decreases with increasing h, an observation referred to as the 'h/R effect.' The h/R effect for pore pressure in the soil surrounding the pile has also been observed by Pestana et al. (2002). Below the pile toe however, Fig. 2.7

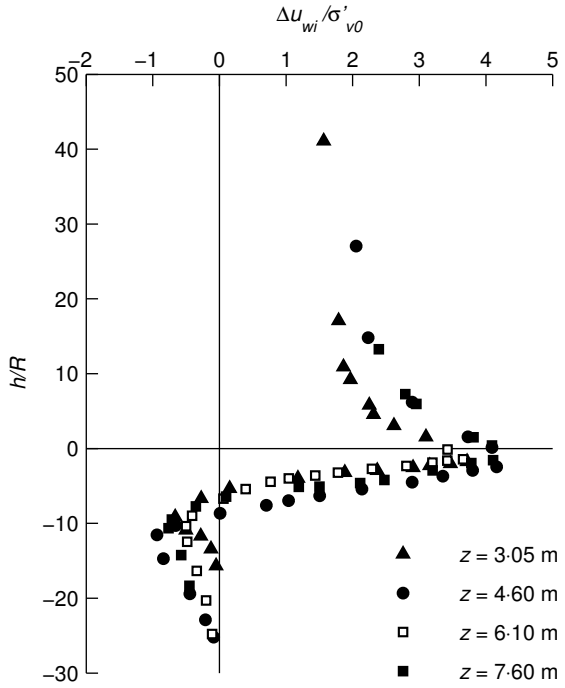

Figure 2.7 Normalised excess pore pressure at 1·8*R* (20 cm) from pile shaft during pile penetration, measured from four pore pressure cells (data from Roy et al., 1981, Champlain clay).

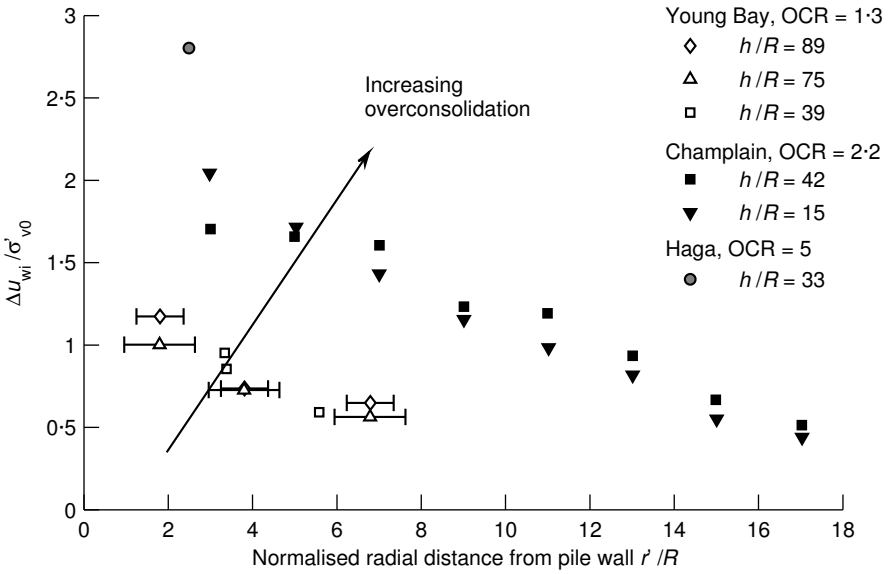

Figure 2.8 Radial distribution of excess pore pressure a few hours after installation in three soft clay sites (Young Bay mud, Champlain clay, and Haga clay; data from Pestana et al., 2002; Roy et al., 1981 and Karlsrud 1986, cited by Karlsrud, 2012).

shows negative excess pore pressure.[3]

Although introduced here with pore pressure measurements, the h/R effect is redundantly observed for all the stresses measured on the pile shaft and in the soil – this is highlighted in the following paragraphs.

At the pile shaft, the h/R effect was observed by Bond and Jardine (1991) and Coop (1987) in London clay, by Konrad and Roy (1987) in Champlain clay, by Soares and Dias (1989) in Rio de Janeiro clay, and by Karlsrud and Haugen (1985) in Haga clay. Konrad and Roy (1987) added that the shape of this decreasing curve was constant with depth. Contradictory observations were made by Coop (1987) in Gault clay and by Lehane (1992) in Cowden till, where the pore pressure at pile toe was *lower* than pore pressure measured higher up the pile.

The radial distribution of excess pore water pressure normalised to the *in situ* vertical effective stress at the end of installation ($\Delta u_{wi}/\sigma'_{v0}$) is reproduced in Fig. 2.8, from three research groups. Fig. 2.8 depicts measurements of pore pressure made in the soil a few hours after installation, which are assimilated to end-of-installation values. It was shown, in Fig. 2.2, that pore pressure *at the pile wall* varies considerably during the first few hours after installation. However, this variation affects soil in close vicinity to the pile shaft (less than a few radii away). Therefore, the points

[3] Although Roy et al. (1981) cautiously warn that it might be associated with the displacement of the rods fixed to the pore pressure cells.

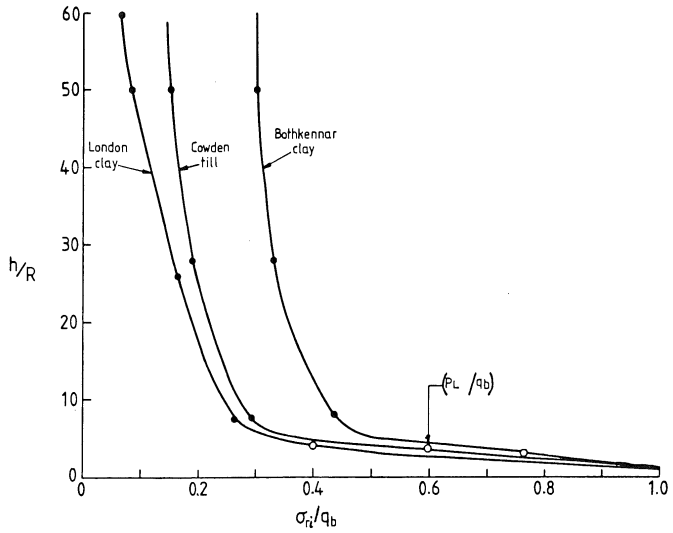

Figure 2.9 Total radial stress at end of installation along closed-ended ICP in three sites (Lehane and Jardine, 1994a) .

of Fig. 2.2 is presented as end-of-installation figures although some caution may be required for the data close to the pile wall.

The pore pressure distribution of Fig. 2.8 shows a monotonic shape decreasing with radius and its value increases with initial overconsolidation. This contradicts the trend observed at the pile wall, where excess pore pressure immediatly after installation was *lower* as overconsolidation ratio increased (Lehane and Jardine, 1994a,b; Bond and Jardine, 1991).

Excess pore pressure at the pile shaft at the end of installation were nearly independent of pile size (Pestana et al., 2002). This was also observed by Soares and Dias (1989) and Konrad and Roy (1987), who compared excess pore pressure measurements from a piezocone and a pile.

(b) Radial total stress

Unlike excess pore pressure, the h/R effect for the total radial stress at the end of installation (σ_{ri}) has been consistently observed by all research groups (Karlsrud and Haugen, 1985; Coop and Wroth, 1989; Soares and Dias, 1989; Bond and Jardine, 1991; Lehane and Jardine, 1994a,b). Fig. 2.9 depicts, for London clay, Cowden till and Bothkennar clay, the h/R effect on σ_{ri} (assuming that $\sigma_{ri} = q_b$ at pile toe). Fig. 2.9 also shows that the reduction of σ_{ri} is more pronounced as overconsolidation ratio is higher. The number and length of each jacking cycle also affected the h/R trend (Lehane, 1992).

Far behind the toe (for $h/R > 20$), the normalised total radial stress $H_i = (\sigma_{ri} - u_{w0})/\sigma'_{v0}$ increased with overconsolidation ratio, as depicted by Fig. 2.10. The

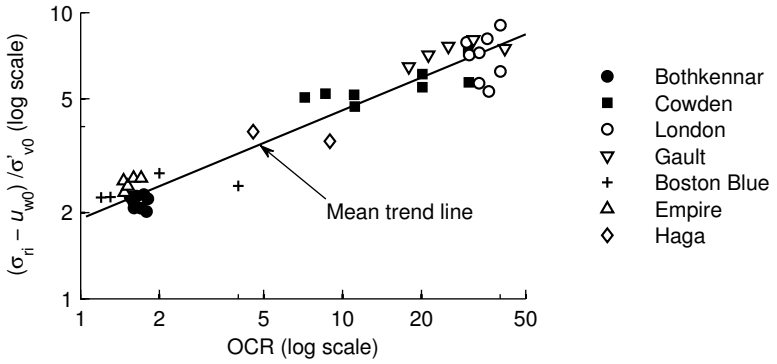

Figure 2.10 Normalised radial total stress at pile wall at the end of installation versus apparent overconsolidation ratio (data compiled by Chow, 1996, for $h/R \geq 20$).

undrained strength (s_{u0}) and the pressuremeter modulus (E_{pm}) also affected σ_{ri}: Coop (1987), in London clay, observed that the jump in s_{u0} and E_{pm} profiles was directly translated in the σ_{ri} measurements.

(c) Radial effective stress

Coop and Wroth (1989) report no h/R effect in Gault clay but do in Hunspill clay, while both sites depict h/R effect of the total radial stress and pore pressure.

In Empire clay (low OCR, moderately sensitive) and in Bothkennar clay (low OCR, sensitive), the radial effective stresse immediately after installation (σ'_{ri}) was lower than the initial undisturbed values (σ'_{r0}) (Azzouz and Lutz, 1986; Lehane and Jardine, 1994a). In contrast, installation in Cowden and London clays (high OCR, insensitive) caused σ'_{ri} to increase to values far greater that σ'_{r0} (Lehane and Jardine, 1994a). As explained in Chapter 1, the radial effective stress governs the shaft shear strength through the Coulomb friction law. Therefore, this observation concurs with the fact that the Soil Resistance to Driving is inferior to the static capacity for lightly overconsolidated clays (Fig. 1.4, p. 4). Conversely, Soil Resistance to Driving would be greater than the static capacity for highly overconsolidated clays.

(d) Shear stress

In Pentre clay-silt, the shear stress (f_{si}) response displayed an h/R dependency with the highest values in a particular stratum recorded close to the pile toe (Chow, 1996). However, in London clay, Coop (1987) and Bond and Jardine (1991) reported that for a given soil horizon, similar shear stress measurements were obtained from sensors located at different distance h from pile toe.

Bond and Jardine (1991), in London clay, observed that the jump in undrained shear strength s_{u0} and (pressuremeter) bulk modulus E_{pm} is not translated in the τ_{rzi}

profile. However, Lehane and Jardine (1992) reports the opposite: that τ_{rzi} reflected closely the undrained shear strength profiles.

Coop (1987), in Gault clay, indicated that the shear stress acting on the pile shaft after installation was seen to depend on the interface roughness, as in ring shear tests.

(e) Displacement

Fig. 2.11 depicts the normalised displacement due to pile installation from four different different technologies: felt-tip markings (Randolph, Steenfelt and Wroth, 1979), radiography (Steenfelt et al., 1981), inclinometer (Hunt et al., 2000), and PIV (Lehane and Gill, 2004). Fig. 2.11 reports measurements that avoid free surface effects ($L_E/R > 40$) while still being far behind the pile toe ($h/R > 40$).

Most of the radial displacement measurements lies between the predictions from undrained cylindrical and spherical cavity expansion (Fig. 2.11a).

Fig. 2.11b shows a downward distortion of the soil layering rather than random remoulding, which was confirmed by Jardine and Bond (1989) and Bond and Jardine (1991) by examination of soil samples taken next to the pile shaft. Also shown in Fig. 2.11b is a soil heave (upward displacement) at radial distances from pile shaft larger than $5R$.

By comparing different sources, Fig. 2.11a and b allow us to conclude that there is no scale effect on the final displacement, that there is no dependence on toe shape (conical or flat-ended) and that final displacement seem not to be too sensitive on the soil properties, as all curves exhibit similar shapes.

(f) Other observations

Shear band/fabric studies Coop (1987), in Gault clay, indicated that for the rough shaft pile, the shear surface was clearly a few millimetres from the shaft, but for the smooth surface used for most of the tests, its location was uncertain.

Bond and Jardine (1991), comparing driven and jacked piles, reported that although the patterns of distortion next to the driven and jacked piles were very similar, there was an important difference in soil fabric in the two cases: a highly polished, striated and continuous shear surface was formed 0·5–1 mm from the shaft of the slow jacked piles, where there were several small but discontinuous residual shear surfaces existing beneath a surface skin of clay for the driven pile.

Interface angle of friction The angle of friction between pile and soil (δ) is essential as it governs the shear stress developed during pile loading. It can depend on the pile surface (roughness and type) or on rate (see Section 2.2f, p. 20) (Bond and Jardine, 1991; Lehane, 1992). Moreover, when subjected to high displacements, some clays are prone to develop a residual friction angle which is much lower than the critical state friction angle (ϕ'_{cs}) (Jardine et al., 2012).

From the literature review, no solid conclusion or trend regarding δ could be attained.

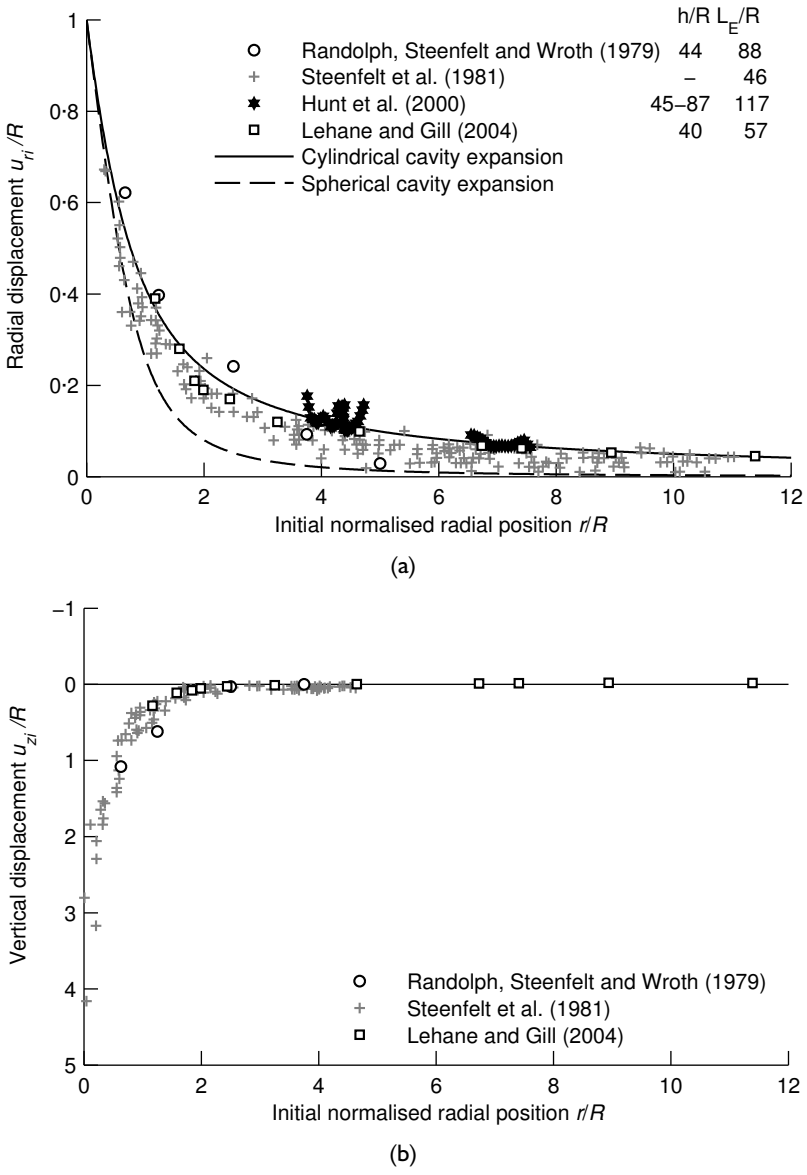

Figure 2.11 (a) Radial and (b) Vertical normalised displacements shortly after installation and far behind pile toe ($h/R > 40$).

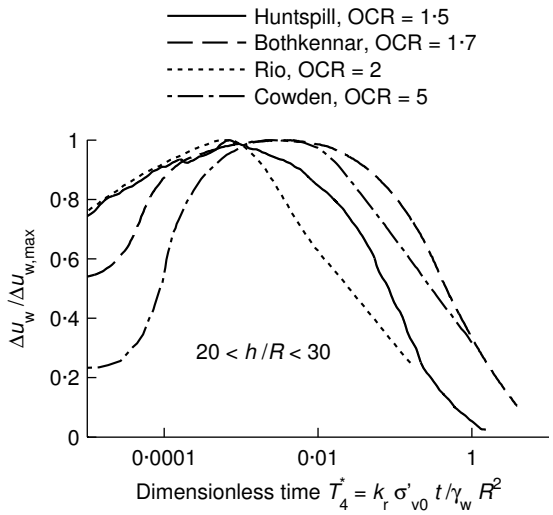

Figure 2.12 Excess pore pressure ratio at pile wall versus dimensionless time (data from Coop and Wroth, 1989; Soares and Dias, 1989; Lehane and Jardine, 1992, 1994b).

2.4 Equalisation

The equalisation stage relates the period beginning at the end of installation and ending at the first load test.

During equalisation, the pile capacity is generally seen to increase; increase which is attributed to consolidation, during which excess pore pressure dissipates, therefore leading to an increase in effective stress on the pile shaft.

Static capacity continues to evolve, however, after the excess pore pressure has dissipated (Cooke et al., 1979), due to what might be called *secondary compression* or *ageing* (Bjerrum, 1967).[4]

In this section, only the consolidation phenomena will be investigated, as it predominantly explains the increase in pile capacity for clays. Equalised quantities are denoted with the subscript 'c.'

(a) Pore pressure

Once the pile was stationary, the pore pressure at pile wall rose to relatively steady values during the first few minutes. After that short term rise, the pore pressure on the pile wall began its decay, following a typical consolidation pattern. Fig. 2.12 depicts the pore pressure ratio at pile wall ($\Delta u_w / \Delta u_{w,max}$) versus dimensionless

[4]The expressions 'primary' and 'secondary' compression separate the consolidation in two components occurring before and after the excess pore pressure has dissipated. The terms 'instant' and 'delayed' compression describe the soil reaction with respect to an increase in the effective stress (Bjerrum, 1967).

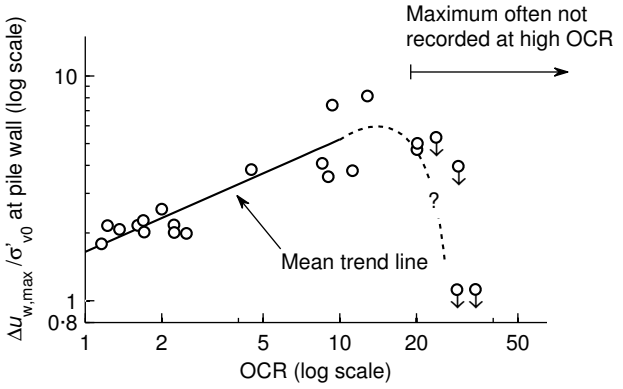

Figure 2.13 Maximum pore pressure recorded at the pile wall during equalisation versus apparent overconsolidation ratio (data compiled by Lehane, 1992).

time for four of the investigated experiments. The data presented in Fig. 2.12 illustrates the short term rise followed by the logarithmic decay in pore pressure. This behaviour was observed in kaolin, Rio de Janeiro, Gault, Hunspill, London and Bothkennar clays (Steenfelt et al., 1981; Soares and Dias, 1989; Coop and Wroth, 1989; Bond and Jardine, 1991; Lehane and Jardine, 1994a,b).

The value of the maximum excess pore pressure ratio ($\Delta u_w/\sigma'_{v0}$) encountered at the pile wall during this short term rise is depicted in Fig. 2.13 against overconsolidation ratio. Up to an OCR of approximately 10, the ratio $\Delta u_{w,max}/\sigma'_{v0}$ rises with OCR. Above 10, $\Delta u_{w,max}/\sigma'_{v0}$ was often not recorded as pore pressure remained negative during most of the consolidation (Bond and Jardine, 1991). One exception to the trends exposed here above are reported in the highly permeable Pentre clay-silt for which no short term rise was observed (Chow, 1996).

This increase appears to be confined to a narrow zone around the pile, since even transducers at 0·5R from pile shaft show no corresponding effect (Steenfelt et al., 1981).

The origin of this increase in pore pressure measured at the pile wall shortly after installation has been attributed to the following factors (Soares and Dias, 1989): (1) Lack of saturation of the pore pressure transducers (porous stones or internal cavities); (2) Lower pore water pressure at pile-soil interface than a few centimetres away (3) Time lag of the pore pressure transducers or data acquisition system; (4) Redistribution of the initial pore pressure around the toe, due to preferential drainage along the pile shaft and the high pore pressure gradient between the toe and the shaft; (5) Mandel-Cryer effect. Factor (1) has been the subject of many discussions (see for instance Gupta, 2003) but also of great care, which is why it is dismissed. Factor (3) is cast out because independent tests have shown the response time of pore pressure transducers to be of the order of a few milliseconds (Steenfelt et al., 1981). Factor (4) can be discarded because Coop and Wroth (1989) observed, in Gault clay, that the pore pressure transducers near the pile toe registered this pore

water pressure rise the last. Factor (5) is a reality but is unlikely to impose such a rise in pore pressure. Therefore, only factor (2) remains as a possible explanation of this rise. Furthermore, this follows measurements reported in Section 2.3b where pore pressure at the pile wall at the end of installation *reduced* with OCR while pore pressure in the soil rose with OCR.

Moreover, the peak excess pore pressure ratio ($\Delta u_w/\sigma'_{v0}$) was lower with increasing h/R, as suggested by Fig. 2.13. This observation implies that the maximum excess pore pressure located a few radii away from the pile shaft decreases with the number of cycles of shaft-soil shearing.

At the pile toe, the short term rise has been observed in Gault clay (Coop and Wroth, 1989) but not in Rio de Janeiro clay nor in Gault clay (Soares and Dias, 1989; Coop and Wroth, 1989). In parallel, pore pressures near the pile toe were found to dissipate more rapidly than those on the pile shaft, likely due to the three-dimensional drainage path near the toe: dissipation at $h = 53R$ was consistently twice as slow as that at $h = 5R$ (Lehane and Jardine, 1994a, for three different soils).

At the pile shaft (except near the ground surface or near the pile toe), the major pore pressure gradients were radial (Randolph and Wroth, 1979; Konrad and Roy, 1987). Nonetheless, some vertical dissipation of excess pore pressure might occur if a layer with higher hydraulic conductivity were present in the ground within the pile length. Furthermore, dissipation curves obtained for the same h/R ratio, but at different soil depths, were closely comparable, showing that local variations in soil parameters were not important (Boston Blue and Bothkennar clays Azzouz and Morrison, 1988; Lehane and Jardine, 1994a).

Finally, Roy et al. (1981) report an initial increase in pore water pressure measured at 8 to 20R from the pile wall, after which pore pressure decreased. Compared to the increase measured at the pile wall, the increase measured by Roy et al. (1981) is much smaller and less sudden.

(b) Radial total stress

As the soil close to the pile undergoes consolidation with a decrease in water content, σ_r on the pile shaft decreases since the soil is contracting away from the pile (Randolph and Gourvenec, 2011). This was consistently observed on the investigated pile tests, with the small difference that the total radial stress first remained constant for the first few minutes after installation (during the pore pressure increase), but then reduced steadily. These steady first few minutes were not observed in Pentre clay-silt where pore pressure reduced right from the end of the jack stroke (Chow, 1996).

(c) Radial effective stress

Due to the sharp increase in pore water pressure, the radial effective stress on the pile shaft σ'_r showed a short-term drop followed by a long-term increase (seen in Boston blue, Empire, Gault, Hunspill, Cowden, and Bothkennar clays; Azzouz

and Lutz, 1986; Azzouz and Morrison, 1988; Coop and Wroth, 1989; Lehane and Jardine, 1994a,b) .

At the end of consolidation, the radial effective stress on the pile shaft σ'_{rc} was higher than the initial radial effective stress σ'_{r0} in both overconsolidated soils (Cowden, London, and Haga clays) and normally consolidated soils (Bothekennar and Empire clays). Azzouz and Morrison (1988), in Boston blue clay, found σ'_{rc} to be in the same range as σ'_{r0}.

The set-up factor ($\sigma'_{rc}/\sigma'_{ri}$) was greater than one in lightly overconsolidated Empire clay and was equal to one in Bothkennar clay ($\sigma'_{rc} \approx \sigma'_{ri}$). In the overconsolidated Cowden till and London clay, the set-up factor was *smaller* than one, which implies that static capacity after equalisation would be inferior to the end of installation static capacity.

Chow (1996) reported that the number of (undrained) jacking cycles had little or no effect on the magnitude of the equalised radial effective stresses σ'_{rc}.

(d) Shear stress

Lehane and Jardine (1994a), in the normally consolidated Bothkennar clay, reported that the average shear stress at the pile wall (τ_{av}) increased during the installation pause periods. Opposite effect was observed in the overconsolidated Cowden till where τ_{av} reduced as the length of the pause increased. In the more permeable Pentre clay-silt, τ_{av} sometimes increased and sometimes decreased during installation pause periods (Chow, 1996).

This leads to believe that shaft shear stress varies with initial overconsolidation and permeability. When undrained penetration can be assumed (unlike in Pentre), the shear stress tends to decrease at the pile wall for overconsolidated soils while it increases for normally consolidated soils.

(e) Displacement

Pestana et al. (2002) observed that as the consolidation process took place, the moved radially towards the pile as the excess pore pressure dissipated. The displacement decreased magnitude as a function of the distance from the pile shaft.

No report of the vertical displacement during consolidation were found.

(f) Other observations

Shear strength Fig. 2.14 presents the shear strength at the end of consolidation (s_{uc}) measured around the pile for two lightly overconsolidated clays. Three zones emerge from Fig. 2.14: (1) the inner zone (from the pile wall to a radial distance of $0{\cdot}5R$) where the soil has been sheared to its critical or even residual state condition, (2) the middle zone ($0{\cdot}5R$ to $4R$ from the pile shaft) where the shear strains are large enough to cause to soil to dilate, but not large enough for it to reach a critical state, and (3) the outer zone ($4R$ and further from the pile wall) where the soil behaves quasi-elastically, and there are no scars from the pile installation (Karlsrud and

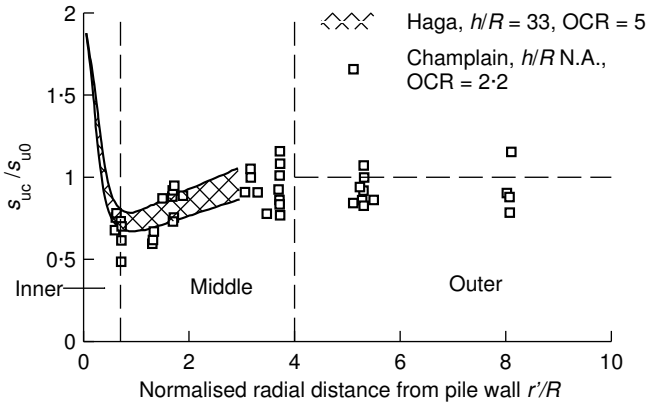

Figure 2.14 Shear strength around a pile after consolidation from fall cone tests (data from Karlsrud and Haugen, 1985) and vane tests (data from Roy and Lemieux, 1986).

Haugen, 1985; Bond and Jardine, 1991). The increase in shear strength at the pile shaft at the end of consolidation corroborates the increase in pile capacity noted during set-up in Haga clay.

As for the number of cycles, Bond (1989), cited by Chow (1996), in London clay, did not detect any differences in the tensile shaft capacities of fast-jacked and driven piles, which were installed in ~ 20 and 4500 undrained cycled respectively.

In London clay, the piles showed no increase in static capacity in first-time loading test spread over a period of 3½ months (Bond and Jardine, 1991). Further, these piles didn't show a systematic relationship between the shear stress at failure and the original undrained soil shear strength s_{u0} or the original horizontal soil effective stress σ'_{h0}. Karlsrud and Haugen (1985), on the other hand, noted a linear increase of first-time static pile capacity versus time. Lehane and Jardine (1994a) also observed a pile capacity increase with time.

Preshearing effect The *preshearing effect* was first discovered by Karlsrud and Haugen (1985). It is the observer effect of the static load test, *i.e.* the static capacity is greater for a pile that has been previously load tested. This is problematic for piles which are being subjected to several load tests, which exhibit a greater increase in static capacity than would be offered by consolidation only. However, the preshearing effect is most pronounced for Norwegian clays. In Pentre for instance, re-tests show responses ranging from positive pre-shearing effects to inexorable capacity decline (Nowacki et al., 1993; Jardine et al., 2012). For example, Azzouz and Lutz (1986) reported that after consolidation, their pile was subjected to rapid pull-out shearing. This rendered the subsequent pile load tests unrepresentative of the state of a pile after consolidation. The results presented herein are exempt from the preshearing effect. The preshearing effect is mostly marked in Norwegian clays

but has nevertheless not a negligible effect (positive or negative) in European clays. Although the mechanisms behind the preshearing effect are not understood, it is an important effect that, if neglected, leads to wrong conclusions about the set-up of piles.

Water content Bond and Jardine (1991) did not find any overall radial variation in water content at the end of equalisation (w_c) around driven and jacked piles in the highly overconsolidated London clay. On the other hand, Karlsrud and Haugen (1985) and Pestana et al. (2002) presented contradictory results, reproduced in Fig. 2.15a. This Figure shows a dramatic 13% reduction in water content at the pile shaft, corresponding to a volume change of around 16–17% (Karlsrud and Haugen, 1985). The middle zone also shows a decrease of water content from its original value (w_0), albeit in a less dramatic fashion.

Mean effective stress Fig. 2.15b depicts the change in mean effective stress at the end of consolidation (p'_c) in highly overconsolidated London clay, showing a maximum at the pile shaft. No difference are found between the stress level from samples retrieve next to jacked and driven piles. Nevertheless, values of p'_c from Fig. 2.15b may not me valid for lower OCR soils.

Permeability Alongside the changes in stress occurring during installation and equalisation, changes in soil permeability are bound to happen. Ting et al. (1990), cited by Whittle (1992), noted that permeability could decrease by up to a factor of 3 at locations close to the pile shaft following complete set-up.

2.5 Conclusion

Installation

From the point of view of a soil horizon, the insertion of the pile toe creates the most disturbance in terms of displacement. This distortion results in a rise in total radial stress (σ_r) and excess pore water pressure (Δu_w).

Once the pile toe is through, the soil is subjected to tens (for a jacked pile) or hundreds (for a driven pile) of cycles of shaft-soil shearing events. During these cycles, the majority of the vertical displacement occurs in a narrow band located close to the pile wall. During the pile downward movement, both σ_r and Δu_w reduce at the pile shaft for a particular soil horizon. As the pile penetrates further into the ground, *i.e.* as the vertical distance between pile toe and the soil horizon (h) increases, the total radial stress (σ_r) decreases. Excess pore pressure (Δu_w) and shear stress (τ) are also affected by the relative distance from pile toe but sometimes increase with h. This phenomenon is called the 'h/R effect.'

The h/R effect has been observed at large depths ($z > 25R$) therefore discarding free surface effects (upward soil displacement at the soil surface) and pile whip (formation of a hole around the pile at the soil surface) as satisfactory explanations

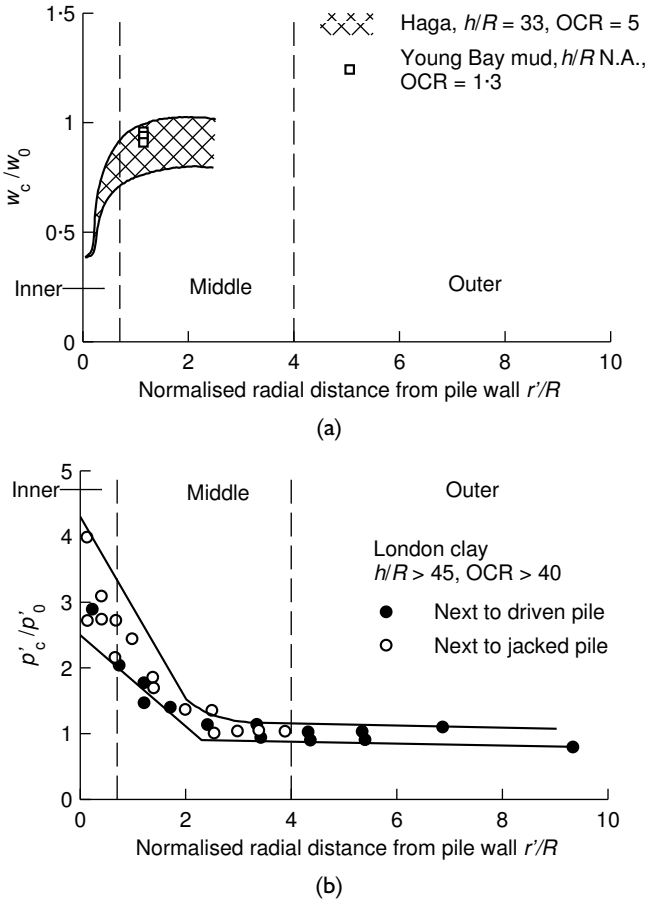

Figure 2.15 Measured water content and effective mean stress after consolidation (data from Karlsrud and Haugen, 1985; Bond and Jardine, 1991; Hunt et al., 2002).

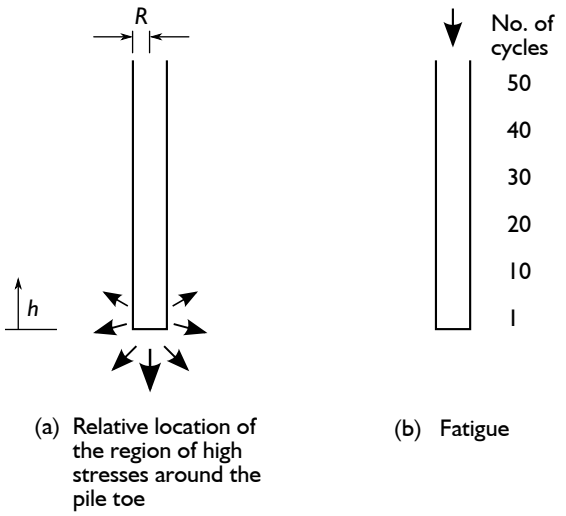

Figure 2.16 Possible reasons for the *h*/*R* effect during deep penetration (after Chow, 1996).

(Randolph, 1993; Chow, 1996). Therefore, two causes may explain the h/R effect. They are illustrated in Fig. 2.16: (a) As the pile toe advances below a soil horizon, the stress concentration which was focused at the toe becomes more remote and the soil unloads radially and (b) *Fatigue*: as the pile advances, a given soil horizon accumulates events of shaft-soil shearing (Heerema, 1980, cited by White and Bolton, 2004).

The h/R effect, and in particular soil fatigue along the shaft (Fig. 2.16b), explains the variation in strength recorded during driving, as explained in Chapter 1.

The pore pressure distribution around the shaft at the end of installation is expected to resemble the plain curve of Fig. 2.17, with a peak value a few radii away from the pile shaft. The excess pore pressure ratio ($\Delta u_w/\sigma'_{v0}$) at the pile shaft is lower as the soil overconsolidation ratio is higher. The peak $\Delta u_w/\sigma'_{v0}$ on the other hand is higher with OCR (up to OCR values of approximately 10). Furthermore, the peak $\Delta u_w/\sigma'_{v0}$ decreases with h/R (again, for OCR < 10), unlike at the pile shaft where $\Delta u_w/\sigma'_{v0}$ shows variable trends with OCR.

Most results presented in this chapter stem from jacked pile installations, which differs from a driven pile installation mainly on two points. Firstly, the number of driving blows is counted in hundreds whereas a few tens of jacking strokes is needed to install a jacked pile. This has an influence on the h/R effect (Fig. 2.16b). Secondly, the velocity peak of a driven pile is between 25 and 1000 times higher than the one of a jacked pile. The corresponding increase in shaft resistance is expected to reach 20 to 60%. Nevertheless, the effect on effective stress after installation is unknown.

At the end of installation, the radial displacement around the shaft (not too close

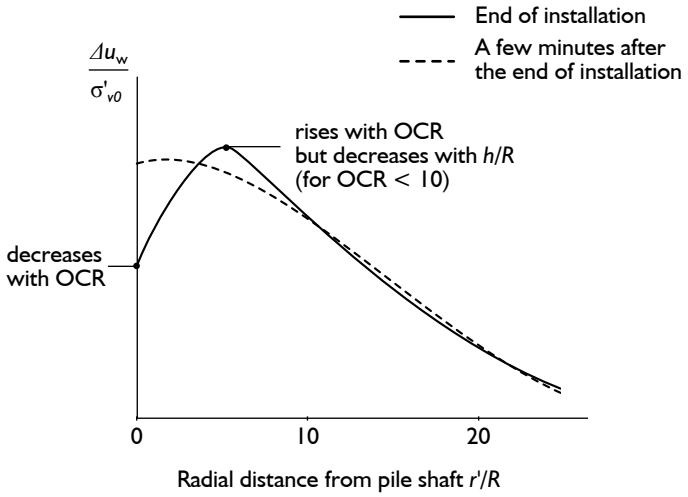

Figure 2.17 Tentative radial distribution of excess pore pressure ratio far behind the pile toe ($h/R > 20$) immediately and a few minutes after installation.

to the soil surface nor to the pile toe) is between the ones predicted by a spherical and cylindrical undrained cavity expansion. Vertical displacement is concentrated at less than two radii from the pile shaft, while a small heave is present at several radii from the pile shaft.

Initial overconsolidation ratio is of utmost importance for the soil stress response around a displacement pile. Other parameters that influence the soil response are pile roughness and soil sensitivity. Furthermore, some clays are inclined to develop residual friction surfaces at angles that are much lower than the critical state friction angle. On the other hand, parameters that do not influence the soil stress state after installation are the plasticity index (PI) and the shape of the toe. Finally, there is no scale effect in the observed measurements: they can be normalised with the pile radius (R).

Equalisation

Whatever the initial overconsolidation ratio, the total radial stress monotonically and mildly decreases throughout equalisation.

For initial overconsolidation ratios smaller than ~ 10, pore water pressure at the pile wall increases during the few minutes of consolidation. This observation excludes the regions close to the pile toe or near the ground. The maximum value of the excess pore pressure ratio ($\Delta u_w/\sigma'_{v0}$) during this short term rise is higher as the overconsolidation is higher. This increase happens because the pore pressure at the pile shaft is lower than it is a few centimetres away, as illustrated by Fig. 2.17.

This rise in pore pressure implies that there is a short term minimum in the pile

shaft capacity.[5]

After this short term increase, the pore pressure at pile wall decreases with time, eventually reaching its hydrostatic value. At the end of equalisation, the radial effective stress (σ'_{rc}) is higher or equal than the overburden radial stress (σ'_{r0}) whatever the initial overconsolidation ratio. The set-up ratio ($\sigma'_{rc}/\sigma'_{ri}$) is greater than one for lightly overconsolidated clays but smaller than one for heavily overconsolidated clays.

Finally, set-up may be over- or under-estimated by repeated loadings, this is referred to as the 'preshearing effect.' First-time static loadings are therefore preferred to measure true set-up.

[5]Shaft capacity is assumed proportional to a Coulomb law of the type $\sigma'_r \tan\delta$, where δ is the angle of friction between the pile wall and the soil. Shaft capacity is therefore assumed to be proportional to the radial effective stress (σ'_r).

Chapter 3

Literature review: simulation

This chapter presents a literature survey of the previous attempts at modelling pile installation and subsequent equalisation. In line with the objectives of this work, this chapter focuses on rational methods aimed at predicting the soil state around the shaft of a pile, during and after its installation. Empirical or semi-empirical estimates of the capacity of displacement piles, such as total stress approaches (α method, API or NGI-99) or effective stress approaches (β method, ICP-05 or NGI-05) are not covered.[1]

Section 3.1 and 3.2 review simulations of the installation and equalisation stages, respectively. Subsequently, Section 3.3 describes the plan of action for the model developped in this thesis, based on the conclusions from Chapters 2 and 3.

3.1 Pile installation

As summarised by Baligh (1985), the development of a sound understanding and reliable predictive method for pile installation effects are complicated by the following factors:

(i) Singularities and high gradients arise during the modelling of the two-dimensional problem of displacement pile installation, where the field variables (displacements, strains, stresses, and pore pressures) depend on the radial and vertical locations;

(ii) Constitutive behaviour of soil is elaborate; it includes non linear, hysteretic, frictional, anisotropic, sensitive, and rate-dependent responses;

(iii) Water (and possibly gas) is present in the pores, requiring the treatment of the soil as a multiphase medium.

Since the second half of the 20th century, a limited amount of approaches have emerged trying to model the installation process. These methods can be divided in three chronologically sorted categories, which compose the first three parts

[1] Jardine and Chow (2007) or Doherty and Gavin (2011) cover these methods.

of this section. Section 3.1.1 presents the Cavity Expansion Method, where the pile installation process is boiled down to the expansion of an initially void cavity. Section 3.1.2 presents the Strain Path Method, an extension of the Cavity Expansion Method using flow theory: a spherical cavity is expanding through a flowing mass of soil. Section 3.1.3 reviews the latest developments in large strain finite element modelling. Alongside these three main simulation paths, alternative methods have been developed, an insight of which is presented in Section 3.1.4.

Like in Chapter 2, the subscript 'i' is used to denote quantities sampled immediately after installation.

3.1.1 Cavity Expansion Method

The oldest method used to predict the soil state after the installation of a displacement pile is to reduce installation to the expansion of an initially void cavity.

The cavity expansion method was first used by Bishop et al. (1945)[2] and Hill (1950) to model metal indentation problems using an elastic perfectly plastic material model with a Tresca yield criterion. They observe that the pressure required to produce a deep hole in an elastic-plastic frictionless medium is proportional to that necessary to the expansion of a cavity of same volume and under the same stress conditions.

Gibson (1950)[3] applied the preceding solutions to the penetration of a pile in a cohesionless medium by assuming that a rigid cone (or wedge) of soil is formed at the pile toe, and that the lateral surface of this cone is subjected to an uniformly distributed stress whose normal component is equal to the spherical cavity limit pressure (Fig. 3.1).

The application of the cavity expansion to soils was further studied over the years, some notable references include Soderberg (1962), Butterfield and Banerjee (1970),[4] or Vesić (1972). All these studies were made considering either a spherical or a cylindrical expansion according to the fact that displacements around a driven pile is midway between these two geometries (as seen in Fig. 2.11 of Chapter 2, p. 31).

Soderberg (1962), for example, assumes that the excess pore pressure due to the pile installation is proportional to the radial total stress after a cylindrical cavity expansion. The radial equilibrium in a plane strain axisymmetric geometry implies that the total radial stress (σ_r) is compressive and therefore that the total hoop stress (σ_θ) is tensile. By assuming that soil cannot support tension, Soderberg (1962) then uses a simplified radial equilibrium equation:

$$\frac{\partial \sigma_r}{\partial r} + \frac{\sigma_r}{r} = 0,$$

which, after being integrated, leads an expression of excess pore pressure after installation (Δu_{wi}) versus radial position: $\Delta u_{wi}/u_{w,p} = R/r$, where r is the radial

[2] Cited by Hill (1950).
[3] Cited by Ladanyi and Johnston (1974).
[4] Cited by Randolph, Carter and Wroth (1979).

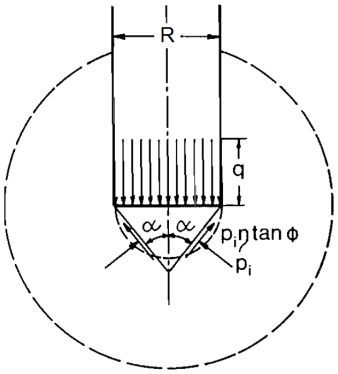

Figure 3.1 Transformation of a deep punching problem to a spherical cavity expansion (q is the average pressure acting on the punch at failure, α is the failure cone semi angle, and p_i the cavity expansion pressure; Ladanyi and Johnston, 1974).

distance from pile centreline, $u_{w,p}$ is the pore pressure at pile shaft, and R is the pile radius.

The next leap is brought by Randolph and Wroth (1979), from Cambridge University, who analytically derive an expression of the excess pore pressure after a cylindrical cavity expansion, based on Hill (1950), with the following assumptions:

(i) the extend of the soil domain tends to infinity,

(ii) the soil is treated as an incompressible monophasic medium (the behaviour of which is thus governed by a total stress behaviour) limited by the Tresca yield criterion: $\sigma_r - \sigma_\theta = 2s_{u0}$ (implicitely assuming that σ_r and σ_θ are respectively the maximum and minimum principal stresses),

(iii) the mean effective stress (p') is constant; therefore, the increase in pore pressure is equal to the increase in total mean stress.

This yields a compact expression of the excess pore water pressure after installation (Δu_{wi}), for a cylindrical cavity expanded from zero to R, the pile radius:

$$\Delta u_{wi} = 2s_{u0} \ln\left(R_p / r\right) \qquad \text{for } R \leq r \leq R_p, \tag{3.1}$$

where r is the radial distance from pile centreline, $R_p = R\sqrt{G/s_{u0}}$ is the radius of the plastic zone, and G and s_{u0} are respectively the secant shear modulus (elastic) and undrained shear strength. The pore pressure distribution predicted by Eq. (3.1) is depicted in Fig. 3.2a for a rigidity index (G/s_{u0}) of 100.

This solution was validated on one hand by field experiments (Randolph and Wroth, 1979) and on the other hand by a numerical simulation of a cavity expansion using the modified Cam clay *effective* stress soil model (Randolph, Carter and Wroth,

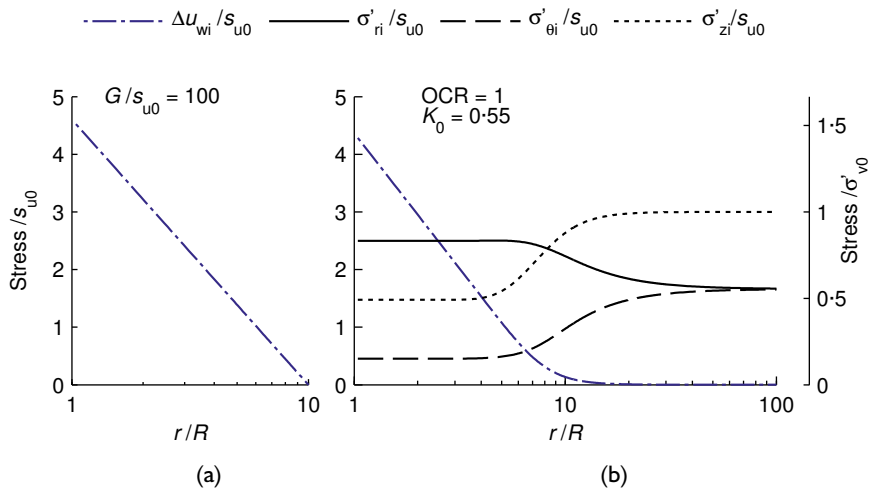

Figure 3.2 (a) Pore pressure distribution after cylindrical cavity expansion using a total stress based elastic perfectly plastic material (after Randolph and Wroth, 1979) and (b) Stress and pore pressure distribution after cylindrical cavity expansion in Boston Blue clay using an effective stress based modified Cam clay model (after Randolph, Carter and Wroth, 1979).

1979). This latter simulation is depicted in Fig. 3.2b where one can notice that the pore pressure distribution is very similar to the one of Fig. 3.2a. For the reasons preceding, Eq. (3.1) is a reference solution which still is used nowadays.

It should be noted that this similarity is far from trivial as the two simulations use very different assumptions: Randolph and Wroth (1979), Fig. 3.2a, use a total stress constitutive model and assume that the mean effective stress (p') is constant to compute the pore pressures; Randolph, Carter and Wroth (1979), Fig. 3.2b, use an effective stress constitutive model while computing pore pressures through the radial equilibrium.

The effective stresses at the pile wall of Fig. 3.2b can be explicitly formulated (Randolph, Carter and Wroth, 1979):

$$\sigma'_{\mathrm{ri}} = \left(\frac{\sqrt{3}}{M_{\mathrm{c}}} + 1\right) s_{\mathrm{u0}}, \tag{3.2a}$$

$$\sigma'_{\theta\mathrm{i}} = \left(\frac{\sqrt{3}}{M_{\mathrm{c}}} - 1\right) s_{\mathrm{u0}}, \tag{3.2b}$$

$$\sigma'_{\mathrm{zi}} = \frac{\sqrt{3}}{M_{\mathrm{c}}} s_{\mathrm{u0}} = p', \tag{3.2c}$$

where M_{c} is a function of the critical state angle of internal friction (ϕ'_{cs}) measured

in triaxial compression:

$$M_c = \frac{6 \sin \phi'_{cs}}{3 - \sin \phi'_{cs}}.$$

As indicated by Eqs. (3.2a-c), the effective stresses at the pile wall after the expansion of a cavity in a modified Cam clay material are only dependent on s_{u0} and ϕ'_{cs} and are independent of the overconsolidation ratio (OCR) or the coefficient of earth at rest (K_0).

Following the work of the Cambridge team, hundreds of papers have emerged on the cavity expansion theory, refining specific cavity expansion problems. Each of these paper can be categorised by using one of each keyword in the following list:

(i) The expansion of a spherical or cylindrical cavity;

(ii) Controlled by pressure or displacement;

(iii) From a void or finite initial radius;

(iv) In a compressible or incompressible material;

(v) Using small strain or large strain theory;

(vi) Subjected to static or dynamic equilibrium;

(vii) Using a (semi-)analytical or numerical approach;

(viii) With a specific constitutive model (elastic, elasto-plastic, associated or non-associated flow rule...).

Therefore, a considerable amount of studies have emerged since the 1980s that, as stated by Baligh (1985), are generating more distraction and confusion than providing useful answers to the pile installation problem.

3.1.2 Strain Path Method

The next step in predicting the installation effects of a displacement pile was introduced by Baligh (1985): The Strain Path Method is an approximate analytical framework that describes the mechanics of the steady penetration of a rigid object (*i.e.* a pile) in an homogeneous isotropic incompressible material (Fig. 3.3). The penetration process is viewed as a steady (quasi-static) flow of soil past a stationary pile which is formed thanks a spherical source emitting an incompressible material at a constant rate.

Compared to the cavity expansion, the two main enhancements offered by the Strain Path Method are that (1) it captures the dependence of the deformations on the vertical coordinate: as the pile descends into the ground, the soil particles undergo vertical *and* radial movement and (2) it predicts displacement reversals around the toe of a displacement pile. These two points are highlighted in Fig. 3.4 which depicts soil trajectories predicted by the Strain Path Method. The soil trajectories depicted

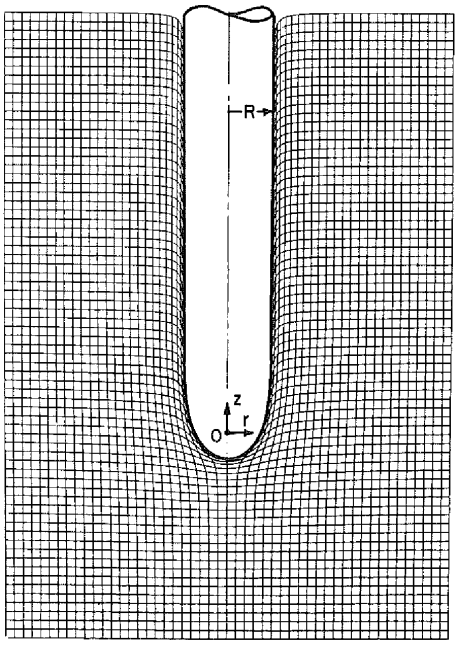

Figure 3.3 Strain Path Method prediction of the deformation of a square grid during pile penetration (Baligh, 1985).

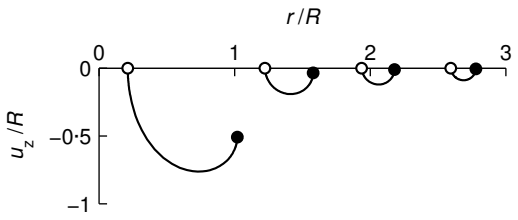

Figure 3.4 Soil trajectories predicted by the Strain Path Method (○ and ● are respectively the initial and final position of a soil particle).

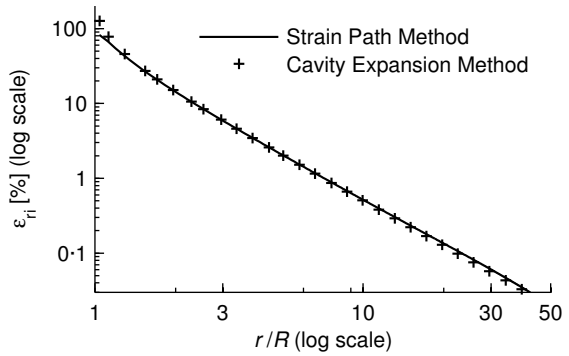

Figure 3.5 Radial strain after Strain Path Method compared to the one predicted by the Cavity Expansion Method.

in Fig. 3.4 are qualitatively similar to those reported in laboratory experiments (see Fig. 2.5, p. 22). The nature of the Strain Path Method means it inherently predicts the h/R effect, although like the cavity expansion method, it does not take into account pile shaft friction.

Nevertheless, the final radial displacement far behind the pile toe (*i.e.* for high values of h/R) is similar to the one predicted by the expansion of a cylindrical cavity in an incompressible soil, as depicted in Fig. 3.5 (Kavvadas, 1982).

The Strain Path Method hinges on the assumption that soil deformations during deep penetration can be estimated with a reasonable degree of accuracy without the need to consider constitutive relations for the soil. This assumption is reasonable as the pile penetration problem in clays is heavily constrained kinematically (due to incompressibility of the soil and the rigid boundary condition that is the pile). However, this 'uncoupling' leads to a violation of either the equilibrium equations or the constitutive relationship (Baligh, 1985). Indeed, due to incompressibility, there is only one stress component that cannot be obtained from the constitutive relationship (either excess pore pressure or mean normal stress) and must be solved from the equilibrium equations (Sagaseta et al., 1997). However, due to the 'uncoupling', it is not possible to match both radial and vertical equilibrium with a single

unknown. This leads to a violation of either the equilibrium or the constitutive relationship.

Teh and Houlsby (1991) attempted to develop several iterative schemes in order to correct the small inequilibrium brought by the Strain Path Method, but none have been completely successful. As an alternative solution, Teh and Houlsby (1991) developed a steady state finite element approach into which all equilibrium equations are accounted for. Yu et al. (2000) pursued this approach observed that the Strain Path Method and finite element solutions were very close. This confirmed the validity of the Strain Path Method assumption that the coupling between soil deformations induced by steady penetration and soil strength or stiffness properties is weak.

Three notable developments should be cited. Levadoux (1980) altered the form of the simple pile depicted in Fig. 3.3 with a series of additional sources in order to come closer to the geometry of a cone. Chin (1986) used a ring source to perform an open-ended pile installation. More recently, Sagaseta et al. (1997) introduced the Shallow Strain Path Method, which predicts soil surface movement due to Strain Path Method installation.

The latest development involving Strain Path Method which is in the scope of this thesis comes from the early 1990s. Whittle (1992) performed a Strain Path Method installation in normally consolidated Boston Blue clay. The simulation results were compared to field measurements obtained with the instrumented Piezo-Lateral Stress device (measurements that were reported in Chapter 2). The constitutive model used by Whittle (1992) is MIT-E3, a critical state based elasto-plastic model that accounts for soil anisotropy, cyclic loading, and shear induced pore pressures. Simulation focuses on the shaft behaviour, *i.e.* far behind the pile toe. The pore pressures are computed using the radial equilibrium equation. The results are summarised in Fig. 3.6, which depicts the distribution of radial effective stress (σ'_{ri}) and excess pore pressure (Δu_{wi}) after installation. Like the cavity expansion result depicted in Fig. 3.2b, the excess pore pressure decreases with radius. However, radial effective stress has reduced at pile wall, contrary to the cavity expansion results.

3.1.3 Finite Element Method

The simulation of continuum mechanics is traditionally split in two frameworks: the Lagrangian and Eulerian frameworks. The Lagrangian framework denotes that the nodal points of the finite element discretisation are coupled with the material points. The advantages of the Lagrangian formulation are that the field variables of a material point can be followed with ease and that irregular mesh can be easily modelled. The main disadvantage occurs when deformations are large: the mesh distortion deteriorates the accuracy of the solution. The Eulerian framework on the other hand uses a mesh fixed in space and time through which the material particles move. Using this framework, it is more difficult to track a single particle and irregular mesh is produced at greater computational cost than with the Lagrangian framework. The advantage of the Eulerian framework is that large deformations do not alter the accuracy of the output.

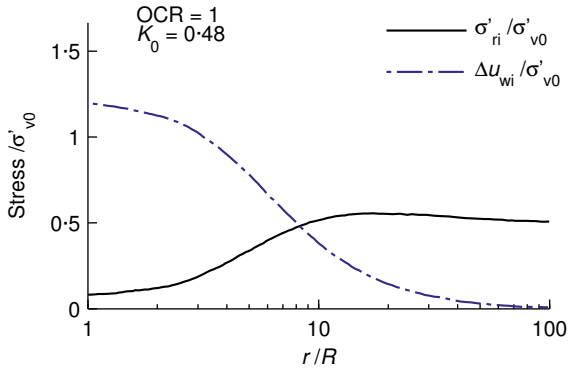

Figure 3.6 Stress state at the shaft after Strain Path Method installation in Boston Blue clay using the MIT-E3 constitutive model (from Whittle, 1992).

The analysis of pile installation using large strain finite element methods started three decades ago (*e.g.* de Borst 1982) and evolved over the years as computer power became increasingly available. Nowadays, three main approaches are used, which combine the advantages of the Lagrangian and Eulerian frameworks described above: the Arbitrary Lagrangian Eulerian (ALE), the Coupled Eulerian Lagrangian (CEL), and the Remeshing and Interpolation Technique with Small Strain (RITSS) methods. The following paragraphs showcase five research groups which focus on simulating the installation effects of various offshore foundation systems (spudcan footings, plate anchors, and piles) using large strain finite element methods.

Jassim et al. (2013), from the University of Stuttgart, use the Material Point Method, a finite element method formulated in an ALE description especially suited for dynamic problems (Więckowski, 2004). The authors simulate the driving of a 35·7 mm diameter cone using an elastoplastic Mohr-Coulomb soil model. Problem geometry, imposed boundary condition and output are depicted in Fig. 3.7. The soil model prevents any account of pore pressure generation or set-up, but further developments are in progress (Jassim et al., 2013).

Hamann et al. (2015), from the University of Hamburg, simulate the jacking of a 15 cm radius cone-ended pile in loose Mai-Liao sand ($D_r = 0{\cdot}2$) under various permeability conditions, going from drained to undrained – only the latter case is presented here. The constitutive model used is hypoplasticity for sands (von Wolffersdorff, 1996) coupled to intergranular strain (Niemunis and Herle, 1997). Although the simulation is made in sand, it is undrained, the soil initial state is loose (therefore on the wet side of critical, which can be compared to a lightly overconsolidated clay), and it is presented in Hamann et al. (2015) in a way that allows a comparison with the results presented earlier in this section. Fig. 3.8 depicts the simulation output for a layer of soil located 13 R below the surface and 20 R behind the pile toe. There is a reduction of effective radial stress (σ'_{ri}) near the pile wall and an increase in excess pore pressure (Δu_{wi}). Apart from the small

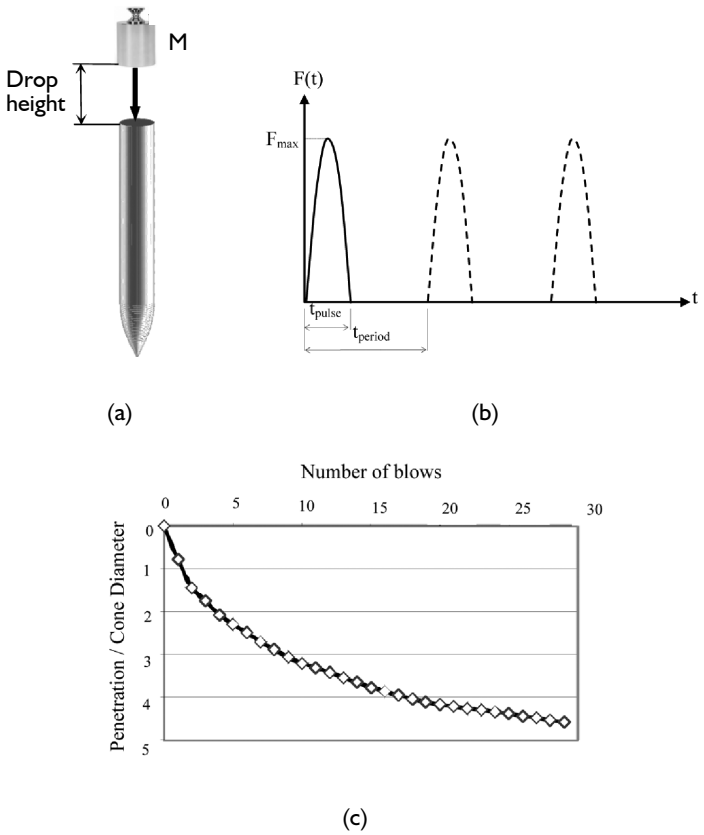

Figure 3.7 Simulation of a dynamic penetration test in an elastoplastic Mohr-Coulomb soil model using the Material Point Method: (a) Hammer and cone geometry, (b) Imposed force at cone head, and (c) Cone penetration ratio versus blow count (Jassim et al., 2013).

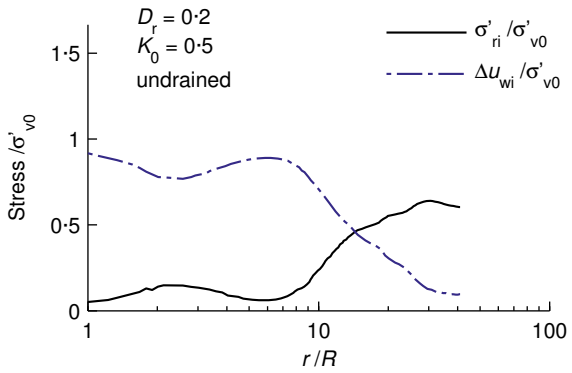

Figure 3.8 Stress state at the shaft of a jacked pile modelled using CEL and hypoplasticity in undrained loose Mai-Liao sand, at vertical position from pile toe $h = 20R$ (from Hamann et al., 2015).

bump observed at $r \approx 2R$, the output is similar to the Strain Path Method output of Fig. 3.6 and therefore presents the same differences compared to the Cavity Expansion output (Fig. 3.2b).

Sabetamal et al. (2014), from the University of Newcastle, use an ALE scheme to jack a pile in clay, modelled as a Modified Cam clay material. Although promising, the Sabetamal et al. (2014) paper does not offer results that can be compared to the previously introduced Cavity Expansion or Strain Path Methods.

Two other research groups perform large strain finite element simulations of installation effects, which cannot be exactly related to piles, but are still close. Firstly, the Norwegian Geotechnical Institute develops ALE and CEL simulations of spudcan and torpedo anchor installation. The simulations are performed using a quasi-static scheme with an elasto-plastic Tresca constitutive model (Andresen and Khoa, 2013). The published results compare very well with centrifuge experiments but cannot be compared to driven pile installation. Second, the University of Western Australia developed the 'remeshing and interpolation technique with small strain' (RITSS) algorithm: a two dimensional Lagrangian finite element method in which the soil domain is periodically remeshed so that the small strain assumption can be used (Hu and Randolph, 1998). After each remeshing, the stress and material properties are interpolated to the new mesh. The RITSS technique is successfully applied to simulations of anchor installation or pipeline penetration, using an elasto-plastic Tresca material (Tian et al., 2014).

Based on the results presented above, the recent developments in finite element schemes produce realistic results. Furthermore, Wang et al. (2015) compared the ALE, CEL, and RITSS frameworks for a cone quasi-static installation in clay and concluded that all three produced similar results.

Nevertheless, all these methods come at a very high computational cost, even using basic soil models.

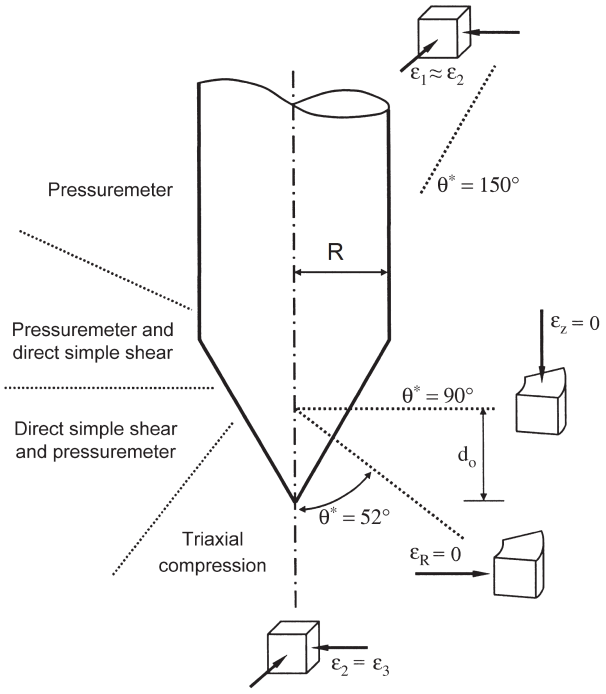

Figure 3.9 Presumed failure modes around an advancing cone, on the left by Keaveny and Mitchell (1986) and on the right by Baligh (1984), both cited by Su (2010).

3.1.4 Alternative methods

Alongside the Cavity Expansion, Strain Path, and Finite Element Methods exist a number of 'alternative' approaches. Hereunder are briefly described two of them. Some of these alternative methods try to decompose the flow around an advancing cone, in order to assess a theoretical framework to simplify the penetration process, as illustrated by Fig. 3.9.

Approaches based on the bearing capacity theory such as the limit equilibrium method or the slip-line method (Yu and Mitchell, 1998) are excluded from this section because the focus of the present work is the prediction of the ground state *around* the pile after installation.

Silva et al. (2006) performed a cylindrical cavity expansion in a steady flow of moving soil. The only difference with the Strain Path Method is that the strains are purely radial as the problem is considered plane strain. Although much cruder than the Strain Path Method, this formulation does not violate equilibrium because there is only one degree of freedom. Although the authors focus on the soil response at the pile wall, the soil state around a pile could also be obtained.

Basu et al. (2009) model the penetration of a jacked pile in London clay. The authors focus on the shaft behaviour by studying a layer of plane strain clay sur-

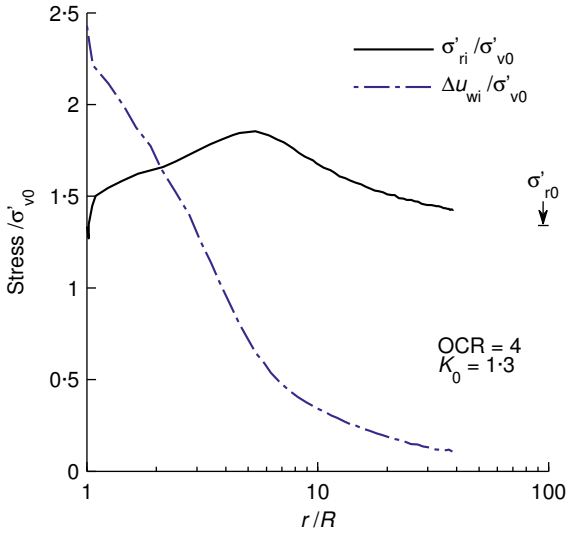

Figure 3.10 Radial distribution of radial effective stress and excess pore pressure at the end of installation in overconsolidated London clay using Chakraborty (2009)'s constitutive model (from Basu et al., 2013).

rounding the pile. The layer is first subjected to a cavity expansion, which stands for the insertion of the pile toe, followed by a series of quasi-static shearing cycles, standing for jacking cycles. The soil model used is a critical state based elastoplastic model capable of predicting residual states, strain rate effects and stress induced anisotropy (Chakraborty, 2009). The constitutive model is very complex but the plane strain approach is relatively straightforward. Unfortunately, the only published result, reproduced in Fig. 3.10, is for an overconsolidated initial state (OCR = 4) which is therefore hazardous to compare with the previous simulations, which all started on the wet side of critical (Figs 3.2b, 3.6, and 3.8).

3.1.5 Conclusion

The Cavity Expansion Method was the first rational approach to account for the installation effects of a displacement pile. It closely replicates the radial displacement field around the pile shaft. Nevertheless, it accounts neither for the complex strain paths followed by the soil near the pile toe nor for the repeated shaft-soil shearing cycles inducing friction fatigue. It is nonetheless considered as a reference solution because it is simple and robust.

The Strain Path Method produces very convincing strain paths by assuming a quasi-static flow of incompressible soil around an expanding spherical cavity. The method has the advantage of being two dimensional, therefore predicting part of the h/R effect as the stress is relieved as the soil flow past the toe. However, it does not respect the equilibrium equations and it does not take into account shaft-soil friction, which implies that friction fatigue (the other part explaining the h/R effect) is not taken into account.

Baligh (1985) argued that realistic finite element solutions are beyond the reach of existing computers. This is not the case any more, as the pile installation simulation through finite elements now begin to produce meaningful results. Nevertheless, they are cumbersome, time consuming and very complex to implement.

The 'alternative' methods offer interesting approaches that try to capture specific aspects of pile installation without being so cumbersome as the Finite Element Method.

Installation simulation should seek a balance between the simulation method, which dictates the soil deformations, and the constitutive model, which predicts the stresses. A Cavity Expansion using a very advanced constitutive model would be as useless as an ALE Finite Element simulation with an elastic soil. Therefore, the correct balance should be sought in accordance with one's objectives.

Important characteristics that should be accounted for – and which are found in the literature – in a realistic simulation of pile installation are (1) the strain reversal around the pile toe, (2) the stress relaxation with vertical distance from pile toe (one aspect of the h/R effect – Fig. 2.16, p. 39), and (3) an effective stress soil model capable of at least tackling high strains, strain reversals, volumetric and shear induced pore pressures, and OCR dependency.

Nevertheless, two other important characteristic, which were seldom modelled in the investigated literature, are to be accounted for, in my opinion. Firstly, soil fatigue (the other reason for the h/R effect observed in field tests – Fig. 2.16, p. 39) is nearly never taken into account: only Jassim et al. (2013) (Section 3.1.3) and Basu et al. (2009) (Section 3.1.4) focus on the cyclic aspect of installation. Secondly, all but one simulation presented – again, Jassim et al. (2013) – are performed in a quasi-static motion, albeit pile driving being highly transient.

3.2 Equalisation

The equalisation stage, in saturated clayey soils, is mainly controlled by the consolidation, during which dissipation of excess pore pressure leads to a variation in

Table 3.1 Surveyed literature of consolidation simulations around a displacement pile in clay.

Reference	*Installation*	*Soil model*	*Consolidation*
Randolph and Wroth (1979)	CEM	Elastic	Uncoupled
Randolph, Carter and Wroth (1979)	CEM	MCC	Coupled
Carter et al. (1979)	CEM	Elastic, Tresca, and MCC	Both
Soares and Dias (1989)	CEM	MCC	Uncoupled
Whittle (1992)	SPM	MIT-E3	Coupled
Basu et al. (2009, 2013)	'Alternative'	Unnamed (Chakraborty, 2009)	Coupled

Notes: CEM: Cavity Expansion Method, SPM: Strain Path Method, MCC: Modified Cam clay, Tresca: Elastoplasticity with Tresca yield criterion.

effective stress around the pile. The references of consolidation results used in this section are summarized in Table 3.1.

Like in Chapter 2, the subscript 'i' is used to denote quantities sampled immediately after installation and the the subscript 'c' for equalised values.

3.2.1 Consolidation theory

The theory of consolidation was developed by Terzaghi (1925), who considered a one dimensional problem where pore pressure and effective stress are coupled. Biot (1941) extended the theory by studying the three dimensional case where pore pressure and effective stress are uncoupled. Nowadays, the theory of consolidation has reached a stage where there is a general consensus on the basic equations (see *e.g.* Coussy, 2004). In Terzaghi's theory, the pore fluid and soil particles are assumed to be incompressible. This means that deformations can only occur by a rearrangement of the soil skeleton and movement of pore water. This is a good approximation of the behaviour of clays which are highly compressible whereas the constituents, particles and fluid, are very stiff (Randolph, Carter and Wroth, 1979; Verruijt, 2010). The governing equations of the consolidation an analysis are explicitly established in Section 5.4.

The results of the consolidation analysis, versus time or versus radius, depend mainly on three factors:

(i) The soil conditions prior to consolidation, described by the (radial) distribution of stress and pore pressure around the shaft at the end of installation;

(ii) The choice of coupled or uncoupled consolidation. Uncoupled consolidation denotes an analysis where stress and pore pressure are independent of each other. This simplification boils down the analysis to the resolution of a classical Terzaghi diffusion equation which rules pore pressure decay over time and space, reproduced hereunder for a one-dimensional case in cylindrical coordinates:

$$\frac{\partial u_w}{\partial t} = c_h \nabla^2 u_w,$$

where $c_h = k_r/\gamma_w m_v$ is the horizontal coefficient of consolidation in which k_r is the radial permeability, γ_w the water unit weight, and m_v the soil compressibility. During coupled consolidation, total stress is constant implying that the variation of excess pore pressure is exactly balanced by the change in effective stress.
Coupled consolidation is a much more intricate analysis in which pore pressure and stress are governed by two coupled equations which are solved iteratively. As announced above, the details concerning coupled consolidation are defined in Section 5.4 (p. 112);

(iii) The constitutive model. There is abundance to choose from, ranging from 2 parameters linear elasticity to 15 or more parameters multiple surface elastoplastic models (*e.g.* MIT-E3; Whittle, 1992). During consolidation, the influence of the constitutive model lays on the compressibility of the soil which, in the most advanced models, depends non linearly on stress, strain, and void ratio.

The constant total radial stress predicted by uncoupled consolidation does not agree with the experiments, which rules out uncoupled consolidation for the prediction of the stress state after equalisation. However, the pore pressure dissipation curve from an uncoupled consolidation is similar to the one predicted by coupled consolidation – at least for elastic and elastoplastic soil models (Carter et al., 1979; Soares and Dias, 1989).

Importance of factors (i) and (iii), respectively the soil conditions prior to consolidation and the choice of constitutive model, is underlined hereunder. Fig. 3.11 compares the pre- and post-consolidation outputs of Randolph, Carter and Wroth (1979) and Whittle (1992) who simulated the installation of a closed-ended pile in normally consolidated Boston Blue clay followed by a coupled consolidation analysis. Randolph, Carter and Wroth (1979) performed a cavity expansion[5] followed by a consolidation analysis, while using the Modified Cam clay model. Whittle (1992)

[5]The cavity expansion performed by Randolph, Carter and Wroth (1979) is described in Section 3.1.1 and the Modified Cam clay parameters are summarised in Table E.1, p. 220.

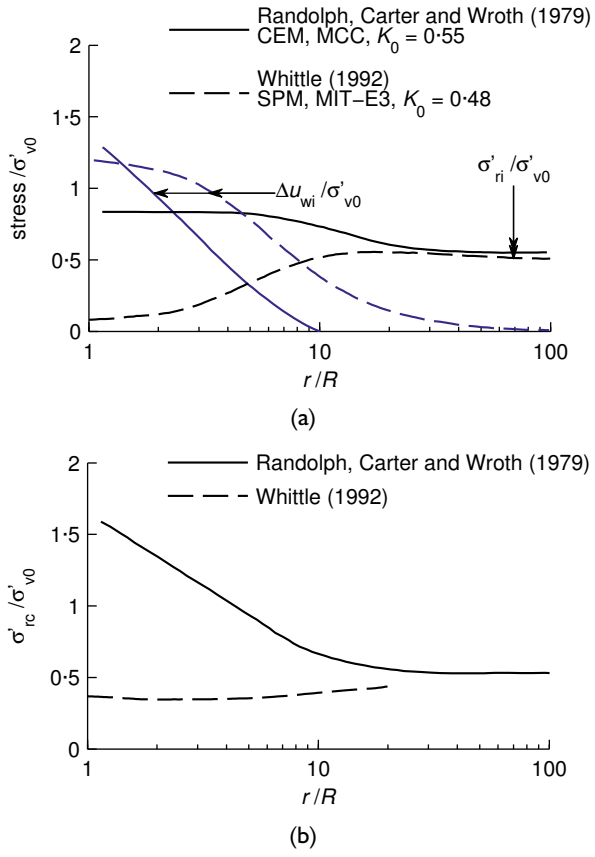

Figure 3.11 Predicted stress distribution (a) after pile installation and (b) after equalisation in Boston Blue clay (from Randolph, Carter and Wroth, 1979; Whittle, 1992).

performed a Strain Path Method installation[6] followed by a consolidation analysis, while using the MIT-E3 constitutive model.

Fig. 3.11a depicts the distribution of radial effective stress and excess pore water pressure after installation from both references (reproduced from Figs. 3.2 and 3.6). Although pore pressures at pile wall are comparable for both simulations, the difference in their radial distribution means that there is in fact much more pore pressure generated with the Whittle (1992) Strain Path Method simulation than by the Randolph, Carter and Wroth (1979) Cavity Expansion simulation. On the other hand, radial stresses do not share any similarity: Whittle (1992)'s radial effective stress after installation (σ'_{ri}) is larger than the initial vertical effective stress (σ'_{v0}) while Randolph, Carter and Wroth (1979)'s output displays the opposite trend.

Fig. 3.11b depicts the radial effective stresses after consolidation (σ'_{rc}. At pile wall, σ'_{rc} from Cavity Expansion is *three times* as large as the one from the Strain Path Method.

The stress state after installation (*i.e.* the simulation model used for installation) and the soil constitutive model are therefore very important for the simulation of installation and equalisation. From the presented data above, one cannot outline the relative importance of the installation model vis-à-vis the constitutive model. However, in my opinion, the installation model is much more critical, as long as the constitutive model is based on the critical state theory.

All the simulations reported in this section were performed with a constant permeability (k_r) and by assuming radial drainage. Therefore, the implication of wavering these assumption cannot be measured.

3.2.2 Dimensionless times

A note is made on the dimensionless times used in consolidation analysis. For uncoupled consolidation or when using a constitutive model that has a constant coefficient of consolidation (c_h), a suitable dimensionless time variable for consolidation is (Soderberg, 1962):

$$T = \frac{c_h t}{R^2} = \frac{k_r t}{\gamma_w R^2} m_v,$$

where k_r is the radial permeability, t is the time, m_v the one-dimensional coefficient of volume compressibility, γ_w is the water unit weight, and R is the pile radius. More advanced soil constitutive models, for which compressibility (m_v) varies during consolidation, require a new definition. Several dimensionless times have been

[6]The Strain Path Method carried out by Whittle (1992) is reported in Section 3.1.2 and the MIT-E3 material parameters can be found in Whittle et al. (1990).

proposed:

$$T^* = \frac{k_r t}{\gamma_w R^2} s_{u0}, \qquad \text{(Randolph, Carter and Wroth, 1979)} \qquad (3.3)$$

$$T_1^* = \frac{k_r t}{\gamma_w R^2} \sigma'_{vy0}, \qquad \text{(Whittle, 1992)}$$

$$T_2^* = \frac{k_r t}{\gamma_w R^2} G', \qquad \text{(Carter et al., 1979)}$$

$$T_3^* = \frac{k_r t}{\gamma_w R^2} p'_0, \qquad \text{(Whittle, 1992)}$$

where s_{u0} is the soil initial (*in situ*) undrained shear strength, σ'_{vy0} is the soil initial apparent vertical preconsolidation stress, G' is the soil effective stress stiffness, and p'_0 is the soil initial mean stress. Using a critical state theory framework, s_{u0} is the projection of the current state on the critical state line (csl) and σ'_{vy0} is the intersect between the unloading-reloading line (url) and the normal compression line (ncl), which is related to the csl.[7] Therefore, T^* and T_1^* are both related to soil strength (s_{u0}). On the other hand, still using the critical state framework, G' and p'_0 are related,[8] which implies that T_2^* and T_3^* are related to soil stiffness (or initial state).

3.2.3 Conclusion

The comparison of six research groups that modelled equalisation around a displacement pile brought the following conclusions:

(i) The equalisation stage in clays can be modelled as the consolidation of the soil around the pile;

(ii) Consolidation analysis is either 'uncoupled,' where the reduction of excess pore pressure is exactly balanced by the increase in effective stress, or 'coupled,' where pore pressure and effective stress are governed by two coupled equations (which are defined later, in Section 5.4, p. 112);

(iii) Coupled consolidation analysis is necessary in order to replicate the total stress decrease at pile wall measured experimentally;

(iv) The distribution of stress after installation and the constitutive model chosen are critical for correct assessment of the equalisation stage.

[7] The position of the csl (Γ) is linked to the position of the ncl (N) through: $\Gamma = N - (\lambda - \kappa)\ln 2$ in the $v : \ln p'$ compression plane. If the compression plane is defined in the $\ln v : \ln p'$ plane (like in the hypoplastic model used in this work), $\Gamma^* = N^*/2^{\lambda^*}$.

[8] Using the (modified) Cam clay model, the small strain shear stiffness (G_0) is equal to $\frac{3(1-2\nu)}{2(1+\nu)} \frac{p'_0}{\kappa}$ where ν and κ are material parameters (assuming a constant ν). Using hypoplasticity, $G_0 = \frac{p'_0}{r\lambda^*}$ where r and λ^* are material parameters (this is explained in Section 4.2, p. 70).

3.3 Proposed course of action

The following section is split in two parts. First of all, the main conclusions of the literature review are summarised. Next, the proposed course of action for the numerical modelling of the pile installation and subsequent equalisation is presented.

The literature review of experimental pile installation and equalisation, the conclusion of which is outlined in Section 2.5 (p. 37), showed that the two most important characteristics of displacement pile installations in clay are: (1) the dependence of soil response on initial overconsolidation ratio (OCR) and (2) the h/R effect: the soil state around the pile varies with increasing vertical distance from pile toe (h) due to stress relaxation away from pile toe and soil fatigue from the accumulation of shaft-soil shearing cycles.

The literature review of pile installation simulation and the equalisation simulation (the conclusion of which are detailed in Sections 3.1.5 and Section 3.2.3, respectively) showed that the simulation should above all be balanced in complexity between the simulation method (Cavity Expansion, Strain Path…) and the constitutive model (elasticity, elastoplasticity…). The following aspects should be accounted for to strive for a realistic and innovative simulation of the pile installation and equalisation stages. The installation simulation should include strain reversal around the pile toe, stress relaxation as the soil passes above the pile toe (on aspect of the h/R effect), and cyclic loading of the soil around the shaft (the other aspect of the h/R effect). The equalisation simulation should be coupled. On the other hand, the constitutive model should be able to tackle OCR dependency, high strains, cyclic loading, and shear induced pore pressures.

Based on the aforementioned conclusions, the course of action for this work is justified hereunder.

Installation simulation The effect of pile installation on the soil surrounding the pile is performed in two steps, similarly to the 'alternative' method of Basu et al. (2009) (see Section 3.1.4). First, a Strain Path Method simulation is performed: it accounts for the insertion of the pile toe. Then, the state of a narrow disk of soil far behind the Strain Path Method toe is extracted, and a series of driving blows is applied to that disk: this second step is named the Disk Shearing Model. These two steps are made using an hypoplastic soil constitutive model which has three desirable features: it is based on the critical state soil mechanics theory, it models cyclic loading, and it predicts shear induced pore pressures.

Using this approach, the two important factors of installation are hoped to be accounted for:

(i) OCR is taken into account through the hypoplastic constitutive model, which is based on the critical state theory; and

(ii) The two factors explaining the h/R effect are taken into account: the Strain Path Method models the stress relaxation as h increases, while the cycles of strain imposed by the Disk Shearing Method will progressively change the

soil state around the pile, thanks to the fact that the hypoplastic model takes into account cyclic loading and shear induced pore pressures.

The simulation method is also chosen because it is relatively simple, compared to large strain Finite Element Method (Section 3.1.3). The latter is the only other approach which could attain the aforementioned goals. However, their implementation is clearly out of reach for a single thesis, as most of the research groups presented in Section 3.1.3 are only just coming close to being capable of reaching the objectives of this thesis, after having been working for more than 10 years on the development of these methods.

Equalisation simulation The equalisation modelling will be performed using a coupled consolidation analysis, using the same hypoplastic soil model as for installation

The hypoplastic soil model is presented in Chapter 4 and the model used to simulate the installation and equalisation is presented in Chapter 5.

Chapter 4

Hypoplastic constitutive model

This chapter presents the constitutive model used to predict the clay stress-strain response, which is eventually used in the pile driving model described in Chapter 5. The constitutive model presented in this section is hypoplasticity for clay (Mašín, 2005) coupled to the intergranular strain concept (Niemunis and Herle, 1997).

Section 4.1 presents the Mašín (2005) critical state based hypoplastic law. It is aimed at reproducing the effective-stress behaviour of clays in three dimensions during one loading-unloading cycle. Affixed to the Mašín (2005) model is the Niemunis and Herle (1997) intergranular strain concept, described in Section 4.2, which accounts for small strain stiffness degradation and strain reversals.

Section 4.3 presents two examples of the model output: an undrained cyclic simple shear test and an oedometric test. The first test outlines the monotonic and cyclic shear behaviour of the model for two initial overconsolidation ratios, while the second one details the volumetric behaviour of the model. Section 4.4 then compares the model output to several triaxial tests performed on London clay.

Section 4.5 presents a discussion on various aspects of the model, and Section 4.6 concludes this chapter.

Incremental form The hypoplastic model is described as an incremental equation relating the effective Jaumann stress rate $\overset{\triangledown}{\boldsymbol{\sigma}}'$ to the strain rate tensor $\mathbf{D}$:

$$\overset{\triangledown}{\boldsymbol{\sigma}}' = \mathscr{M}' : \mathbf{D}, \tag{4.1}$$

where:

$\overset{\triangledown}{\boldsymbol{\sigma}}'$ is the Jaumann objective rate of the effective stress. In any constitutive law that expresses the stress rate as a function of the deformation rate, the definition of stress rate employed should strictly be frame indifferent (Prager, 1961). The Jaumann objective stress rate is a convenient way of making the stress rate measure independent of body rotation (Norbury and Wheeler, 1987), and is defined as:

$$\overset{\triangledown}{\boldsymbol{\sigma}}' = \dot{\boldsymbol{\sigma}}' + \mathbf{W} \cdot \boldsymbol{\sigma}' - \boldsymbol{\sigma}' \cdot \mathbf{W}, \tag{4.2}$$

where $\mathbf{W}$ is the spin tensor (the opposite of the skew-symmetric part of the velocity gradient, defined in Appendix C);

$\mathscr{M}'$ is the tangent stiffness tensor, defined in the next two sections. It depends on the state parameters (*e.g.* stress $\boldsymbol{\sigma}'$ and void ratio e) and material parameters (*e.g.* the critical state friction angle ϕ'_{cs} and the slope of the normal compression line λ^*); it does not however depend on the strain level;

$\mathbf{D}$ is the strain rate tensor: the symmetric part of the velocity gradient (defined in Appendix C).

The incremental formulation of Eq. (4.1) implies that strain and stress are computed through small increments of strain rate ($\mathbf{D}$). These increments and tensor $\mathscr{M}'$ are independent of the current strain, which allows the constitutive model to comfortably reach the high strains imposed during pile driving.

4.1 Hypoplasticity for clays

In the hypoplastic Mašín (2005) clay model, the $\mathscr{M}'$ tensor of Eq. (4.1) is defined by:

$$\mathscr{M}' = f_s \mathscr{L} + f_s f_d \mathbf{N} \otimes \frac{\mathbf{D}}{||\mathbf{D}||} \qquad \text{with} \quad \mathbf{N} = \mathscr{L} : \left(-Y \frac{\mathbf{m}}{||\mathbf{m}||} \right), \tag{4.3}$$

where f_s, f_d, $\mathscr{L}$, Y and $\mathbf{m}$ depend on the state and material parameters (which are described in the following paragraph) and contain the definition of the model, which is summarised in Table 4.1. Due to the symmetry of the stress and strain rate tensors, $\mathscr{M}'$ has 36 independent components (instead of 81).

The Mašín (2005) constitutive model is isotropic, rate-independent, frictional, and follows quasi-logarithmic compression. It assumes the following: the position of the critical state line (csl) is shifted of a factor 2 from the position of the isotropic normal compression line (iso-ncl; Fig. 4.1a) , the lower limit for the void ratio (e) is 0, the soil is insensitive, and the critical state surface is defined by the Matsuoka and Nakai (1974) surface (Fig. 4.1b). Furthermore, the model has the desirable feature of modelling shear dilatancy.

The state is defined by seven state variables: the effective stress matrix ($\boldsymbol{\sigma}'$, which has 6 components) and the void ratio (e). There are five material parameters, which have a similar meaning as the five (modified) Cam clay model (Roscoe and Schofield, 1968) parameters:

ϕ'_{cs} is the critical state friction angle controlling the Matsuoka-Nakai surface (Fig. 4.1b depicts its deviatoric sections for three friction angles);

N^* and λ^* control the slope and position of the isotropic normal compression line (iso-ncl) in the $\ln v$:$\ln p'$ plane[1] (Fig. 4.1a). The soil follows the iso-ncl during isotropic compression when it is normally compressed;

[1] N^* has been used instead of $N = \ln N^*$ defined in Mašín (2005). N^* is the specific volume (v) of an isotropically compressed soil at 1 kPa.

κ^* controls the initial slope of the unloading-reloading line (url) from a normally compressed state (Fig. 4.1a); for further unloading, the soil follows a non linear curve in the $\ln v : \ln p'$ plane, the slope of which decreases with decreasing mean effective stress (p');

r is defined as the ratio of the bulk modulus (K) to the shear modulus (G'), starting from an isotropic normally compressed state: $r = K_{\text{iso}}/G'_{\text{iso}}$. However, this definition is not used to calibrate the model, because the integrannular strain enhancement (presented in the next section) overwrites the small strain behaviour of of the model.

Calibration of ϕ'_{cs} is made using any sort of shear test (*e.g.* a triaxial test). Determination of N^* and λ^* is straightforward if the soil is non-structured (insensitive) by using an oedometric or isotropic compression test. Parameter κ^* is preferably calibrated through simulation of unloading at the desired stress level, as the predicted url is a non linear curve in the $\ln p' : \ln p'$ plane. Finally, r is calibrated to adjust the curvature of the model shear response (Mašín, 2012c).

In hypoplasticity, the overconsolidation ratio is defined as:

$$\text{OCR}^* = p'_{\text{e}}/p'_0, \tag{4.4}$$

where p'_{e} is Hvorslev's equivalent pressure on the iso-ncl and p'_0 is the current mean effective stress (Fig. 4.1a). This definition has been chosen because the hypoplastic model predicts a non linear url in the $\ln v : \ln p'$ compression plane.

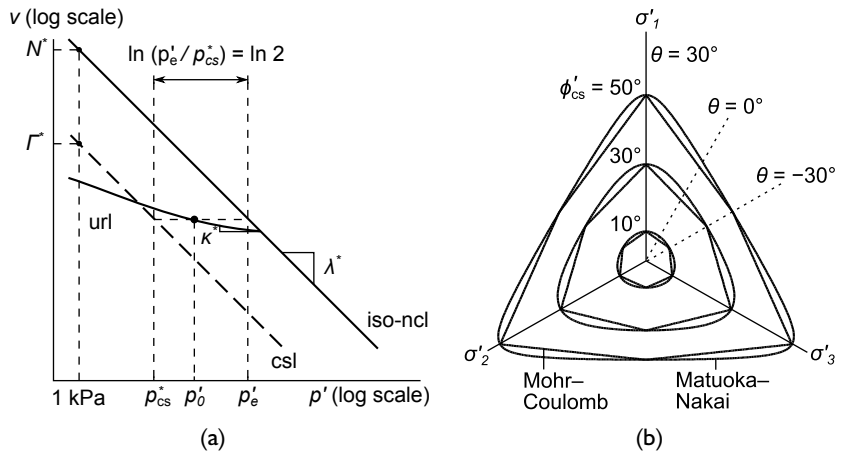

Figure 4.1 Definition of (a) parameters N^*, λ^* and κ^*, and quantities p^*_{cs} and p'_{e} in the compression plane and (b) the Matsuoka-Nakai and Mohr-Coulomb surfaces in the octahedral plane for three friction angles (ϕ'_{cs}); the Lode angle (θ) also is represented for one sector of the deviatoric plane.

Table 4.1 Equations defining the Mašín (2005) hypoplastic model.

Description	*Equation(s)*	*Parameter(s)*	*Reference(s)*
Generalised stress rate-strain rate relationship (equivalent to Eq. 4.1 with Eq. 4.3)	$\overset{\triangledown}{\boldsymbol{\sigma}}' = f_s \mathscr{L} : \left(\mathbf{D} - f_d Y \frac{\mathbf{m}}{\|\mathbf{m}\|} \|\mathbf{D}\| \right)$		Niemunis (2003)
Hypoelastic tensor	$\mathscr{L} = 3(c_1 \mathscr{I} + c_2 a^2 \hat{\boldsymbol{\sigma}}' \otimes \hat{\boldsymbol{\sigma}}')$		Herle and Kolymbas (2004)
where	$\hat{\boldsymbol{\sigma}}' = \boldsymbol{\sigma}'/(3p')$		
and	$a = \frac{\sqrt{3}(3 - \sin\phi'_{cs})}{2\sqrt{2}\sin\phi'_{cs}}$	ϕ'_{cs}	
and by using definition of r	$c_1 = \frac{2(3 + a^2 - f_{di} a\sqrt{3})}{9r}$ with $f_{di} = \varsigma^{\alpha}$	r	
and by imposing the symmetry of $\mathscr{L}$	$c_2 = 1 + 3(1 - c_1)/a^2$		Herle and Kolymbas (2004)
Pyknotropy: dependency on density (or OCR*):	$f_d = \left(\frac{p'}{p^*_{cs}} \right)^{\alpha}$		
By using the definition of the iso-ncl	$\ln v = \ln N^* - \lambda^* \ln p'$	N^*, λ^*	Butterfield (1979)
and the position of the csl	$p'/p^*_{cs} = \varsigma$	$\varsigma = 2$	

Continued on next page

f_d becomes	$f_d = \left(\varsigma p' \left(\frac{v}{N^*}\right)^{\frac{1}{\lambda^*}}\right)^{\alpha} = \left(\frac{\varsigma}{\mathrm{OCR}^*}\right)^{\alpha}$		
while κ^*, the slope of the url leads to	$\alpha = \frac{1}{\ln 2} \ln\left[\frac{\lambda^* - \kappa^*}{\lambda^* + \kappa^*}\left(\frac{2 + a^2}{a\sqrt{3}}\right)\right]$	κ^*	
Barotropy: dependency on mean stress	$f_s = \frac{3p'}{\lambda^*}(3 + a^2 - f_{di} a\sqrt{3})^{-1}$		
Limit stress condition (critical state)	$Y = f_Y + 1$ and $f_d = 1$		Niemunis (2003)
with	$f_Y = \frac{-I_1 I_2}{I_3} - \frac{9 - \sin^2\phi'_{cs}}{1 - \sin^2\phi'_{cs}} \leq 0$	ϕ'_{cs}	Matsuoka and Nakai (1974)
Hypoplastic flow rule	**m** which is a tensorial function of ϕ'_{cs} and $\boldsymbol{\sigma}'$		Kirkgard and Lade (1993); von Wolffersdorff (1996)

4.2 Intergranular strain

From its definition, the Mašín (2005) model has one major weakness: it ratchets when being subjected to strain reversals, therefore limiting it to the prediction of monotonic loadings. In order to overcome this shortcoming inherent to any hypoplastic formulation, Niemunis and Herle (1997) introduced the intergranular strain concept which accounts for cyclic loading by creating an 'elastic' bubble defined in the strain space (similar to the Y_1 yield surface defined by Smith et al., 1992). When strains are small enough to be inside this bubble, the model predicts a high stiffness elastic response.

To achieve this, a new state variable is introduced: the intergranular strain ($\boldsymbol{\delta}$), a strain-like tensor which acts as the soil memory, remembering the latest loading direction and intensity. In other words, $\boldsymbol{\delta}$ contains the position of the current state, in the strain space, with regards to the bubble.

The intergranular strain bubble size is delimited by parameter R, which has strain units (Fig. 4.2). When inside the bubble, soil stiffness is m_R times larger than the stiffness predicted without intergranular strain for initial or reverse loading, *i.e.* when the previous direction of loading is the opposite of the current one (Fig. 4.2). For a direction perpendicular to the previous loading direction, the stiffness is multiplied by m_T, and for any other direction the stiffness is multiplied by a value that stands between m_R and m_T. When the soil state steps out of the bubble, the stiffness decreases and tends towards the one predirected by the Mašín (2005) model (Fig. 4.2), using the following interpolation:

$$\begin{aligned}\mathscr{M}' =& [\rho^{\chi} m_T + (1-\rho^{\chi}) m_R] f_s \mathscr{L} \\ &+ \begin{cases} \rho^{\chi}(1-m_T) f_s \mathscr{L} : \hat{\boldsymbol{\delta}} \otimes \hat{\boldsymbol{\delta}} - f_s f_d \rho^{\chi} \mathbf{N} \otimes \hat{\boldsymbol{\delta}} & \text{for } \hat{\boldsymbol{\delta}} : \mathbf{D} > 0 \\ \rho^{\chi}(m_R - m_T) f_s \mathscr{L} : \hat{\boldsymbol{\delta}} \otimes \hat{\boldsymbol{\delta}} & \text{for } \hat{\boldsymbol{\delta}} : \mathbf{D} \leq 0 \end{cases},\end{aligned}$$

where $\hat{\boldsymbol{\delta}}$ is the direction of intergranular strain:

$$\hat{\boldsymbol{\delta}} = \begin{cases} \boldsymbol{\delta}/\|\boldsymbol{\delta}\| & \text{for} \boldsymbol{\delta} \neq 0, \\ 0 & \text{otherwise.} \end{cases}$$

The shape of the stiffness degradation is controlled by parameter β_r, as illustrated in Fig. 4.2. The fifth and last intergranular strain parameter (χ) controls the value of the strain at which the soil is swept out of memory, *i.e.* the strain at which the stiffness for any loading direction would be equal to the initial stiffness.

A simplified calibration of the five intergranular parameters, advised by Mašín (2012c), is the following: parameters $R = 10^{-4}$ and $\chi = 1$ are treated as material independent parameters, m_R is calibrated through bender element measurements (or any other mean of determining the small strain stiffness G_0), m_T is taken as half of m_R, and β_r is adjusted by comparing a simulation output to a cyclic test.

The five parameters needed for the intergranular strain, in addition to the five parameters prescribed for the Mašín (2005) model, are defined in Table 4.2 for reconstituted London clay. These parameters have been calibrated by Mašín (2005)

and the model output against several triaxial tests on remoulded and resedimented samples of London clay is presented in Section 4.4. It should be noted that even though the parameters have been calibrated for London clay, some notable features of this clay (*e.g.* residual strength) are out of its reach – the limitations of the model are described in Section 4.5.1.

Although parameter r is smaller than one, the intergranular strain 'corrects' the small strain behaviour, which yields $K_0/G_0 \approx 1{\cdot}6$ (at very small strains).

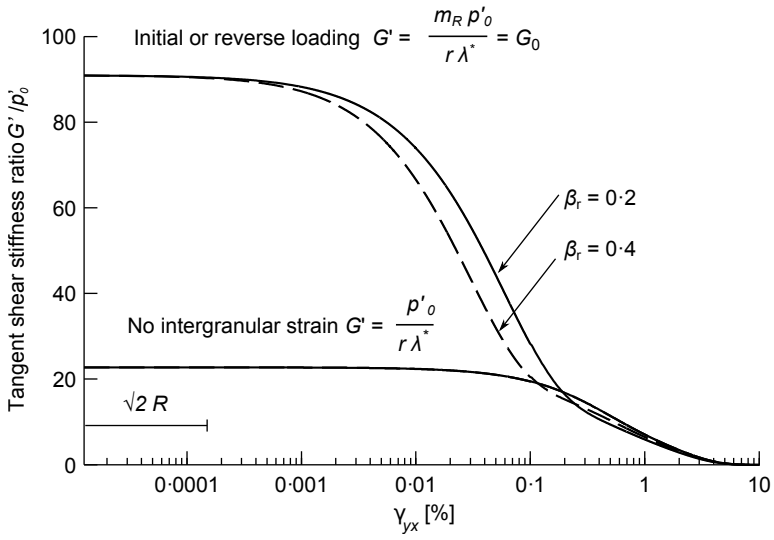

Figure 4.2 Shear stiffness degradation modelled by the intergranular strain.

Table 4.2 London clay parameters (adapted from Mašín, 2005).

Clay hypoplasticity					*Intergranular strain*				
ϕ'_{cs} [°]	λ^*	κ^*	N^*	r	m_R	m_T	R	β_r	χ
22·6	0·11	0·016	3·96	0·4	4	2	10^{-4}	0·2	1

NOTE: Parameter N^* is used instead of $N = \ln N^*$ defined in Mašín (2005).

4.3 Simulation of two laboratory tests

In this section, the hypoplastic model capabilities are displayed by showing 'one element' predictions of an undrained simple shear test and an oedometer test in Sections 4.3.1 and 4.3.2, respectively.

The tests are performed by applying the aforementioned hypoplastic model to a single element. The numerical implementation of the hypoplastic model is described in Appendix D.

4.3.1 Undrained cyclic simple shear test

An undrained cyclic shear test (Fig. 4.3) is performed on two different initial states of London clay. The two initial states of the samples are summarised in Table 4.3. The first sample is normally compressed with a coefficient of earth at rest (K_0) taken from the Jâky (1944)[2] approximation:

$$K_{0\text{nc}} = 1 - \sin\phi'_{\text{cs}}. \tag{4.5}$$

The second sample has an overconsolidation ratio of 5 and its coefficient of earth at rest is computed from the Mayne and Kulhawy (1982) relationship:

$$K_0 = K_{0\text{nc}}\,\text{OCR}^{\sin\phi'_{\text{cs}}}, \tag{4.6}$$

where OCR is the conventional definition of overconsolidation ratio ($\text{OCR} = \sigma'_{\text{vy}}/\sigma'_{\text{v0}}$), which is close to the hypoplastic OCR^* for lightly overconsolidated soils (this is discussed in Section 4.5.3).

Both initial states have the same initial void ratio (e_0) so that they have the same shear strength (s_{u0}) of 107·80 kPa.[3] The two initial states are depicted in the $\ln v : \ln p'$ compression plane in Fig. 4.4. The first sample isn't isotropically compressed, therefore, its overconsolidation ratio (OCR^*) is slightly higher than 1.

The test is performed as follows: an initial loading of $\gamma_{\text{yx}} = 10\%$ is carried out followed by a series of 2·5% amplitude cycles.

The results are depicted in Fig. 4.5. On Fig. 4.5a, one can observe that during the first 10% loading, both samples tend to the critical state strength, which depends on ϕ'_{cs} and the initial current stress (as the void ratio does not vary). The stiffness is much lower for the overconsolidated soil than the normally consolidated one, the former being at a initial stress five times lower than the latter.

The cyclic loading shows very similar behaviour between both soils, the state having almost been swept out of memory by the 10% initial shearing. At each cycle, the soil dissipates energy through hysteretic damping. The shape of each cycle depends on the state (stress, strain and void ratio) and on parameters m_{R}, R, β_{r}, and χ. The first two parameters respectively control the stiffness on reloading and the size of the elastic bubble, thus the initial response upon cycling loading, while the latter two effectively control the amount of hysteretic damping.

[2] Cited by Muir Wood (1990).

[3] The analytical expression of s_{u0} is developed in Section 4.5.3c, p. 87.

The excess pore pressure normalised to the initial vertical effective stress ($\Delta u_w/\sigma'_{v0}$) is shown in Fig. 4.5b. During the initial shearing, the normally consolidated sample exhibits contractancy while the other sample tends to negative excess pore pressure. The cycles create positive excess pore pressure for both soils, the amplitude of which decreases with the number of cycles, as the effective stress decreases.

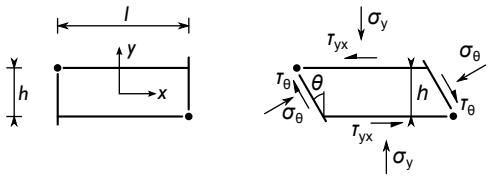

Figure 4.3 Deformation in simple shear (after Randolph and Wroth, 1981).

Table 4.3 Initial states for the cyclic simple shear tests.

OCR^*	σ'_{v0} [kPa]	K_0	e_0
1·1	590	0·615	1
5	90	1·143	1

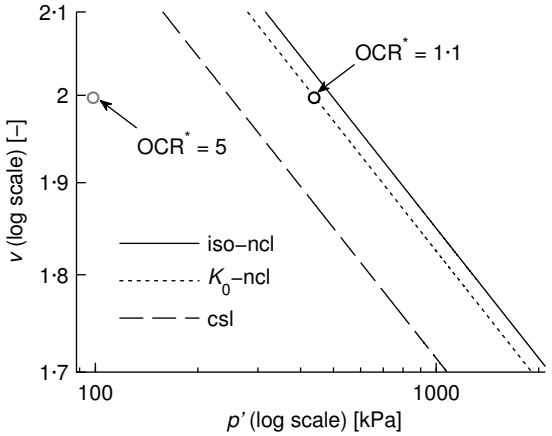

Figure 4.4 Initial states in the compression plane for the cyclic simple shear tests.

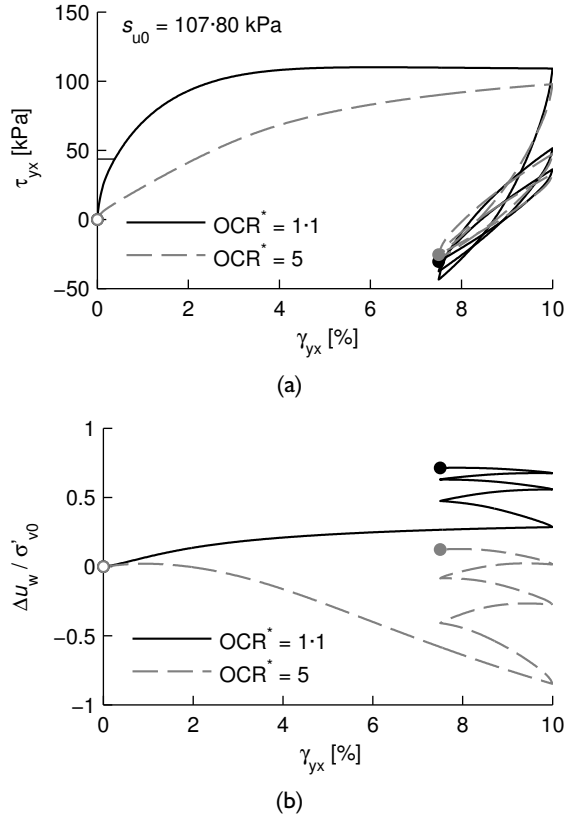

Figure 4.5 Predictions of the cyclic simple shear test: (a) Shear stress versus shear strain and (b) Normalised excess pore pressure versus shear strain. The white and plain bullets correspond to the start and end of the simulation, respectively.

4.3.2 Oedometric test

Starting from the same isotropic state as the overconsolidated sample of the previous section ($\sigma'_{v0} = 90\,\text{kPa}$, $K_0 = 1.143$, and $\text{OCR}^* = 5$), a 'one element' oedometric test is performed (Fig. 4.6). A 2000 kPa vertical stress (σ'_y) is applied for loading and then removed for unloading.

Fig. 4.7a shows the resulting compression plot. Initially, the path in the $\ln v : \ln p'$ plane follows the unloading-reloading (url) curve of slope κ^* before gradually tending towards the K_0-ncl of slope λ^*. When the soil is on the K_0-ncl, it is slightly overconsolidated, as the hypoplastic model defines overconsolidation ratio OCR^* with regards to the iso-ncl.

When the soil is unloaded, it first follows the url curve, with a slope very close to κ^*, gradually increasing.

The horizontal to vertical stress ratio σ'_x/σ'_y during loading is shown in Fig. 4.7b. Three slopes are also depicted on Fig. 4.7b: the coefficient of earth at rest (K_{0nc}, Jâky, Eq. 4.5), the unity ($\sigma'_x = \sigma'_y$), and the passive failure ($K_p = \tan^2(45° + \phi'_{cs}/2)$, Rankine). During the loading, the stress ratio is lower than Jâky while the soil is overconsolidated, and is slightly higher than Jâky when the stress path is on the K_0-ncl. During unloading, the stress path is much steeper than the loading path, during which the horizontal stress (σ'_x) eventually becomes larger than the vertical stress (σ'_y). As depicted in Fig. 4.7b, the model predictions become unrealistic for large unloadings as the stress ratio exceeds the passive failure (K_p).

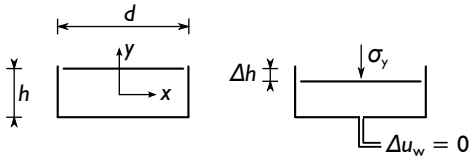

Figure 4.6 Deformation in oedometer.

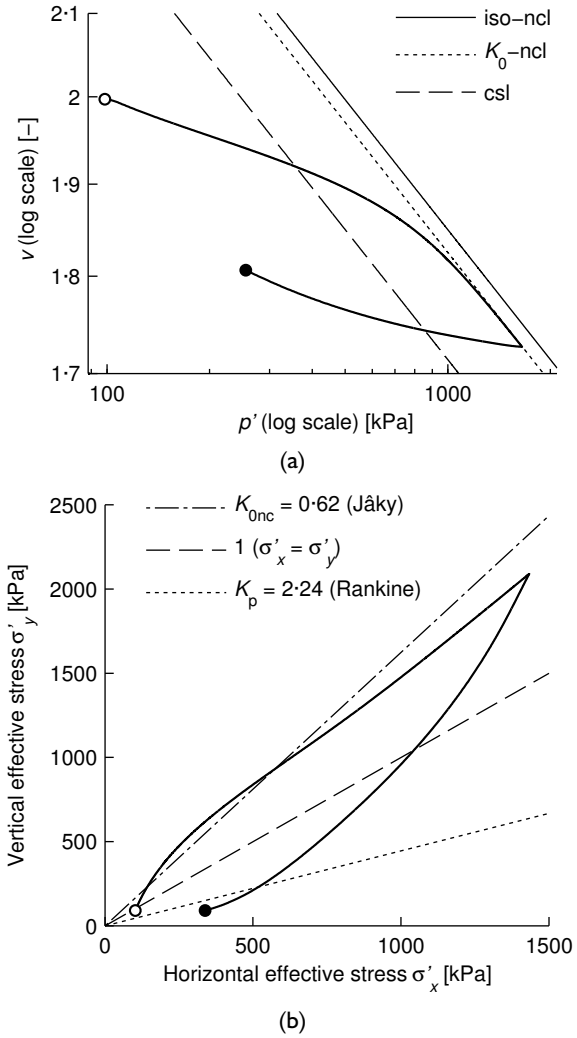

Figure 4.7 Hypoplastic model prediction of oedometric loading and unloading.

4.4 Model output against triaxial tests

The following section presents several 'one-element' simulations against results of triaxial tests performed by Mašín (2004) on London clay. Eight tests are investigated, the initial states and imposed loading paths of which are summarised in Table 4.4. All the tests are performed on remoulded or resedimented samples of London clay, which are isotropically or K_0 consolidated before being sheared. The initial void ratio (e_0) is carefully selected so that the overconsolidation ratio of the simulations match the stress history of the samples.

The 'one-element' simulations outputs are compared to the laboratory tests in Figs. 4.8 to 4.11. The hypoplastic model offers a realistic output, except for the stress path of the normally consolidated samples PhM18 and PhM21 in the $p' : q$ plane (Fig. 4.11). This shortcoming is discussed in Section 4.5.1.

Table 4.4 Summary of triaxial tests on London clay (data from Mašín, 2004) .

Test number	p'_0 *[kPa]*	q'_0 *[kPa]*	e_0	Loading
PhM10 (recons.)	135	39	1·13	K_0-UC
PhM12 (recons.)	305	138	1·02	K_0-DC (constant p')
PhM13 (recons.)	47	0	1·53	I
PhM14 (recons.)	213	78	1·06	K_0-DE (constant p')
PhM17 (resed.)	200	104	1·06	K_0-DE (constant p')
PhM18 (resed.)	450	0	0·95	I-UC
PhM19 (resed.)	110	−17·5	1·10	K_0-DC (constant p')
PhM21 (recons.)	450	0	0·95	I-UC

NOTE: recons.: reconstituted, resed.: resedimented, K_0: K_0 consolidated, I: isotropically consolidated, D: drained, U: undrained, C: compression, E: extension.

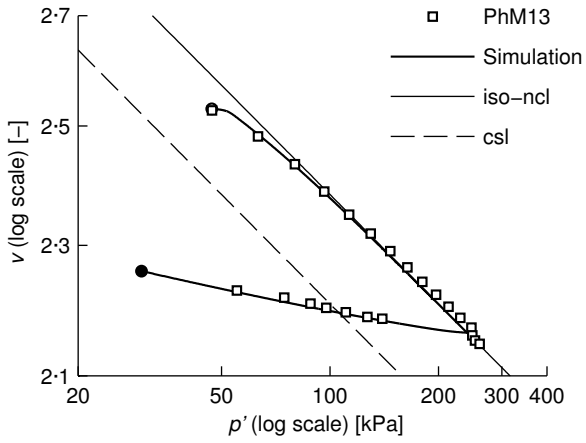

Figure 4.8 Isotropic compression of London clay: experiment versus simulation (data from Mašín, 2004).

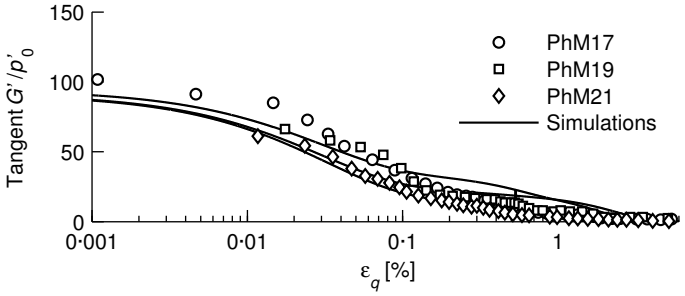

Figure 4.9 Stiffness degradation curve for several triaxial tests: experiment versus simulation (data from Mašín, 2004).

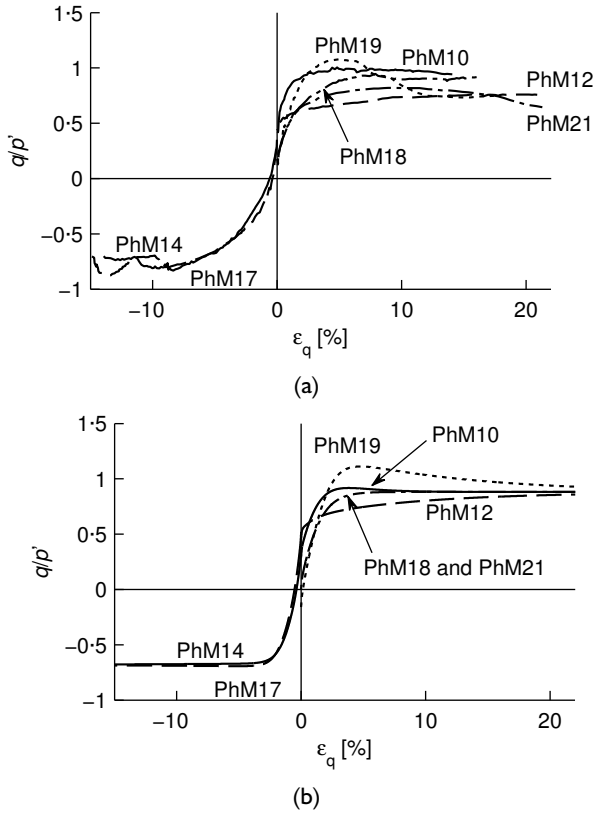

Figure 4.10 Stress ratio versus shear strain for triaxial tests on London clay, (a) experiment (data from Mašín, 2004) and (b) simulation.

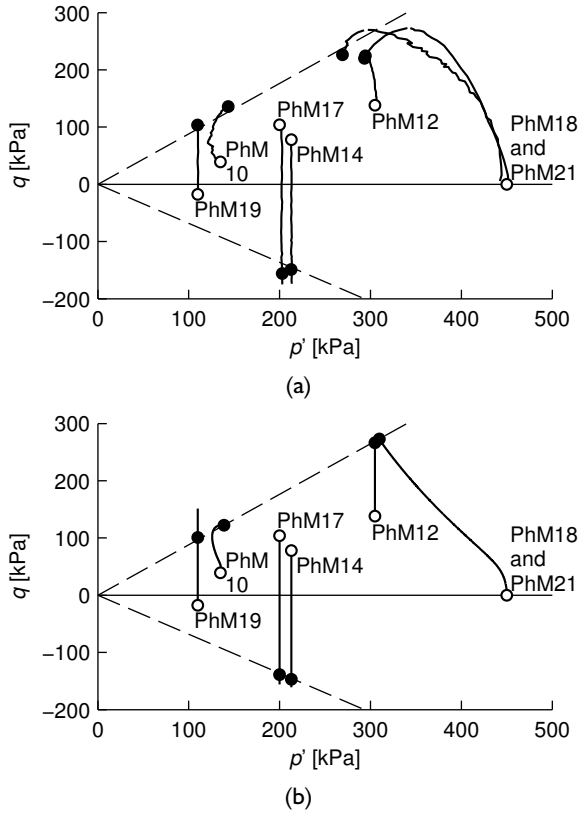

Figure 4.11 Stress path of triaxial tests on London clay, (a) experiment (data from Mašín, 2004) and (b) simulation.

4.5 Discussion

This section presents a discussion about various aspects of the constitutive model. Section 4.5.1 offers a discussion about the model strengths and weaknesses and a comparison to constitutive models used for previous attempts at modelling pile installation. Section 4.5.2 justifies the use of the Mastuoka-Nakai surface as the critical state criterion. Finally, Section 4.5.3 relates the model to geotechnical quantities: void ratio, overconsolidation ratio, and shear strength.

4.5.1 Critical review

The major difference with elastoplasticity (framework embracing most of the soil models: Cam clay, HK, MIT-E3, S1-CLAY…) is the absence of separation between elastic reversible deformations and plastic irreversible deformations. Although the intergranular strain, defined in Section 4.2, adds an 'elastic' bubble, the formulation of hypoplasticity prevents the explicit definition of a yield function, a plastic potential, and a hardening rule. Therefore, the hypoplastic model is quite straightforward to implement.

Apart from this practical consideration, the present model was chosen for the three reasons cited in Section 3.3 (p. 62), namely:

- it is based on the critical state soil mechanics theory which means that the state and the soil response are governed by overconsolidation ratio;
- it predicts a smooth degradation of the shear modulus and possesses a cyclic memory so that cyclic loading can be modelled;
- its volumetric and shear responses are coupled, *i.e.* it predicts shear induced dilatancy.

These characteristics, alongside with other desirable characteristics, are summarised in Table 4.5 and compared to constitutive models used for previous attempts at the simulation of pile installation reviewed in Chapter 3: Modified Cam clay (Roscoe and Schofield, 1968), MIT-E3 (Whittle, 1987) and Chakraborty (2009)'s model. As indicated by Table 4.5, MIT-E3 and Chakraborty (2009)'s model not only possess the desired characteristics for the present work, but offer more advanced features. However, what they gain in attributes is lost in complexity and ease of use, as evidenced for example by the number of constitutive parameters required.

The three shortcomings listed in Table 4.5 alongside with the most notable drawbacks of the presented hypoplastic model are briefly described hereunder. Some of them have been taken into account in add-ons to the hypoplastic model, but none have been implemented in this thesis.

(i) In reference to the aim of this thesis, the biggest flaw is maybe the absence of rate dependence in the model. Niemunis (2003), Wu (2006), Niemunis et al. (2009) and Gudehus (2011) are some of the authors who offer approaches to incorporate viscous effects (which include rate dependence, creep and relaxation) but these come while sacrificing other parts of the model.

Table 4.5 Comparison of the hypoplastic model with other models used for the pile installation simulations reviewed in Chapter 3.

	Modified Cam clay (Roscoe and Schofield, 1968)	*MIT-E3 (Whittle, 1987)*	*Unnamed (Chakraborty, 2009)*	*Present hypoplastic model*
Critical state soil mechanics	✓	✓	✓	✓
Shear modulus smooth degradation	×	✓	✓	✓
Cyclic memory	×	✓	✓	✓
Shear induced dilatancy	×	✓	✓	✓
Rate dependency	×	×	✓	×
Anisotropy	×	✓	✓	×
Residual strength	×	×	✓	×
Number of parameters	5	15	19	10

(ii) Another flaw is the fact that the model is isotropic, while clay is by definition anisotropic. A discussion of the matter is proposed in Wu (1998) and Kopito and Klar (2013).

(iii) Another feature the model is lacking is the residual state: During large shearing of certain soils, soil particles align along a localised failure plane and the strength may decrease even further from the critical state condition, leading to the residual state (Mitchell and Soga, 2005). This advanced feature has never, to my knowledge, been implemented for hypoplasticity.

(iv) The original Mašín (2005) model suffers from unrealistic stress paths for undrained solicitations of lightly overconsolidated clays, as demonstrated by the stress path of tests PhM18 and PhM21 in Fig. 4.11b. The new Mašín (2012a,b) version of the model does not suffer from this flaw, which is why its use is advised for future endeavours.

(v) The small strain behaviour offered by the interganular strain concept is also perfectible. According to Wroth et al. (1979), cited by Viggiani and Atkinson (1995), the small strain shear modulus G_0 is function of $(p')^n$, with n ranging from 0·6 to 0·8, whereas the intergranular strain predicts a value of $n = 1$ (see Fig. 4.2). Furthermore, the size of the elastic bubble of the intergranular strain model does not vary with stress, although Gasparre et al. (2007) present experimental evidence that it does. Thirdly, Gasparre et al. (2007) showed that letting the clay creep before strain reversal could lower the soil stiffness. These shortcomings are certainly irrelevant for large monotonic solicitations but may have significant influence for small strain behaviour or for cyclic tests.

(vi) Finally, the model does not account for structure, as defined in Appendix A. Therefore, in a nutshell, the model can be used for insensitive or reconstituted soils. An addition that takes into account the soil structure – and the structure degradation – is proposed by Mašín (2007).

4.5.2 Matsuoka-Nakai failure criterion

The Matsuoka-Nakai and Mohr-Coulomb deviatoric sections,[4] which are illustrated in Fig. 4.1b, are both endowed with sixfold symmetry and expand non-homothetically for increasing values of the friction angle (Mortara, 2008).

For $\phi'_{cs} = 90°$ both sections are triangular. When ϕ'_{cs} approaches zero, the Mohr-Coulomb deviatoric section is a regular hexaedron inscribed in the Matsuoka-Nakai surface, which is a cone.

The two surfaces yield the same value both for triaxial compression and extension conditions (respectively for Lode angles θ equal to 30° and −30°) but differ for all other conditions for which the Matsuoka-Nakai section predicts higher strength

[4] A deviatoric section is an intersept with the $p' =$ constant plane in the $\sigma'_1 : \sigma'_2 : \sigma'_3$ principal stress space.

than the Mohr-Coulomb one. This is supported by experimental data, see for example Nakai et al. (1986) (true triaxial test on Fujinomori clay) or Nishimura et al. (2007) (hollow cylinder apparatus on London clay), which show that the Mohr-Coulomb criterion underestimates the strength at failure for intermediate Lode angles.

4.5.3 Geotechnical quantities

(a) Water content

The considered soil being saturated, the water content (w) is linked to the void ratio (e):

$$e = G_s w, \tag{4.7}$$

where G_s specific gravity of the soil.

(b) Overconsolidation ratio

The hypoplastic overconsolidation ratio (OCR*), defined in Eq. (4.4), differs from the definition of overconsolidation ratio used in Cam clay based models: $n_p = p'_y/p'_0$, where the yield pressure (p'_y) is defined as the intersection of the url passing through the current stress and the iso-ncl (Fig. 4.12a defined in the $v : \ln p'$ compression plane).

These two definitions of overconsolidation ratio are linked by the following relationship (Muir Wood, 1990):

$$\mathrm{OCR}^* = \frac{p'_e}{p'_0} = \left(\frac{p'_y}{p'_0}\right)^{\Lambda} = \left(n_p\right)^{\Lambda}, \quad \text{where} \quad \Lambda = \frac{\lambda - \kappa}{\lambda}, \tag{4.8}$$

which is plotted for typical values of Λ in Fig. 4.12b.

These definition all differ from the conventional definition of overconsolidation ratio ($\mathrm{OCR} = \sigma'_{vy}/\sigma'_{v0}$), relating vertical stresses (in oedometric conditions) instead of mean stresses. By using Eq. (4.8) and the definition of the mean stress (Muir Wood, 1990), the following relationship can be obtained relating the hypoplastic OCR* to the conventional OCR:

$$\mathrm{OCR}^* = \frac{3}{1+2K_{0nc}}\left(\frac{1+2K_{0nc}}{1+2K_0}\mathrm{OCR}\right)^{\Lambda}, \tag{4.9}$$

$$\text{where} \quad K_{0nc} = 1 - \sin\phi'_{cs}, \tag{4.5bis}$$

$$K_0 = K_{0nc}\mathrm{OCR}^{\sin\phi'_{cs}}, \tag{4.6bis}$$

$$\Lambda = \frac{\lambda - \kappa}{\lambda}.$$

Eq. (4.9) depends only on ϕ'_{cs}, κ and λ and is plotted in Fig. 4.13 for $\phi'_{cs} = 22{\cdot}6°$. For overconsolidation ratios smaller than 5, both definitions closely match.

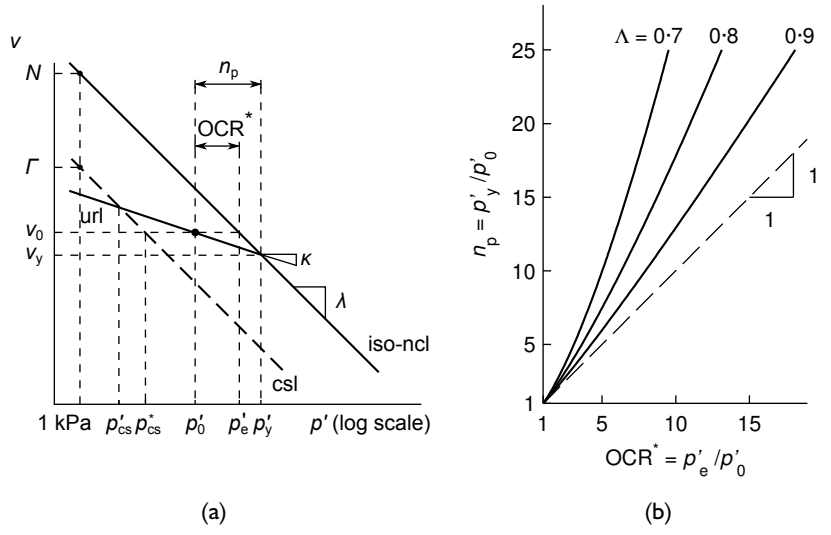

Figure 4.12 Hypoplastic OCR* versus modified Cam clay n_p: (a) Definitions in the $v : \ln p'$ compression plane and (b) Relationship for various values of Λ.

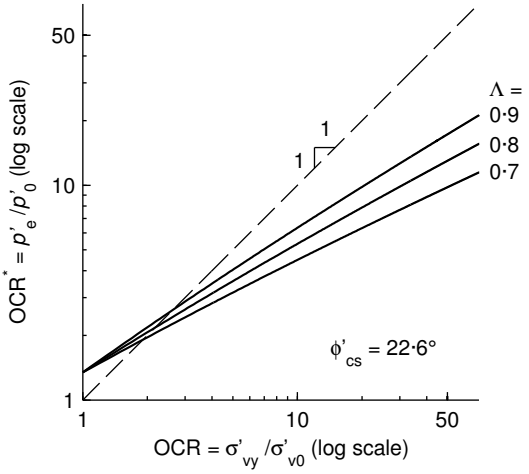

Figure 4.13 Conventional overconsolidation ratio (OCR) versus hypoplastic overconsolidation ratio (OCR*) for $\phi'_{cs} = 22{\cdot}6°$.

(c) Undrained shear strength

As the model is based on the critical state theory, the undrained shear strength (s_{u0}) is the constant-volume projection of the current state on the critical state line (csl). The state is defined by the void ratio (e_0) and the initial stress (p'_0). The csl is defined (1) in the $\ln v : \ln p'$ compression plane as a straight line and (2) in the $\sigma'_1 : \sigma'_3 : \sigma'_3$ stress space or, equivalently, in the $p' : q : \theta$ stress space, as the Matsuoka-Nakai surface. From Point (1), mean effective stress at critical state (p'_{cs}) is related to the specific volume at critical state (v_{cs}) which is equal to the initial specific volume: $v_{cs} = v_0$. Furthermore, the undrained shear strength (s_{u0}) is related to the deviator stress at critical state: $s_{u0} = q_{cs}/2$ in triaxial conditions and $s_{u0} = q_{cs}/\sqrt{3}$ in plane strain conditions (see Eq. B.3, p. 192). Therefore, from Point (2), for any given Lode angle (θ), the shear strength (s_{u0}) depends only on the initial void ratio (e_0); this is developed hereunder for particular Lode angles corresponding to traxial compression, triaxial extension, and simple shear.

For triaxial conditions ($\theta = \pm 30°$), the Matsuoka-Nakai and Mohr-Coulomb yield criteria coincide, as shown in Fig. 4.1b. Therefore, the stress ratios (q/p') at critical state, for triaxial conditions, also coincide (Muir Wood, 1990):

$$M_c = \frac{6\sin\phi'_{cs}}{3-\sin\phi'_{cs}}, \quad \text{for triaxial compression, and} \tag{4.10}$$

$$M_e = \frac{6\sin\phi'_{cs}}{3+\sin\phi'_{cs}}, \quad \text{for triaxial extension.} \tag{4.11}$$

For intermediate Lode angles, the stress ratio q/p' given by the Matsuoka-Nakai surface is between M_e and M_c. In particular, for constant-volume simple shear conditions, the hypoplastic model tends to $\theta = 0$ at critical state, implying that the q/p' ratio can be expressed as (Bardet, 1990):

$$M_{ps} = \frac{6\sin\phi'_{cs}}{\sqrt{3\left(3+\sin^2\phi'_{cs}\right)}}. \tag{4.12}$$

The three stress ratios of Eqs. (4.10)–(4.12) are depicted in Fig. 4.14 for a range of friction angles.

As the critical state predicted by the constitutive model is isotropic, the undrained shear strength during simple shear (s_{u0}) can be related to the critical state mean stress p^*_{cs} thanks to Eq (4.12):

$$s_{u0} = \frac{2\sin\phi'_{cs}}{\sqrt{3+\sin^2\phi'_{cs}}}\, p^*_{cs}, \tag{4.13}$$

where p^*_{cs} is defined in Fig. 4.12a. The mean effective stress at critical state p^*_{cs} is also analytically derivable by using the definition of the critical state line (csl):

$$\ln v_0 = \ln\Gamma^* - \lambda^* \ln p^*_{cs}, \tag{4.14}$$

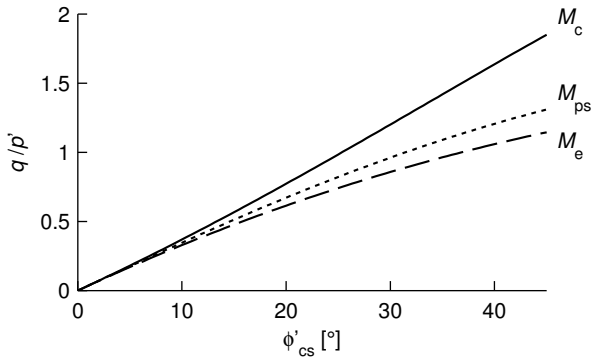

Figure 4.14 Stress ratio (q/p') at critical state for triaxial compression (M_c), triaxial extension (M_e), and simple shear (M_{ps}) for the Matuoka-Nakai surface.

where $v_0 = 1 + e_0$ is the initial specific volume, a constant for undrained shearing, and Γ^* is the intercept of the csl at 1 kPa, given by:

$$\Gamma^* = \frac{N^*}{2^{\lambda^*}}. \tag{4.15}$$

Using Eqs. (4.13), (4.14), and (4.15), the simple shear undrained strength (s_{u0}) is related one state variable, the initial specific volume (v_0), through the following expression:

$$s_{u0} = \frac{\sin\phi'_{cs}}{\sqrt{3+\sin^2\phi'_{cs}}}\left(\frac{N^*}{v_0}\right)^{1/\lambda^*}, \qquad \text{(simple shear)} \tag{4.16}$$

where ϕ'_{cs}, N^*, and λ^* are material parameters defined in Fig. 4.1.

The undrained shear strength of the simple shear test described in Section 4.3.1 can be computed using Eq. (4.16): $s_{u0} = 107{\cdot}80$ kPa.

By comparison, the undrained shear strength for triaxial compression and extension is given by:

$$s_{u0} = \frac{3\sin\phi'_{cs}}{2(3-\sin\phi'_{cs})}\left(\frac{N^*}{v_0}\right)^{1/\lambda^*}, \qquad \text{(triaxial compression)} \tag{4.17}$$

$$s_{u0} = \frac{3\sin\phi'_{cs}}{2(3+\sin\phi'_{cs})}\left(\frac{N^*}{v_0}\right)^{1/\lambda^*}. \qquad \text{(triaxial extension)} \tag{4.18}$$

4.6 Conclusion

The hypoplastic model with intergranular strain presented in this chapter is a critical state based model aimed at predicting the behaviour of clay. It is isotropic, rate-independent, and frictional. It has 10 model parameters and 13 state parameters: the six stress components, the six intergranular strain components, and the void ratio.

The mathematical formulation of the model is defined in Sections 4.1 and 4.2. Section 4.3 presents the model capabilities by performing a 'one element' simulation of a cyclic simple shear test and of an oedometric test. Finally, Section 4.5 offers a discussion about various aspects of the model. In particular, two equations are derived, using critical state theory concepts:

- Eq. (4.9) relates the overconsolidation ratio used by the model (OCR^*) with the conventional definition of overconsolidation ratio (OCR); and
- Eq. (4.16) defines simple shear strength (s_{u0}) offered by the Matsuoka-Nakai criterion, which is different to the shear strength in triaxial compression (Eq. 4.17) or extension (Eq. 4.18).

Like any model, the hypoplastic model with intergranular strain presented in this chapter is unrealistic, in the sense in which the word is most commonly used (Baran and Sweezy, 1968). In other words, it captures a fraction of the complex behaviour of clays. Therefore, like for any model, it is important to realise its shortcomings before using it. Its weaknesses are summarised in Section 4.5.1.

The principal advantages of the presented model are that: (a) it follows the conceptual framework of critical state soil mechanics (Schofield and Wroth, 1968), (b) it uses a small number of material parameters that can be determined from standard laboratory tests, (c) it predicts stiffness degradation with strain, (d) it takes into account cyclic loading by modelling stiffness increase with loading direction, (e) it models shear induced dilatancy, and (f) it is straightforward to implement.

Chapter 5

Pile driving model presentation

This chapter presents the model used to simulate pile driving and subsequent equalisation of a open- or closed-ended pile. The general concept behind the model is introduced in Section 5.1. The following sections describe, in detail, the installation and equalisation modelling.

Firstly, the mathematical and numerical background of the installation stage modelling is described in Section 5.2, which is followed by a typical output for a closed-ended pile installation in Section 5.3. Secondly, the equalisation stage modelling is presented in Section 5.4 and a typical output is depicted in Section 5.5.

5.1 Conceptual model

Installation In saturated clay, the brutality of pile driving coupled to the low permeability of clays mean that pile installation can be considered to be an *undrained* process. Furthermore, it can be reasonably assumed that soil not too close to the surface nor to the pile toe is kinematically constrained in *plane strain* conditions (Fig. 5.1). These two assumptions lay the foundation of the conceptual model: instead of studying all the soil surrounding the pile, I focus on a disk of incompressible

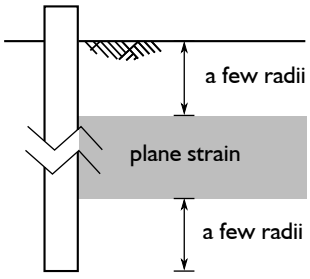

Figure 5.1 Plane strain assumption around a pile installation.

plane strain soil located somewhere along the shaft, not too close to the pile toe nor to the soil surface.

This disk of soil represents a layer of soil thin enough so that vertical stress can be considered constant within. Thanks to the plane strain assumption, the disk of soil does not take into account interaction with the soil above or below it. To simulate installation, a series of driving blows is imposed at the inner boundary of the disk – boundary representing the pile wall (Fig. 5.2b). This stage is named the *Disk Shearing Model*.

However, the first driving blow of the Disk Shearing Model can only be imposed on a soil that is in plane strain conditions, *i.e.* that is a few radii above the pile toe. Therefore, it is unrealistic for the disk to start from K_0 conditions. The history of each of the disk soil particles, which would have been subjected to a large amount of shearing and distortion due to the insertion of the pile toe, has to be taken into account. In other words, the soil contained in the disk has to be prepared so that its state reflects the history of a layer of soil having been through the penetration of a pile toe.

To predict the 'early life' of the soil disk, I use the *Strain Path Method* (Baligh, 1985), introduced in Chapter 3, which creates the straining history of each of the soil disk particles. The Strain Path Method is an analytical method modelling the penetration of a pile, closed- or open-ended, without considering the shaft-soil shearing. Depicted in Fig. 5.2a are the streamlines followed by each soil particle during the closed-ended Strain Path Method. Each soil particle will have been subjected to the insertion of the pile toe, and will be taken as starting point for the Disk Shearing Model simulation.

Although splitting installation between the Strain Path Method and the Disk Shearing Model brings out a drawback: because the Strain Path Method is monotonic, cycles happening below the pile toe and before the Disk Shearing Model are neglected. This is further discussed when the model results are compared to field experiments, in Section 6.1 and Chapter 7.

Equalisation Once installation is completed, the equalisation stage begins. Again, only a layer of soil is considered, which reflects the behaviour of a layer of soil not too close to the pile toe nor to the soil surface (Fig. 5.2c). Thanks to this assumption the flow of water can be assumed to occur only in the radial direction. Therefore, the equalisation stage is modelled as the coupled consolidation of a similar plane strain disk of soil as the one described above, only now radial drainage is allowed.

The pile installation modelling, composed of the Strain Path Method and the Disk Shearing Model, is described in Section 5.2 for a closed- and open-ended pile. The equalisation modelling is described in Section 5.4. Sections 5.3 and 5.5 depict a typical output for a closed-ended pile installation and equalisation, respectively.

The geometry of the problem presented throughout this chapter is the following: the pile radius (R) is 25 cm, the radial discretisation (Δr) is $0{\cdot}08R = 2$ cm, the outer boundary radial position (r_b) is $60R$ (except during the Disk Shearing Model

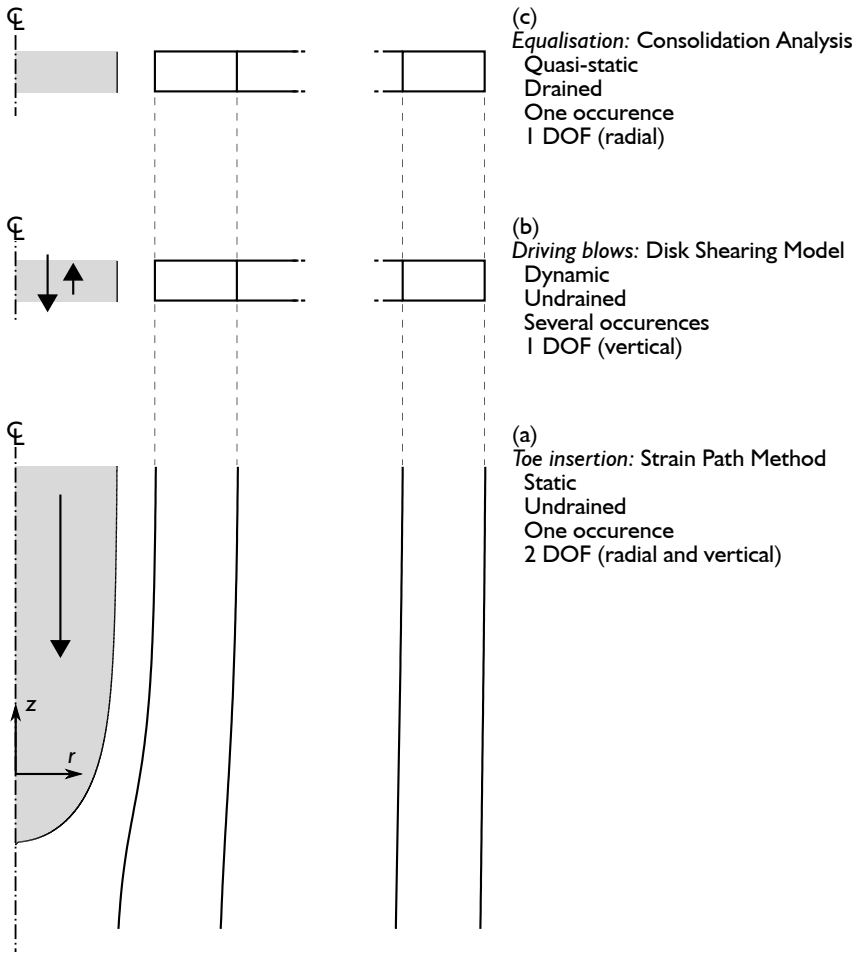

Figure 5.2 Study of a disk of soil around a closed-ended driven pile: (a) and (b) simulate the installation stage and (c) simulates the equalisation stage.

simulations where $r_b = 16R$), and the vertical extend of the Strain Path Method is $80R$ ($40R$ behind and $40R$ below the pile toe). Appendix E (p. 209) justifies the choice of discretisation parameters and validates the numerical accuracy of the simulation. The soil constitutive model is the hypoplastic law described in Chapter 4 for London clay. The soil initial state is the normally consolidated state introduced in Section 4.3.1: $\sigma'_{v0} = 590\,\text{kPa}$, $K_0 = 0{\cdot}615$, $e_0 = 1$, and $\text{OCR}^* = 1{\cdot}1$.

Except for the implementation of the constitutive model (the Driver, defined in Appendix D), every line of code is original and genuine work written on Matlab.

5.2 Pile installation

Before the Strain Path Method and the Disk Shearing Model are examined in Sections 5.2.2 and 5.2.3, Section 5.2.1 presents the large strain particularities that both methods make use of.

5.2.1 Eulerian description

An important feature of the present analysis is that deformations are large, both for the Strain Path Method and the Disk Shearing Model. This calls for the choice of a proper framework, which is discussed hereunder.

In the infinitesimal strain theory, strain is defined in a unique and unambiguous way. This is not the case in large (or finite) displacement theory, since different coordinate systems may be used to describe the kinematics of deformation and these give rise to different strain measures (Burd and Houlsby, 1990). The most usual approaches are either to use a Lagrangian description, with an appropriate stress measure, or to use an Eulerian description, in which the constitutive equation relates Cauchy stress rate to Eulerian strain rate (Burd and Houlsby, 1990).

Herein, the Eulerian approach is adopted and the Cauchy stresses at each discretised node are accumulated as the calculation proceeds. Four particularities inherent to large strains and to the Eulerian framework exist: they are presented hereafter.

Location of the boundaries The adopted Eulerian viewpoint requires that the location of an imposed boundary condition has to be computed before the boundary condition itself can be imposed (Gibson et al., 1967). However this difficulty vanishes because the (pile) boundary position is always known: it is imposed for the Strain Path Method (analytical expression) and fixed in the radial direction for the Disk Shearing Model.

Material derivative Unlike the Lagrangian description where time differentiation is straightforward, the Eulerian approach requires the use of the material derivative in order to ensure a true determination of the rate of change of any quantity (Segall, 2010). The material derivative of a scalar b, in cylindrical coordinates with axial

symmetry, is:

$$\dot{b} = \frac{Db}{Dt} = \frac{\partial b}{\partial t} + v_{\mathrm{r}}\frac{\partial b}{\partial r} + v_{\mathrm{z}}\frac{\partial b}{\partial z}, \tag{5.1}$$

where v_{r} and v_{z} are the radial and vertical soil velocities, respectively.

Velocity to strain rate In the Eulerian description, the kinematics of deformation are described in terms of velocity (rather than displacement) which are defined in the same way as for infinitesimal theory. This has the desirable feature that some aspects of the small strain theory are preserved (Malvern, 1969; McGinty, 2013). The relationship between velocity and strain rate is described in detail in Appendix C, but abridged here for a cylindrical coordinate system (r, θ, z) assuming axial symmetry and positive compression (using Voigt notation):

$$\begin{aligned}\mathbf{D} &= (\dot{\varepsilon}_{\mathrm{r}}, \dot{\varepsilon}_{\theta}, \dot{\varepsilon}_{\mathrm{z}}, \dot{\gamma}_{\mathrm{r}\theta}, \dot{\gamma}_{\theta\mathrm{z}}, \dot{\gamma}_{\mathrm{rz}})^{\mathrm{T}},\\ &= -\nabla\mathbf{v},\\ &= \left(\frac{-\partial v_{\mathrm{r}}}{\partial r}, \frac{-v_{\mathrm{r}}}{r}, \frac{-\partial v_{\mathrm{z}}}{\partial z}, 0, 0, -\left[\frac{\partial v_{\mathrm{r}}}{\partial z} + \frac{\partial v_{\mathrm{z}}}{\partial r}\right]\right)^{\mathrm{T}}.\end{aligned} \tag{5.2}$$

The strain rate tensor ($\mathbf{D}$) is composed of three volumetric components ($\dot{\varepsilon}_{\mathrm{r}}$, $\dot{\varepsilon}_{\theta}$, and $\dot{\varepsilon}_{\mathrm{z}}$) and three shear components ($\dot{\gamma}_{\mathrm{r}\theta}$, $\dot{\gamma}_{\theta\mathrm{z}}$, and $\dot{\gamma}_{\mathrm{rz}}$). The soil velocity vector ($\mathbf{v}$) is composed of the three terms: v_{r}, v_{θ}, and v_{z}.

The strain rates defined by Eq. (5.2) are used at each time step to compute the effective stresses through to the hypoplastic constitutive model (Chapter 4). The constitutive model being defined incrementally, strains are never used as an input. This allows, by small increments of strain rates, to reach the high strains imposed by pile driving. Furthermore, at each time step, the precision of the constitutive model output is verified through a corrective Runge-Kutta-Felhberg integration scheme (described in Appendix D).

Unlike in all other engineering fields where the strain rate tensor ($\mathbf{D}$) is the velocity gradient ($\nabla\mathbf{v}$), it is defined as the opposite of the velocity gradient in Eq. (5.2) so that compression is positive – a usual convention in soil mechanics. However, this means, with the axes defined in Fig. 5.2a, that the shear strain and stress are negative around a loaded pile. This being counter intuitive, I have chosen to introduce γ and τ, defined as:

$$\gamma = -\gamma_{\mathrm{rz}}, \tag{5.3a}$$

$$\tau = -\tau_{\mathrm{rz}}, \tag{5.3b}$$

which are positive around a loaded pile.

Objective stress rate The large deformations require an objective stress rate, essentially to have a zero stress rate under rigid body rotation. The Jaumann stress rate, which is almost universally adopted as an objective stress rate (Burd, 1986;

Bardet and Choucair, 1991), is used hereafter. The Jaumann stress rate ($\overset{\triangledown}{\boldsymbol{\sigma}}'$), already introduced in Eq. (4.2), is related to the stress rate tensor ($\dot{\boldsymbol{\sigma}}'$) through the following relationship (using Einstein notation):

$$\overset{\triangledown}{\sigma}'_{ij} = \dot{\sigma}'_{ij} + W_{ik}\sigma'_{kj} - \sigma'_{ik}W_{kj}, \tag{5.4}$$

where W_{ij} (or $\mathbf{W}$ using the vector notation) is the spin tensor (the opposite of the skew-symmetric part of the velocity gradient, defined in Appendix C).

5.2.2 Toe insertion: Strain Path Method

The Strain Path Method (Baligh, 1985) is developed hereunder for a closed- and open-ended pile. Both developments follow the same logic, so the focus is put on closed-ended Strain Path Method, while the open-ended equations are introduced only when they differ from the closed-ended ones.

Introduced in Chapter 3, the Strain Path Method hinges on the assumption that soil deformations during deep penetration can be estimated with a reasonable degree of accuracy without the need to consider constitutive relations for the soil. The method consists of a spherical cavity emitting an incompressible material at a volume rate of V per unit of time, embedded in an uniform flow field with velocity U in the z direction. The resulting streamlines for a closed- and open-ended pile are depicted in Fig. 5.3. The soil is considered incompressible, the geometry axisymmetric and the flow irrotational. The Strain Path Method allows to follow streamlines of soil, starting from below the toe, the distortions of which are shaped by the pile toe insertion.

The integration scheme of the Strain Path Method is depicted in Fig. 5.4 and, for each time step, goes as follows. First of all, the velocity along each streamline is computed from analytical expressions described hereunder, in Paragraph (a). From the velocity field, strain rates are computed (Paragraph (b)) . These are used, along with the soil state at the previous time step, to compute the effective stresses using the hypoplastic model defined in Chapter 4 (Paragraph (c)).

All of these calculation are made along the streamlines; the initial position of which is carefully chosen so that their final position coincide with the discretisation chosen for the Disk Shearing Model, presented in the next section.

(a) Velocity field The Strain Path Method equations are expressed in a spherical coordinate system (ρ,θ,ϕ), which can be converted to the cylindrical coordinate system (r,θ,z) through the following equations:

$$\rho^2 = r^2 + z^2, \qquad r = \rho\sin\phi, \qquad z = \rho\cos\phi.$$

The closed-ended Strain Path Method can be elegantly defined using a stream function:

$$\Psi = \frac{V}{4\pi}\cos\phi - \frac{r^2}{2}U, \tag{5.5}$$

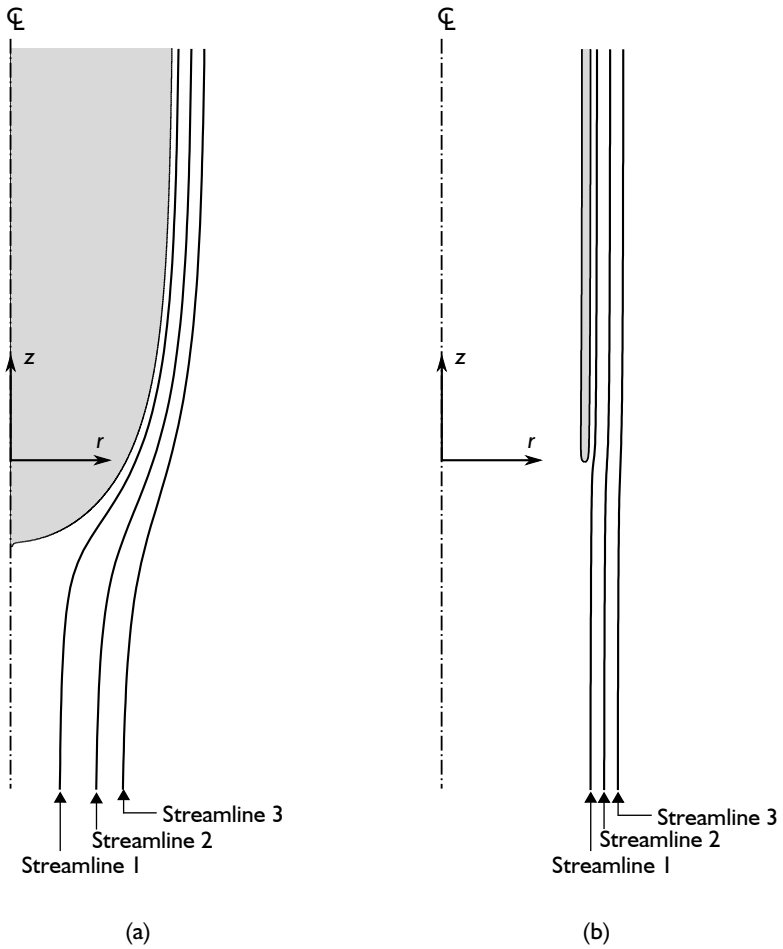

Figure 5.3 Representation of the three first Strain Path Method streamlines for (a) a closed-ended pile and (b) an open-ended pile.

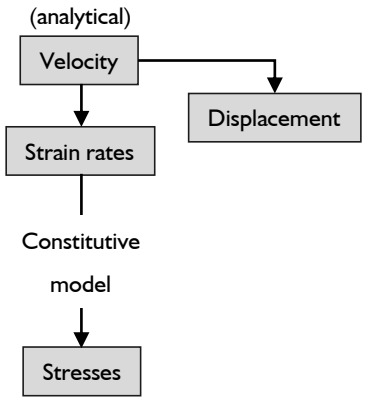

Figure 5.4 Integration scheme for each *time step* during the Strain Path Method (all quantities are evaluated on the streamlines).

in which the first term corresponds to the spherical cavity expansion and the second one to the flow field. Radial and vertical velocities of the soil are given by:

$$v_r = \frac{1}{r}\frac{\partial \Psi}{\partial z} = \frac{V}{4\pi}\frac{\sin\phi}{\rho^2}, \tag{5.6a}$$

$$v_z = \frac{-1}{r}\frac{\partial \Psi}{\partial r} = \frac{V}{4\pi}\frac{\cos\phi}{\rho^2} + U. \tag{5.6b}$$

The stream defined by Eq. (5.5) predicts a pile the shape of which is depicted in Fig. 5.3a. Far behind the pile toe, the shaft radius R of the pile tends to:

$$R \to \sqrt{\frac{V}{\pi U}}. \tag{5.7}$$

Eq. (5.7) is obtained by continuity between the cavity expansion and the flow field, and is used to select a value of V that produces a radius R. Although the simple pile radius increases indefinitely with the vertical distance the pile radius exceeds $0{\cdot}99R$ at a vertical distance of $4R$ behind the pile toe (Baligh, 1985).

For the open-ended Strain Path Method, no explicit expression of the stream function Ψ can be developed. For a pile with outer radius R and wall thickness t, the velocities are given by (Küchemann and Weber, 1953; Chin, 1986):

$$v_r = \frac{V}{4\pi^2}\frac{1}{r\sqrt{z^2+(r+R')^2}}\left\{K(k) - \left(1 - \frac{2r(r-R')}{z^2+(r-R')^2}\right)E(k)\right\}, \tag{5.8a}$$

$$v_z = \frac{V}{4\pi^2}\frac{2z}{\sqrt{z^2+(r+R')^2}\,[z^2+(r-R')^2]}E(k) + U, \tag{5.8b}$$

where R' is the ring source radius, which is approximately equal to $R - 0{\cdot}75t$, $k = 4rR'/\left[z^2 + (r + R')^2\right]$ and functions $K(k)$ and $E(k)$ are the complete elliptical integrals of the first and second kind, respectively (Abramowitz and Stegun, 1964). The first three (outer) streamlines defined by Eqs. (5.8) are depicted in Fig. 5.3b.

Far behind the pile toe, the shaft radius of the open-ended pile tends to:

$$R \to \frac{1}{2}\left(t + \frac{V}{2\pi U t}\right), \tag{5.9}$$

As for the closed-ended version, Eq. (5.9) is used to select a value of V which imposes a pile radius of R.

(b) Strain rates As explained in Section 5.2.1, the Eulerian standpoint requires the use of the material derivative. With the Strain Path Method, time derivatives are made following each streamline, which implies that the time derivative *is* the material derivative. Therefore, the strain rates can be analytically computed from the velocity defined in Eq. (5.6), using the strain rate definition (Eq. 5.2):

$$\dot{\varepsilon}_{\mathrm{r}} = \frac{-\partial v_{\mathrm{r}}}{\partial r} = \frac{-V}{4\pi\rho^3}(\cos^2\phi - 2\sin^2\phi),$$
$$\dot{\varepsilon}_{\mathrm{z}} = \frac{-\partial v_{\mathrm{z}}}{\partial z} = \frac{-V}{4\pi\rho^3}(\sin^2\phi - 2\cos^2\phi),$$
$$\dot{\varepsilon}_{\theta} = \frac{-v_{\mathrm{r}}}{r} = \frac{-V}{4\pi\rho^3},$$
$$\dot{\gamma}_{\mathrm{rz}} = -\left(\frac{\partial v_{\mathrm{r}}}{\partial z} + \frac{\partial v_{\mathrm{z}}}{\partial r}\right) = \frac{3V}{4\pi\rho^3}\sin 2\phi.$$

The open-ended Strain Path Method velocity field defined by Eq. (5.8) cannot be integrated analytically, so it has to be numerically integrated, using the definition of the strain rate (Eq. 5.2).

(c) Stresses The analytical strain rates defined here above are then used along each streamline to compute the effective stress, using the hypoplastic model described in Chapter 4.

The hypoplastic model being formulated in terms of Jaumann objective stress rate (Eq. 5.4), one has to compute the spin tensor $\mathbf{W}$ for each time step, in principle. However, the Strain Path Method considers the soil to follow an irrotational flow, implying that:

$$\frac{\partial v_{\mathrm{r}}}{\partial z} = \frac{\partial v_{\mathrm{z}}}{\partial r},$$

so that the spin tensor (see Appendix C.2) is null, $\mathbf{W} = 0$, therefore the stress rate *is* objective: $\dot{\boldsymbol{\sigma}}' = \overset{\nabla}{\boldsymbol{\sigma}}'$.

Table 5.1 Equations and unknowns of the Strain Path Method analysis.

Name	*Equation*	*Components*
Velocity	(5.6)	2
Velocity to strain rate	(5.2)	6
Constitutive law	(4.1)	6
14 unknown components: v_r, v_z, $\mathbf{D}$, $\boldsymbol{\sigma}'$		

The equations and unknowns of the Strain Path Method analysis are listed in Table 5.1.

Finally, a note should be made on the inequilibrium issue of the Strain Path Method: the assumption that the soil deformations can be estimated without the need to consider constitutive relations for the soil brings an elegant formulation but also implies that the strain paths violate equilibrium conditions. In other words, the pore pressure depends on the path of integration, using the vertical or the radial equilibrium equation.

The approach chosen was to not compute the pore pressure during Strain Path Method penetration, accepting some lack of equilibrium, and to correct it only once the soil gets far behind the pile toe, using the Disk Shearing Model.

5.2.3 Driving blows: Disk Shearing Model

The Disk Shearing Model takes as initial state the one computed by the Strain Path Method. As explained in the previous section, the Strain Path Method discretisation was carefully chosen so that the stresses computed on the streamlines could be directly inserted as initial values of the internodes of the Disk Shearing Model discretisation (Fig. 5.5).

The core of the integration scheme of the Disk Shearing Model, depicted in Fig. 5.6, is quite similar to the one used for the Strain Path Method: velocity is derived to strain rates, which are then used to compute the effective stresses thanks to the hypoplastic constitutive model described in Chapter 4. However, there are four distinctions between the Strain Path Method and Disk Shearing Model integration schemes.

Firstly, only the pile velocity is imposed. The soil velocities are computed from the previous time step: the stresses are used to compute the vertical acceleration, using the vertical equation of motion, which is then integrated to obtain the soil vertical velocity at the next time step (Fig. 5.6). Each time step is explicitly dependent on the previous one. There is no particular interface element between pile and soil: the behaviour at the pile shaft is predicted by the hypoplastic constitutive model. The imposed velocity boundary condition is detailed hereunder, in Paragraph (a), while Paragraphs (b) to (d) specify the three other steps of the main loop of the

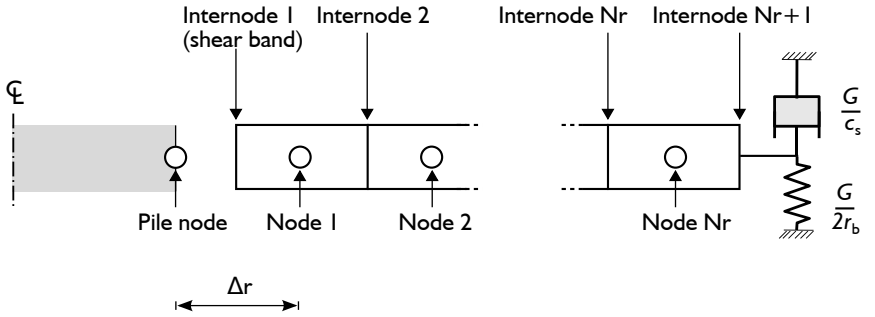

Figure 5.5 Disk Shearing Model discretisation, depicting nodes, internodes, and the absorbing outer boundary.

integration scheme (Fig. 5.6).

The second distinction is that strain, stress, and void ratio are evaluated at the internodes (which are the extension of the streamlines) while the kinematic quantities (displacement, velocity, and acceleration) are evaluated at the nodes (as shown by the grey and white boxes of Fig. 5.6). The need for nodes and internodes comes from the finite difference approach that is taken to perform the calculations. The distinction between node and internode is particularly important near the pile shaft, where the distortion of the soil is the greatest.

Thirdly, the dynamic aspect of the Disk Shearing Model integration scheme requires the use of an absorbing boundary. This is described in Paragraph (f), p. 106.

Fourthly, the pore pressures are computed, unlike for the Strain Path Method where some lack of equilibrium prevented their derivation. The pore pressures are computed using the radial equilibrium equation, explained hereunder, in Paragraph (e), p. 105. As the starting point for the Disk Shearing Model is the end of the Strain Path Method simulation, it is also out of equilibrium. Therefore, before any shearing can be imposed, the inequilibrium is corrected using a procedure also explained in Paragraph (g), p. 106.

(a) Inner boundary: imposed velocity The inner boundary of the soil disk *is* a node representing the pile wall (Fig. 5.5). This boundary does not move in the radial direction. The boundary condition is therefore easily applied even using the Eulerian standpoint. The boundary condition has been chosen as the impact of a hammer of mass M onto an elastic cap having a stiffness k protecting an infinite pile represented by a dashpot whose coefficient is I (Fig. 5.7a). The closed form of the pile velocity ($v_{z,p}$) for an underdamped system ($kM < 4I^2$) is given by (Holeyman, 1984):

$$v_{z,p} = 2v_0 \frac{\alpha}{\beta} e^{-\alpha t} \sin(\beta t), \tag{5.10}$$

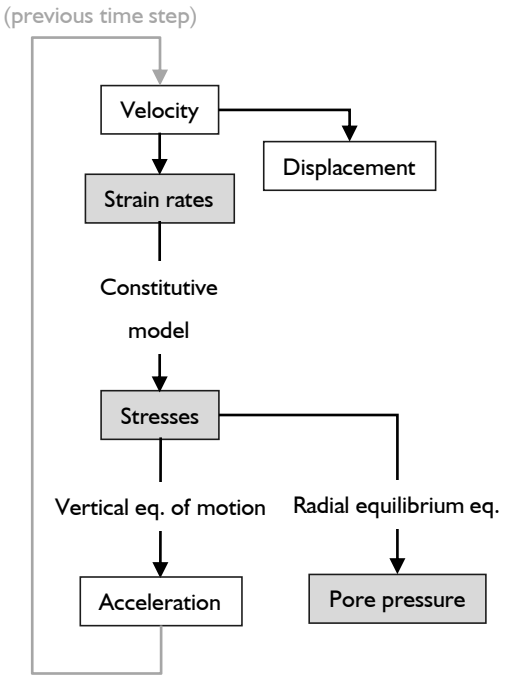

Figure 5.6 Integration scheme for each *time step* during the Disk Shearing Model (greyed boxes are quantities evaluated at the internodes while white boxes are quantities evaluated at the nodes).

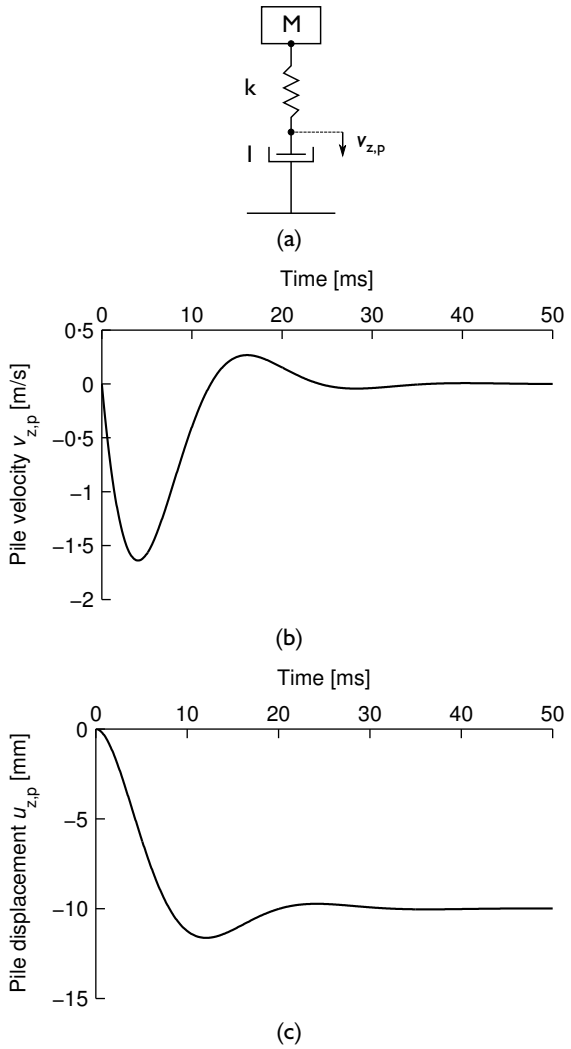

Figure 5.7 Analytical boundary condition: (a) mass spring dashpot system, (b) resulting pile velocity and (c) corresponding pile displacement ($v_0 = -3\,\text{m/s}$, $\omega_n = 300\,\text{rad/s}$, and $\alpha = 0{\cdot}5\omega_n$).

where v_0 is the ram initial velocity and α and β are defined below:

$$\alpha = \frac{k}{2I}, \qquad \beta = \sqrt{\omega_n^2 - \alpha^2}, \qquad \omega_n = \frac{k}{M},$$

α being the spring-dashpot constant and ω_n the natural frequency of the spring-mass system.

Eq. (5.10) is governed by the initial velocity of the ram (v_0) which controls the final set, the period of the sine ($2\pi/\beta$), and the ratio α/ω_n which controls the damping of the signal.

The imposed pile velocity ($v_{z,p}$) given by Eq. (5.10) for parameters corresponding to a typical driving blow is displayed in Fig. 5.7b, and the corresponding pile displacement ($u_{z,p}$) is depicted in Fig. 5.7c. The signal presents a rebound and a final set lower than the peak displacement, as observed during pile driving.

(b) Strain rates During undrained shearing of the Disk Shearing Model, the relationship between velocity and strain rate (Eq. 5.2) can be simplified. Firstly, the plane strain condition voids all partial derivatives with regards to the vertical coordinate (z). Secondly, the soil being undrained imposes a volumetric strain rate ($\dot{\varepsilon}_v$) equal to 0. Therefore, one can write:

$$\dot{\varepsilon}_v = \frac{\partial}{\partial r}(r v_r) = 0. \tag{5.11}$$

Since at the pile boundary, radial velocity ($v_{r,p}$) is always null, Eq. (5.11) can be integrated[1] to obtain $v_r = 0$ over the entire disk domain.

The only non trivial component of the velocity strain rate relationship is therefore:

$$\dot{\gamma}_{rz} = \frac{-\partial v_z}{\partial r}. \tag{5.12}$$

Using finite differences, the strain rate is computed at each internode using Eq. (5.12).

(c) Stresses Similar to the Strain Path Method scheme, the strain rates computed following Eq. (5.12) are used to compute the effective stresses, using the hypoplastic model described in Chapter 4.

However, unlike the Strain Path Method, the soil motion is rotational, implying that the spin tensor is non null and that Eq. (5.4) has to be used to ensure that the stress rates remain objective.

[1]The two independent variables are radial position (r) and time (t).

(d) Vertical acceleration From the effective stresses computed here above, the soil acceleration (a_z) is computed using the vertical equation of motion:

$$\frac{1}{r}\frac{\partial}{\partial r}(r\tau_{rz}) = \rho a_z, \tag{5.13}$$

where $\rho = n\rho_w + (1-n)\rho_s$ is the soil density, with ρ_w and ρ_s being the densities of the fluid and solid phases and n the water porosity.

The final step of the integration scheme consists of integrating the vertical acceleration (a_z) of each soil node to obtain the vertical velocity (v_z). Due to the geometric simplifications of the Disk Shearing Model, the problem is independent of the vertical coordinate (z), the hoop velocity (v_θ) is null because of the axial symmetry, and the radial velocity v_r) is null, as explained in Paragraph (b). Therefore, the convective part of the material derivative (Eq. 5.1) conveniently vanishes:

$$a_z = \frac{Dv_z}{Dt} = \frac{\partial v_z}{\partial t}. \tag{5.14}$$

Therefore, v_z can be easily integrated from a_z, as for the displacement from velocity or the strain from the strain rate.

(e) Radial equilibrium As the constitutive model used is an effective stress constitutive model, pore pressures (u_w) can be computed either from the vertical or the horizontal equation of motion. The vertical equation of motion (Eq. 5.13) is automatically satisfied as it contains only shear stresses. Therefore, the radial equation is used to compute u_w:

$$\frac{\partial \sigma'_r}{\partial r} + \frac{\partial u_w}{\partial r} + \frac{1}{r}(\sigma'_r - \sigma'_\theta) = \rho a_r. \tag{5.15}$$

As the Disk Shearing Model is undrained, all volumetric strain rates are null and the radial velocity is also null (explained earlier, in Paragraph (b)). Using the same assumptions, radial acceleration of the soil disk must also be null. Therefore, Eq. (5.15) resumes itself to the radial equilibrium equation:

$$\frac{\partial \sigma'_r}{\partial r} + \frac{\partial u_w}{\partial r} + \frac{1}{r}(\sigma'_r - \sigma'_\theta) = 0, \tag{5.16}$$

which can be solved for the pore water pressure (u_w) when the effective stresses (σ'_r and σ'_θ) are known.

Now, all the equations involved in the Disk Shearing Model integration scheme have been described. The governing equations and unknowns are listed in Table 5.2.

Two more points have to be made before ending the presentation of the Disk Shearing Model: an absorbing boundary has to be defined (Paragraph (f)) and the equilibrium of the initial state taken from the Strain Path Method simulation has to be corrected (Paragraph (g)).

Table 5.2 Equations and unknowns of the Disk Shearing Model analysis.

Name	*Equation*	*Components*
Velocity to strain rate	(5.2)	6
Constitutive law	(4.1)	6
Vertical equation of motion	(5.13)	1
Acceleration to velocity	(5.14)	1
Radial equilibrium	(5.16)	1
15 unknown components: v_z, $\mathbf{D}$, $\boldsymbol{\sigma}'$, a_z, u_w		

(f) Outer boundary: absorbing boundary Dynamic problems require the use of an absorbing boundary to model the radiation of waves from the mesh into the far field. If no absorbing boundary is used, all the energy arriving at the outer boundary will be reflected back into the mesh. The absorbing boundary used is briefly described hereunder, in complement to the description and validation given in Appendix E.1.

Typically, an absorbing boundary consists of a dashpot (a viscous boundary) which is assuming that no energy is reflected from the boundary in an elastic medium (Lysmer and Kuhlmeyer, 1969, cited by Deeks and Randolph, 1994):

$$\tau_{rz} = \frac{G'}{c_s} v_z,$$

where G' is the soil shear modulus and c_s the soil shear wave velocity. This expression is not function of the boundary radius (r_b).

In addition to the viscous boundary, a linear spring is needed in order for the boundary to be in equilibrium even when being under residual stress. In the absence of this spring, the shear stresses will eventually become null over the whole domain with all final displacements being equal to the pile shaft displacement (Loukidis et al., 2008). Following Deeks and Randolph (1994), the spring coefficient taken herein is:

$$\tau_{rz} = \frac{G'}{2r_b} u_z,$$

where r_b is the boundary radius.

(g) Equilibrium correction As pointed out in Section 5.2.2, the Strain Path Method solution is out of equilibrium, meaning that at any vertical position of the Strain Path Method discretisation (Fig. 5.3), the radial and vertical equilibrium are satisfied for different values of pore water pressure (u_w). The solution chosen herein is to

accept the inequilibrium of the Strain Path Method and correct it right before the Disk Shearing Model simulations, using local damping to slowly allow the soil disk to come to equilibrium. The damping term added to the acceleration (a_z^n) of each time step n is (Itasca, n.d.):

$$\alpha_d |a_z^n| \operatorname{sgn}(v_z^{n-1}),$$

where α_d is the damping constant and v_z^{n-1} the vertical velocity at time step $n-1$.

5.3 Pile installation output

A typical output of the pile driving model is shown in the following section for a closed-ended pile installation. The Strain Path Method is applied to simulate the insertion of the pile toe. The state predicted by the Strain Path Method is taken as starting point for the Disk Shearing Model simulations, which consist of firstly correcting the small inequilibrium inherent to the Strain Path Method, and then imposing a series of driving blows to a thin disk of plane strain soil.

As described in Section 5.1, the soil initial state is the following: $\sigma'_{v0} = 590\,\text{kPa}$, $K_0 = 0{\cdot}615$, $e_0 = 1$, and $\text{OCR}^* = 1{\cdot}1$. The pile radius is $R = 25\,\text{cm}$. The soil discretisation is chosen in order to have a pile interface located at $r = R$ and a radial discretisation (Δr) of 2 cm after the Strain Path Method simulation. Therefore the location of the first streamline/internode is 1 cm from the pile wall.

5.3.1 Strain Path Method

The soil flow velocity is taken as $U = 1\,\text{m/s}$, and the volume insertion (V) is chosen according to Eq. (5.7) to model a pile of radius R. The domain size is $60R$ in the radial direction and $80R$ in the vertical direction. A total of 10 000 time steps are used for the simulation.

The Strain Path Method output is depicted in Figs. 5.8 and 5.9. Fig 5.8 shows the strains encountered by two streamlines during the simulation. The strains are not only very large, but present multiple reversals.

Fig. 5.9 depicts the radial and vertical effective stresses, normalised to the initial vertical effective stress (σ'_{v0}). Although Fig 5.9 depicts only penetration to a depth of $20R$, the simulation is performed until a penetration of $z = 40R$.

As the soil is normally consolidated ($\text{OCR}^* = 1{\cdot}1$), the effective stresses decrease as the pile toe is inserted into the soil. Another feature showed in Fig. 5.9 is the stress reversal, which is very clear for soil particles close the pile wall. The variation of σ'_z changes sign at the pile toe level, while the variation of σ'_r changes sign twice, in symmetry with the pile toe.

Far behind the pile toe, the minimum of the radial effective stress is at the pile-soil interface, while the minimum of the vertical effective stress is a few radii away.

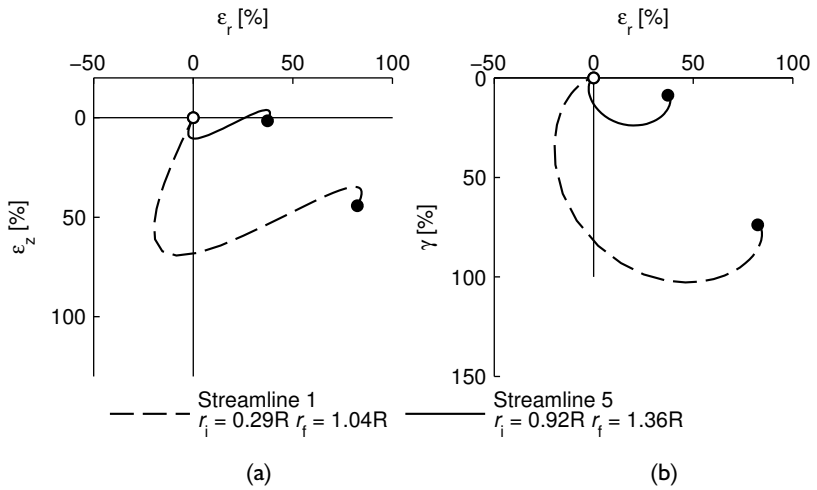

Figure 5.8 Strain Path Method output: strain paths of two streamlines: (a) radial versus vertical strain and (b) radial versus shear strain (r_i and r_f are their initial and final radial position, respectively).

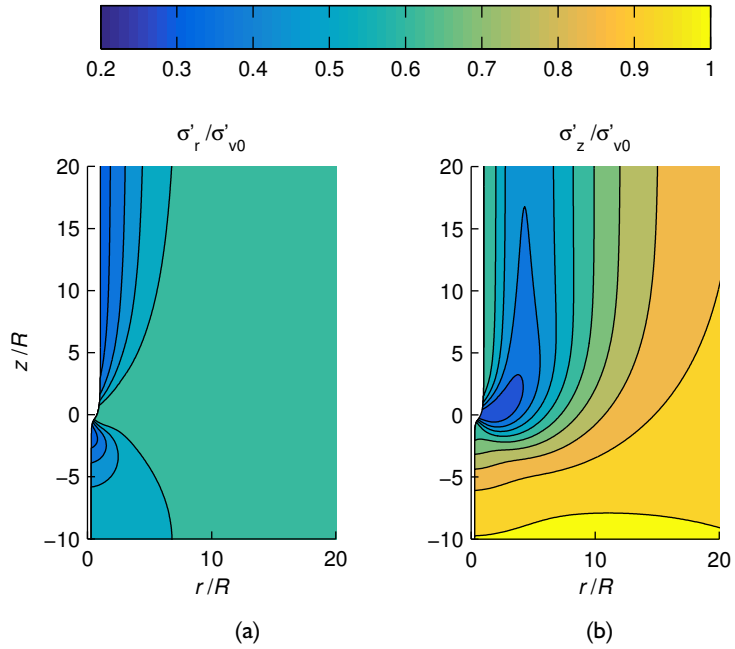

Figure 5.9 Strain Path Method output: (a) effective radial stress ratio and (b) vertical effective stress ratio.

5.3.2 Disk Shearing Model

The Disk Shearing Model simulation takes as starting state the one predicted by the Strain Path Method, far behind the toe (here, for $z = 40R$), a distance at which a soil layer can be considered to be plane strain.[2] The first step is to correct the inequilibrium of the Strain Path Method output. Then, a series of driving blows is applied to reproduce the cycles of shaft-soil shearing.

Equilibrium correction The results are depicted in Fig. 5.10 in terms of shear stress (τ), radial effective stress (σ'_r) and excess pore pressure (Δu_w) normalised to the initial vertical effective stress (σ'_{v0}).

Fig. 5.10a shows that the shear stress is *negative* at the pile wall and in the soil surrounding it after the Strain Path Method because of the strain reversal encountered by the soil close to the pile. After equilibrium correction, the shear stress stays negative, but adopts a monotonic shape. The change brought by the equilibrium correction is quite obvious and reaches more than 100% at some radii.

The variation induced by the equilibrium correction is much less noticeable for the radial effective stress and the pore pressure (Fig. 5.10b and c).

Driving blows Starting from the previous 'at equilibrium' state (called blow 0), a series of driving blows is simulated by imposing the velocity signal defined in Eq. (5.10) at the pile radius.

The result of the Disk Shearing Model simulations are depicted on Fig. 5.11 and Fig. 5.12. Fig. 5.11a displays the variation of normalised excess pore pressure ($\Delta u_w/\sigma'_{v0}$) around the shaft during driving. Each driving blow, depicted by the grey lines, induces a reduction of Δu_w at the pile wall but a rise in Δu_w a few radii away from the pile shaft. The state after the 100^{th} blow is highlighted in black. Furthermore, the change of pore pressure at the pile wall is represented on Fig. 5.11b, where the dots are the state after each blow and the lines show the variation of pore pressure *during* each blow. Fig. 5.11b indicates that pore pressure decreases during each blow.

Fig. 5.12 shows a similar representation of the radial effective stress ratio (σ'_r/σ'_{v0}). The radial effective stress is seen to decrease over the whole domain as driving progresses. At the pile wall (Fig. 5.12b), the radial effective stress rises during pile movement, as would be expected by an overconsolidated soil.

The pile driving model predicts hysteretic damping thanks to the constitutive law (see Section 4.3.1), as well as geometric/radiation damping through the cylindrical geometry of the problem. The pile driving model does not however predict damping associated with velocity, *i.e.* viscous or failure damping.

[2] In fact, the radial distribution of stresses behind the Strain Path Method is almost in a plane state $20R$ behind the toe. Therefore, the cycles imposed by the Disk Shearing Method for a cumulative displacement of less than $20R$ represent cycles that should have happened during the Strain Path Method. This is one inevitable drawback of splitting the installation in two separate processes.

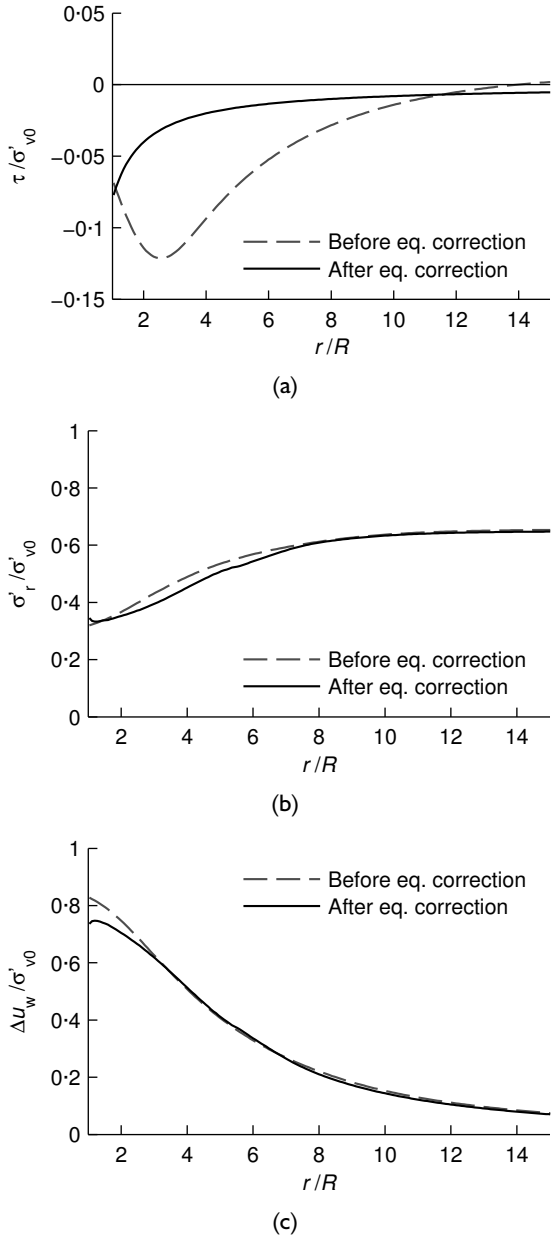

Figure 5.10 Equilibrium correction of the Disk Shearing Model initial state: normalised (a) shear stress, (b) effective radial stress, and (c) excess pore pressure.

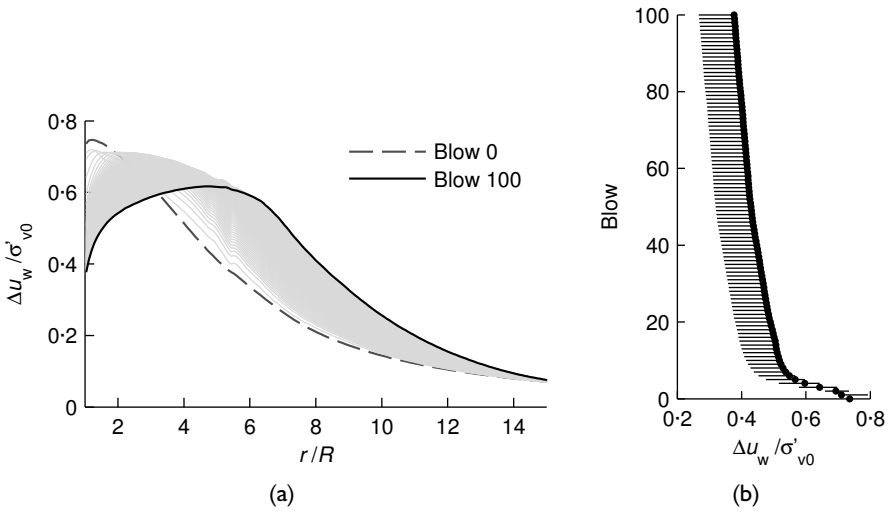

Figure 5.11 Disk Shearing Model: pore pressure ratio after each driving blow (a) over the domain and (b) at the pile wall.

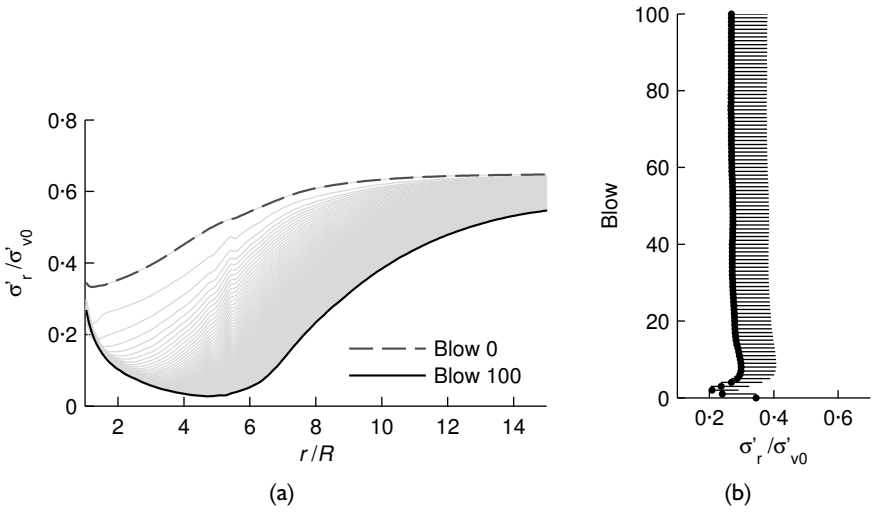

Figure 5.12 Disk Shearing Model: effective radial stress ratio after each driving blow (a) over the domain and (b) at the pile wall.

5.4 Equalisation

The equalisation stage is modelled as the coupled consolidation of the soil disk used during the Disk Shearing Model. The initial condition for the equalisation stage is the end of the last Disk Shearing Model blow.

As for the pile installation stage, an Eulerian standpoint is taken: each node refers to a small element, the dimensions of which do not change with time and through which soil particles and pore fluid flow.

The integration scheme of the consolidation analysis is outlined in Fig. 5.13 for each time step of the analysis. Similarly to the integration schemes used for the installation stage, the strain rates are computed from the velocity (Section 5.2.1) from which the effective stresses are computed (Chapter 4). Afterwards, the pore pressures are computed using the radial equilibrium equation. The pore pressures are then used to, again, compute the velocity and this loop is run until a prescribed tolerance is reached.

The relationship between pore pressure (u_w) and soil radial velocity (v_r) is the cornerstone of the analysis and also an original result developed in this thesis. Hereunder are described the assumptions and steps that lead to this relationship, which is presented in Eq. (5.26).

The assumptions are:

(c1) Two phases are occupying the soil: the porous soil skeleton and the pore water, according to the Biot theory;

(c2) The skeleton behaviour is governed an effective stress constitutive law, like the one defined in Chapter 4;

(c3) The water flows though the porous skeleton according to Darcy's law. Tortuosity and dynamic inertia are neglected;

(c4) The fluid flow is quasi-static, *i.e.* inertial forces are disregarded;

(c5) The soil grains composing the soil skeleton are much less compressible than the two-phase soil;

(c6) The pore water is much less compressible than the two-phase soil;

(c7) The permeability is assumed to be constant throughout the consolidation analysis.

Assumption (c1) implies that the two kinematic quantities are the skeleton velocity $\mathbf{v}$, which describes the motion of the skeleton and the specific discharge $\mathbf{q} = n(\mathbf{v}_w - \mathbf{v})$, which is the volume flow per area of porous solid and describes the motion of the fluid relative to the skeleton (Detournay and Cheng, 1993). Assumptions (c5) and (c6) imply that any change in volume of an element of soil is entirely due to the expulsion or absorption of water from the element, *i.e.* that Skempton (1954)'s B parameter is equal to 1.

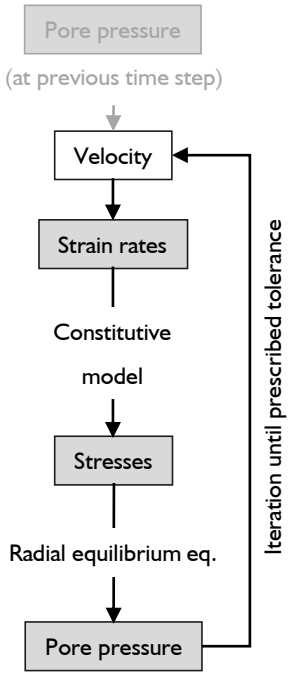

Figure 5.13 Integration scheme for each *time step* during the coupled consolidation analysis of the disk of soil (greyed boxes are quantities evaluated at the internodes).

The relationship between pore pressure and velocity is obtained by expressing the mass balance and Darcy's law. These two steps are detailled hereunder for the general three dimensional case.

Mass balance The (Eulerian) mass balance equations (or continuity equations) for the solid and the liquid phase are, respectively (Coussy, 2004):

$$\frac{\partial}{\partial t}[\rho_s(1-n)] + \nabla \cdot [\rho_s(1-n)\mathbf{v}] = 0, \tag{5.17}$$

$$\frac{\partial}{\partial t}(\rho_w n) + \nabla \cdot (\rho_w n \mathbf{v}_w) = 0, \tag{5.18}$$

where ρ_s and ρ_w are respectively the densities of the solid and liquid phase, n is the skeleton porosity, and $\mathbf{v}$ and $\mathbf{v}_w$ are respectively the skeleton and water velocity vectors. Eqs. (5.17) and (5.18) can be expressed in an alternate form:

$$\frac{\mathrm{D}}{\mathrm{D}t}[\rho_s(1-n)] - \rho_s(1-n)\dot{\varepsilon}_v = 0, \tag{5.19}$$

$$\frac{\mathrm{D}}{\mathrm{D}t}(\rho_w n) - (\rho_w n)\dot{\varepsilon}_v + \nabla \cdot [\rho_w n(\mathbf{v}_w - \mathbf{v})] = 0, \tag{5.20}$$

where $\dot{\varepsilon}_v = -\nabla \cdot \mathbf{v}$ is the skeleton volumetric strain rate (minus sign because compression is positive).

Introducing assumption (c5) means that ρ_s can be considered constant so Eq. (5.19) becomes:

$$\dot{\varepsilon}_v = \frac{-\dot{n}}{1-n}. \tag{5.21}$$

Similarly, introducing assumption (c6) means ρ_w is constant so Eq. (5.20) becomes:

$$\dot{n} - n\dot{\varepsilon}_v = -\nabla \cdot [n(\mathbf{v}_w - \mathbf{v})]. \tag{5.22}$$

Combining Eqs. (5.21) and (5.22) yields an expression for the overall volume behaviour of the soil (Carter et al., 1977):

$$\dot{\varepsilon}_v = \nabla \cdot [n(\mathbf{v}_w - \mathbf{v})]. \tag{5.23}$$

Darcy's law Ignoring tortuosity, body forces and viscous forces, the general form of Darcy's law reads (Coussy, 2004):

$$n(\mathbf{v}_w - \mathbf{v}) = \frac{-\mathbf{K}}{\gamma_w} \nabla u_w, \tag{5.24}$$

where $\mathbf{K}$ stands for the permeability tensor.

Finally, combining Eq. (5.23), Eq. (5.24), and the definition of the volumetric strain rate ($\dot{\varepsilon}_v = -\nabla \cdot \mathbf{v}$) yields:

$$\nabla \cdot \left(\mathbf{v} - \frac{\mathbf{K}}{\gamma_w} \nabla u_w \right) = 0, \tag{5.25a}$$

$$\nabla \cdot [n\mathbf{v}_w] + \nabla \cdot [(1-n)\mathbf{v}] = 0. \tag{5.25b}$$

For the one dimensional case that is of concern, Eqs. (5.25a-b) boil down to:

$$v_r = \frac{k_r}{\gamma_w} \frac{\partial u_w}{\partial r}, \tag{5.26}$$

$$v_{r,w} = \frac{n-1}{n} v_r. \tag{5.27}$$

where k_r is the radial permeability of the soil, and v_r and $v_{r,w}$ are respectively the skeleton and water velocities.

Using Assumptions (c1) to (c7), the coupled consolidation analysis of a disk of soil around a pile allowing only radial drainage boils down to Eq. (5.26), which relates pore pressure (u_w) to *soil* radial velocity (v_r).

During each time step of which there are 14 equations and 14 unknowns, as detailed in Table 5.3. This approach is validated in Appendix E.3 against a coupled consolidation analysis performed by Randolph, Carter and Wroth (1979).

Table 5.3 Equations and unknowns of the consolidation analysis.

Name	*Equation*	*Components*
Velocity to strain rate	(5.2)	6
Constitutive law	(4.1)	6
Radial equilibrium	(5.16)	1
Pore pressure to velocity	(5.26)	1
14 unknown components: v_r, $\mathbf{D}$, $\boldsymbol{\sigma}$, u_w		

5.5 Equalisation output

An output of the consolidation analysis is presented in this section. Starting from the last shearing cycle, the soil is allowed to move radially as the water escapes from the outer boundary. The radial permeability $k_r = 10^{-8}$ m/s and is assumed to be constant with time and radial position. Radial discretisation is the same as the one taken for the Disk Shearing Model.

Fig. 5.14 depicts the isochrones of pore pressure during consolidation. As the initial pore pressure distribution (at $t = 0$) is not monotonic but presents a maximum a few radii away from the pile wall, the excess pore pressure at the pile wall first increases before decreasing. This trend is displayed in detail in Fig. 5.15 for the soil at the pile wall. Also depicted is the radial effective stress σ'_r, which follows a curve approximately inversely proportional to the pore pressure one, while the total radial stress σ_r is only mildly varying with time.

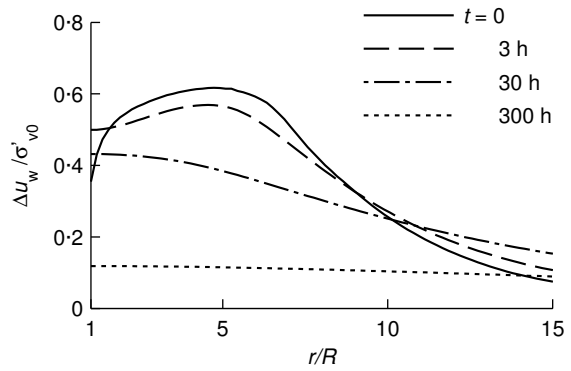

Figure 5.14 Pore pressure isochrones during consolidation.

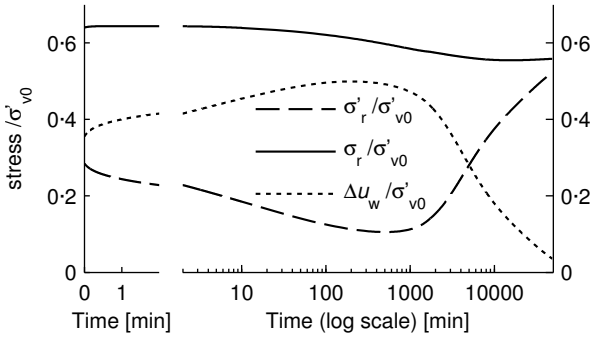

Figure 5.15 Stress state of the soil at the pile wall during consolidation.

5.6 Conclusion

The pile driving model has been presented in this chapter, the aim of which is to compute the radial stress distribution around the shaft of a pile, open- or closed-ended, during and after driving.

During installation, the main assumption of the model is to consider that a thin layer of soil around the pile can be considered as plane strain, as long as it is not too close to the pile toe nor to the ground surface. The installation modelling is split in two parts:

(i) The Strain Path Method is applied to a layer of soil at a certain depth. This simulates the insertion of the pile toe;

(ii) Far behind the toe, the Strain Path Method output is taken as input to the Disk Shearing Model which, after a correction of the Strain Path Method equilibrium, simulates a series of driving blow by imposing a velocity signal at the pile wall.

After installation, a coupled consolidation analysis is performed where only radial drainage is permitted.

The hypoplastic constitutive model presented in Chapter 4 is used for both installation and equalisation.

Chapter 6

Pile driving model results

This chapter expands on the pile driving simulation results introduced in Chapter 5 by investigating several aspects of the model.

The model introduced in Chapter 5 focuses on the behaviour of a single layer of clay around a driven pile. The installation is split in two steps: the Strain Path Method simulation accounts for the penetration of the pile toe, and is followed by the Disk Shearing Model simulation, which applies a series of driving blows to the disk of clay. The equalisation stage is modelled as a coupled consolidation analysis.

Section 6.1 compares the pile driving model results of five soils of different overconsolidation ratio to the trends reported in the literature review of experimental pile installations of Chapter 2. Section 6.2 presents a parametric study in which the influence of the hammer initial velocity is studied. Section 6.3 exposes a sensitivity analysis on the 10 hypoplastic constitutive model parameters as well as on the initial void ratio (e_0), the initial vertical effective stress (σ'_{v0}), and the initial coefficient of earth pressure at rest (K_0). Finally, Section 6.4 presents an open-ended pile installation and compares it to a closed-ended simulation.

Unless stated otherwise, constitutive or discretisation parameters are the same as in Chapter 5: the radial discretisation (Δr) is 2 cm, the extend of domain in the radial direction is $60R$ (except for the Disk Shearing Model for which the domain extends to $16R$), and the vertical extent of the Strain Path Method is $80R$. The Strain Path Method soil flow velocity (U) is taken as 1 m/s while the volume insertion (V) is chosen according to Eq. (5.7) (p. 98). The soil constitutive model is the hypoplastic law described in Chapter 4 for London clay. The imposed velocity at the boundary of the disk is the one presented in Chapter 5 (summarised in Fig. 5.7, p. 103). The radial permeability coefficient (k_r) is taken as 10^{-8} m/s.

6.1 Effect of initial overconsolidation ratio

In this section, the results of the pile driving simulation are presented for five initial overconsolidation ratios and are compared to trends obtained from the literature review of Chapter 2.

Table 6.1 Initial states used in Section 6.1.

Simulation No	σ'_{v0}	K_0	OCR^*	OCR
S140	590	0·615	1·1	1·0
S141	170	0·939	3	3·4
S142	90	1·143	5	7·1
S143	37	1·492	10	21·1
S144	15	1·947	20	64·1

The five initial states, described by the vertical effective stress (σ'_{v0}), the coefficient of earth at rest (K_0), and the overconsolidation ratio (OCR^*), are summarised in Table 6.1. The normally consolidated initial state ($OCR^* = 1{\cdot}1$) is the same as the one presented in Chapter 5. All five states have the same void ratio (e_0) of 1, which implies that they also have the same initial shear strength (s_{u0}) of 107·80 kPa. Like in Chapter 5, the value of the coefficient of earth pressure at rest (K_0) is obtained through the Mayne and Kulhawy (1982) empirical relationship (Eq. 4.6, p. 72). The conventional definition of the overconsolidation ratio ($OCR = \sigma'_{vy}/\sigma_{v0}$), obtained thanks to Eq. (4.9) (p. 85), is also shown in Table 6.1. For the sake of clarity, most of the figures of this section depict only the first four initial overconsolidation ratios.

Similarly to Chapter 2, this section is divided in three parts corresponding to a time period in the life of a pile:

- Section 6.1.1: when the pile is actually moving as a result of the driving blow (or from the jack stroke in the literature survey);
- Section 6.1.2: immediately after installation, when equalisation has not yet begun; and
- Section 6.1.3: equalisation.

Although the simulations are based on effective stress soil behaviour, the field data measurements are not, as total radial stress and pore pressure are measured and subtracted to compute effective stress. Therefore simulation results are presented in the same order as in Chapter 2: pore pressure, radial total stress, radial effective stress, shear stress, and other observations. Following the literature review, the total radial stress (σ_r) and the excess pore pressure (Δu_w) are normalised with the *in situ* vertical effective stress (σ'_{v0}). The radial effective stress (σ'_r) on the other hand is normalised with the *in situ* radial effective stress (σ'_{r0}) in order to appreciate any variation with regards to its initial value.

6.1.1 Pile installation – Moving pile

Pore pressure The excess pore pressure ratio ($\Delta u_w/\sigma'_{v0}$) at pile wall versus blow count is depicted in Fig. 6.1a for the first four initial overconsolidation ratios. The

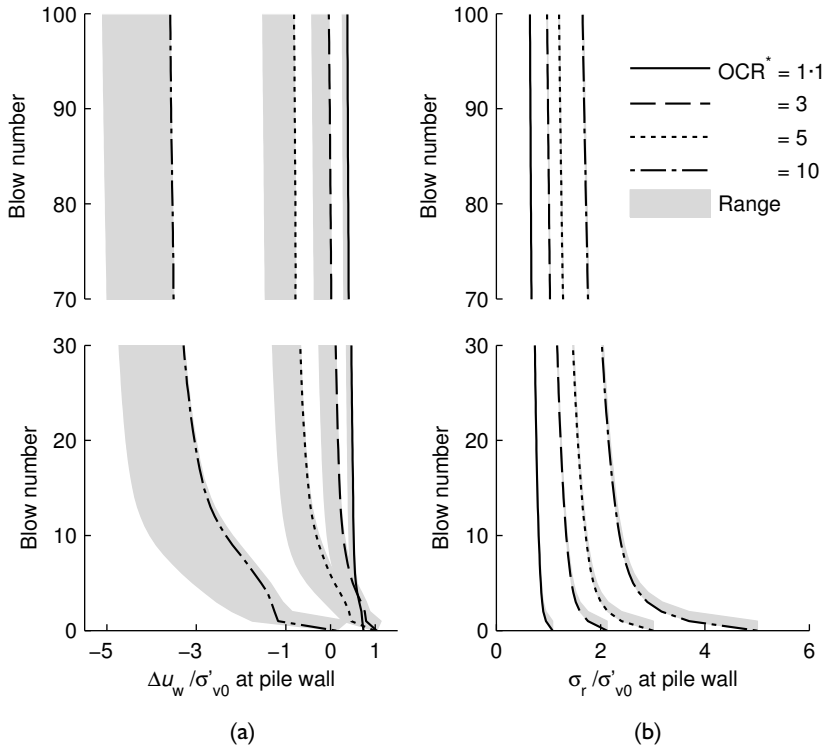

Figure 6.1 Normalised (a) pore pressure and (b) radial total stress at pile wall. Black lines are values after each blow while greyed area correspond to the range covered during each blow.

greyed area of Fig. 6.1a represents the range of values encountered *during* each blow while the black lines are values at the end of each blow.

The four curves exhibit similar trends: (1) a reduction of pore pressure with increasing number of blows, (2) a reduction in $\Delta u_w/\sigma'_{v0}$ which is stronger as OCR^* is higher, and (3) excess pore pressure during the pile movement is always less than that after the blow (except for the first few blows).

Point (1) was not consistently measured in the field, as the opposite was sometimes observed (Section 2.3a, p. 25). Points (2) and (3), on the other hand, were consistently reported whatever the initial overconsolidation ratio (Section 2.2a, p. 18).

The pore pressure reduction during each blow is counter intuitive for the critical state theory, for which a normally consolidated soil should tend to contract during shearing therefore leading to an increase in excess pore pressure. It is the cycles imposed by the Strain Path Method and the Disk Shearing Method that incite effective stress to reduce, therefore moving the state further on the dry side of critical, leading to a more and more overconsolidated state as the cycles progress.

Radial total stress Fig. 6.1b depicts the total radial stress ratio (σ_r/σ'_{v0}) at the pile wall during installation. Again, the four soils exhibit comparable trends, which are: (1) σ_r decreases with the number of blows, (2) this reduction is more pronounced as overconsolidation ratio grows, but (3) σ_r stays relatively constant *during* pile movement (Figs. 6.1a and b have the same horizontal scale). Points (1) and (2) are also concluded for the pore pressure (Fig. 6.1a) whereas Point (3) differs.

These three points have been steadily measured in field experiments. Section 2.2b (p. 19) reported the decrease of σ_r after each jack and the relatively small variation of σ_r during each jack stroke. Section 2.3b (and especially Fig. 2.9, p. 28) depicts a more pronounced reduction in σ_r as overconsolidation ratio is higher.

The reduction with number of blows shown in Fig. 6.1a and b shows the ability of the pile driving model to simulate fatigue: one of the presumed mechanisms behind the h/R effect.

Radial effective stress During the experiments, the radial effective stress (σ'_r) was computed from total stress and pore pressure. *During* pile movement, uncertainties in the pore pressure measurements made σ'_r hazardous to compute. Therefore, comparison between experimental and simulation is difficultly achievable.

Shear stress Fig. 6.2a depicts the maximum shear stress (τ_{max}) predicted by the Disk Shearing Model during each blow. Apart for the first blows, the τ_{max} values for each overconsolidation ratio tend to a relatively steady value as blow count rises. Except for the most overconsolidated soil, τ_{max} does not attain critical state (which is the same for all initial states, $s_{u0} = 107{\cdot}80\,\text{kPa}$). This results from the dynamic integration scheme of the Disk Shearing Model and can be explained by looking at Fig. 6.2b, which depicts the stress strain response at the pile wall for the last blow. Fig. 6.2b shows that the shear strain reached during each blow grows with initial overconsolidation ratio. That happens because the stresses after a few blows *increase* with increasing overconsolidation ratio (even though initial stress is lower with increasing overconsolidation ratio; this is shown later, in Table 6.2, p. 124). This increase in effective stress brings (1) an increase in initial stiffness (G_0), but more importantly, (2) an increase in shear wave velocity (c_s), which brings down the ratio $v_{z,p}/c_s$, and increases slippage (the impact of velocity is covered in the upcoming Section 6.2). Therefore, after a series of blows, initially overconsolidated soils reach critical state more easily than normally consolidated ones.

In Section 2.2d (p. 19), the shear stress *during* each jack stroke sometime rose and sometime decreased. The simulation is therefore inconsistent with the observations, as simulated τ always rises *during* pile movement. Furthermore, Fig. 6.2a also shows that no matter how many blows are applied, the shear stress always tends to the critical state strength, which is one of the disadvantages of choosing a critical state theory based constitutive model, without any interface element. Therefore, the model cannot be used to predict (undrained) shear strength developed at the shaft during driving.

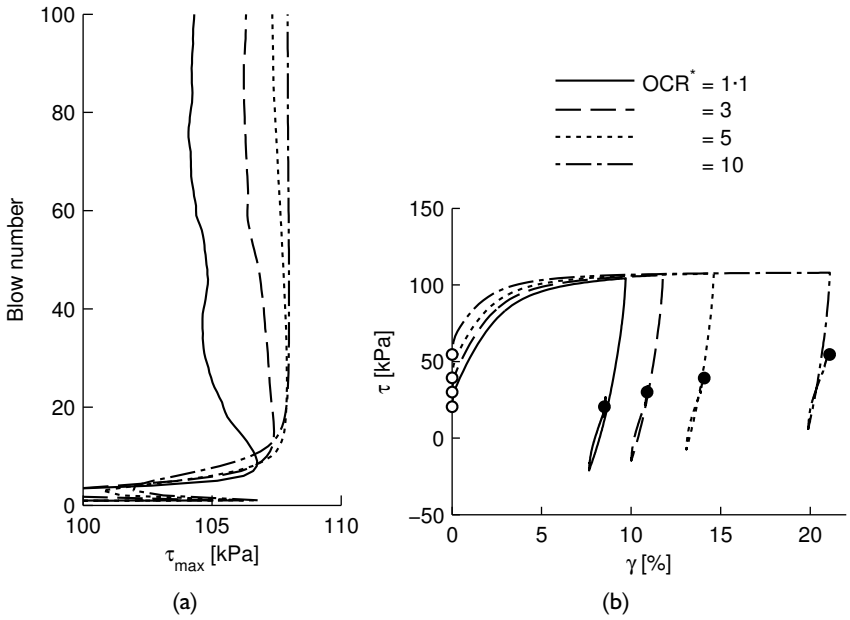

Figure 6.2 (a) Maximum shear stress at pile wall during each blow and (b) Shear stress versus shear strain at the pile wall during the last blow.

6.1.2 Pile installation – Immediately after installation

This section presents the results of the Disk Shearing Model simulation immediately after installation. The subscript 'i' is added to any quantity to denote that it is immediately after installation.

The Disk Shearing Method focuses on a layer of soil. This layer, depending on its depth and pile embedment, would encounter a various amount of driving blows. Herein, I have performed the Disk Shearing Model simulation until a relatively steady-state was attained (100 blows) and considered that it represented the 'after installation' state.

The numerical values of stress and pore pressure at pile wall after installation are summarised in Table 6.2.

Table 6.2 Numerical values at pile wall for the simulations of Section 6.1.

Initial state	After installation		During consolidation		After 95% consolidation	
OCR^*	σ'_{ri} *[kPa]*	Δu_{wi} *[kPa]*	$\Delta u_{w,max}$ *[kPa]*	*at t [h]*	σ'_{rc} *[kPa]*	*Set-up*
1·1	158·44	222·30	294·64	3	305·85	1·93
3	171·82	—6·21	109·90	20	121·25	0·70
5	181·60	—73·44	60·44	32	89·50	0·49
10	193·83	—132·65	20·04	76	56·70	0·28
20	201·79	—167·46	3·00	273	25·84	0·13

Pore pressure Fig. 6.3a and b depict the excess pore pressure ratio ($\Delta u_w/\sigma'_{v0}$) distribution at the beginning and at the end of the Disk Shearing Model simulation, respectively. Fig. 6.3a essentially[1] shows the pore pressure distribution after the Strain Path Method: $\Delta u_w/\sigma'_{v0}$ is monotonic for initial overconsolidation ratio values (OCR^*) of 1·1, 3, and 5 and values at pile wall are slightly below 1. For the heavily overconsolidated soil ($OCR^* = 10$), the excess pore pressure ratio is close to 0 at pile wall and is negative up to a distance of 4 radii from the pile wall.

After 100 blows, the distribution of excess pore pressure has drastically changed (Fig. 6.1b). The excess pore pressure ratio at pile wall is lower as overconsolidation ratio is higher, but the peak is located between 3 and 6 radii away from the pile wall and is *higher* as overconsolidation ratio is higher.

Experimental data measured far behind the pile toe (Section 2.3a, p. 25) evidenced the *same trends* as those reported in Fig. 6.1b . However, the simulated $\Delta u_{wi}/\sigma'_{v0}$ is lower than the measured ratio: whereas $\Delta u_{wi}/\sigma'_{v0}$ does not reach any higher values than 1 in the simulations, the experimental data suggests that

[1]For the rest of this chapter, the results presented as 'after the Strain Path Method simulation' have been through the equilibrium correction procedure described in Section 5.2.3g, p. 106.

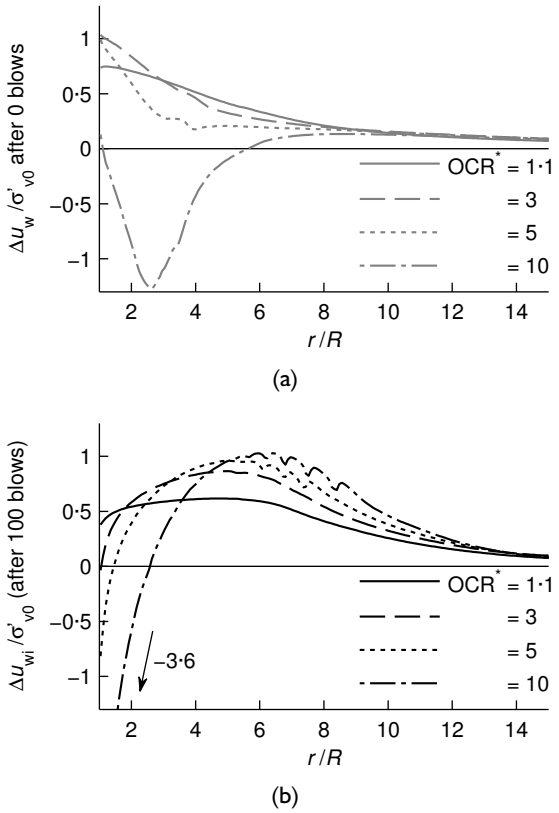

Figure 6.3 Distribution of pore pressure (a) after the Strain Path Method and (b) at the end of installation (after 100 blows of the Disk Shearing Model).

the excess pore pressure ratio maximum attains values over 2, even for moderately overconsolidated soils (see Fig. 2.8, p. 27, for Champlain clay).

The concave shape of simulated excess pore pressure after installation depicted in Fig. 6.1b has never been published before. This result is one of the most important of this thesis, as the distribution of pore pressure dictates the variation of radial effective stress during equalisation (covered in Section 6.1.3). This non-monotonous shape stems from two aspects of the model: (1) the dynamic integration scheme of the Disk Shearing Model takes into account soil inertia: each blow involves a cycle of strain[2] enough. and (2) the constitutive model predicts excess pore pressure reduction when being subjected to shearing cycles.

[2]The rebound of the imposed pile displacement is not that relevant, as even a signal with no rebound (critically damped) creates a cycle of strain when pile velocity is high

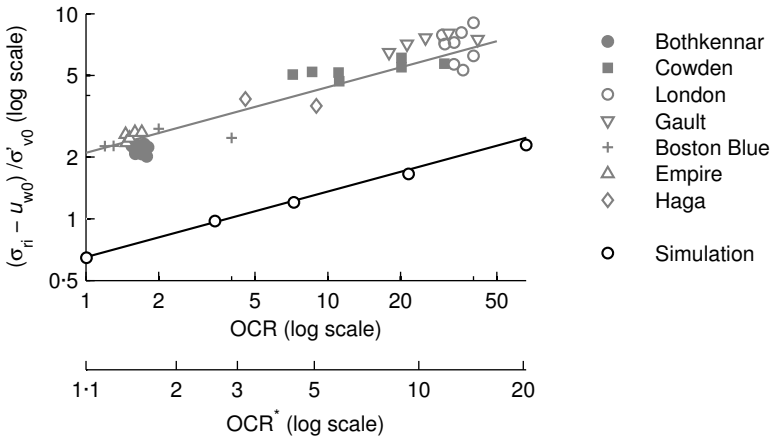

Figure 6.4 Normalised radial total stress after installation versus overconsolidation ratio (hypoplastic OCR* and conventional OCR): experiments (reproduced from Fig. 2.10, p. 29; data compiled by Chow, 1996) and simulation.

Radial total stress The radial total stress ratio at pile wall after installation (σ_{ri}/σ'_{v0}) is depicted in Fig. 6.4 versus overconsolidation ratio (hypoplastic OCR* and conventional OCR) and compared to the experimental data presented in the literature review (Fig. 2.10, p. 29).

All five simulated points align perfectly in a log:log plot and values of σ_{ri}/σ'_{v0} range from 0·65 to 2 for the overconsolidation ratios investigated. The simulation results concur with the field results concerning the positive gradient and the linear trend in a log:log plot. However, as for the peak excess pore pressure ratio, the measurements exceed the simulated data by at least a factor 3.

Radial effective stress The radial effective stress ratio after installation ($\sigma'_{ri}/\sigma'_{r0}$ – this time normalised to the initial *radial* effective stress) is displayed in Fig. 6.5. At the pile wall, the radial effective stress after installation (σ'_{ri}) has decreased from its initial value (σ'_{r0}) for the lightly overconsolidated soil whereas it has increased for the overconsolidated ones. For increasing radial position, the stress tends to its initial value. However, all soils show a minimum σ'_{ri} between 3 and 6 radii away from the pile wall, corresponding to the peak Δu_{wi}.

In Section 2.3c (p. 29), the experimentally computed σ'_{ri} were available only at the pile wall and had the same conclusions: $\sigma'_{ri} < \sigma'_{r0}$ for the lightly overconsolidated Bothkennar and Empire clays whereas $\sigma'_{ri} > \sigma'_{r0}$ for the overconsolidated Cowden till and London clay.

Other observations The vertical displacement predictions after installation (u_{zi}) are depicted in Fig. 6.6 for the four overconsolidation ratios. The vertical displacement

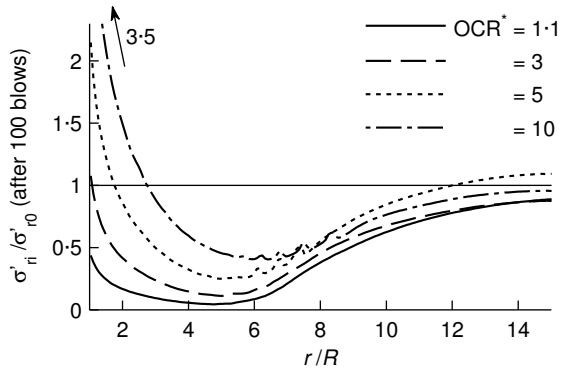

Figure 6.5 Distribution of radial effective stress after installation.

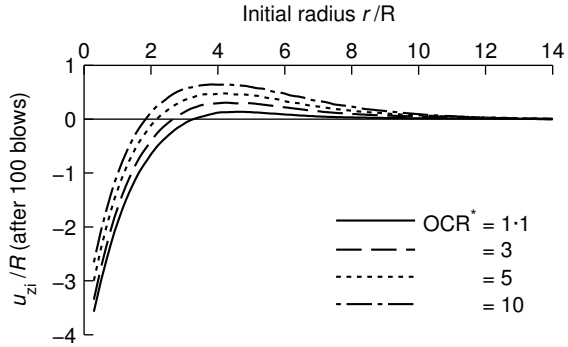

Figure 6.6 Distribution of vertical displacement after installation.

is the greatest closest to the pile and there is a heave a few radii away from the pile wall. As overconsolidation ratio increases, pile slippage and soil heave increase.

The displacement pattern of Fig. 6.6 agrees with the experimental data presented in Fig. 2.11b (p. 31) for $h > 40R$: the majority of soil downward displacement is contained within an initial radius $r < 2R$. However, the experimentally observed soil heave, for jacked piles, was much smaller than the predicted one.

The predicted radial displacement is the one imposed by the Strain Path Method, which closely agrees with a radial cavity expansion (comparison was made in Section 3.1.2, p. 47), which also was in the same range as the measured radial displacement (Fig. 2.11a, p. 31).

6.1.3 Equalisation

Following the 100 blows imposed by the Disk Shearing Model, the equalisation stage is modelled using a radial coupled consolidation analysis. The subscript 'c' is used to denote equalised quantities, which is taken after 95% consolidation, *i.e.* for

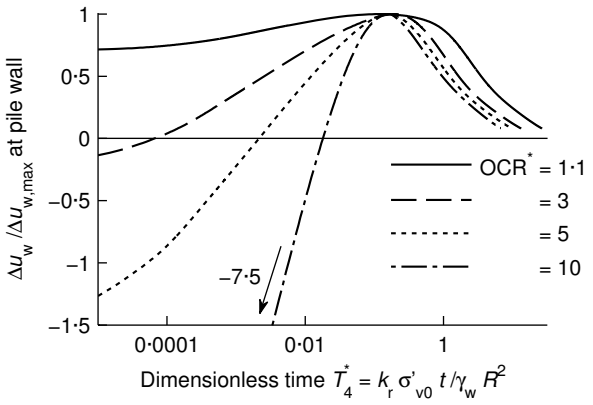

Figure 6.7 Excess pore pressure ratio at pile wall versus dimensionless time.

a normalised pore pressure ratio ($\Delta u_w / \Delta u_{w,max}$) of 0·05 ($\Delta u_{w,max}$ is the maximum pore pressure attained *at the pile wall* during equalisation). The numerical values attained at pile wall during and after equalisation are summarised in Table 6.2 (p. 124).

Pore pressure The normalised pore pressure ratio at pile wall ($\Delta u_w / \Delta u_{w,max}$) is depicted in Fig. 6.7 against dimensionless time (T_4^*). For all four overconsolidation ratios presented, Δu_w initially increases to a maximum ($\Delta u_{w,max}$) before reducing. The origin of this initial increase is the concave shape of the excess pore pressure distribution at the end of installation (Fig. 6.3b). As the maximum value of excess pore pressure is a few radii away from pile shaft, the water initially flows towards the pile, leading to an increase in Δu_w. As a consequence of this short term inward flow of water, not only does the effective stress decrease (this is elaborated later) but the void ratio at pile wall increases, which leads to a *drop* in shear strength (s_u) during this short-term increase of pore pressure.

The normalised results presented in Fig. 6.7 agree well with field data (see Figs 2.12, p. 32). The differences were that the peak in excess pore pressure happened at dimensionless times T_4^* ranging from 10^{-3} to 10^{-2} whereas for the simulation, T_4^* ranges from 0·1 to 0·2 (Fig. 6.7). This time difference tends to indicate that the apex of the radial distribution of Δu_w is closer to the pile wall for slow jacked installations than driven installations (this is also evidenced in Chapter 7).

Fig. 6.8 depicts values of $\Delta u_{w,max}$ at pile wall normalised to the vertical effective stress (σ'_{v0}) versus overconsolidation ratio. Fig. 6.8a is a reproduction of Fig. 2.13 (p. 33) and depicts the experimental data, while Fig. 6.8b presents the simulation results. For overconsolidation ratios (OCR) up to approximately 10, the model predicts a relatively linear curve in double log coordinates (Fig. 6.8b). However, $\Delta u_{w,max}$ falls for higher overconsolidation ratio. This stems from the Δu_{wi} distribution at the end of installation (Fig. 6.3b): with increasing OCR, $\Delta u_{wi} / \sigma'_{v0}$ at pile

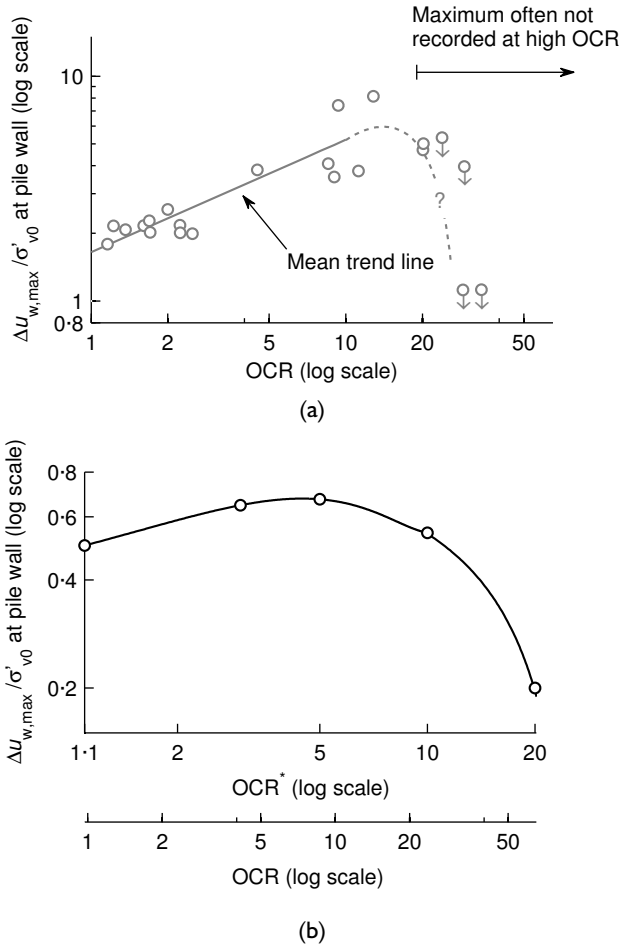

Figure 6.8 Maximum pore pressure at pile wall during equalisation versus overconsolidation ratios: (a) experiments (reproduced from Fig. 2.13, p. 33; data compiled by Lehane, 1992) and (b) simulation.

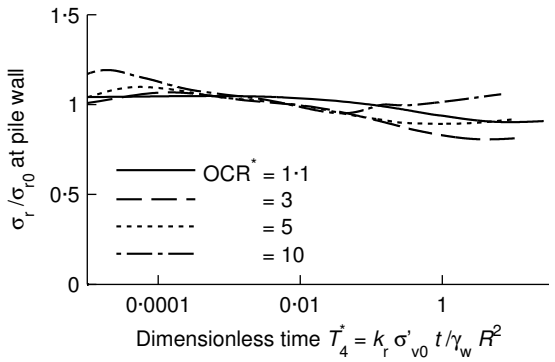

Figure 6.9 Radial total stress ratio at pile wall (σ_r/σ_{r0}) versus dimensionless time (T_4^*).

wall reduces more strongly than the maximum $\Delta u_{wi}/\sigma'_{v0}$, located a few radii away from pile shaft, rises. Again, simulated $\Delta u_{w,max}/\sigma'_{v0}$ is underestimated compared to the experiments by a factor of at least 3. Nevertheless, the qualitative shape depicted in Fig. 6.8b agrees particularly well with the measurements.

Radial total stress The radial total stress ratio at pile wall (σ_r/σ_{r0}) for all simulations is depicted in Fig. 6.9. Apart for the most overconsolidated soil, σ_r decrease steadily its their equalised value. This was also recorded in the field measurements for normally to lightly overconsolidated soils (Section 2.4b, p. 34).

Radial effective stress The radial effective stress ratio (σ'_r/σ'_{r0}) at pile wall is depicted in Fig. 6.10 versus normalised time (T_4^*). The sharp short-term increase in pore water pressure (Fig. 6.7) leads to a rapid reduction in σ'_r. The minimum in σ'_r occurs slightly later than the maximum in Δu_w, for dimensionless times (T_4^*) ranging from 0·2 to 0·3. After that short term decrease, σ'_r increases to values close – but inferior – to σ'_{r0}. The set-up factors are summarised in Table 6.2 (p. 124). Set-up is greater than one for the normally consolidated soil ($\sigma'_{rc} > \sigma'_{ri}$) and is smaller than one for the overconsolidated soils.

The distribution of the equalised values of radial effective stress (σ'_{rc}) is depicted in Fig. 6.11. The short term increase has left a permanent scar for the overconsolidated soils, for which σ'_{rc} is lower at the pile shaft than at one radii from it. On the contrary, the normally compressed soil shows a monotonic distribution of equalised radial stress.

The simulation results presented above are observed in the literature review (Section 2.4c, p. 34): σ'_r at pile wall decreased rapidly to a minimum before increasing, the set-up was greater than one in lightly overconsolidated clays but smaller than one in overconsolidated clays. The only difference is that the simulation predicts an equalised radial stress that is in the same range as σ'_{r0} whereas the experiments report higher values. This is again linked to the underestimation of the excess pore

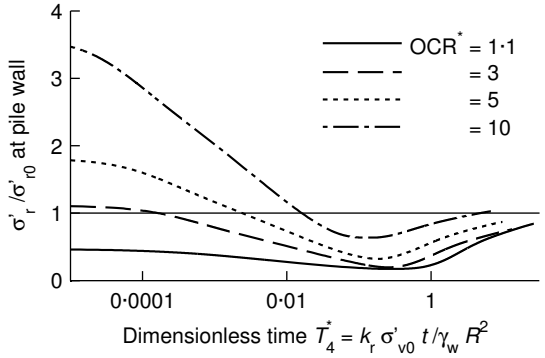

Figure 6.10 Radial effective stress ratio at pile wall (σ'_r/σ'_{r0}) versus dimensionless time (T^*_4).

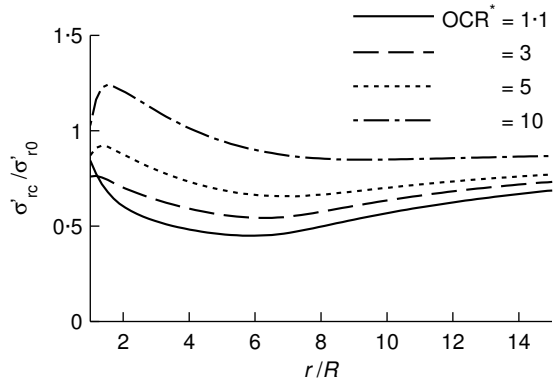

Figure 6.11 Distribution of effective radial stress ratio after consolidation.

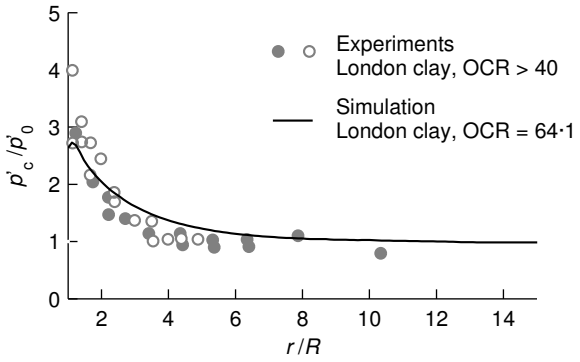

Figure 6.12 Comparison between measured and simulated mean effective stress after installation and equalisation in London clay (experimental data reproduced from Fig. 2.15b, p. 38 after Bond and Jardine, 1991).

pressure during driving.

Finally, Fig. 6.12 depicts the mean effective stress after equalisation for the largest initial overconsolidation ratio investigated, so that it can be compared to measurements made in London clay around jacked and driven piles (already presented in Fig. 2.15b, p. 38). Simulation results agree reasonably well with measured values.[3]

Additional figures are depicted in Appendix F (p. 223), while the conclusion of this section is reported at the end of this chapter (p. 143).

6.2 Effect of the hammer velocity

This subsection presents a parametric study on the shape of the imposed velocity at pile wall during the Disk Shearing Model simulations. Described in Section 5.2.3a (p. 101), the velocity imposed at the pile wall ($v_{z,p}$) is the analytical solution of a mass-spring-dashpot system where the mass has an initial velocity equal to v_0 and has the following analytical form:

$$v_{z,p} = 2v_0 \frac{\alpha}{\beta} e^{-\alpha t} \sin(\beta t), \qquad \text{(5.10bis) (6.1)}$$

where $\beta = \sqrt{\omega_n^2 - \alpha^2}$, α is the spring-dashpot constant and ω_n the natural frequency of the spring-mass system.

Five v_0 values are investigated ranging from —0·75 to —12 m/s (Table 6.3). The spring-dashpot constant α and the natural frequency of the spring-mass system ω_n are varied in unison with v_0 in order to maintain the same final set of 10 mm and with the same rebound. The pile displacements resulting from this parametric study

[3]The distribution of mean effective stress after equalisation for other simulations is depicted in Fig. F.12 (p 229).

are depicted in Fig. 6.13. The maximum pile velocity ($v_{z,p,max}$) is also depicted in Table 6.3.

Table 6.3 Parametric study on the shape of the imposed velocity of the Disk Shearing Model.

Simulation No	v_0 *[m/s]*	ω_n *[rad/s]*	α *[rad/s]*	$v_{z,p,max}$ *[m/s]*
S36	—0·75	75	37·5	—0·41
S35	—1·5	150	75	—0·82
S30	—3	300	150	—1·64
S33	—6	600	300	—3·28
S34	—12	1200	600	—6·56

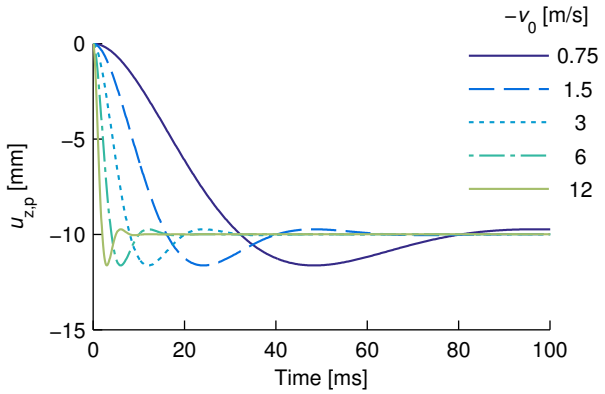

Figure 6.13 Pile displacements for the five v_0 values investigated.

The soil initial state is isotropically normally consolidated: $\sigma'_{v0} = \sigma'_{r0} = 500\,\text{kPa}$ and $e_0 = 1$. The radial discretisation is $\Delta r = 1\,\text{cm}$ and the critical time increment parameter (P_{time}) is equal to 50. The Disk Shearing Model simulation time is 150 ms for each blow, except for simulation No S36, where it is raised to 300 ms. Like earlier, 100 driving blows are given.

It should be noted that the hypoplastic constitutive model, described in Chapter 4, does not take into account any rate effects. However, the dynamic integration scheme of the Disk Shearing Model implies that soil inertia effects are taken into account, as is demonstrated hereunder.

Fig. 6.14 depicts the distribution of the radial effective stress ratio after 100 blows ($\sigma'_{ri}/\sigma'_{v0}$). The convex shape of σ'_{ri} is similar for all five boundary conditions with a minimum value located a few radii away from the pile wall. However, this minimum is lower as the maximum velocity $|v_0|$ gets higher. The pore pressure distribution, although not shown, has the same shape as the one depicted Section 6.1 for normally consolidated soils with a local minimum at the pile wall while the maximum lies a few radii away.

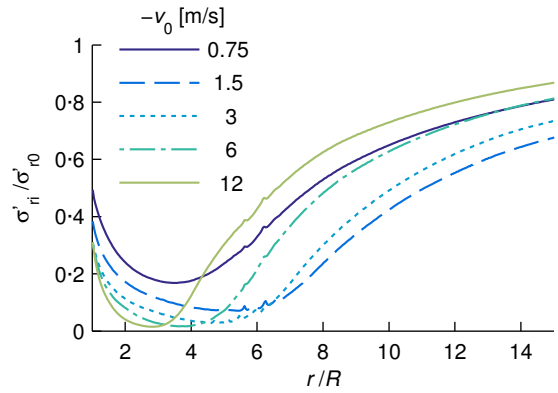

Figure 6.14 Distribution of radial effective stress after installation for the five v_0 values investigated.

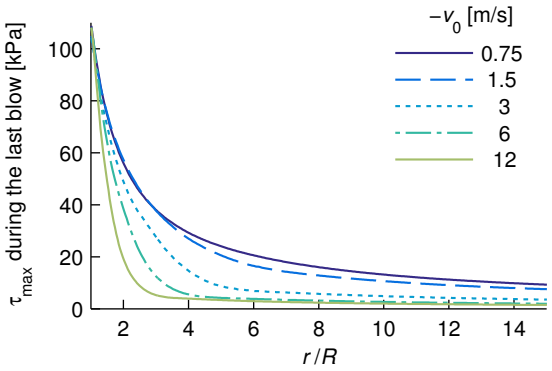

Figure 6.15 Distribution of the maximum shear stress during the 100th blow for the five v_0 values investigated.

Fig. 6.15 exposes the radial distribution of maximum shear stress during the last blow (τ_{max}). The shape of the τ_{max} distribution also is similar for the five cases investigated. Unlike the radial effective stress, τ_{max} decreases monotonically with radius because of geometric attenuation. The value of τ_{max} at the pile wall is constant for all the simulations because it is limited by the hypoplastic model, which is rate independent. However as v_0 increases, the soil is mobilised in a more localised area around the pile. This reflects the inertia effect simulated by the Disk Shearing Model: increasing v_0 makes the blow more sudden, which mobilises a smaller amount of soil. This confirms that the soil inertia, mobilised thanks to the high pile velocity, is essential to understand Soil Resistance to Driving (Holeyman, 1992).

The shear stress (τ) at pile wall may be limited by the critical state condition of the hypoplastic model but the shear strain (γ) is not. Fig. 6.16a depicts the maximum and final values of shear strain[4] at the pile wall versus $|v_0|$ and Fig. 6.16b displays the corresponding maximum shear strain rates ($\dot{\gamma}_{max} = D\gamma_{max}/Dt$).[5] The shear strain and shear strain rate at pile wall represents the displacement and velocity difference, respectively, between the pile and the soil.

Fig. 6.16a depicts a minimum, implying that there is a critical hammer velocity v_0 for which the slippage between pile and soil is minimum, *i.e.* for which the pile adheres the most to the pile. At either sides of this minimum value, the shear strain rises thanks to two mechanisms:

- For values of $|v_0|$ larger than $\sim 1{\cdot}5\,\mathrm{m/s}$, the shear strain rises, in accordance with the shear strain rate $\dot{\gamma}_{max}$ depicted in Fig. 6.16b. This result stems from the dynamic integration scheme of the Disk Shearing Model. In other words, it is the brutality of the blow that shears off the soil.

- For values of $|v_0|$ smaller than $\sim 1{\cdot}5\,\mathrm{m/s}$, the shear strain also rises, which is less intuitive. It cannot be associated with the rise in strength depicted in the literature survey as the velocity decreases (Fig. 2.6a, p. 24) which results in the transition between undrained and drained penetration because the presented simulation are always undrained. In fact, as velocity decreases, so does the difference between γ_{max} and γ_{end}, which eventually leaves the soil closer to critical state after each blow. In other words, it is the critical state based constitutive model that governs failure for low values of velocity.

Finally, it should be noted that the simulations performed in this section have all the same initial state and consequently, the same initial shear wave velocity (c_s). In fact, the soil response depends not only on the pile velocity ($v_{z,p}$) but on the ratio ($v_{z,p}/c_s$).

[4]The strain values are for the last blow only, not taking into account the accumulated strain.

[5]It should be noted that the strain rate depends on the radial discretisation chosen, as explained in Appendix E.2 (p. 214).

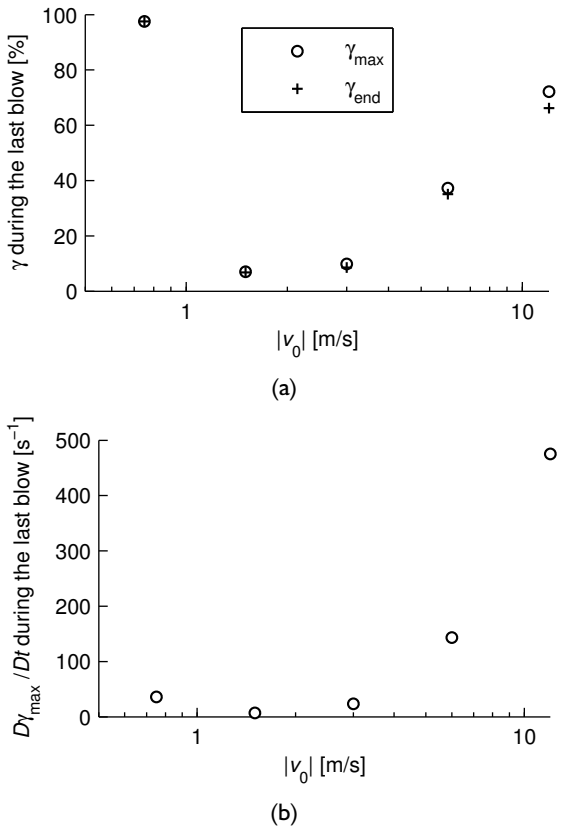

Figure 6.16 Values of (a) Shear strain and (b) Shear strain rate at pile wall during the last blow.

6.3 Sensitivity analysis

This section presents a sensitivity analysis aimed at apprehending the individual influence of each of the ten material parameter of the hypoplastic constitutive model (described in Chapter 4) and of some state parameters (e_0, p'_0, and K_0). The sensitivity analysis has been made by varying the aforementioned quantities and monitoring the simulation output in terms of effective radial stress (σ'_r) at the pile wall.

The sensitivity is measured thanks to the the one-percent scaled sensitivity (dss), defined for each of the 13 parameters studied, as (Hill, 1998):

$$\mathrm{dss}_j = \frac{\partial \sigma'_r}{\partial b_j} \frac{b_j}{100}, \qquad \text{(in percent of } \sigma'_r\text{)}, \tag{6.2}$$

where b_j is the j–th parameter studied ($j = 1 \ldots 13$).

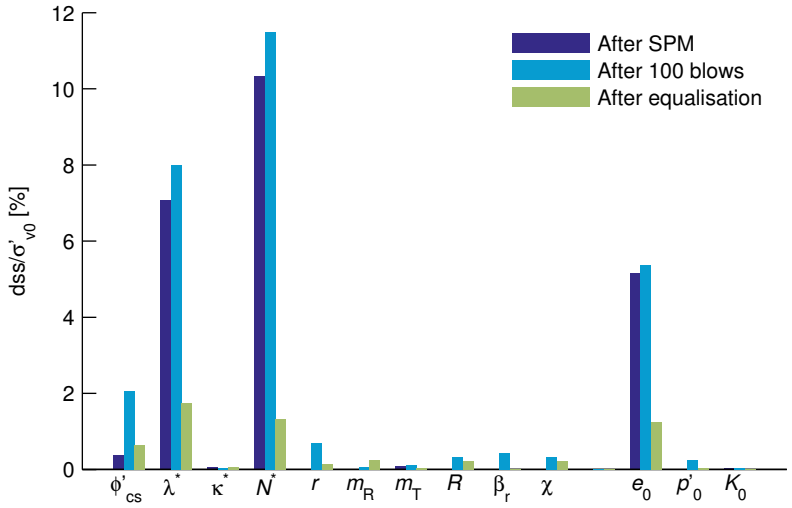

Figure 6.17 One-percent scaled sensitivity normalised to the vertical effective stress after Strain Path Method, 100 blows of Disk Shearing Model, and equalisation.

The one-percent scaled sensitivity is approximately equal to the amount that σ'_r would change if the parameter value were increased by one percent.

The initial reference state is isotropic with an initial mean effective stress (p'_0) of 167 kPa, an initial void ratio (e_0) of 1 (therefore an initial overconsolidation ratio, OCR*, of 3). As in the previous sections, the Strain Path Method is first applied to a layer of clay, followed by a series of 100 driving blows with the Disk Shearing Model, and finally, equalisation is modelled as a coupled consolidation analysis. The hypoplastic model parameters are those of London clay (Table 4.2, p. 71). Each parameters has been varied 2·5% above and below its default value. By choosing this variation, each simulation starts from the dry side of critical. For the sensitivity of K_0, the value of K_0 has been varied while keeping p'_0 constant (therefore, by varying σ'_{v0} at the same time).

The one-percent scaled sensitivity normalised to the initial vertical effective stress ($\mathrm{dss}/\sigma'_{v0}$) is shown in Fig. 6.17 at three stages of the pile driving model simulation: after Strain Path Method, after 100 blows of the Disk Shearing Model, and after equalisation.

The 10 material parameters of the hypoplastic constitutive model have uneven influences over the response, and so do the 3 state variables investigated. The most influential parameters, regardless of the stage of simulation, are λ^* and N^* (which control the normal compression line) and e_0, the initial void ratio. The reason for this can be found by looking at the hypoplastic overconsolidation ratio, defined as:

$$\mathrm{OCR}^* = p'_e / p'_0. \qquad (4.4\text{bis}) \ (6.3)$$

Hvorslev's equivalent pressure on the isotropic normal compression line (p'_e)

can be explicitly defined so that Eq. (6.3) becomes:

$$\mathrm{OCR}^* = \frac{1}{p'_0}\left(\frac{N^*}{1+e_0}\right)^{1/\lambda^*}. \tag{6.4}$$

The most influential terms of Eq. (6.4) are N^* and e_0 as they are affected by the exponent $1/\lambda^*$ (which is at least 7, Mašín, 2012c), and the exponent $1/\lambda^*$ itself. By comparison, the initial mean stress (p'_0) has a much smaller influence on OCR^*. This is reflected in Fig. 6.17. Therefore, the initial overconsolidation ratio is very important for the simulation output.

The critical state friction angle (ϕ'_{cs}) is the third most influential material parameter because it controls the critical state stress, which is approached during each blow.

Other hypoplastic model parameters have only a mild influence on the output. Except m_{T}, the four other integranular strain parameters (m_{R}, R, β_{r}, and χ) have no influence for the Strain Path Method simulation, where only one cyclic loading happen. On the other hands, these parameters are important for the 100 blows (thus cycles) of the Disk Shearing Model.

Finally, the coefficient of earth at rest (K_0) has no influence on the output, as the constitutive model is isotropic.

6.4 Open-pile installation

An unplugged open-pile installation is performed hereunder and compared to the closed-ended results. The soil initial state is the normally compressed one used in Chapter 5 and Section 6.1: $\sigma'_{\mathrm{v0}} = 590\,\mathrm{kPa}$, $K_0 = 0{\cdot}615$, and $e_0 = 1$, with $\mathrm{OCR}^* = 1{\cdot}1$. The outer radii ($R$) for both piles is 25 cm. The the open-ended pile thickness (t) is 1·25 cm, leading to a thickness ratio (D/t) of 40 where D is the pile outer diameter.

The open-ended simulation is done with the same discretisation parameters as the closed-ended one. Only the soil flow velocity (U) is lowered to 1 mm/s to avoid high strain rate gradients near the pile shoulder, and the volume insertion (V) is chosen according to Eq. (5.9), p. 99 – instead of Eq. (5.7), p. 98, for the closed-ended Strain Path Method. After the open-ended Strain Path Method simulation, the Disk Shearing Model is applied to the outer soil only, while the soil contained inside is neglected. The simulation is therefore performed by assuming that penetration happens in an unplugged manner.

The results of this section are presented after 100 blows for the closed-ended installation, which sums up to a pile penetration ($u_{\mathrm{z,p}}$) of $4R$, while the open-ended results are presented after 31 blows, for $u_{\mathrm{z,p}}$ of $4R^*$, where R^* is the open-pile equivalent radius (Randolph, 2003):

$$R^* = \sqrt{R^2 - (R-t)^2} = 0{\cdot}31R.$$

Fig. 6.18 compares the soil vertical displacements (u_{r}) after the closed- and open-ended pile installation. As the vertical and horizontal axis are normalised with R^*,

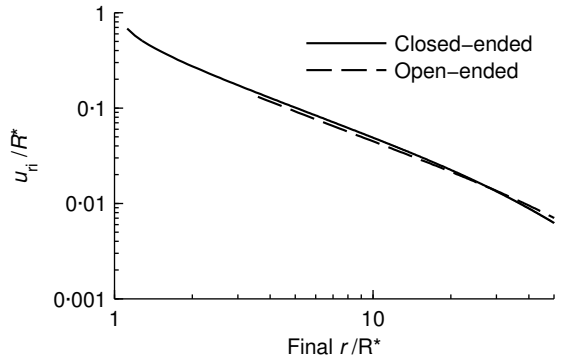

Figure 6.18 Comparison of radial displacement between a closed- and an open-pile installation.

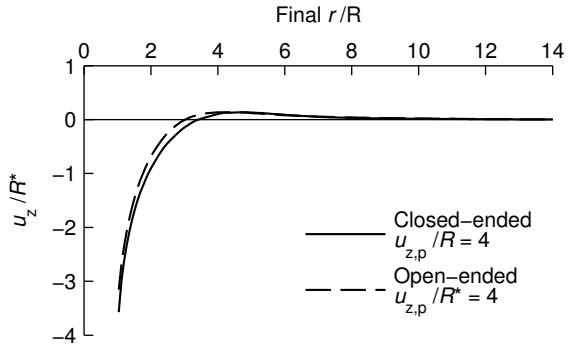

Figure 6.19 Comparison of vertical displacement between a closed- and an open-pile installation.

both curves coincide. However, the radial displacement is not surprisingly much smaller for the open-pile, with a maximum difference at the pile wall where the open-ended pile produces a displacement 20 times lower than the closed-ended one.

The vertical displacement (u_z) results predominantly from the Disk Shearing Method blows. Therefore, u_z is comparable for both simulations after the same number of blows, or when normalising u_z with R^*, as it is done in Fig. 6.19. It should be noted that the horizontal axis is normalised with R, for the same reason.

The excess pore pressure ratio ($\Delta u_w/\sigma'_{v0}$) is depicted before and after the blows of the Disk Shearing Model in Figs. 6.20a and b, respectively. Again, before the Disk Shearing Model blows (Figs. 6.20a), the excess pore pressure distribution is comparable when the horizontal axis is normalised with R^*. However, far behind the toe (Figs. 6.20b), the succession of driving blows gradually erases the soil memory, as pore pressure distribution becomes comparable when the horizontal axis is normalised to R. This is reflected in Fig. 6.21, which depicts the radial

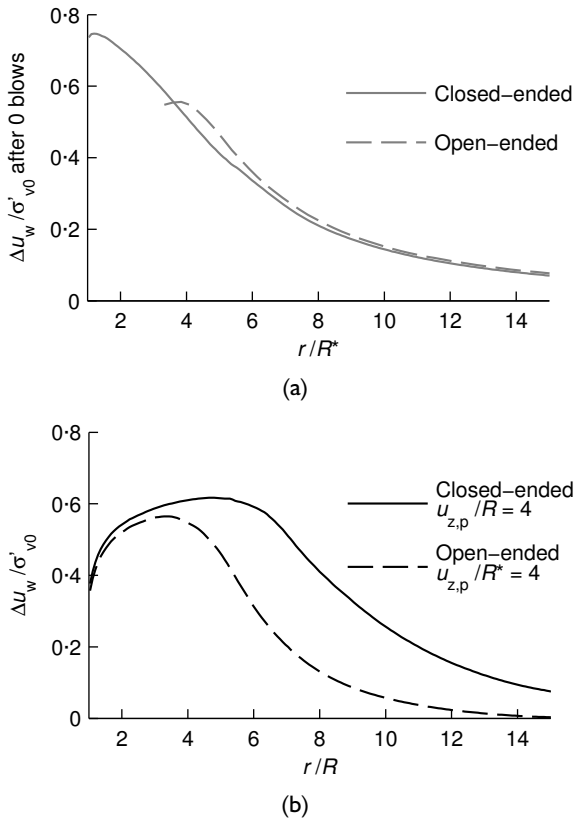

Figure 6.20 Distribution of pore pressure (a) after the Strain Path Method and (b) at the end of installation (after 100 and 31 blows, for an closed- and an open-pile installation respectively, of the Disk Shearing Model).

effective stress distribution: the soil close to the pile ($r < 3R$) has been so intensely sheared that both distributions coincide.

During equalisation, the radial effective stresses at the pile wall are depicted in Fig. 6.22 for both piles. Both curves have the same time scale, *i.e.* the dimensionless time (T_4^*) is normalised with the outer radius (R), which allows both curve to follow the same short term decrease.[6] Following the short term decrease, radial effective stress increases. The equalised radial effective stress (after 95% consolidation) is reached approximately 4 time more quickly for the open-ended pile than for the closed-ended one.

The distribution of radial effective stress at the end of equalisation is depicted in Fig. 6.23. Likewise after installation, stresses close to the pile wall (for $r < 3R$)

[6]If the time were normalised with the equivalent radius (R^*), neither the short term decrease nor the long term increase in σ'_r would be comparable.

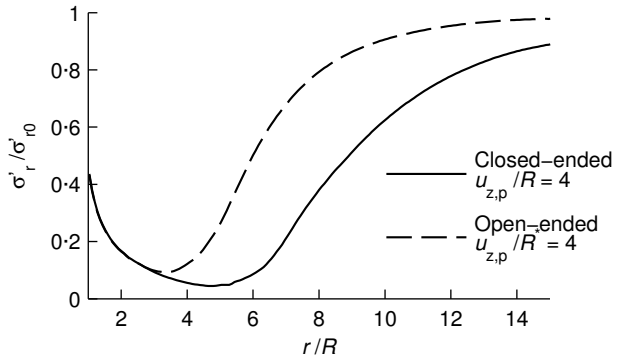

Figure 6.21 Distribution of radial effective stress after a closed- and an open-pile installation.

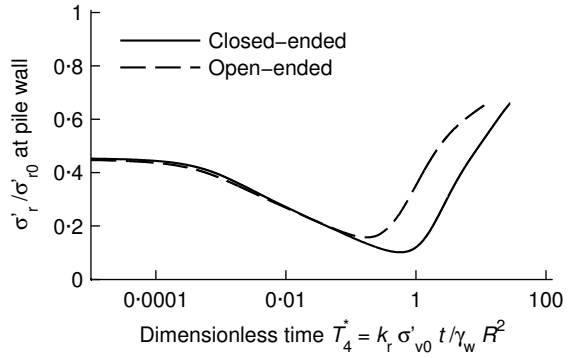

Figure 6.22 Radial effective stress at pile wall during equalisation for a closed- and open-ended pile.

coincide. For $r > 3R$, radial effective stress for the open-ended simulation is approximately 15% higher than for the closed-ended one (when the radial position is normalised to the outer pile radius R).

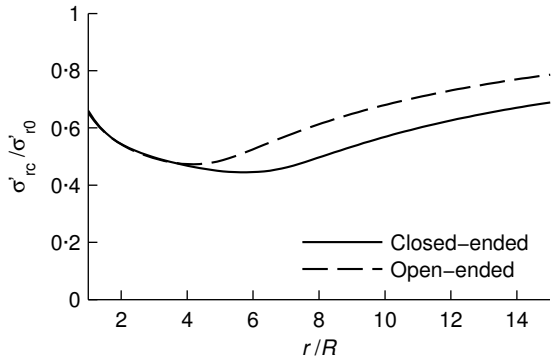

Figure 6.23 Distribution of effective radial stress ratio after consolidation for a closed- and open-ended pile.

6.5 Conclusion

This chapter presents results of the pile driving model, introduced in Chapter 5, which studies a plane strain disk of soil surrounding a driven pile. The simulation of installation is performed in two steps: the Strain Path Method is applied, followed by a series of driving blows imposed by the Disk Shearing Model. Emphasis is placed on the results of the Disk Shearing Model, *i.e.* the effect of the cycles of shaft-soil shearing during driving. The equalisation stage is modelled as a coupled consolidation analysis. The four sections composing this chapter each investigate a particular aspect of the model. These sections and their conclusion are summarized hereunder.

Section 6.1 compares the simulation results of four initial overconsolidation ratio to the literature review conducted in Chapter 2. The main results are the following. The h/R effect due to the cycles of shaft-soil shearing (fatigue) is predicted for pore pressure and total radial stress. However, no cyclic degradation is modelled for the shear stress at pile wall because the constitutive model follows the critical state theory. During each blow, excess pore pressure decreases whereas total radial stress only mildly varies. After installation, the radial distribution of excess pore pressure distribution is concave, with a maximum a few radii away from the pile shaft. The excess pore pressure at the pile wall is positive for lightly overconsolidated soils but negative for heavily consolidated soils. The effective stress is in the range of values measured, but excess pore water pressure is underestimated. Therefore, the total radial stress is also underestimated, but follows the correct trend of increasing linearly with overconsolidation ratio in a log:log plot. During equalisation, the pore pressure at pile wall goes through a short term increase followed by an inexorable decrease. This leads to a short term minimum in radial effective stress. The value of this maximum in pore pressure at pile wall seems to be underestimated – by comparison the the experiments – but it follows the experimentally observed trend of increasing with OCR up to OCR $= 10$, after which it *decreases* with OCR. Set-up values ($\sigma'_{\mathrm{rc}}/\sigma'_{\mathrm{ri}}$) match the experimental data although σ'_{rc} is underestimated.

Section 6.2 studies the influence of varying the initial velocity of the hammer blow (v_0), while maintaining a set of 10 mm per blow. As the hammer velocity increases, the soil is mobilised in a closer region around the shaft. Nevertheless, there is a critical hammer velocity for which there is maximum adherence between pile and soil. The distribution of radial effective stress and excess pore pressure are only mildly affected by v_0, which would make set-up equivalent whatever the hammer velocity.

Section 6.3 presents a sensitivity analysis of all ten hypoplastic material parameters (ϕ'_{cs}, λ^*, κ^*, N^*, r, m_{R}, m_{T}, R, β_{r}, and χ), the initial void ratio (e_0), the initial mean stress (p'_0), and the coefficient of earth at rest (K_0). Parameters N^*, λ^*, and state variable e_0 are the most influential quantities because they control the overconsolidation ratio. Intergranular strain parameters (r, m_{T}, R, β_{r}, and χ) are important for the Disk Shearing Model simulation, which imposes many strain reversals. Finally, K_0 has no influence on the output because the hypoplastic constitutive model is isotropic.

Section 6.4 compares a closed-ended and an open-ended pile installation with a thickness ratio (D/t) of 40. The radial displacement due to the open-ended pile is 20 times smaller than the one from the closed-ended pile, but vertical displacement is comparable as it results mainly from the driving blows. Pore pressures around the pile are generally smaller for the open-ended installation. After a series of driving blows, the soil close to the pile has been so intensely sheared that it is in a similar state for both closed- and open-ended pile installation. After equalisation, the radial effective stress at pile wall is similar in magnitude for both piles, but full set-up is attained 4 times more quickly for the open-ended pile.

Chapter 7

Application to a case study

This chapter presents a comparison between an *in situ* pile installation and the simulation output of the pile driving model described in Chapter 5. The simulation is performed for a soil horizon located at a depth of 3 m, a choice which is justified hereunder (in Section 7.2).

Already introduced in Chapter 2, the Bothkennar field test (Lehane, 1992; Lehane and Jardine, 1994a) was selected for two reasons. Firstly, the measurements were made by Barry Lehane with the Imperial College Pile (ICP), a model pile which had been extensively used prior to the test and which had proven to be reliable and accurate. The second reason is that the Bothkennar clay material parameters have been calibrated by Mašín (2007) for the hypoplastic constitutive model.

This chapter is divided in the following manner: Section 7.1 presents the Bothkennar site conditions and describes the ICP test procedure. Section 7.2 presents the soil initial state and the constitutive model parameters. The simulation results are described in Sections 7.3 and 7.4 for the installation and equalisation, respectively.

7.1 Site conditions and test procedure

The site conditions and ICP test procedure are described in Lehane (1992) and Lehane and Jardine (1994a) and summarized hereunder.

Soil description The ground conditions at Bothkennar comprise a 1 m thick weathered firm crust overlying the lightly overconsolidated Bothkennar marine clay down to a depth of 15 m. The water table depth varies between 0·5 m and 1 m. Within the depths penetrated by the instrumented piles (1–6 m), plasticity indices (PI) increase from $\sim$ 25% at 1·5 m to $\sim$ 50% between 4 and 6 m. The average water content (w_0) increases from 0·4 at 1 m to 0·7 at 6 m and the unit weights reduce correspondingly. Organic fraction is 2–3% of the dry weight. The soil has a typical vane sensitivity of 5.

The profile obtained in piezocone tests is shown in Fig. 7.1a. Below 2 m, cone penetration resistance (q_c) and pore pressure (u_2) increase in a way similar to the shear strength (s_{u0}) depicted in Fig. 7.1b. The peak shear strength values vary with

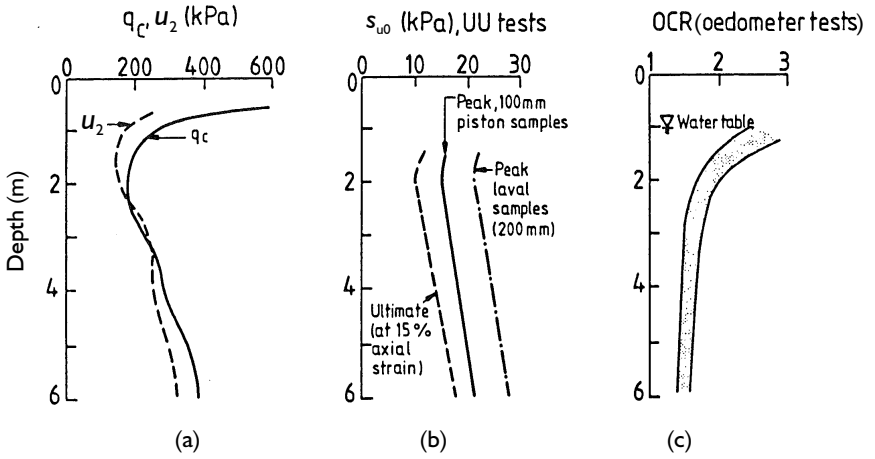

Figure 7.1 Bothkennar geotechnical profile (after Lehane and Jardine, 1994a).

the sample size, a trend typical of lightly overconsolidated clays. The ultimate s_{u0} is 5–10 kPa lower than the peak value and corresponds to the remoulded vane strength. The conventional overconsolidation ratio ($OCR = \sigma'_{vy}/\sigma'_{v0}$) reduces from 1·9 at 2 m to 1·5 at 6 m (Fig. 7.1c). The coefficient of earth at rest (K_0), estimated from self-boring pressuremeter tests, reduces from 0·65 at 2 m to 0·5 at 6 m.

Imperial College Pile Already briefly introduced in Section 2.1.1, the ICP is a 7 m long and 50·8 mm (2") radius cone-ended steel instrumented tubular pile. One ICP is depicted in Fig. 7.2 for three penetration depths (this is explained later). The ICP has three clusters of instruments that each comprise at least one surface stress transducer and one pore pressure unit. The sensors position (h) is defined relative to pile toe: the pore pressure units are located at $h/R = 5$, 30, and 53 and the surface stress transducers are a few radii above or below the pore pressure units.

Four ICP were jacked through 200 mm pushes at a typical rate of 8·3 mm/s from the base of a 1 m deep cased borehole to final depths of either 3·2 or 6 m – only the latter penetration depths will be presented below. The pushes were interspersed by pauses lasting between 3 and 6 min which allowed the jack to be retracted. The four installations are named BK1 to BK4.

7.2 Constitutive model parameters and initial state

The simulation, using the pile driving model described in Chapter 5, is performed at a depth of 3 m, represented in Fig. 7.2. This depth was chosen for four reasons:

(i) It is located 60 radii below the ground surface so that surface effects can be neglected and a plane strain state can be assumed;

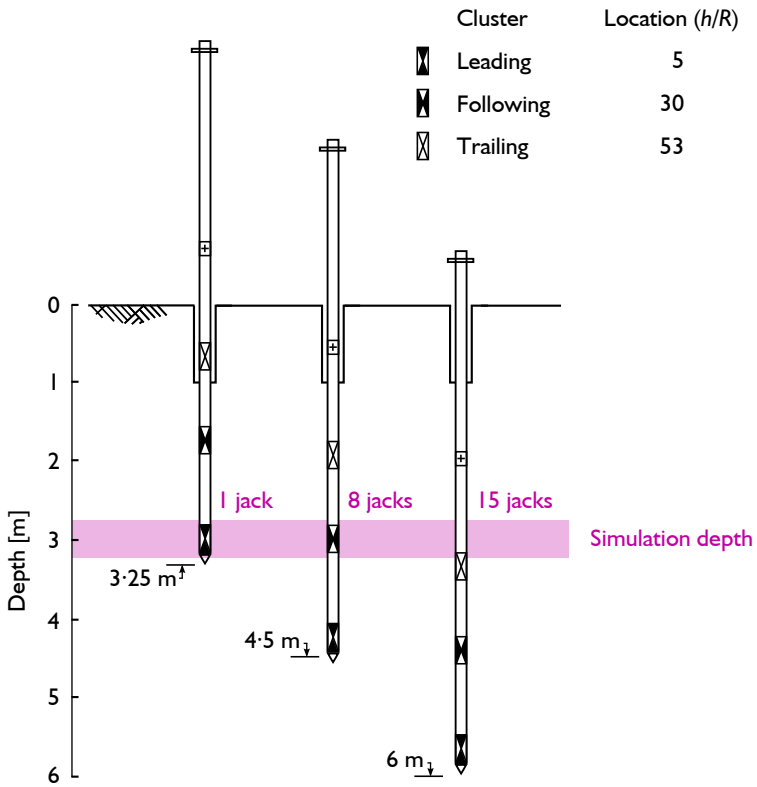

Figure 7.2 Schematic representation of the Imperial College Pile (ICP) at 3·25, 4·5 and 6 m embedment; embedment at which the measurements are compared to the simulation.

(ii) Bothkennar clay is relatively homogeneous below 3 m;

(iii) Once the ICP has reached its final embedment of 6 m, the soil horizon located at 3 m has been traversed by all three ICP clusters of sensors, which gives three comparison points during the pile installation simulation;

(iv) Once the ICP has reached its final embedment of 6 m, the trailing cluster of sensor ($h/R \sim 53$) is $\sim 3{\cdot}3$ m deep, which gives a comparison point for the equalisation modelling.

Referring to Fig. 7.2, when the ICP toe is at a depth of 3·25 m, the soil horizon has been through approximately one jack push. Similarly, for embedments of 4·5 and 6 m, the soil horizon has encountered 8 and 15 jack strokes, respectively.

Material parameters As Bothkennar clay presents a vane sensitivity of 5, the reconstituted and intact states of structure have different material parameters (especially parameter N^*, controlling the position of the normal compression line, see Fig. 4.1a, p. 67). The soil close to the pile is expected to be in a state of structure closer to the reconstituted state of structure than to the intact one, so the material parameters are calibrated for reconstituted Bothkennar clay.

The five material parameters of the Mašín (2005) hypoplastic model have been calibrated by Mašín (2007) for reconstituted Bothkennar clay using data from Smith et al. (1992). The five intergranular strain material parameters are calibrated following the simplified Mašín (2012c) procedure, where R and χ are taken as material independent parameters. Parameters m_R and β_r have been calibrated against undrained triaxial tests performed by Smith et al. (1992), depicted in Figs. 7.3 and 7.4. Parameter m_T is taken as half of m_R (Mašín, 2012c).

The 10 parameters of reconstituted Bothkennar clay for the Mašín (2005) hypoplastic model with intergranular strain are reproduced in Table 7.1.

Table 7.1 Bothkennar clay parameters (Mašín, 2007).

Clay hypoplasticity					*Intergranular strain*				
ϕ'_{cs} [°]	λ^*	κ^*	N^*	r	m_R	m_T	R	β_r	χ
35	0·119	0·003	3·83	0·07	4	2	10^{-4}	0·25	1

NOTE: Parameter N^* is used instead of $N = \ln N^*$ defined in Mašín (2005).

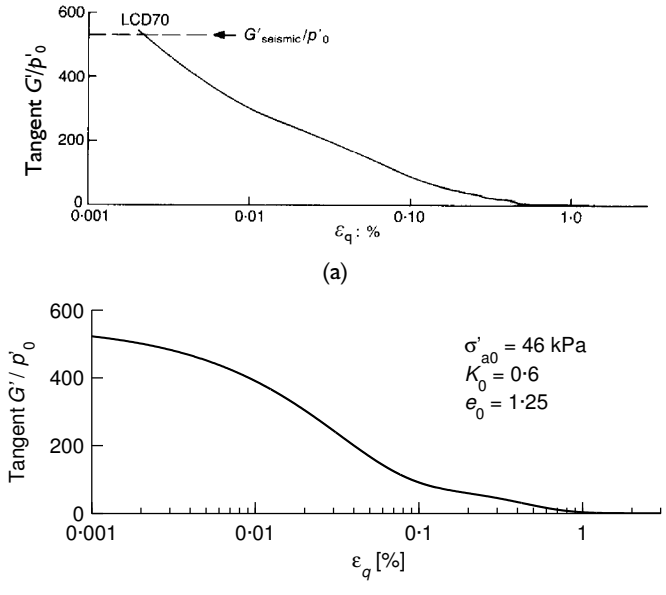

Figure 7.3 Small strain shear modulus in a K_0-consolidated drained triaxial test, (a) experiment (Smith et al., 1992) and (b) simulation.

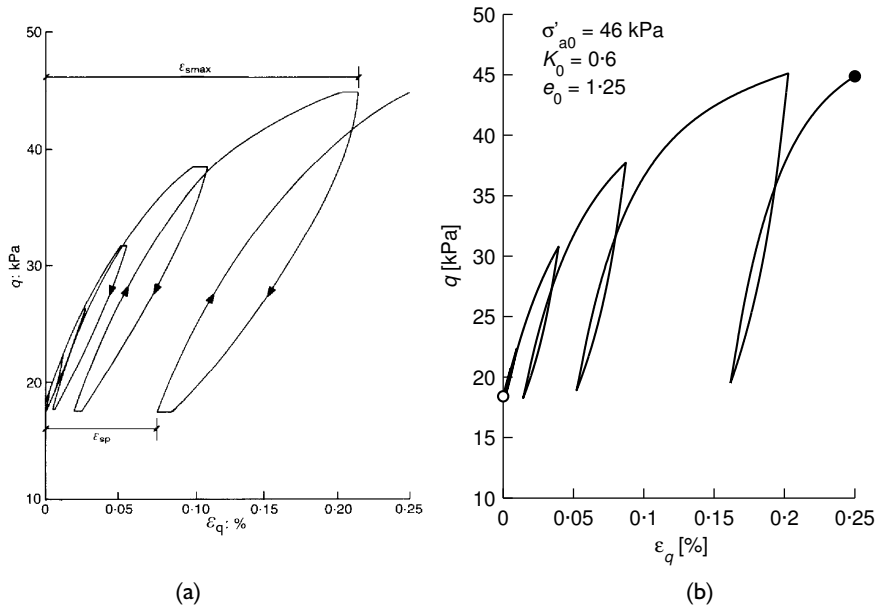

Figure 7.4 Cyclic K_0-consolidated undrained triaxial test, (a) experiment (Smith et al., 1992) and (b) simulation.

Initial state The chosen initial state corresponding to the 3 m deep soil horizon is described by stress (σ'_{v0}, u_{w0}, and K_0) and void ratio (e_0). These are described hereunder:

(i) The vertical effective stress (σ'_{v0}), computed by Lehane and Jardine (1994a), is 30 kPa. The pore pressure at rest (u_{w0}) is estimated from the ICP dissipation tests at 28 kPa;

(ii) The coefficient of earth at rest (K_0) has been estimated from oedometer and self-boring pressuremeter tests at 0·6;

(iii) Finally, the initial void ratio (e_0) has to be selected carefully as it has to correspond to the initial water content (w_0) (see Eq. 4.7, p. 85) and, most importantly, it dictates the initial overconsolidation ratio (OCR*) and shear strength (s_{u0}) (see Eqs. 6.4 and 4.16, pp. 138 and 88, respectively). Here, a value of $e_0 = 1{\cdot}5$ is selected, which corresponds to OCR$^* = 1{\cdot}65$ and a shear strength $s_{u0} = 11$ kPa. The shear strength is comparable to the measured (ultimate or vane) shear strength measured on site (Fig. 7.1b).

A simple shear test output is depicted in Fig. 7.5 versus the experimental data for two intact samples of Bothkennar clay from a depth of ~ 3 m.

Using Eq. (4.7) (p. 85), the chosen initial void ratio corresponds to a specific gravity (G_s) of 2·75.

7.3 Installation

Using the pile driving model described in Chapter 5, the ICP installation is simulated for the 3 m deep soil horizon depicted in Fig. 7.2. First, the Strain Path Method simulation is performed. Following, 15 jack strokes are imposed by the Disk Shearing Model. After these two steps, the installation is completed, the pile sits at its final embedment of 6 m (Fig. 7.2).

As explained in Section 7.1, the ICPs were installed through pushes lasting 24 s at a rate of 8·3 mm/s. For the Strain Path Method, the speed of installation has no influence because the constitutive model is rate independent. For the Disk Shearing Model, the same velocity (8·3 mm/s) is selected for each push. However, after $\sim 0{\cdot}2$ s of constant velocity penetration, the soil reaches a steady state during which stresses remain constant throughout the downward movement. Therefore, the length of the imposed jack can be reduced – so does the computation time – and still produce the same output. The pile displacement resulting from the imposed velocity is depicted in Fig. 7.6 for one simulated jack, which lasts 0·5 s.

The second difference with the field installation is that the 15 simulated jacks are performed in a fully undrained mode. During the *in situ* installation, the 3 to 6 min lasting pause periods between the jacks allowed partial consolidation, during which pore pressure rose by 20–45 kPa for the soil horizon of concern. Therefore, the predicted pore pressures are compared to the 'moving' values instead of the 'stationary' ones (Lehane and Jardine, 1994a).

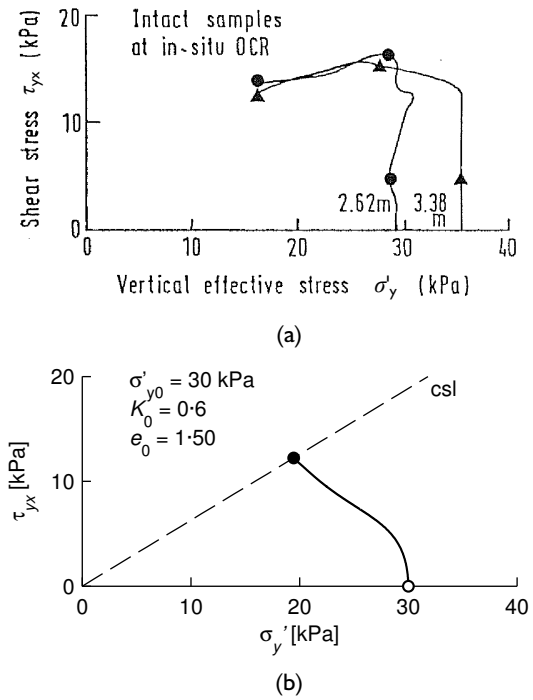

Figure 7.5 Simple shear at *in situ* state; (a) experiment (Lehane, 1992) and (b) simulation.

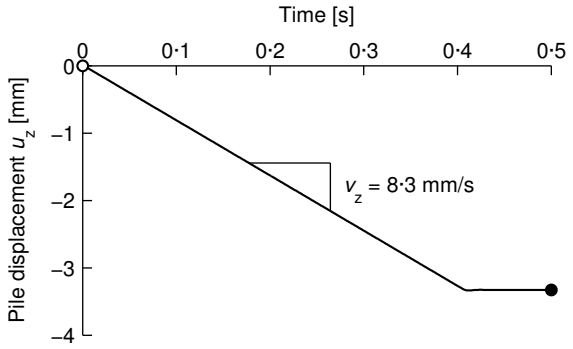

Figure 7.6 Imposed pile displacement during one jacking stage.

The installation simulation output of the Disk Shearing Method is presented in Fig. 7.7 in terms of total stress (σ_r) and excess pore pressure (Δu_w) at pile wall versus jack count. Alongside the simulation output are depicted the measured ranges of σ_r and Δu_w during ICP installations BK1 to BK3.

As explained in Chapter 5, the numerical model splits the pile installation process by first applying the Strain Path Method followed by the Disk Shearing Model. This separation means that the Disk Shearing Model output does not fully account for the h/R effect for values of h/R smaller than 20 (for a closed-ended pile). In other words, the Disk Shearing Model has to 'catch up' with the position at which the Strain Path Method simulation was ended. For the present case study, $h/R = 20$ occurs after the fifth jack stroke. Therefore, the simulation output depicted in Fig. 7.7 can be compared to the measurements after the 5th jack stroke.

After the 5th jack stroke, the simulation slightly underestimates the total radial stress but lies in the range of measured excess pore pressure. Therefore, radial effective stress is also slightly underestimated by the simulation, during installation.

Before the 5th jack stroke, the cycles of shaft-soil shearing of the Disk Shearing Method output shows negligible h/R effect (contrary to what happened during driving, as presented in Section 6.1, p. 119, for which the first cycles of shaft-soil shearing had a drastic effect on the stress state around the pile). Therefore, most of the h/R effect for the jacked piles in Bothkennar comes from the stress relief away from the pile toe and not from fatigue.

Finally, it should be noted that Δu_w measured during the cone penetration test (at the cone shoulder, located at $h = R$ behind the toe) was in excess of 200 kPa (Fig. 7.1a). By comparison, Δu_w predicted by the Strain Path Method, at the same location, is 140 kPa. This is supplementary evidence that the excess pore pressure is underestimated by the Strain Path Method using the hypoplastic constitutive model.

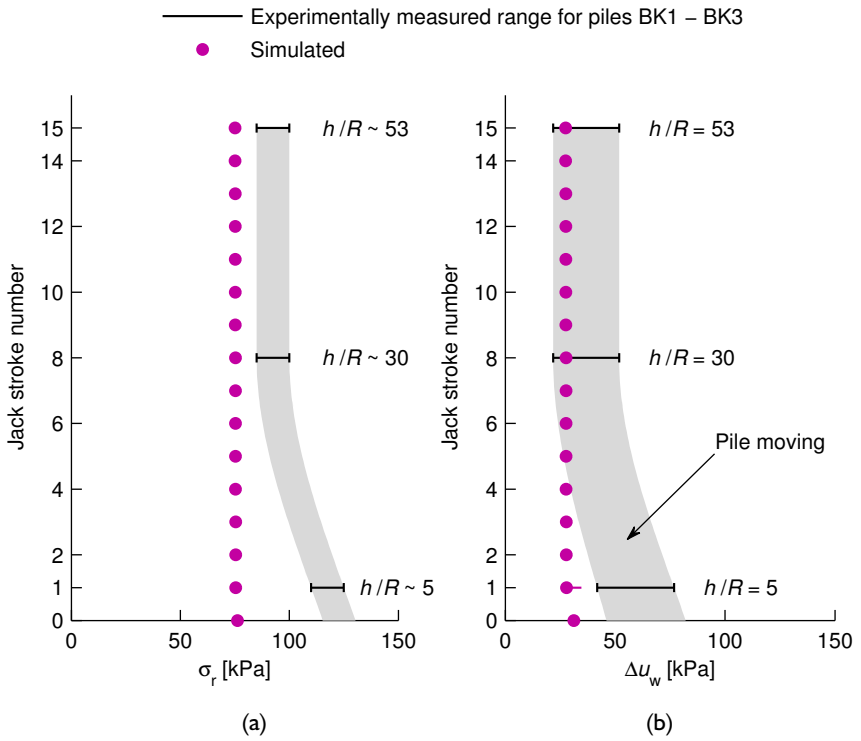

Figure 7.7 Values at pile wall of (a) radial total stress and (b) excess pore pressure during jacking.

7.4 Equalisation

Starting from the previous state, the equalisation stage is modelled as a coupled consolidation analysis, described in Chapter 5. The radial permeability (k_r) is taken as 10^{-9} m/s, which is in good agreement with permeability range of 0·5–$1{\cdot}5 \times 10^{-9}$ m/s deduced from self-boring permeameter and pushed piezometer tests performed on site (Lehane, 1992).

The simulation output is compared to the measured data in Figs. 7.8 to 7.10. The dashed lines represent average measured values and the greyed areas, plotted when available, correspond to the range measured.

Fig. 7.8a shows that the short term rise in simulated excess pore pressure (Δu_w) is underestimated. This suggests that the pore pressure peak, located a few radii away from the pile shaft, is underestimated by the model. From 50 min onwards, both simulated and measured Δu_w begin their inexorable decrease.

Fig. 7.8b depicts the excess pore pressure normalised to the maximum value measured at the pile wall ($\Delta u_w/\Delta u_{w,max}$). The normalised ratios of Fig. 7.8b are very closely matched during the rise and during beginning of the the fall in pore pressure. Towards the end of dissipation, both curves tend to drift apart, which indicates that permeability may be underestimated by the simulation.

The simulation of the equalisation stage considers a constant permeability. Therefore, should void ratio increase (as during the short term rise in Δu_w) or decrease (as during the decrease in Δu_w), permeability remains constant. However, the discrepancy between measured and simulated pore pressure during the pore pressure drop would be even broader by taking a permeability varying with void ratio, because the permeability of the model would decrease. Hence, radial permeability ought to be selected with even greater care should the permeability be variable.

Fig. 7.9 depicts the change in radial effective stress (σ'_r) at the pile wall. Apart from the first seconds of consolidation for which the simulated drop in σ'_r is underestimated, the simulation closely matches the measurements. This underlines the capabilities of the model, σ'_r being the most important quantity as it governs shaft static capacity.

Finally, the radial distribution of excess pore pressure and stress is depicted in Fig. 7.10. Equalised values correspond to 95% consolidation. Fig. 7.10a shows the distribution of excess pore pressure at the end of installation (Δu_{wi}), which presents an apex located at approximately one radii from pile wall. This is much closer than what was obtained for the driven pile simulation where the apex was located between 3 and 6 radii from pile shaft (see Fig. 6.3b, p. 125).

Fig. 7.10b depicts the distribution of simulated radial effective stress after installation (σ'_{ri}) and after equalisation (σ'_{rc}). The radial effective stress after installation has a convex shape, similar to the results presented in Chapters 5 and 6 for a lightly overconsolidated soil: there is a minimum in σ'_{ri} a few radii away from the pile wall and σ'_{ri} is close to σ'_{r0} at the pile wall. The equalisation has had a positive effect on the radial effective stress as σ'_{rc} is higher than σ'_{r0} at the pile shaft. Furthermore, the 3 m deep soil horizon studied has encountered set-up, as σ'_{rc} is 1·57 times higher than σ'_{ri}.

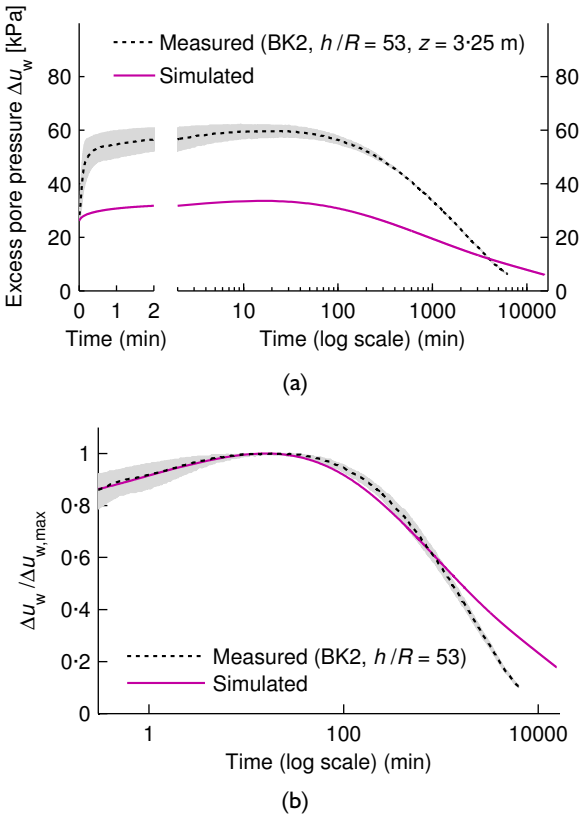

Figure 7.8 (a) Excess pore pressure and (b) Excess pore pressure ratio at pile wall during equalisation.

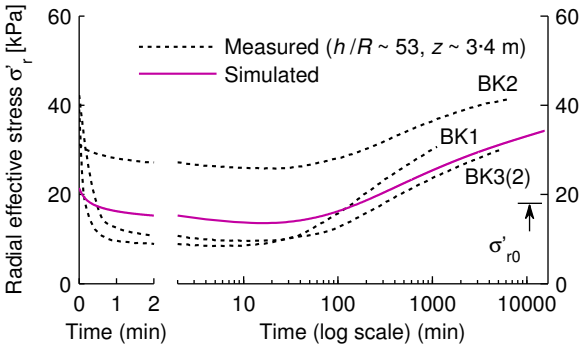

Figure 7.9 Radial effective stress at pile wall during equalisation.

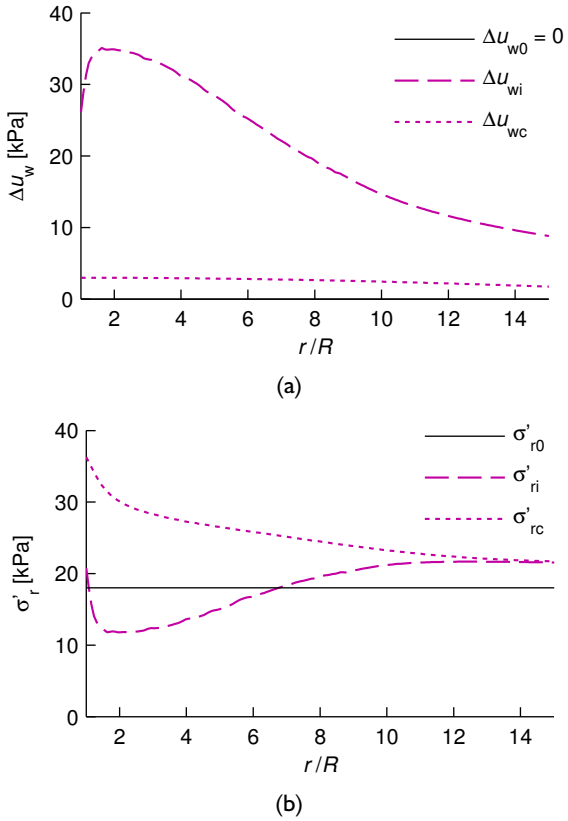

Figure 7.10 Distribution of (a) excess pore pressure and (b) radial effective stress; initial, end of installation, and post-equalisation values.

7.5 Conclusion

The simulation of a jacked pile in Bothkennar clay is compared to experimental measurements made by Lehane and Jardine (1994a) using the instrumented Imperial College Pile (ICP). The simulation is performed for a soil horizon located at a depth of 3 m.

Bothkennar clay is a lightly overconsolidated plastic marine clay. The five hypoplastic constitutive parameters have been calibrated by Mašín (2007) for reconstituted Bothkennar clay, while the five constitutive parameters for intergranular strain are calibrated here above. The initial state of the 3 m deep soil horizon is then carefully chosen so that it reflects the *in situ* stress (σ'_{v0} and K_0), void ratio (e_0), strength (s_{u0}), and overconsolidation ratio (OCR*).

Fifteen jack strokes are simulated and the output is compared with experimental data collected at various locations along the shaft of the ICP. The simulation is made in an undrained mode until the last jack stroke, after which the coupled consolidation analysis is performed.

During installation, total radial stress at pile wall is slightly underestimated, but the pore pressure at pile wall falls within the measured data. The numerical model, being split into the Strain Path Method for the insertion of the pile toe, and the Disk Shearing Method for the cycles of shaft-soil shearing, allows to quantify the importance of the two factors explaining the h/R effect, described in Fig. 2.16, p. 39, namely: stress relief away from the pile toe and fatigue due to the cycles of shaft-soil shearing. The model reveals that the h/R effect for the *jacked* ICP stems mainly from stress relief away from the pile toe, whereas the cycles of shaft-soil shearing only mildly affect the soil. This contrasts with the driven pile installation simulations performed in Chapter 6.

During equalisation, the simulation shows the same trends as the ICP measurements: the pore pressure at pile wall displays a short term rise until approximately 50 min after the end of installation, which is followed by an inexorable decrease towards its hydrostatic value. The radial effective stress at pile wall follows the inverse trend, with a minimum value at 50 min, followed by an increase. The radial total stress decreases steadily during consolidation. The pore pressure at the pile wall is underestimated by the model. A possible explanation for these disparities is the underestimation of excess pore pressure at pile toe by the Strain Path Method, which affects all the subsequent simulations. However, the radial effective stress, which governs pile shaft capacity, is a close match to the measurements during equalisation.

Chapter 8

Conclusion

This final chapter is divided in three parts. Section 8.1 provides a summary of the contents of this thesis, Section 8.2 summarises the main conclusions of this work, and Section 8.3 offers perspectives for future research.

8.1 Contents

Chapter 1 lays the context of this research: offshore open-ended driven piles in clay which are typically installed to support oil/gas platforms or windmills. At the end of driving, pile capacity is seen to evolve with time. A process named set-up (if pile capacity increases). In clayey soils, this change in pile capacity is mainly related to the dissipation of the excess pore pressure which has developed during driving. As offshore piles are open-ended, most of the pile capacity stems from shaft resistance. Therefore, my work focuses on the radial effective stress at the pile wall, which is directly related to the shaft capacity of a driven pile in clay.

Chapter 2 compiles and compares field data from reliable instrumented pile installation experiments. Although these onshore field tests involve almost exclusively jacked closed-ended piles, they do share valuable similarities to the offshore piles. The measured quantities on the pile are: total stress, pore pressure, and shear stress, and in the soil: pore pressure and displacement. The conclusion of Chapter 2 outlines recurrent trends of displacement pile installations in clays.

Chapter 3 presents a literature review of previous attempts at numerically modelling the installation and subsequent equalisation of displacement piles in clay. The final section of Chapter 3 (Section 3.3, p. 62) sums up the observations of Chapter 2 and the simulations of Chapter 3 to lay down the required components for a numerical model to be innovative and useful. Chapters 4 and 5 present this model.

Chapter 4 presents the constitutive law used to model the effective stress behaviour of the soil: hypoplasticity for clays coupled to the intergranular strain concept.

Chapter 5 introduces the pile driving model developed in this thesis, which hinges on the assumption that soil around a driven pile can be considered in a plane

strain state, as long as it is not too close to the pile toe nor to the soil surface. The model focuses on the soil state of a *disk of plane strain soil* around a driven pile during driving and subsequent equalisation. The main asset of the model is to take into account the cycles of shaft-soil shearing. The output of the model is the soil state (most importantly, the radial effective stress at pile wall, governing shaft capacity) during and after installation. The model imposes pile displacement to investigate the effect on the state of the soil around the pile. The simulation of the installation stage is split in two steps:

(i) The first step accounts for the insertion of the pile toe: the quasi-static Strain Path Method (Baligh, 1985) is applied to the disk of soil of concern;

(ii) The second step accounts for shaft-soil shearing cycles: starting from the state predicted by Step (i), a series of driving blows is applied to the plane strain disk of soil using the 'Disk Shearing Model' developed in this thesis.

Following the simulation of installation, a coupled consolidation analysis is performed allowing only radial drainage.

Chapter 6 presents the pile driving model results and is divided in four sections. Section 6.1 compares the pile driving model results to the trends reported in the literature review of experimental pile installations of Chapter 2. Section 6.2 presents a parametric study in which the influence of the hammer initial velocity is studied. Section 6.3 exposes a sensitivity analysis on the constitutive model parameters as well as on the initial void ratio, vertical effective stress, and coefficient of earth pressure at rest. Finally, Section 6.4 presents an open-ended pile installation.

Lastly, Chapter 7 compares the pile driving model output to a jacked pile installation in Bothkennar clay.

8.2 Main conclusions

The model results and conclusions are summarised below. Unless stated otherwise, the conclusions are for closed-ended piles.

Installation

The pile driving model captures some essential features of displacement pile installation in clays, which confirm or explain measured trends of Chapter 2:

- As the pile toe goes through a soil layer, the Strain Path Method predicts high radial and vertical gradients of displacement with reversals of strain. This results in a rise in total radial stress (σ_r) and in excess pore water pressure (Δu_w).
- As the pile penetrates further into the ground, stresses decrease for a given soil horizon. This is called the h/R effect and is successfully modelled thanks to (1) the stress relief away from pile toe predicted by the Strain Path Method and (2) the cycles imposed by the Disk Shearing Model as blow-count builds up.

The h/R effect is predicted for radial total stress (σ_r) and excess pore pressure (Δu_w) whatever the initial overconsolidation ratio (OCR). However, the shear stress and radial effective stress do not display particular h/R patterns, contrary to experiments, because the soil tends to critical state during every blow.

Radial total stress and pore pressure at pile wall normalised to the vertical effective stress (σ'_{v0}) degrade more steeply with the number of blows as the overconsolidation ratio increases.

- During pile movement, Δu_w at the pile wall decreases whatever the initial OCR, while σ_r decreases only slightly.

- At the end of installation, the radial distribution of excess pore pressure presents a convex shape, similar to the one depicted in Fig. 8.1.

  The pore pressure ratio ($\Delta u_w/\sigma'_{v0}$) at the pile wall is lower for increasing OCR, whereas the peak $\Delta u_w/\sigma'_{v0}$, located a few radii away from the pile wall, increases with OCR. Although this is comparable to experimental data, the value of $\Delta u_w/\sigma'_{v0}$ is underestimated by the model.

- At the end of installation and at the pile wall, the radial total stress (σ_{ri}) follows a linear trend with OCR in a loglog plot, but is underestimated compared to the experimental values (because Δu_w is underestimated).

  The radial effective stress at the end of installation (σ'_{ri}) governs the shaft capacity and is higher than the initial radial stress (σ'_{r0}) for overconsolidated soils, but lower for normally consolidated ones.

- Jacking is performed at penetration rates of 1–100 mm/s, with pauses of a few minutes between the strokes, and in no more than 50 jacks. These three facts are the main differences between jacked and driven pile installation, for which the maximum velocity ranges from 1 to 5 m/s, the blows interspersed by pauses of the order of one second, and hundreds of blows are required to attain required pile embedment. Having simulated both driven and jacked pile installations allows one to conclude that fatigue due to shaft-soil cyclic loading is almost nonexistent during jacked piles, contrary to driven piles.

Furthermore, simulations extending outside of the scope of the available experimental data yielded the following conclusions:

- Increasing the installation velocity (*i.e.* the hammer drop height) reduces the radius of mobilised soil around the pile.

  Furthermore, there is a critical installation velocity for which the soil around the pile offers maximum adherence.

- Overconsolidation ratio is crucial as it affects drastically the output of the simulation. Other soil characteristics, such as strength and stiffness, have a much milder effect on the output.

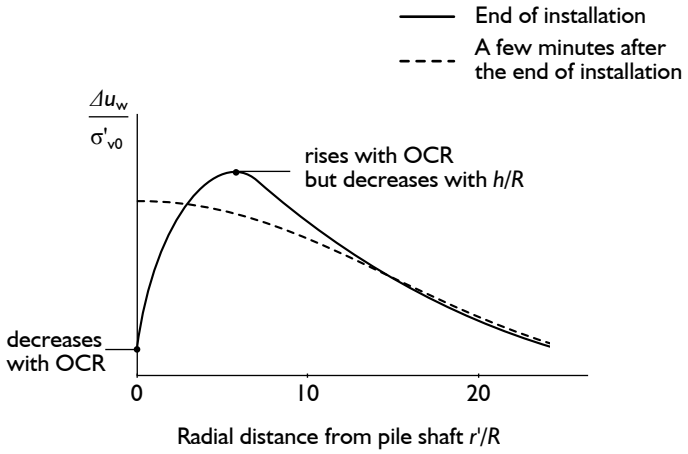

Figure 8.1 Tentative radial distribution of excess pore pressure ratio far behind the pile toe ($h/R > 20$) immediately and a few minutes after installation.

- Modelling an open-ended pile installation suggested that although pore pressures were lower for an open-ended pile than a closed-ended one, the radial effective stress was equivalent during installation.

Equalisation

The equalisation stage conclusions are the following:

- Using realistic assumptions, three equations governing coupled consolidation (the mass balance equations for the solid and liquid phases and Darcy's law) could be boiled down to a single equation relating radial velocity of the skeleton to the pore water pressure: Eq. (5.26), p. 114;
- During the first few minutes of equalisation, excess pore pressure (Δu_w) rises to a maximum, before inexorably decreasing to naught. This leads to a short-term minimum in radial effective stress (σ'_r). This was simulated for all overconsolidation ratios investigated and was consistently measured in field experiments.
- The maximum Δu_w recorded at the shaft during the short-term increase is linearly increasing with OCR in a loglog plot, until an overconsolidation ratio (OCR) of approximately 10. For higher overconsolidation ratios, the pore pressure maximum decreases with increasing OCR. This was also measured in field experiments.
- Except one simulation of highly overconsolidated soil (OCR = 64·1), total radial stress (σ_r) decreases steadily during consolidation.

- As for installation, excess pore pressure was underestimated during equalisation.

- At the pile wall, the set-up is higher than one ($\sigma'_{rc} > \sigma'_{ri}$) in lightly overconsolidated clay but lower than one ($\sigma'_{rc} < \sigma'_{ri}$) in overconsolidated clays. This was measured in field experiments.

  Equalised values of effective stress (σ'_{rc}) are in the same range as initial values (σ'_{r0}). This contradicts with field experiments where $\sigma'_{rc} > \sigma'_{r0}$ for all tests.

- Comparison with the Imperial College test pile installation in Bothkennar clay results in comparable radial effective stress during the entire equalisation.

- Although the set-up ratio during for the open-pile was comparable to the one predicted for the closed-ended one, equalisation was four times quicker for the open-ended pile.

The successful predictions of the model can be attributed to five of its characteristics: (1) the constitutive model is based on the critical state soil mechanics, which leads to a strong dependency on the initial overconsolidation ratio; (2) the constitutive model handles cyclic loading; (3) the constitutive model is capable of simulating shear induced dilatancy (4) the Strain Path Method predicts the distortions and reversals associated with the insertion of a pile toe, and (5) each Disk Shearing Model blow induces a cycle of strain thanks to its dynamic integration scheme.

8.3 Perspectives

Several improvements or perspectives are proposed hereunder.

- The excess pore water pressure (Δu_w) was almost consistently underestimated which lead to an underestimation of the total radial stress. Possible reasons for the discrepancy between the (higher) measured Δu_w and the (lower) predicted Δu_w are:

  - The pore pressure is already underestimated with the Strain Path Method. This was also reported by Whittle et al. (1990) who used the MIT-E3 model. It is possible that the lack of cycles of the Strain Path Method may be a cause for the underestimation of the pore pressure;
  - It is possible that the outer boundary of the Disk Shearing Model was too close, which led to an underestimation of the shear induced pore pressures;
  - Partial consolidation between the jacking stages of the field experiments could imply that measured pore pressures were *over*estimated.

- The complex behaviour of clay was only merely approached through the hypoplastic constitutive model. Three facets of soil behaviour that were not accounted for by the model are described hereunder, in order of importance, in my opinion:
  - Overconsolidation ratio and sensitivity are usually related as low OCR soils are frequently sensitive and high OCR soil are not. Therefore, the effect of sensitivity and OCR could not be distinguished neither during the field experiments nor during the numerical modelling. Incorporating sensitivity (structure) to the constitutive model would answer this question.
  - Rate effects were only taken into account through the dynamic integration scheme of the Disk Shearing Model. However, as presented in Section 2.2f (p. 20), the rate of shearing has a strong influence over soil strength, and possibly other soil characteristics. Including rate effect would take the model a step closer to driven pile installation.
  - The constitutive model used was isotropic although soil, by nature and because of its depositional history, is anisotropic.
- Because the constitutive model is based on critical state theory and that the installation process is viewed as undrained, the shear strength at the pile wall during each driving blow is the critical state strength. This contradicts with field experiments and could be improved by adding an interface element.
- The open-ended pile installation preliminary trends should be confirmed and compared to available field experiments.

Bibliography

Abramowitz, M. and Stegun, I. (eds) (1964). *Handbook of Mathematical Functions With Formulas, Graphs, and Mathematical Tables*, Dover Publications. Tenth Printing, December 1972.

Andresen, L. and Khoa, H. D. V. (2013). LDFE analysis of installation effects for offshore anchors and foundations, *in* M. A. Hicks, J. Dijkstra, M. Lloret-Cabot and M. Karstunen (eds), *Installation Effects in Geotechnical Engineering*, CRC Press/Balkema, Leiden, The Netherlands, pp. 162–168.

Atkinson, J. H. (2007). *The Mechanics of Soils And Foundations*, Spoon Text, Taylor & Francis, Milton, U.K.

Atkinson, J. H. and Bransby, P. L. (1978). *The Mechanics of Soils, An Introduction to Critical State Soil Mechanics*, McGraw-Hill Book Company Limited, Maidenhead, U.K.

Azzouz, A. S. and Lutz, D. G. (1986). Shaft behavior of a model pile in plastic empire clays, *Journal of Geotechnical Engineering* **112**(4): 389–406.

Azzouz, A. S. and Morrison, M. J. (1988). Field measurements on model pile in two clay deposits, *Journal of Geotechnical Engineering* **114**(1): 104–121.

Baligh, M. M. (1985). Strain Path Method, *Journal of Geotechnical Engineering* **111**(9): 1108–1136.

Baran, P. A. and Sweezy, P. M. (1968). *Monopoly capital: An essay on the American economic and social order*, Modern Reader, New York, U.S.A.

Bardet, J. P. (1990). Lode dependences for isotropic pressure-sensitive elastoplastic materials, *Journal of Applied Mechanics* **57**(3): 498–506.

Bardet, J. P. and Choucair, W. (1991). A linearized integration technique for incremental constitutive equations, *International Journal for Numerical and Analytical Methods in Geomechanics* **15**(1): 1–19.

Basu, P., Prezzi, M., Salgado, R. and Chakraborty, T. (2013). Shaft resistance and setup factors for piles jacked in clay, *Journal of Geotechnical and Geoenvironmental Engineering* **140**(3): 16.

Basu, P., Salgado, R., Prezzi, M. and Chakraborty, T. (2009). A method for accounting for pile setup and relaxation in pile design and quality assurance, *Technical Report Publication FHWA/IN/JTRP-2009/24*, Joint Transportation Research Program, Indiana Department of Transportation and Purdue University, West Lafayette, Indiana.

Been, K., Jefferies, M. G. and Hachey, J. (1991). The critical state of sands, *Géotechnique* **41**(3): 365–381.

Biot, M. A. (1941). General theory of three-dimensional consolidation, *Journal of Applied Physics* **12**: 155–164.

Bjerrum, L. (1967). Engineering geology of Norwegian normally-consolidated marine clays as related to settlements of buildings, *Géotechnique* **17**(2): 81–118.

Bond, A. J. and Jardine, R. J. (1991). Effects of installing displacement piles in a high OCR clay, *Géotechnique* **41**(3): 341–363.

BP (2015). Statistical Review of World Energy – June 2015, A report by BP plc. Pureprint Group Limited, U.K. 64th edn.

Brown, M. J., Hyde, A. F. L. and Anderson, W. F. (2006). Analysis of a rapid load test on an instrumented bored pile in clay, *Géotechnique* **56**(9): 627–638.

Burd, H. J. (1986). *A large displacement finite element analysis of a reinforced unpaved road*, PhD thesis, Oxford University, Oxford, U.K.

Burd, H. J. and Houlsby, G. T. (1990). Finite element analysis of two cylindrical expansion problems involving nearly incompressible material behaviour, *International Journal for Numerical and Analytical Methods in Geomechanics* **14**(5): 351–366.

Burland, J. B. (1990). On the compressibility and shear strength of natural clays, *Géotechnique* **40**(3): 329–378.

Butterfield, R. (1979). A natural compression law for soils (an advance on e–log p'), *Géotechnique* **29**(4): 469–480.

Carter, J. P., Randolph, M. F. and Wroth, C. P. (1979). Stress and pore pressure changes in clay during and after the expansion of a cylindrical cavity, *International Journal for Numerical and Analytical Methods in Geomechanics* **3**(4): 305–322.

Carter, J. P., Small, J. C. and Booker, J. R. (1977). A theory of finite elastic consolidation, *International Journal of Solids and Structures* **13**(5): 467–478.

Casagrande, A. and Carrillo, N. (1944). Shear failure of anisotropic materials, *Journal of the Boston Society of Civil Engineers* **31**(4): 74–87. Reprinted in Contributions to Soil Mechanics 1941-1953, Boston Society of Civil Engineers, 122-135.

Cathie, D. (2012). Offshore pile design: International practice, Presentation dated the 16th of October 2012.

Chakrabarti, S., Halkyard, J. and Capanoglu, C. (2005). Historical development of offshore structures, *in* S. Chakrabarti (ed.), *Handbook of Offshore Engineering*, Elsevier Limited, Amsterdam, The Netherlands, chapter 1, pp. 1–38.

Chakraborty, T. (2009). *Development of a Clay Constitutive Model and Its Application to Pile Boundary Value Problems*, PhD thesis, Purdue University, West Lafayette, Indiana, U.S.A.

Chin, C.-T. (1986). *Open-ended pile penetration in saturated clays*, PhD thesis, Massachusetts Institute of Technology, Cambridge, Massachusetts, U.S.A.

Chow, F. C. (1996). *Investigations into the behaviour of displacement piles for offshore foundations*, PhD thesis, University of London (Imperial College), London, U.K.

Chung, S. F., Randolph, M. F. and Schneider, J. A. (2006). Effect of penetration rate on penetrometer resistance in clay, *Journal of Geotechnical and Geoenvironmental Engineering* **132**(9): 1188–1196.

Cooke, R. W., Price, G. and Tarr, K. (1979). Jacked piles in London Clay: a study of load transfer and settlement under working conditions, *Géotechnique* **29**(2): 113–147.

Coop, M. R. (1987). *The axial capacity of driven piles in clay*, PhD thesis, Oxford University, Oxford, U.K.

Coop, M. R. and Wroth, C. P. (1989). Field studies of an instrumented model pile in clay, *Géotechnique* **39**(4): 679–696.

Coussy, O. (2004). *Poromechanics*, John Wiley & Sons, Limited, Chichester.

Das, B. M. (2006). *Principles of Geotechnical Engineering*, seventh edn, Cengage Learning, Stamford, Connecticut, U.S.A.

Dean, E. T. R. (2010). *Offshore Geotechnical Engineering: Principles and Practice*, Thomas Telford Limited, London, U.K.

Deeks, A. J. and Randolph, M. F. (1994). Axisymmetric time-domain transmitting boundaries, *Journal of Engineering Mechanics* **120**(1): 25–42.

Detournay, E. and Cheng, A. H.-D. (1993). Fundamentals of poroelasticity, *in* J. A. Hudson, E. T. Brown, C. Fairhust and E. Hoek (eds), *Comprehensive Rock engineering: Principles, Practice and Projects, Volume 2: Analysis and Design Methods*, Pergamon Press, Oxford, U.K., pp. 113–171.

Doherty, P. and Gavin, K. (2011). The shaft capacity of displacement piles in clay: A state of the art review, *Geotechnical and Geological Engineering* **29**(4): 389–410.

ENI (2014). World Oil and Gas Review, A report by Ente Nazionale Idrocarburi, S.p.A. 13th edn.

EWEA (2015). The European offshore wind industry - Key trends and statistics 2014, A report by the European Wind Energy Association.

Ferentinos, J. (2013). Global Offshore Oil and Gas Outlook, Infield presentation, Gas/Electric Partnership Conference, Houston, Texas, U.S.A.

Gasparre, A., Nishimura, S., Minh, N. A., Coop, M. R. and Jardine, R. J. (2007). The stiffness of natural London Clay, *Géotechnique* **57**(1): 33–47.

Gibson, R. E., England, G. L. and Hussey, M. J. L. (1967). The theory of one-dimensional consolidation of saturated clays, *Géotechnique* **17**(3): 261–273.

Gudehus, G. (2011). *Physical Soil Mechanics*, Advances in Geophysical and Environmental Mechanics and Math, Springer, Berlin, Germany.

Gupta, R. (2003). Discussion of "Soil deformation and excess pore pressure field around a closed-ended pile" by Pestana, J. M., Hunt, C. E., and Bray, J. D., *Journal of Geotechnical and Geoenvironmental Engineering* **129**(7): 669–671.

GWEC (2015). Global wind report, Annual market update 2014, A report by the Global Wind Energy Council, Brussels, Belgium.

Hamann, T., Qiu, G. and Grabe, J. (2015). Application of a Coupled Eulerian-Lagrangian approach on pile installation problems under partially drained conditions, *Computers and Geotechnics* **63**: 279–290.

Herle, I. and Kolymbas, D. (2004). Hypoplasticity for soils with low friction angles, *Computers and Geotechnics* **31**(5): 365–373.

Hill, M. C. (1998). Methods and guidelines for effective model calibration, *Technical Report 98-4005*, U.S. Geological Survey, Denver, Colorado, U.S.A.

Hill, R. (1950). *The Mathematical Theory of Plasticity*, Oxford University Press, London, U.K.

Holeyman, A. E. (1984). *Contribution à l'étude du comportement dynamique non-lineaire des pieux lors de leur battage*, PhD thesis, Faculté des sciences appliquées, Université libre de Bruxelles, Belgium.

Holeyman, A. E. (1992). Keynote lecture: Technology of pile dynamic testing, *in* F. B. J. Barends (ed.), *Proceedings of the 4th Internatinoal Conference on the Application of Stress-Wave Theory to Piles*, A. A. Balkema, Rotterdam, The Netherlands, pp. 195–215.

Hu, Y. and Randolph, M. F. (1998). A practical numerical approach for large deformation problems in soil, *International Journal for Numerical and Analytical Methods in Geomechanics* **22**(5): 327–350.

Hunt, C. E., Pestana, J. M., Bray, J. D. and Riemer, M. (2002). Effect of pile driving on static and dynamic properties of soft clay, *Journal of Geotechnical and Geoenvironmental Engineering* **128**(1): 13–24.

Hunt, C. E., Pestana, J. M., Bray, J. D., Riemer, M. and Seed, R. B. (2000). Geotechnical measurements after pile installation in a soft clay deposit, *Technical Report UCB/GT/2000-05*, Department of Civil and Environmental Engineering, University of California, Berkeley.

Itasca (n.d.). FLAC Version 5.0 - Online Manual.

Jardine, R., fiona Chow, Overy, R. and Standing, J. (2005). *ICP design methods for driven piles in sands and clays*, Thomas Thelford, London, U.K.

Jardine, R. J., Andersen, K. H. and Puech, A. (2012). Cyclic loading of offshore piles: potential effects and practical design, *Proceedings of the 7th International Conference on Offshore Site Investigation and Geotechnics*, Society for Underwater Technology, London, U.K., pp. 59–100.

Jardine, R. J. and Bond, A. J. (1989). Behaviour of displacement piles in a heavily overconsolidated clay, *Proceedings of the 12th International Conference on Soil Mechanics and Foundations Engineering*, Vol. 2, A. A. Balkema, pp. 1147–1151.

Jardine, R. J. and Chow, F. C. (2007). Some recent developments in offshore pile design, *Proceedings of the 6th International Offshore Site Investigation and Geotechnical Conference: Confronting New challenges and Sharing Knowledge*, London, U.K., pp. 303–332.

Jardine, R. J., Standing, J. R. and Chow, F. C. (2006). Some observations of the effects of time on the capacity of piles driven in sand, *Géotechnique* **56**(4): 227–244.

Jassim, I., Coetzee, C. and Vermeer, P. A. (2013). A dynamic material point method for geomechanics, *in* M. A. Hicks, J. Dijkstra, M. Lloret-Cabot and M. Karstunen (eds), *Installation Effects in Geotechnical Engineering*, CRC Press/Balkema, Leiden, The Netherlands, pp. 15–23.

Karlsrud, K. (2012). *Prediction of load-displacement behaviour and capacity of axially loaded piles in clay based on analyses and interpretation of pile load test results*, PhD thesis, Norwegian University of Science and Technology, Trondheim, Norway.

Karlsrud, K. and Haugen, T. (1985). Axial static capacity of steel model piles in overconsolidated clay, *Proceedings of the 11th International Conference on Soil Mechanics and Foundations Engineering*, Vol. 3, A. A. Balkema, pp. 1401–1406.

Kavvadas, M. (1982). *Non-linear consolidation around driven piles in clays*, PhD thesis, Massachusetts Institute of Technology, Cambridge, Massachusetts, U.S.A.

Küchemann, D. and Weber, J. (1953). *Aerodynamics of Propulsion*, McGraw-Hill.

Kim, K., Prezzi, M., Salgado, R. and Lee, W. (2008). Effect of penetration rate on cone penetration resistance in saturated clayey soils, *Journal of Geotechnical and Geoenvironmental Engineering* **134**(8): 1142–1153.

Kirkgard, M. M. and Lade, P. V. (1993). Anisotropic three-dimensional behavior of a normally consolidated clay, *Canadian Geotechnical Journal* **30**(5): 848–858.

Kolk, H. J. and van der Velde, E. (1996). A reliable method to determine the friction capacity of piles driven into clays, *Proceedings of the 28th Annual Offshore Technology Conference*, Houston, Texas, U.S.A., pp. 337–346. OTC Paper No. 7993.

Konrad, J. M. and Roy, M. (1987). Bearing capacity of friction piles in marine clay, *Géotechnique* **37**(2): 163–175.

Kopito, D. and Klar, A. (2013). Discussion of "Hypoplastic Cam-clay model" by Mašín, D., *Géotechnique* **63**(10): 889–890.

Kuhlemeyer, R. L. and Lysmer, J. (1973). Finite element method accuracy for wave propagation problems, *Journal of the Soil Mechanics and Foundations Division* **99**(5): 421–427.

Kulhawy, F. H. and Mayne, P. W. (1980). Manual on estimating soil properties for foundation design, *Technical Report 1493-6*, Cornell University, Ithaca, New York, U.S.A.

Ladanyi, B. and Johnston, G. H. (1974). Behavior of circular footings and plate anchors embedded in permafrost, *Canadian Geotechnical Journal* **11**(4): 531–553.

Ladd, C. C., Germaine, J. T., Baligh, M. M. and Lacasse, S. M. (1980). Evaluation of self-boring pressuremeter tests in Boston Blue Clay, *Technical Report FHWA/RD-80/052*, Department of Civil Engineering, Massachusetts Institute of Technology, Cambridge, Massachusetts, U.S.A.

Lehane, B. (1992). *Experimental investigatinos of pile behaviour using instrumented field piles*, PhD thesis, University of London (Imperial College), London, U.K.

Lehane, B. M. and Gill, D. R. (2004). Displacement fields induced by penetrometer installation in an artificial soil, *International Journal of Physical Modelling in Geotechnics* **4**(1): 25–36.

Lehane, B. M. and Jardine, R. J. (1992). Residual strength characteristics of Bothkennar clay, *Géotechnique* **42**(2): 363–367.

Lehane, B. M. and Jardine, R. J. (1994a). Displacement-pile behaviour in a soft marine clay, *Canadian Geotechnical Journal* **31**(2): 181–191.

Lehane, B. M. and Jardine, R. J. (1994b). Displacement pile behaviour in glacial clay, *Canadian Geotechnical Journal* **31**(1): 79–90.

Leroueil, S., Tavenas, F. and Locat, J. (1985). Discussion of "Correlations between index tests and the properties of remoulded clays" by Carrier III, W. D. and Beckman, J. F., *Géotechnique* **35**(2): 223–229.

Levadoux, J.-N. (1980). *Pore pressures in clays due to cone penetration*, PhD thesis, Massachusetts Institute of Technology, Cambridge, Massachusetts, U.S.A.

Litkouthi, S. and Poskitt, T. J. (1980). Damping constants for pile driveability calculations, *Géotechnique* **30**(1): 77–86.

Loukidis, D., Salgado, R. and Abou-Jaoude, G. (2008). Assessment of axially-loaded pile dynamic design methods and review of indot axially-loaded pile design procedure, *Technical Report Publication FHWA/IN/JTRP-2008/06*, Indiana Department of Transportation and Purdue University, West Lafayette, Indiana.

Malvern, L. E. (1969). *Introduction to the Mechanics of a Continuous Medium*, Prentice-Hall, Inc., Englewood Cliffs, New Jersey, U.S.A.

Mašín, D. (2004). *Laboratory and numerical modelling of natural clays*, Master's thesis, City University, London, U.K.

Mašín, D. (2005). A hypoplastic constitutive model for clays, *International Journal for Numerical and Analytical Methods in Geomechanics* **29**(4): 311–336.

Mašín, D. (2007). A hypoplastic constitutive model for clays with meta-stable structure, *Canadian Geotechnical Journal* **44**(3): 363–375.

Mašín, D. (2012a). Clay hypoplasticity with explicitly defined asymptotic states, *Acta Geotechnica* **7**(4): 1–16.

Mašín, D. (2012b). Hypoplastic Cam-clay model, *Géotechnique* **62**(6): 549–553.

Mašín, D. (2012c). Workshop on hypoplasticity for practical applications. Institute of Geotechnical Engineering, Stuttgart University, Germany.

Matsuoka, H. and Nakai, T. (1974). Stress-deformation and strength characteristics of soil under three different principal stresses, *Proceedings of the Japanese Society of Civil Engineers*, Vol. 232, pp. 59–70.

Mayne, P. W. and Kulhawy, F. H. (1982). K_0-OCR relationships in soil, *Journal of Geotechnical Engineering* **108**(GT6): 851–872.

McClelland, B. (1974). Design of deep penetration piles for ocean structures, *Journal of the Geotechnical Engineering Division* **100**(7): 709–747.

McGinty, B. (2013). Finite deformation continuum mechanics, http://www.continuummechanics.org.

Mitchell, J. K. and Soga, K. (2005). *Fundamentals of soil behavior*, John Wiley & Sons.

Mortara, G. (2008). A new yield and failure criterion for geomaterials, *Géotechnique* **58**(2): 125–132.

Muir Wood, D. (1990). *Soil Behaviour and Critical State Soil Mechanics*, Cambridge University Press, Cambridge, U.K.

Nakai, T., Matsuoka, H., Okuno, N. and Tsuzuki, K. (1986). True triaxial tests on normally consolidated clay and analysis of the observed shear behavior using elastoplastic constitutive models., *Soils and Foundations* **26**(4): 67–78.

Ni, Q., Hird, C. C. and Guymer, I. (2010). Physical modelling of pile penetration in clay using transparent soil and particle image velocimetry, *Géotechnique* **60**(2): 121–132.

Niemunis, A. (2003). *Extended hypoplastic models for soils*, PhD thesis, Ruhr-Universität Bochum, Germany. Habilitation thesis.

Niemunis, A., Grandas-Tavera, C. E. and Prada-Sarmiento, L. F. (2009). Anisotropic visco-hypoplasticity, *Acta Geotechnica* **4**(4): 293–314.

Niemunis, A. and Herle, I. (1997). Hypoplastic model for cohesionless soils with elastic strain range, *Mechanics of Cohesive-frictional Materials* **2**(4): 279–299.

Nishimura, S., Minh, N. A. and Jardine, R. J. (2007). Shear strength anisotropy of natural London Clay, *Géotechnique* **57**(1): 49–62.

Norbury, J. and Wheeler, A. A. (1987). On the penetration of an elastic-plastic material by a slender body, *The Quarterly Journal of Mechanics and Applied Mathematics* **40**(4): 477–491.

Novak, M., Aboul-Ella, F. and Nogami, T. (1978). Dynamic soil reactions for plane strain case, *Journal of the Engineering Mechanics Division* **104**(4): 953–959.

Nowacki, F., Karlsrud, K. and Sparrevik, P. (1993). Comparison of recent tests on OC clay and implications for design, *in* J. Clarke (ed.), *Proceedings of the conference Recent large-scale fully instrumented pile tests in clay*, Thomas Telford Services Limited, London, U.K., pp. 511–537.

Pestana, J., Hunt, C. and Bray, J. (2002). Soil deformation and excess pore pressure field around a closed-ended pile, *Journal of Geotechnical and Geoenvironmental Engineering* **128**(1): 1–12.

Potts, D. M. and Zdravković, L. (1999). *Finite element analysis in geotechnical engineering: Theory*, Vol. 1, Thomas Telford Publishing, London, U.K.

Poulos, H. G. (1988). *Marine Geotechnics*, Unwin Hyman Limited, London, U.K.

Prager, W. (1961). *Introduction To Mechanics Of Continua*, Dover Phoenix Editions, Ginn, Boston, Massachusetts, U.S.A.

Quinn, T. A. C., Robinson, S. and Brown, M. J. (2012). High strain rate characterisation of kaolin and its application to rapid load pile testing, *in* T. Matsumoto (ed.), *Proceedings of the 9th International Conference on Testing and Design Methods for Deep Foundations*, Kanasawa e-Publishing Compagny, Limited, Kakuma-machi, Japan, pp. 311–319.

Randolph, M. F. (1993). Contribution to discussion on low skin friction at the top of piles, *in* J. Clarke (ed.), *Proceedings of the conference Recent large-scale fully instrumented pile tests in clay*, Thomas Telford Services Limited, London, U.K., p. 579.

Randolph, M. F. (2003). Science and empiricism in pile foundation design, *Géotechnique* **53**(10): 847–875.

Randolph, M. F., Carter, J. P. and Wroth, C. P. (1979). Driven piles in clay–the effects of installation and subsequent consolidation, *Géotechnique* **29**(4): 361–393.

Randolph, M. F. and Hope, S. (2004). Effect of cone velocity on cone resistance and excess pore pressures, *in* T. Matsui, Y. Tanaka and M. Mimura (eds), *Proceedings of the International Symposium on Enginnering Practice and Performance of Soft Deposits*, pp. 147–152.

Randolph, M. F., Steenfelt, J. S. and Wroth, C. P. (1979). The effect of pile type on design parameters for driven piles, *Proceedings of the 7th European Conference on Soil Mechanics and Foundation Engineering*, British Geotechnical Society, London, U.K., pp. 107–114. Vol. 2.

Randolph, M. F. and Wroth, C. P. (1979). An analytical solution for the consolidation around a driven pile, *International Journal for Numerical and Analytical Methods in Geomechanics* **3**(3): 217–229.

Randolph, M. F. and Wroth, C. P. (1981). Application of the failure state in undrained simple shear to the shaft capacity of driven piles, *Géotechnique* **31**(1): 143–157.

Randolph, M. and Gourvenec, S. (2011). *Offshore Geotechnical Engineering*, Spoon Press, Milton Park, U.K.

Rausche, F., Robinson, B., and Likins, G. (2004). On the prediction of long term pile capacity from end-of-driving information, *in* J. A. DiMaggio; and M. H. Hussein (eds), *Current Practices and Future Trends in Deep Foundations, Geotechnical Special Publication No. 125*, American Society of Civil Engineers, Reston, Virginia, U.S.A., pp. 77–95.

Robinson, S. and Brown, M. J. (2013). Towards a framework for the prediction of installation rate effects, *in* M. A. Hicks, J. Dijkstra, M. Lloret-Cabot and M. Karstunen (eds), *Installation Effects in Geotechnical Engineering*, CRC Press/Balkema, Leiden, The Netherlands, pp. 128–134.

Roscoe, K. H. and Schofield, A. N. (1968). On the generalised stress-strain behaviour of 'wet' clay, *in* J. Heyman and F. A. Leckie (eds), *Engineering plasticity*, Cambridge University Press, London, U.K., pp. 535–609.

Roy, M., Blanchet, R., Tavenas, F. and La Rochelle, P. (1981). Behaviour of a sensitive clay during pile driving, *Canadian Geotechnical Journal* **18**(1): 67–85.

Roy, M. and Lemieux, M. (1986). Long-term behaviour of reconsolidated clay around a driven pile, *Canadian Geotechnical Journal* **23**(1): 23–29.

Sabetamal, H., Nazem, M., Carter, J. and Sloan, S. (2014). Large deformation dynamic analysis of saturated porous media with applications to penetration problems, *Computers and Geotechnics* **55**: 117–131.

Sagaseta, C., Whittle, A. J. and Santagata, M. (1997). Deformation analysis of shallow penetration in clay, *International Journal for Numerical and Analytical Methods in Geomechanics* **21**(10): 687–719.

Sandrea, I. and Sandrea, R. (2007). Global offshore oil, Part 1: Exploration trends show continued promise in world's offshore basins, *Oil and Gas Journal* **105**(9): 34–40.

Schofield, A. and Wroth, P. (1968). *Critical State Soil Mechanics*, McGraw-Hill, Maidenhead, U.K.

Segall, P. (2010). *Earthquake and Volcano Deformation*, Princeton University Press, Princeton, New Jersey, U.S.A., chapter 1.

Silva, M. F., White, D. J. and Bolton, M. D. (2006). An analytical study of the effect of penetration rate on piezocone tests in clay, *International Journal for Numerical and Analytical Methods in Geomechanics* **30**(6): 501–527.

Skempton, A. W. (1954). The pore pressure coefficients A and B, *Géotechnique* **4**(4): 143–147.

Sloan, S. W. (1987). Substepping schemes for the numerical integration of elastoplastic stress-strain relations, *International Journal for Numerical Methods in Engineering* **24**(5): 893–911.

Smith, P. R., Jardine, R. J. and Hight, D. W. (1992). The yielding of Bothkennar clay, *Géotechnique* **42**(2): 257–274.

Soares, M. M. and Dias, C. R. R. (1989). Behavior of an instrumented pile in the Rio de Janeiro clay, *Proceedings of the 12th International Conference on Soil Mechanics and Foundations Engineering*, Vol. 1, A. A. Balkema, pp. 319–322.

Soderberg, L. O. (1962). Consolidation theory applied to foundation pile time effects, *Géotechnique* **12**(3): 217–225.

Steenfelt, J. S., Randolph, M. F. and Wroth, C. P. (1981). Instrumented model piles jacked into clay, *Proceedings of the 10th International Conference on Soil Mechanics and Foundations Engineering*, Vol. 2, A. A. Balkema, pp. 857–864.

Su, S.-F. (2010). Undrained shear strengths of clay around an advancing cone, *Canadian Geotechnical Journal* **47**(10): 1149–1158.

Tamagnini, C. (2012). ALERT Summerschool, the 4th Olek Zienkiewicz Course 'Constitutive Modelling of Soils'. Technische Universität Dresden, Germany.

Tamagnini, C., Viggiani, G., Chambon, R. and Desrues, J. (2000). Evaluation of different strategies for the integration of hypoplastic constitutive equations: Application to the CLoE model, *Mechanics of Cohesive-frictional Materials* **5**(4): 263–289.

Tatsuoka, F. (2007). Inelastic deformation characteristics of geomaterial, *in* H. I. Ling, L. Callisto, D. Leshchinsky and J. Koseki (eds), *Soil Stress-strain Behavior: Measurement, Modeling and Analysis. A Collection of Papers of the Geotechnical Symposium in Rome (March 16-17, 2006)*, Springer, Dordrecht, The Netherlands, pp. 2–108.

Taylor, D. W. (1942). Research on consolidation of clays, *Technical Report Serial 82*, Massachusetts Institute of Technology, Cambridge, Massachusetts, U.S.A.

Teh, C. I. and Houlsby, G. T. (1991). An analytical study of the cone penetration test in clay, *Géotechnique* **41**(1): 17–34.

Terzaghi, K. (1925). *Erdbaumechanik auf bodenphysikalischer grundlage*, F. Deuticke. Translated by A. Casagrande in From Theory to Practice in Soil Mechanics (1960), pp. 146–148, John Wiley and Sons, Inc., New York, U.S.A.

Terzaghi, K., Peck, R. B. and Mesri, G. (1996). *Soil Mechanics in Engineering Practice*, third edn, John Wiley & Sons, Incorporated, New York, U.S.A.

Tian, Y., Cassidy, M. J., Randolph, M. F., Wang, D. and Gaudin, C. (2014). A simple implementation of RITSS and its application in large deformation analysis, *Computers and Geotechnics* **56**: 160–167.

Verruijt, A. (2010). *An Introduction to Soil Dynamics*, Vol. 24 of *Theory and Applications of Transport in Porous Media*, Springer, Dordrecht, Netherlands.

Vesić, A. S. (1972). Expansion of cavities in infinite soil mass, *Journal of the Soil Mechanics and Foundations Division* **98**(3): 265–290.

Viggiani, G. and Atkinson, J. (1995). Stiffness of fine-grained soil at very small strains, *Géotechnique* **45**(2): 249–265.

Vijayvergiya, V. N., Cheng, A. P. and Kolk, H. J. (1977). Effect of soil set up on pile driveability in chalk, *Journal of the Geotechnical Engineering Division* **103**(10): 1069–1082.

von Wolffersdorff, P.-A. (1996). A hypoplastic relation for granular materials with a predefined limit state surface, *Mechanics of Cohesive-frictional Materials* **1**(3): 251–271.

Wang, D., Bienen, B., Nazem, M., Tian, Y., Zheng, J., Pucker, T. and Randolph, M. F. (2015). Large deformation finite element analyses in geotechnical engineering, *Computers and Geotechnics* **65**: 104–114.

White, D. J. and Bolton, M. D. (2004). Displacement and strain paths during plane-strain model pile installation in sand, *Géotechnique* **54**(6): 375–397.

White, D. J., Take, W. A. and Bolton, M. D. (2003). Soil deformation measurement using particle image velocimetry (PIV) and photogrammetry, *Géotechnique* **53**(7): 619–631.

Whitham, G. B. (1974). *Linear and Nonlinear Waves*, John Wiley and Sons, New York, U.S.A.

Whittle, A. J. (1987). *A constitutive model for overconsolidated clays with application to the cyclic loading of friction piles*, ScD thesis, Massachusetts Institute of Technology, Cambridge, Massachusetts, U.S.A.

Whittle, A. J. (1992). Assessment of an effective stress analysis for predicting the performance of driven piles in clays, *in* D. A. Ardus (ed.), *Proceedings of the International Conference on Offshore Site Investigation and Foundation Behavior*, Society for Underwater Technology, pp. B29–B68. Reprinted in the Proceedings of the Workshop on Effects of Piles on Soil Properties, 1995, J. M. Andersen and W. M. Myers (eds).

Whittle, A. J., Aubeny, C. P., Rafalovich, A., Ladd, C. C. and Baligh, M. M. (1990). Interpretation of in-situ testing of cohesive soils using rational methods, *Technical report*, Constructed Facilities Division, Department of Civil Engineering, Massachusetts Institute of Technology, Cambridge, Massachusetts, U.S.A.

Więckowski, Z. (2004). The material point method in large strain engineering problems, *Computer Methods in Applied Mechanics and Engineering* **193**(39-41): 4417–4438.

Wu, W. (1998). Rational approach to anisotropy of sand, *International Journal for Numerical and Analytical Methods in Geomechanics* **22**(11): 921–940.

Wu, W. (2006). On high-order hypoplastic models for granular materials, *Journal of Engineering Mathematics* **56**(1): 23–34.

Yu, H. and Mitchell, J. (1998). Analysis of cone resistance: Review of methods, *Journal of Geotechnical and Geoenvironmental Engineering* **124**(2): 140–149.

Yu, H.-S. (2006). *Plasticity and Geotechnics*, Vol. 13 of *Advances in mechanics and mathematics*, Springer, New York, U.S.A.

Yu, H. S., Herrmann, L. R. and Boulanger, R. W. (2000). Analysis of steady cone penetration in clay, *Journal of Geotechnical and Geoenvironmental Engineering* **126**(7): 594–605.

Zdravković, L. and Potts, D. M. (2000). Advances in modelling soil anisotropy, *in* D. Kolymbas (ed.), *Constitutive Modelling of Granular Materials*, Springer, Berlin, Germany, pp. 491–519.

List of Figures

List of Tables

Appendix A

Terminology

A brief description and background to the terminology used in this work is presented hereafter.

The *state* of the soil is the description of the physical conditions under which it exists (Been et al., 1991). Void ratio and effective stress are the primary *state variables*. Structure, temperature, and degree of saturation are also state variables.

The *(intrinsic) material parameters* characterise the soil, independently of the mechanical process or the state. Examples are grain size distribution, specific gravity, and critical state friction angle.

Soil properties that depend on the state, the test type, or the material parameters are called *behavioural properties* (Been et al., 1991) or *derived properties*. They include peak friction angle, undrained shear strength, and shear modulus.

Constitutive parameters are the parameters defining a constitutive model and may be intrinsic material parameters or derived quantities.

According to Casagrande and Carrillo (1944), two different kind of anisotropic behaviour can be distinguished:

(a) *inherent anisotropy*, defined as 'a physical characteristic inherent in the material and entirely independent of the applied strains;' and

(b) *induced anisotropy*, defined as 'a physical characteristic due exclusively to the strain associated with the applied stress.'

The above distinction is somewhat arbitrary (Tamagnini, 2012) and the anisotropy of an intact soil is a combination of both inherent and induced anisotropy (Zdravković and Potts, 2000).

Clayey soils can be encountered or produced in five different *states of structure*[1,2] (Leroueil et al., 1985; Burland, 1990):

[1] In order to avoid any confusion with the soil state, I will use the term 'state of structure' and not the usual short-cut 'state.'

[2] The state of structure is a collective term used to describe the combined effects of soil fabric and interparticle bonding (Mitchell and Soga, 2005).

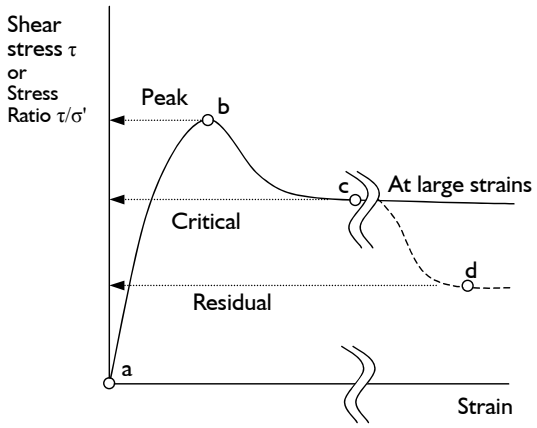

Figure A.1 Peak, critical, and residual strengths (after Mitchell and Soga, 2005).

(a) the *intact* state of structure, as it occurs in natural deposits, which is the result of complex geological processes involving deposition environment, consolidation, erosion, etc;

(b) the *destructured* state of structure, obtained when an initially intact clay is submitted to volumetric or shear deformations of such magnitude that the original clay structure is broken;

(c) the *remoulded* state of structure, observed when sufficient mechanical energy is imparted to a clay mass to reduce its strength to a minimum;

(d) the *resedimented* state of structure, obtained by deposition, under their self weight, of clay particles originally remoulded;

(e) the *reconstituted* state of structure, defined as on that has been thoroughly mixed at a water content equal to or greater than the liquid limit.

The sensitivity of a soil (S_t) is defined as the ratio of undisturbed to remoulded strengths:

$$S_t = \frac{s_u \text{ (undisturbed)}}{s_u \text{ (remolded)}},$$

and indicates 'the effect of remoulding on the consistency of a clay, regardless of the physical nature of the causes of the change' (Terzaghi et al., 1996).

Critical state is an 'ultimate condition in which plastic shearing could continue indefinitely without changes in volume or effective stresses' (Muir Wood, 1990), as shown in Fig. A.1. During critical state, the soil is completely destructured and the strength at critical state depends only on the critical state friction angle (ϕ'_{cs}). The critical state friction angle values are independent of stress history and original structure (Mitchell and Soga, 2005).

Under further deformation, soil particles align along a localised failure plane and the strength may decrease even further from the critical state condition (Fig. A.1), leading to the *residual state* (Mitchell and Soga, 2005).

The state and the state of structure are also arbitrary distinctions that were created in order to categorise a very complex material and are sometimes inter mingled. For example the remoulded state of structure is attained when the soil is at its residual state.

Throughout this work, I tried to observe consistency and logics in the use of terms. The three parts of a pile are referred to as the *head*, the *shaft* or the *wall*, and the *toe*. The life of a displacement pile is split into three *stages*: installation, equalisation, and loading. Saturated soil is constituted of two *phases*: *skeleton* (composed of grains) and water.

Appendix B

Strain and stress invariants

Stress tensor The state of stress of a soil particle is defined by the second order effective stress tensor $\boldsymbol{\sigma}'$ (or σ'_{ij}, using Einstein's notation). Thanks to the moment equilibrium, the effective stress tensor has only six independent components, which are usually expressed as a square matrix:

$$\sigma'_{ij} = \begin{bmatrix} \sigma'_x & \tau_{xy} & \tau_{xz} \\ \tau_{xy} & \sigma'_y & \tau_{yz} \\ \tau_{xz} & \tau_{yz} & \sigma'_z \end{bmatrix}.$$

Principal stresses The state of stress of a soil particle can also be defined by three principal stresses, acting on facets that have no shear stress, which are obtained by solving this determinant:

$$\begin{vmatrix} \sigma'_x - \sigma & \tau_{xy} & \tau_{xz} \\ \tau_{xy} & \sigma'_y - \sigma & \tau_{yz} \\ \tau_{xz} & \tau_{yz} & \sigma'_z - \sigma \end{vmatrix} = 0,$$

which leads to the characteristic equation:

$$\sigma^3 - I_1\sigma^2 + I_2\sigma - I_3 = 0, \tag{B.1}$$

where I_1, I_2, and I_3 are the three principal invariants and are defined as follows:

$$\begin{aligned} I_1 &= \operatorname{tr}\boldsymbol{\sigma}' = \sigma'_x + \sigma'_y + \sigma'_z, \\ I_2 &= \frac{1}{2}\left(I_1^2 - \boldsymbol{\sigma}' : \boldsymbol{\sigma}'\right) = \sigma'_x\sigma'_y + \sigma'_y\sigma'_z + \sigma'_z\sigma'_x - \tau_{xy}^2 - \tau_{yz}^2 - \tau_{zx}^2, \\ I_3 &= \det\boldsymbol{\sigma}' = \sigma'_x\sigma'_y\sigma'_z - \sigma'_x\tau_{yz}^2 - \sigma'_y\tau_{xz}^2 - \sigma'_z\tau_{xy}^2 + 2\tau_{xy}\tau_{yz}\tau_{xz}. \end{aligned}$$

Another set of invariants is J_1, J_2 and J_3: the invariants of the deviatoric part of

the stress tensor $\mathbf{s}' = \boldsymbol{\sigma}' - I_1/3\,\mathbf{I}$ (Atkinson and Bransby, 1978):

$$
\begin{aligned}
J_1 &= \operatorname{tr} \boldsymbol{s}' = 0, \\
J_2 &= \frac{1}{2}\boldsymbol{s}' : \boldsymbol{s}' = \frac{1}{3}(I_1^2 + 2I_3) \\
&= \frac{1}{6}\Big[(\sigma'_{\mathrm{x}} - \sigma'_{\mathrm{y}})^2 + (\sigma'_{\mathrm{y}} - \sigma'_{\mathrm{z}})^2 + (\sigma'_{\mathrm{z}} - \sigma'_{\mathrm{x}})^2 + 6\left(\tau_{\mathrm{xy}}^2 + \tau_{\mathrm{yz}}^2 + \tau_{\mathrm{xz}}^2\right)\Big], \\
J_3 &= \frac{1}{3}(\boldsymbol{s}' \cdot \boldsymbol{s}') : \boldsymbol{s}' = \frac{1}{27}(2I_1^3 + 9I_1 I_2 + 27I_3).
\end{aligned}
$$

A convenient choice of invariants is p', the mean effective stress; q, the deviator stress (also named distortional, shear, or 'deviatoric'); and θ, the Lode angle:

$$p' = \frac{1}{3}I_1 = \frac{1}{3}(\sigma'_{\mathrm{x}} + \sigma'_{\mathrm{y}} + \sigma'_{\mathrm{z}}), \tag{B.2}$$

$$
\begin{aligned}
q &= \sqrt{3J_2} \\
&= \frac{\sqrt{2}}{2}\sqrt{(\sigma'_{\mathrm{x}} - \sigma'_{\mathrm{y}})^2 + (\sigma'_{\mathrm{y}} - \sigma'_{\mathrm{z}})^2 + (\sigma'_{\mathrm{z}} - \sigma'_{\mathrm{x}})^2 + 6\left(\tau_{\mathrm{xy}}^2 + \tau_{\mathrm{yz}}^2 + \tau_{\mathrm{xz}}^2\right)},
\end{aligned} \tag{B.3}
$$

$$\sin 3\theta = \frac{-3\sqrt{3}}{2}\frac{J_3}{J_2^{3/2}}. \tag{B.4}$$

This choice of invariants is not arbitrary because the above quantities have geometric significance in principal effective stress space $\sigma'_1 : \sigma'_2 : \sigma'_3$ represented in Fig. B.1a (Potts and Zdravković, 1999). The value of p' is a measure of the distance along the space diagonal ($\sigma'_1 = \sigma'_2 = \sigma'_3$), of the current deviatoric plane from the origin, in principal effective stress space (a deviatoric plane is defined as perpendicular to the space diagonal). The value of q provides a measure of the distance of the current stress state from the space diagonal in the deviatoric plane, and the magnitude of θ defines the orientation of the stress state. For a particular order of the principal effective stresses (for example $\sigma'_{\mathrm{I}} = \sigma'_3 \geq \sigma'_{\mathrm{II}} = \sigma'_1 \geq \sigma'_{\mathrm{III}} = \sigma'_2$), θ is constrained to lie between the lines marked $\theta = -30°$ and $\theta = 30°$ of Fig. B.2. If the current state lies in a position that is a cyclic permutation of σ'_1, σ'_2, σ'_3 then these limiting values of θ correspond to triaxial extension and compression respectively (Fig. B.2)[1]

Using the cubic formula (the closed-form solution for a cubic equation) to solve Eq. (B.1), the principal stresses can be expressed in terms of the three invariants (p',

[1]If not a cyclic permutation, then these limiting values of θ correspond to triaxial compression and extension.

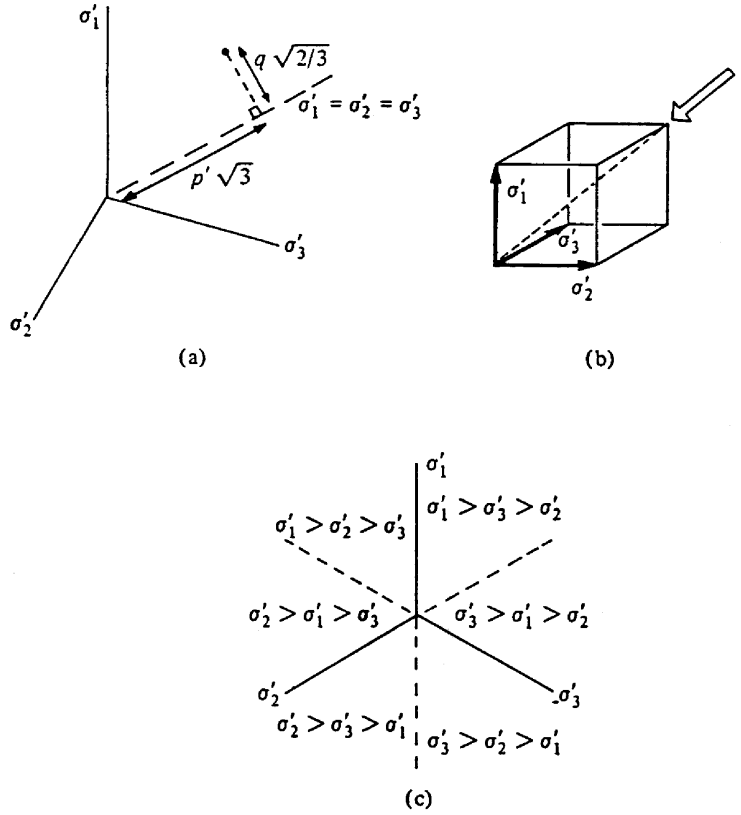

Figure B.1 (a) General mean stress p' and deviator stress q in principal effective stress space; (b) cube with sides defined by principal stress axes $\sigma'_1 : \sigma'_2 : \sigma'_3$; and (c) assignment of major, intermediate, and minor principal stresses in sectors of the deviatoric view of the principal stress space (Muir Wood, 1990).

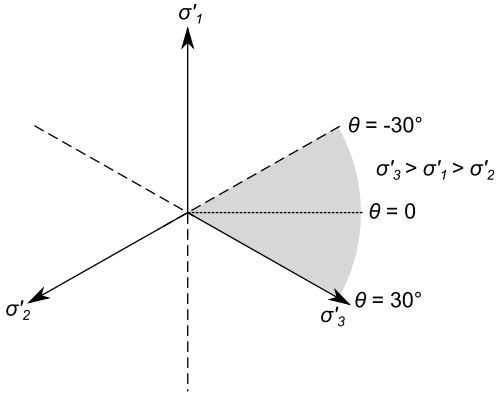

Figure B.2 Lode angle for $\sigma'_3 > \sigma'_1 > \sigma'_2$.

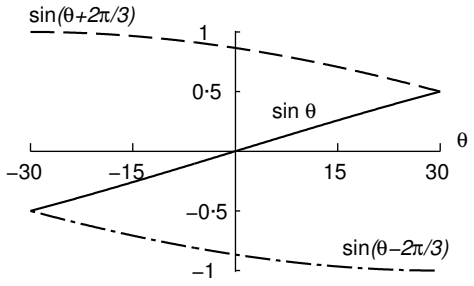

Figure B.3 Principal stresses dependency on Lode angle.

q, θ) (Potts and Zdravković, 1999; Yu, 2006) (Fig. B.3):

$$\sigma'_{\mathrm{I}} = p' + \frac{2}{3} q \sin\left(\theta + \frac{2\pi}{3}\right),$$
$$\sigma'_{\mathrm{II}} = p' + \frac{2}{3} q \sin\theta,$$
$$\sigma'_{\mathrm{III}} = p' + \frac{2}{3} q \sin\left(\theta - \frac{2\pi}{3}\right).$$

In triaxial loading, the deviator stress is usually defined as to $q = \sigma'_1 - \sigma'_3$ (so it can become negative).

The Lode angle is sometimes defined with a cosine (Mortara, 2008) or a tangent (Potts and Zdravković, 1999) instead of a sine (Eq. B.4). This only changes the value of the angle by a constant phase shift (e.g. if the Lode angle is defined in terms of cosine instead of sine in Eq. (B.4), then θ spans from 0° for TXC to 60° for TXE).

Strain While it is possible to talk about a state of stress with respect to zero stress (taken as atmospheric pressure), there is no absolute zero for strain so we have to talk about changes, or increments, of strain (Atkinson, 2007). A small increment of strain is noted $\delta\varepsilon$.

Principal strain increments The principal strain increments $\delta\varepsilon_1$, $\delta\varepsilon_2$ and $\delta\varepsilon_3$ are calculated the same way as the principal stresses, *i.e.* by solving:

$$\begin{vmatrix} \delta\varepsilon_{\mathrm{x}} - \delta\varepsilon & \delta\varepsilon_{\mathrm{xy}} & \delta\varepsilon_{\mathrm{xz}} \\ \delta\varepsilon_{\mathrm{xy}} & \delta\varepsilon_{\mathrm{y}} - \delta\varepsilon & \delta\varepsilon_{\mathrm{yz}} \\ \delta\varepsilon_{\mathrm{xz}} & \delta\varepsilon_{\mathrm{yz}} & \delta\varepsilon_{\mathrm{z}} - \delta\varepsilon \end{vmatrix} = 0.$$

Strain invariants The strain invariants corresponding to p' and q are the volumetric and distortional strains. The volumetric strain increment is defined as:

$$\delta\varepsilon_{\mathrm{v}} = \delta\varepsilon_1 + \delta\varepsilon_2 + \delta\varepsilon_3,$$

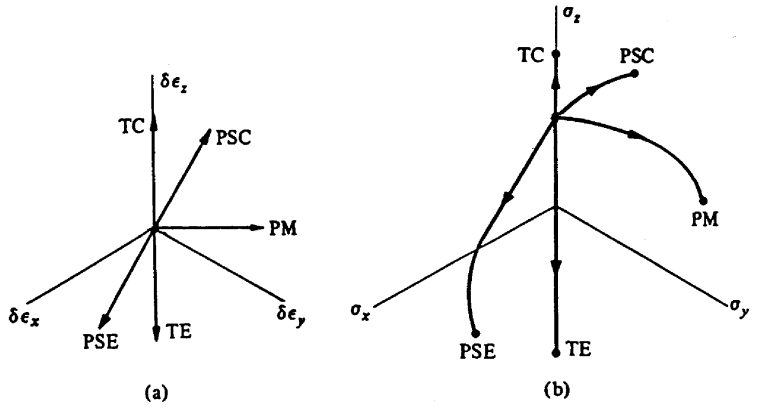

Figure B.4 (a) Deviatoric strain paths and (b) deviatoric stress paths according to Cam clay model with Mohr–Coulomb failure in *constant volume* triaxial compression TC, triaxial extension TE, plane-strain compression PSC, plane strain extension PSE, and pressuremeter cylindrical cavity expansion PM (Muir Wood, 1990).

while the distortional strain as (Muir Wood, 1990):

$$\delta\varepsilon_q = \frac{1}{3}\sqrt{2\left[\left(\delta\varepsilon_x - \delta\varepsilon_y\right)^2 + \left(\delta\varepsilon_y - \delta\varepsilon_z\right)^2 + \left(\delta\varepsilon_z - \delta\varepsilon_x\right)^2\right] + 3\left(\delta\gamma_{xy}^2 + \delta\gamma_{yz}^2 + \delta\gamma_{xz}^2\right)}.$$

In triaxial loading, the distortional strain reduces to: $\delta\varepsilon_q = \frac{2}{3}\left(\delta\varepsilon_z - \delta\varepsilon_x\right)$.

Appendix C

Rate of deformation and spin tensors

The rate of deformation tensor ($\mathbf{D}$) and the spin tensor ($\mathbf{W}$) are defined in this work as the symmetric and skew-symmetric parts of the *opposite* of the velocity gradient ($-\nabla\mathbf{v}$), respectively. The minus sign enables the normal stresses to be positive in compression. Fig. C.1 depicts an infinitesimal element surrounded by positive normal and shear stresses.[1] Unfortunately, the minus sign in front of the velocity gradient implies that shear stresses are negative around a loaded pile, which is the reason why γ and τ were introduced in Eq. (5.3), p. 95.

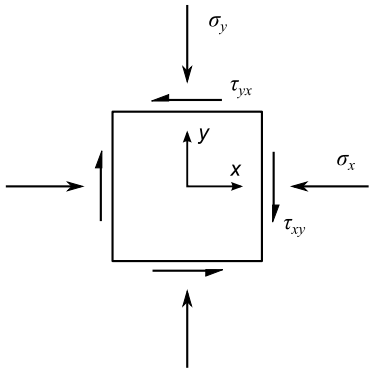

Figure C.1 Stress convention in physical space: normal stress is positive in compression and shear stress is positive if it acts on a positive face and negative direction or if it acts in a negative face and positive direction.

The following two subsections present the expression of $\mathbf{D}$ and $\mathbf{W}$ for a cartesian coordinate system (Section C.1) and for a cylindrical coordinate system (Section C.2).

[1] The shear stress convention in the physical space is not to be confused with the shear stress convention used to draw a Mohr circle, for which anticlockwise shear stresses are positive.

C.1 Cartesian coordinates

$$\mathbf{D} = \begin{bmatrix} \dfrac{-\partial v_x}{\partial x} & \dfrac{-1}{2}\left(\dfrac{\partial v_x}{\partial y} + \dfrac{\partial v_y}{\partial x}\right) & \dfrac{-1}{2}\left(\dfrac{\partial v_x}{\partial z} + \dfrac{\partial v_z}{\partial x}\right) \\ & \dfrac{-\partial v_y}{\partial y} & \dfrac{-1}{2}\left(\dfrac{\partial v_y}{\partial z} + \dfrac{\partial v_z}{\partial y}\right) \\ \text{sym} & & \dfrac{-\partial v_z}{\partial z} \end{bmatrix},$$

and:

$$\mathbf{W} = \begin{bmatrix} 0 & \dfrac{-1}{2}\left(\dfrac{\partial v_x}{\partial y} - \dfrac{\partial v_y}{\partial x}\right) & \dfrac{-1}{2}\left(\dfrac{\partial v_x}{\partial z} - \dfrac{\partial v_z}{\partial x}\right) \\ & 0 & \dfrac{-1}{2}\left(\dfrac{\partial v_y}{\partial z} - \dfrac{\partial v_z}{\partial y}\right) \\ \text{anti} & & 0 \end{bmatrix}.$$

C.2 Cylindrical coordinates

$$\mathbf{D} = \begin{bmatrix} \dot{\varepsilon}_r & \frac{1}{2}\dot{\gamma}_{r\theta} & \frac{1}{2}\dot{\gamma}_{rz} \\ & \dot{\varepsilon}_\theta & \frac{1}{2}\dot{\gamma}_{\theta z} \\ \text{sym} & & \dot{\varepsilon}_z \end{bmatrix}$$

$$= \begin{bmatrix} \dfrac{-\partial v_r}{\partial r} & \dfrac{-1}{2}\left(\dfrac{1}{r}\dfrac{\partial v_r}{\partial \theta} + \dfrac{\partial v_\theta}{\partial r} - \dfrac{v_\theta}{r}\right) & \dfrac{-1}{2}\left(\dfrac{\partial v_r}{\partial z} + \dfrac{\partial v_z}{\partial r}\right) \\ & \dfrac{-1}{r}\dfrac{\partial v_\theta}{\partial \theta} - \dfrac{v_r}{r} & \dfrac{-1}{2}\left(\dfrac{\partial v_\theta}{\partial z} + \dfrac{1}{r}\dfrac{\partial v_z}{\partial \theta}\right) \\ \text{sym} & & \dfrac{-\partial v_z}{\partial z} \end{bmatrix},$$

and:

$$\mathbf{W} = \begin{bmatrix} 0 & \frac{-1}{2}\left(\frac{1}{r}\frac{\partial v_r}{\partial \theta} - \frac{\partial v_\theta}{\partial r} - \frac{v_\theta}{r}\right) & \frac{-1}{2}\left(\frac{\partial v_r}{\partial z} - \frac{\partial v_z}{\partial r}\right) \\ & 0 & \frac{-1}{2}\left(\frac{\partial v_\theta}{\partial z} - \frac{1}{r}\frac{\partial v_z}{\partial \theta}\right) \\ \text{anti} & & 0 \end{bmatrix}.$$

When the problem is axisymmetric, these tensors reduce to:

$$\mathbf{D} = \begin{bmatrix} \frac{-\partial v_r}{\partial r} & 0 & \frac{-1}{2}\left(\frac{\partial v_r}{\partial z} + \frac{\partial v_z}{\partial r}\right) \\ 0 & \frac{-v_r}{r} & 0 \\ \frac{-1}{2}\left(\frac{\partial v_r}{\partial z} + \frac{\partial v_z}{\partial r}\right) & 0 & \frac{-\partial v_z}{\partial z} \end{bmatrix},$$

and

$$\mathbf{W} = \begin{bmatrix} 0 & 0 & \frac{-1}{2}\left(\frac{\partial v_r}{\partial z} - \frac{\partial v_z}{\partial r}\right) \\ 0 & 0 & 0 \\ \frac{1}{2}\left(\frac{\partial v_r}{\partial z} - \frac{\partial v_z}{\partial r}\right) & 0 & 0 \end{bmatrix}.$$

Appendix D

Driver

The *Driver* is the numerical implementation of the constitutive model for an infinitesimal soil particle. The Driver contains an outer shell that integrates any incremental type constitutive equation and an inner shell: the incremental type constitutive equation. The outer shell has been proposed by Bardet and Choucair (1991) and written by Claudio Tamagnini. The hypoplastic (and intergranular strain enhancement) inner shell used herein is presented in Chapter 4 and has been written by David Mašín.

Unfortunately, the hypoplastic inner shell contained a few errors which compromised the Driver results when subjected to shear stress or strain. Theses errors were corrected and then validated by comparison with the Plaxis SoilTest module.

The input of the Driver is composed of the current strains (6 components) and state of the soil, and the prescribed strain/total stress (6 components). The state depends on the constitutive model; for the (modified) Cam clay model, the state is defined by effective stress and void ratio (7 components); for clay hypoplasticity with intergrannular strain, the state is defined by effective stress, void ratio, and intergrannular strain (13 components). The driver output is the state and strains resulting from the prescribed strain and/or stress.

This appendix is composed of four sections: Section D.1 presents the Driver inner parts, Section D.2 shows the validation of the Driver against a one-element test from the Plaxis SoilTest module, and Section D.3 lists the useful tensor operations and their equivalence in Voigt notation.

D.1 Driver inner parts

D.1.1 Strain or stress/mixed control

When imposing strain, the solution of a constitutive model is reasonably straightforward. However, when imposing stress or mixed control, the soil state at the next time step has to be found by iteration.

The equation to solve is the following:

$$\overset{\triangledown}{\boldsymbol{\sigma}}' = \mathscr{M}' : \mathbf{D}, \qquad \text{(4.1bis) (D.1)}$$

where the right side of Eq. (D.1) is the soil skeleton effective response (from the constitutive model, Section 4).

During a time step (from time t_n to time t_{n+1}) of *strain* control:

- The 6 components of stress and the 6 components of strain at time t_n are known;
- The 6 components of strain at time t_{n+1} are imposed;
- And the 6 components of stress at time t_{n+1} are directly computed from Eq. (D.1).

However, during mixed or stress control, things are less straightforward:

- The 6 components of stress and the 6 components of strainat time t_n are known;
- 6 components of stress and/or strain at time t_{n+1} are imposed;
- And the last 6 components of stress and/or strain at time t_{n+1}, the ones which are not imposed, are computed from Eq. (D.1). To perform this computation (*i.e.* finding the zero of Eq. D.1), a modified Newton-Raphson iteration scheme is used (Bardet and Choucair, 1991).

D.1.2 Explicit integration

Independently of strain or stress/mixed control, and after having solved Eq. (D.1) as explained above, the stress rate (the left part of Eq. D.1) has to be integrated in order to obtain the stress at time t_{n+1}.

In the Driver, the constitutive model is integrated using an explicit adaptive Runge-Kutta-Felhberg integration scheme with local substepping and error control (Sloan, 1987; Tamagnini et al., 2000).

In fact, the constitutive model (Eq. D.1) forms an initial value problem (ordinary differential equation with initial condition) of the form:

$$\frac{\partial \mathbf{y}}{\partial t} = \mathbf{f}(t, \mathbf{y}), \qquad \mathbf{y}(t_0) = \mathbf{y}_0. \tag{D.2}$$

The vector $\mathbf{y}$ is a column vector:

$$\mathbf{y}^{\mathrm{T}} = (\boldsymbol{\sigma}'^{\mathrm{T}} \ \boldsymbol{\varepsilon}^{\mathrm{T}} \ \mathbf{q}^{\mathrm{T}})^{\mathrm{T}},$$

where $\boldsymbol{\sigma}'$ is the effective stress tensor (6 components), $\boldsymbol{\varepsilon}$ is the strain tensor (6 components) and $\mathbf{q}$ contains the state variables, other than stress. Vector $\mathbf{q}$ depends on the constitutive model used: for modified Cam clay, state can be defined with the preconsolidation pressure and the void ratio (or any two equivalent quantities defining state on the compression plot relative to the ncl); for hypoplasticity for clays with intergranular strain, state is defined by void ratio, effective stress (defining the state in the compression plot relative to the ncl), and intergranular strain.

The approximation of the solution $\mathbf{y}(t_n)$ of Eq. (D.2) is computed by a numerical integration. The time domain is discretised into N_t time steps where the step size is Δt, so that $t^{n+1} = t^n + \Delta t$. The numerical integration produces an approximate $\mathbf{Y}^{n+1} \approx \mathbf{y}(t_{n+1})$.

The numerical integration used in the driver is the finite difference adaptive Runge-Kutta-Fehlberg method of second and third orders. This finite difference scheme computes two estimates of $\mathbf{Y}^{n+1}$: a second order estimate ($\hat{\mathbf{Y}}^{n+1}$) and a third order estimate ($\tilde{\mathbf{Y}}^{n+1}$). If the difference between the two estimates is small enough (error control), the integration is accepted, *i.e.* $\mathbf{Y}^{n+1} = \hat{\mathbf{Y}}^{n+1}$. If not, the time step is severed (substeppping) and the process is started again for each *sub* time step.

In more details:

$$\hat{\mathbf{Y}}^{n+1} = \mathbf{Y}^n + \Delta t\, K_2,$$
$$\tilde{\mathbf{Y}}^{n+1} = \mathbf{Y}^n + \frac{\Delta t}{6}(K_1 + 4K_2 + K_3),$$

where:

$$K_1 = f(t^n, \mathbf{Y}^n),$$
$$K_2 = f\left(t^n + \frac{1}{2}\Delta t, \mathbf{Y}^n + \frac{\Delta t}{2}K_1\right),$$
$$K_3 = f\left(t^n + \frac{1}{2}\Delta t, \mathbf{Y}^n - \Delta t K_1 + 2\Delta t K_2\right).$$

For the time increment $n+1$, the accuracy of the solution is estimated by an estimate of the local error θ^{n+1} of the second order method. The integration is accepted if:

$$\theta^{n+1} \triangleq \frac{||\tilde{\mathbf{Y}}^{n+1} - \hat{\mathbf{Y}}^{n+1}||}{||\tilde{\mathbf{Y}}^{n+1}||} < \mathrm{TOL},$$

where TOL is the prescribed error tolerance, equal to 1000 in the Driver. In order to prevent infinite loops, there is a maximum number of time substeps allowed, the default value of which is 10 000.

D.1.3 Rates

Since we are only concerned with inviscid relations, rates are equivalently replaced by increments (Bardet and Choucair, 1991). The increments of deformation, rotation, objective stress and material stress are equal to their respective rates multiplied by an arbitrary time interval δt:

$$\delta\boldsymbol{\varepsilon} = \mathbf{D}\delta t, \quad \delta\overset{\triangledown}{\boldsymbol{\sigma}}' = \overset{\triangledown}{\boldsymbol{\sigma}}'\delta t, \quad \delta\boldsymbol{\sigma}' = \dot{\boldsymbol{\sigma}}'\delta t, \quad \ldots$$

Furthermore, when objective and material stress rates coincide (*e.g.* for the Strain Path Method integration defined in Section 5.2.2, p. 96), then $\delta\overset{\triangledown}{\boldsymbol{\sigma}}' = \delta\boldsymbol{\sigma}'$.

D.1.4 Voigt notation

In order to skim the high order tensors describing the constitutive relationship, Voigt notation is used, which transforms second order tensors in vectors and fourth order tensors into second order tensors.

The indicial convention used is as in Bardet and Choucair (1991):

$$\dot{\boldsymbol{\sigma}}^{\mathrm{T}} = (\dot{\sigma}'_{\mathrm{x}} \;\; \dot{\sigma}'_{\mathrm{y}} \;\; \dot{\sigma}'_{\mathrm{z}} \;\; \dot{\tau}_{\mathrm{xy}} \;\; \dot{\tau}_{\mathrm{yz}} \;\; \dot{\tau}_{\mathrm{xz}}). \tag{D.3}$$

The shear strain components are doubled:

$$\mathbf{D}^{\mathrm{T}} = (\dot{\varepsilon}_{\mathrm{x}} \;\; \dot{\varepsilon}_{\mathrm{y}} \;\; \dot{\varepsilon}_{\mathrm{z}} \;\; 2\dot{\varepsilon}_{\mathrm{xy}} \;\; 2\dot{\varepsilon}_{\mathrm{yz}} \;\; 2\dot{\varepsilon}_{\mathrm{xz}}) = (\dot{\varepsilon}_{\mathrm{x}} \;\; \dot{\varepsilon}_{\mathrm{y}} \;\; \dot{\varepsilon}_{\mathrm{z}} \;\; \dot{\gamma}_{\mathrm{xy}} \;\; \dot{\gamma}_{\mathrm{yz}} \;\; \dot{\gamma}_{\mathrm{xz}}), \tag{D.4}$$

which allows the use 4th order stiffness matrix coefficients (m_{klmn}) without modification into the 2nd order Voigt notation stiffness matrix (M_{ij}):

$$\mathscr{M} = \begin{bmatrix} m_{\mathrm{xxxx}} & m_{\mathrm{xxyy}} & m_{\mathrm{xxzz}} & m_{\mathrm{xxxy}} & m_{\mathrm{xxyz}} & m_{\mathrm{xxxz}} \\ m_{\mathrm{yyxx}} & m_{\mathrm{yyyy}} & m_{\mathrm{yyzz}} & m_{\mathrm{yyxy}} & m_{\mathrm{yyyz}} & m_{\mathrm{yyxz}} \\ m_{\mathrm{zzxx}} & m_{\mathrm{zzyy}} & m_{\mathrm{zzzz}} & m_{\mathrm{zzxy}} & m_{\mathrm{zzyz}} & m_{\mathrm{zzxz}} \\ m_{\mathrm{xyxx}} & m_{\mathrm{xyyy}} & m_{\mathrm{xyzz}} & m_{\mathrm{xyxy}} & m_{\mathrm{xyyz}} & m_{\mathrm{xyxz}} \\ m_{\mathrm{yzxx}} & m_{\mathrm{yzyy}} & m_{\mathrm{yzzz}} & m_{\mathrm{yzxy}} & m_{\mathrm{yzyz}} & m_{\mathrm{yzxz}} \\ m_{\mathrm{xzxx}} & m_{\mathrm{xzyy}} & m_{\mathrm{xzzz}} & m_{\mathrm{xzxy}} & m_{\mathrm{xzyz}} & m_{\mathrm{xzxz}} \end{bmatrix}$$

$$= \begin{bmatrix} M_{11} & M_{12} & M_{13} & M_{14} & M_{15} & M_{16} \\ M_{12} & M_{22} & M_{23} & M_{24} & M_{25} & M_{26} \\ M_{13} & M_{23} & M_{33} & M_{34} & M_{35} & M_{36} \\ M_{14} & M_{24} & M_{34} & M_{44} & M_{45} & M_{46} \\ M_{15} & M_{25} & M_{35} & M_{45} & M_{55} & M_{56} \\ M_{16} & M_{26} & M_{36} & M_{46} & M_{56} & M_{66} \end{bmatrix}.$$

For example, for isotropic linear elasticity, the stress rate-strain rate relationship in Voigt notation is:

$$\begin{bmatrix} \dot{\sigma}_{\mathrm{x}} \\ \dot{\sigma}_{\mathrm{y}} \\ \dot{\sigma}_{\mathrm{z}} \\ \dot{\tau}_{\mathrm{xy}} \\ \dot{\tau}_{\mathrm{yz}} \\ \dot{\tau}_{\mathrm{xz}} \end{bmatrix} = \frac{E}{(1+\nu)(1-2\nu)} \begin{bmatrix} 1-\nu & \nu & \nu & 0 & 0 & 0 \\ \nu & 1-\nu & \nu & 0 & 0 & 0 \\ \nu & \nu & 1-\nu & 0 & 0 & 0 \\ 0 & 0 & 0 & \frac{1-2\nu}{2} & 0 & 0 \\ 0 & 0 & 0 & 0 & \frac{1-2\nu}{2} & 0 \\ 0 & 0 & 0 & 0 & 0 & \frac{1-2\nu}{2} \end{bmatrix} \begin{bmatrix} \dot{\varepsilon}_{\mathrm{x}} \\ \dot{\varepsilon}_{\mathrm{y}} \\ \dot{\varepsilon}_{\mathrm{z}} \\ 2\dot{\varepsilon}_{\mathrm{xy}} \\ 2\dot{\varepsilon}_{\mathrm{yz}} \\ 2\dot{\varepsilon}_{\mathrm{xz}} \end{bmatrix}.$$

D.2 Validation

The Driver has been validated by comparing its results to the Plaxis SoilTest module. The aim was to validate the model using hypoplasticity by Mašín (2005) enhanced by intergranular strain (Niemunis and Herle, 1997).

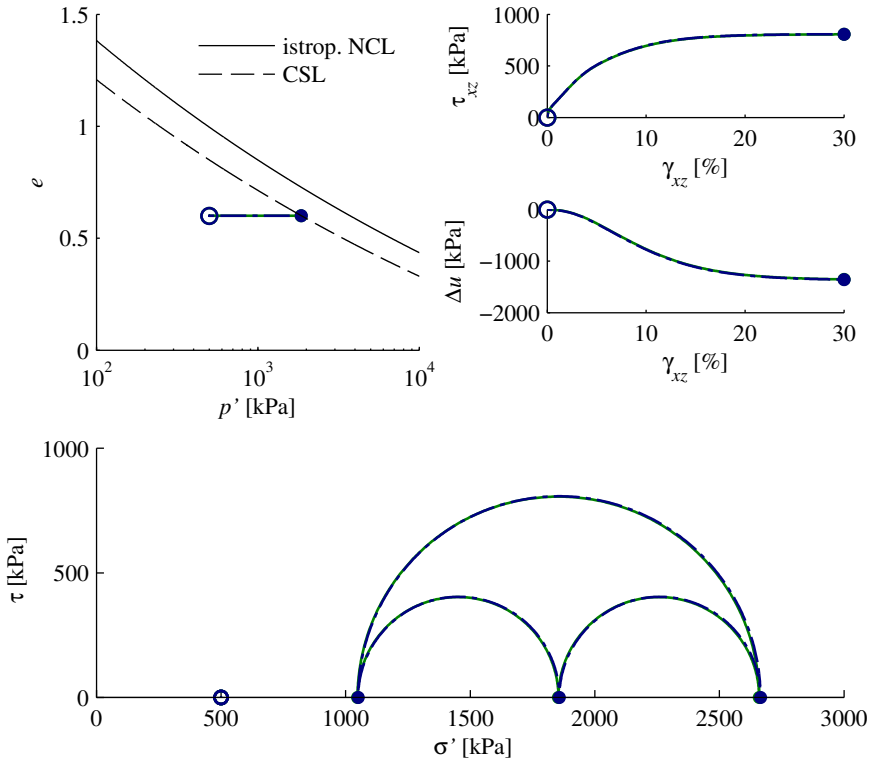

Figure D.1 Driver validation with Plaxis SoilTest; initial state on the dry side of critical (○ is initial state and ● is final state, the blue and green line correspond respectively to Plaxis SoilTest and the Driver).

A simple shear test (see Fig. 4.3, p. 73) was performed to validate the Driver. The shear strain was imposed up to a value of $\gamma_{xz} = 30\%$ and the constitutive parameters where those of London clay (Table 4.2, p. 71)

Validation for two initial states is presented:

1. Dry side of critical: $e_0 = 0{\cdot}6$ and isotropic initial state $\sigma_{x0} = \sigma_{y0} = \sigma_{z0} = 500\,\text{kPa}$, $u_{w0} = 0$;

2. Wet side of critical: $e_0 = 0{\cdot}95$ and $K_0 = 0{\cdot}7$ initial state $\sigma_{x0} = \sigma_{y0} = 350\,\text{kPa}$, $\sigma_{z0} = 500\,\text{kPa}$, $u_{w0} = 0$.

The results from each test are respectively on Figs. D.1 and D.2.

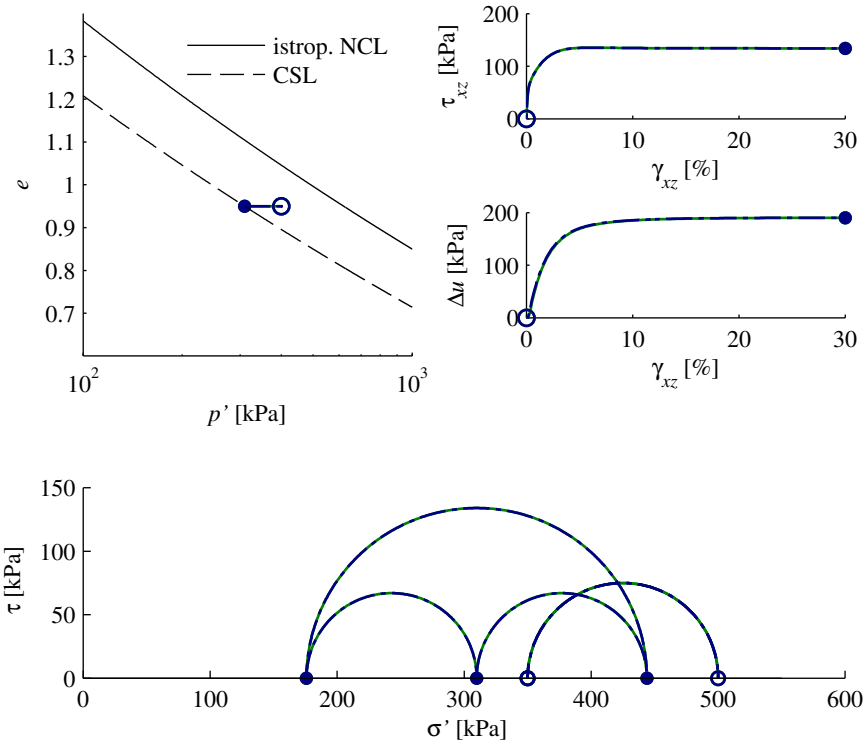

Figure D.2 Driver validation with Plaxis SoilTest; initial state on the wet side of critical (○ is initial state and ● is final state, the blue and green line correspond respectively to Plaxis SoilTest and the Driver).

D.3 Tensor operations

Contracted (inner) product

- Tensor product (or simple inner product):
  $\mathbf{X} = \mathbf{A} \cdot \mathbf{B}$ $\quad X_{ik} = A_{ij} B_{jk}$ (result: 2nd order tensor),
  $x = \underline{a} \cdot \underline{b} = |\underline{a}||\underline{b}| \cos\theta$ $\quad x = a_i b_i$ (result: scalar);

- Double inner product (or scalar product):
  $X = \mathbf{A} : \mathbf{B}$ $\quad X = A_{ij} B_{ji}$, $= A_{ij} B_{ij}$ if $\mathbf{A}$ and $\mathbf{B}$ are symmetric (result: scalar),
  $\mathbf{X} = \mathscr{A} : \mathbf{B}$ $\quad X_{ij} = A_{ijkl} B_{kl}$ (result: 2nd order tensor),
  $\mathscr{X} = \mathscr{A} : \mathscr{B}$ $\quad X_{ijkl} = A_{ijkl} B_{ijkl}$ (result: 4th order tensor);

Dyadic (outer) product

$\mathscr{X} = \mathbf{A} \otimes \mathbf{B}$ $\quad X_{ijkl} = A_{ij} B_{kl}$ (result: 4th order tensor)

Tensor operations in Voigt notation

Using the Voigt notation (defined in Eqs. D.3 and D.4), the tensor products become quite tricky. Furthermore, the operations are not the same for strains and for stresses because the three shear strain terms are doubled (see Eq. D.4). The following table summarizes the tensor products used in Voigt notation in the Driver:

Operation	Matlab (Voigt notation) operation
$\mathbf{A} \cdot \mathbf{B}$	stress_mult(A,B)
$\mathbf{A} : \mathbf{B}$	A'∗M∗B
$\mathbf{A} \otimes \mathbf{B}$	A∗B'
$\mathbf{D} : \mathbf{E}$	D'∗M2∗E
$\mathscr{L} : \mathbf{D}$	L∗D
$\mathscr{A} \otimes \mathbf{D}$	A∗(C∗D)'

where:

A and B are 6×1 "stress like" vectors (corresponding to second-order symmetric stress tensors);

D and E are 6×1 "strain like" vectors (corresponding to second-order symmetric strain tensors) which means the last three components are the engineering shear strain (see Section D.1);

$$\text{stress\_mult(A,B)} = \begin{pmatrix} A_1 * B_1 + A_4 * B_4 + A_6 * B_6 \\ A_4 * B_4 + A_2 * B_2 + A_5 * B_5 \\ A_6 * B_6 + A_5 * B_5 + A_3 * B_3 \\ A_1 * B_4 + A_4 * B_2 + A_6 * B_5 \\ A_4 * B_6 + A_2 * B_5 + A_5 * B_3 \\ A_6 * B_1 + A_5 * B_4 + A_3 * B_6 \end{pmatrix};$$

M is a diagonal 3×3 matrix, the diagonal being (from top to bottom): (1 1 1 2 2 2);

M2 is a diagonal 3×3 matrix, the diagonal being (from top to bottom): (1 1 1 0·5 0·5 0·5);

C is a 6x1 vector: $(1\ 1\ 1\ 0{\cdot}5\ 0{\cdot}5\ 0{\cdot}5)^{T}$.

Appendix E

Pile driving model validation

The following appendix is divided in three sections. Appendix E.1 validates the choice and location of the Disk Shearing Model absorbing boundary. Appendix E.2 discusses the numerical stability and accuracy of the Disk Shearing Model. Finally, Appendix E.3 presents a validation of the consolidation analysis.

E.1 Disk Shearing Model absorbing boundary

The boundary of a numerically solved dynamic problem has to be treated with care. Without any specific formulation for the boundary, the waves are reflected back into the mesh when they hit the outer boundary. Two solutions exist: either extend the mesh enough so that the reflected waves do not hit back the domain of interest or use an absorbing boundary. The first solution being prohibitive in calculation time, an absorbing boundary is to be used.

This section describes the absorbing boundary used for the Disk Shearing Model. It is divided in four parts. The first on describes the analytical boundary condition developed by Novak et al. (1978) for harmonic solicitations in an elastic medium. Following, the Deeks and Randolph (1994) absorbing boundary is presented: an approximation of the Novak et al. (1978) solution for transient solicitations, which is the adsorbing boundary used for the Disk Shearing Model simulations. The last two parts of this section expose Disk Shearing Model simulations using the aforementioned Deeks and Randolph (1994) boundary, first for an elastic soil model under harmonic solicitations and then for an hypoplastic soil model under a hammer blow.

Novak et al. (1978) boundary for harmonic solicitations

Novak et al. (1978) developed an exact frequency dependent solution for an elastic soil subjected to an harmonic pile displacement. The development is presented for a plane strain disk of unit thickness. The inner boundary radius is R. Following Deeks and Randolph (1994), the equations following are presented in terms of stress rather than in term of force as in the original Novak et al. (1978) paper.

The hyperbolic wave equation which dictates the vertical motion of the soil u_z is:

$$\frac{\partial^2 u_z}{\partial t^2} = c_s^2 \frac{1}{r} \frac{\partial}{\partial r}\left(\frac{1}{r}\frac{\partial u_z}{\partial r}\right),$$

where $c_s = \sqrt{G/\rho}$ is the shear wave velocity of the soil with G being the soil shear modulus and ρ the soil density.

When a pile is subjected to a vertical harmonic solicitation of angular frequency ω, the shear stress of the elastic soil at radius r is (Novak et al., 1978):

$$\tau = k_z u_z \tag{E.1}$$

where u_z is the vertical displacement of the soil and k_z the complex stiffness:

$$k_z = \frac{G}{2r}(S_{z1} + iS_{z2}). \tag{E.2}$$

The real and imaginary shear stiffnesses, respectively S_{z1} and S_{z2}, are functions of the dimensionless frequency $a_0 = \omega r / c_s$:

$$\begin{aligned} S_{z1} &= 2a_0 \frac{J_1(a_0)J_0(a_0) + Y_1(a_0)Y_0(a_0)}{J_0^2(a_0) + Y_0^2(a_0)}, \\ S_{z2} &= \frac{1}{\pi} \frac{4}{J_0^2(a_0) + Y_0^2(a_0)}, \end{aligned} \tag{E.3}$$

where J_0 and J_1 are respectively the zero– and first–order Bessel function of the first kind and Y_0 and Y_1 are respectively the zero– and first–order Bessel function of the second kind (Abramowitz and Stegun, 1964).

Function S_{z1} and S_{z2} can be related to equivalent spring and dashpot coefficients, respectively k_b and c_b:

$$\begin{aligned} k_b &= \frac{G}{2r} S_{z1}, \\ c_b &= \frac{G}{2r} \frac{S_{z2}}{\omega}. \end{aligned}$$

Functions S_{z1} and S_{z2}, denoted as the 'exact solution,' are plotted in Fig. E.1 dimensionless frequency a_0.

Deeks and Randolph (1994) frequency independent boundary

However, the exact solution presented above includes frequency dependent terms, which complicate implementation for transient solicitations of broad frequency content, like a hammer blow. Therefore, Deeks and Randolph (1994) developed an approximated solution which is independent of the frequency content of the input

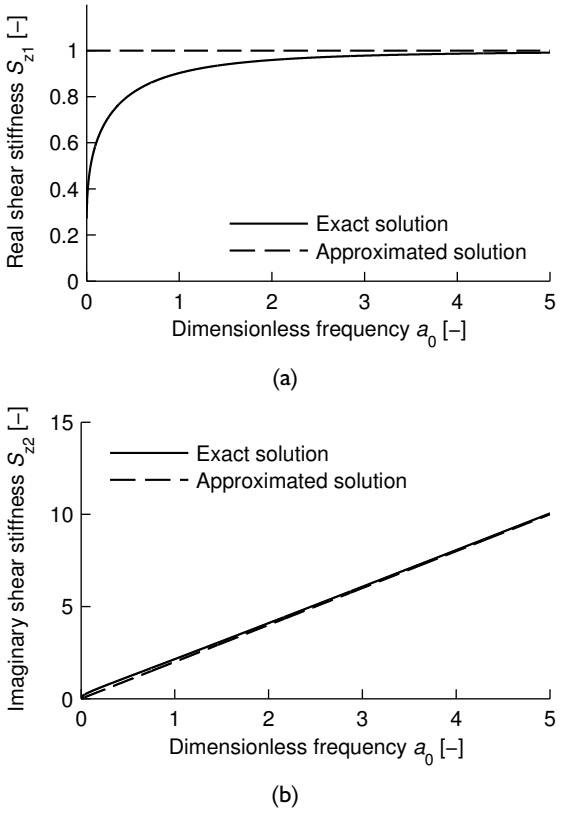

Figure E.1 Real and imaginary shear stiffnesses versus dimensionless frequency.

solicitation. This solution, which is presented below, is the absorbing boundary used for the Disk Shearing Model. The main assumption behind Deeks and Randolph (1994)'s proposal is that a wave of arbitrary shape propagating along the cylindrical soil in the positive radial direction may be closely approximated by (Whitham, 1974):

$$u_z(r,t) = \frac{1}{\sqrt{r}} f\left(\frac{r}{c_s} - t\right),$$

where f represents the wave shape and which leads to the approximated solution:

$$S_{z1} = 1,$$
$$S_{z2} = 2a_0,$$

or, in terms of equivalent spring and dashpot coefficients:

$$k_b = \frac{G}{2r},$$
$$c_b = \frac{G}{c_s}.$$

This approximated solution is plotted against the exact solution in Fig. E.1. Above a dimensionless frequency $a_0 = \omega r / c_s$ of 4, both solutions are very close.

For the Disk Shearing Model, the Deeks and Randolph (1994) absorbing boundary will produce acceptable results if the soil is elastic (therefore at the largest possible radius, where deformations are small) and if the dimensionless frequency a_0 is high (which also happens for a large radius).

Hereunder, the Deeks and Randolph (1994) absorbing boundary is applied to the Disk Shearing Model and validated for two cases: an elastic harmonic case similar to Novak et al. (1978)'s problem and a hypoplastic case similar to a hammer blow simulated in Chapter 5 and following.

Elastic harmonic validation

The first case is the pile harmonic displacement in an elastic soil, which has an exact numerical solution defined by Eqs (E.1)–(E.3).

The simulation parameters are the following: an elastic soil ($G = 5\,\text{MPa}$), an harmonic sollicitation ($\omega = 150\,\text{rad/s}$) and a boundary radius $r_b = 4\,\text{m}$ large enough for the dimensionless frequency a_0 to be higher than 4. The simulation is done with a soil weight of $\rho = 1901{\cdot}63\,\text{kg/m}^3$, which leads to $a_0 = 11{\cdot}70$. The pile radius is $R = 0{\cdot}5\,\text{m}$. The harmonic velocity imposed at the pile wall is of the following form:

$$v_{z,p} = v_{z0}\cos(\omega t),$$

where $v_{z0} = \omega u_{z0}$ and u_{z0} is the maximum pile displacement.

The comparison between the theoretical and numerical solution is presented in Fig. E.2, where the numerical and analytical solutions coincide perfectly. Selected contours of the vertical velocity in the elastic soil are plotted in Fig. E.3.

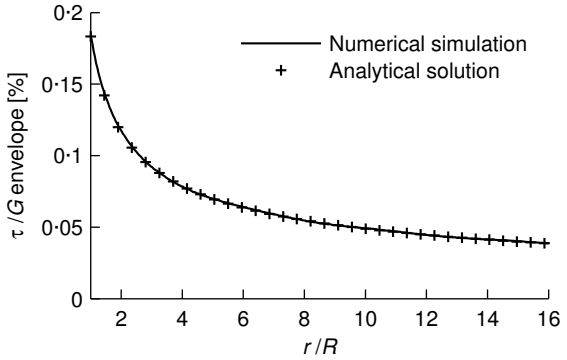

Figure E.2 Radial distribution of the shear stress envelope in an elastic soil around a harmonically moving pile.

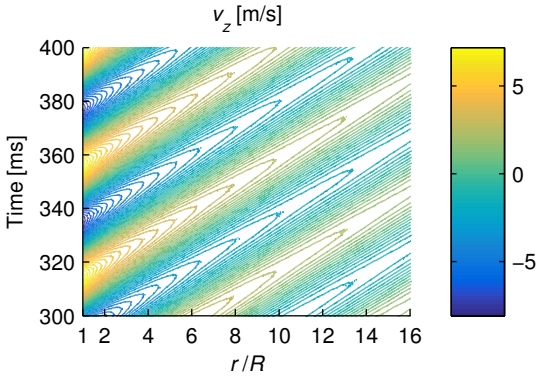

Figure E.3 Selected contours of the vertical velocity around a harmonically moving pile.

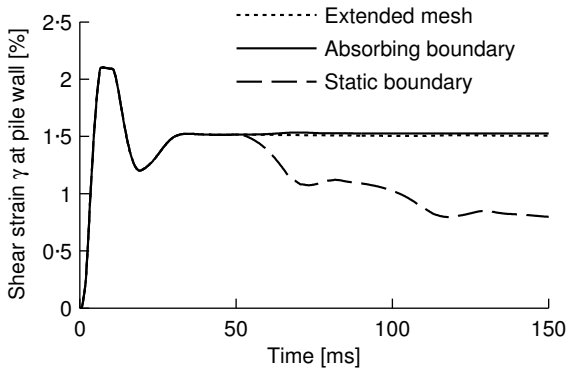

Figure E.4 Shear strain at pile wall during a driving blow for various outer boundary conditions.

Hypoplastic validation

The second validation case involves the Disk Shearing Model subjected to a hammer blow while using the hypoplastic constitutive model.

The Disk Shearing Model parameters are the following: a pile radius of $R = 0{\cdot}25\,\text{m}$, a radial discretisation of $\Delta r = 1\,\text{cm}$, a simulation time of 150 ms, and the critical time increment parameter $P_{\text{time}} = 50$. The imposed hammer blow is the one described in Fig. 5.7 (p. 103) and the constitutive model parameters are those of London clay described in Table 4.2 (p. 71).

Three different outer boundaries are compared: (1) a mesh extended to $r_{\text{b}} = 32R$, far enough for the outgoing waves not to be reflected during the 150 ms simulation, (2) the Deeks and Randolph (1994) absorbing boundary located at $r_{\text{b}} = 16R$, and (3) a static boundary located at $r_{\text{b}} = 16R$.

The results are depicted in Figs. E.4 and E.5. Fig. E.4 compares the shear strain at pile wall for the three boundaries explored. Using the static boundary, the wave reflected on the boundary hits the pile wall at 55 ms, greatly affecting the shear strain output. The Deeks and Randolph (1994) solution offers a final shear strain very close to the extended mesh, showing its validity. Fig. E.5 depicts the velocity contours for the three boundaries, confirming the aforementioned conclusion.

E.2 Disk Shearing Model numerical stability and accuracy

Two conditions are required for the Disk Shearing Model to produce stable and accurate results, one acting as a condition for the time step Δt and the second as a condition for the internodal distance Δr.

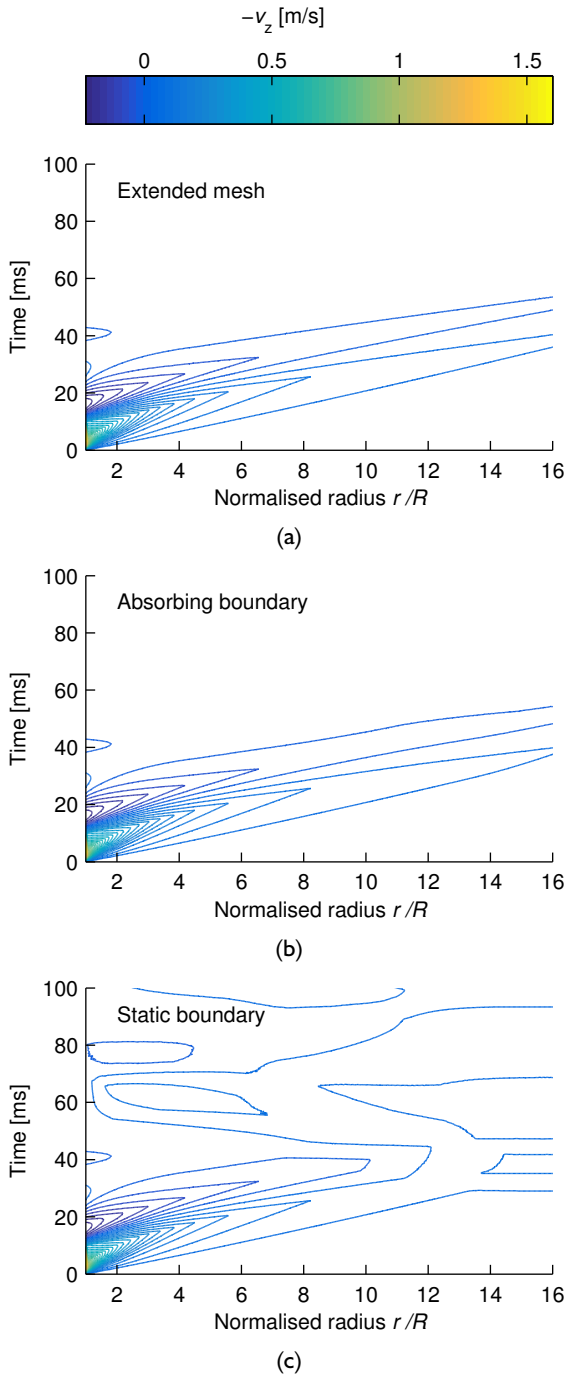

Figure E.5 Selected contours of the vertical velocity for (a) an extended mesh, (b) the Deeks and Randolph (1994) absorbing boundary, and (c) a free boundary.

Time step First of all, the time step has to be small enough to allow capturing the information transmitted through the shear waves. The critical time step is:

$$\Delta t < \Delta r / c_s,$$

where $c_s = \sqrt{G/\rho}$ is the shear wave velocity, G is the shear modulus of the soil,[1] and ρ is the soil density. In the Disk Shearing Model, this condition is enforced by dividing the critical time increment by the parameter $P_{time} \geq 1$:

$$\Delta t < \frac{1}{P_{time}} \frac{\Delta r}{c_s}. \tag{E.4}$$

Eq. (E.4) presents the $P_{time} \geq 1$ as a necessary stability condition, as the problem is conditionally stable. However, P_{time} is also an accuracy condition, as is explained hereunder, by comparing work and energy.

In the most general terms, the work W_{AB} to go from point A to point B is related to the change of kinetic energy from point A to point B through the work–energy theorem:

$$W_{AB} = K_B - K_A.$$

This relationship is satisfied for the Disk Shearing Model mathematical formulation (Section 5.2.3, p. 100). The force acting on any soil node is F_{unbal} in the vertical direction. The velocity acting on any soil node is v_z, in the vertical direction also. From the integration scheme, $F_{unbal} = Ma_z = M\partial v_z/\partial t$. The work done by any soil particle (non trivial only in the vertical direction) is:

$$W_{AB} = \int_{t_A}^{t_B} F_{unbal} v_z \mathrm{d}t = \int_{t_A}^{t_B} M \frac{\partial v_z}{\partial t} v_z \mathrm{d}t = \left[\frac{1}{2} M v_z^2 \right]_{t_A}^{t_B} = K_B - K_A.$$

However, the forward integration scheme used in the Disk Shearing Model ensues that the work–energy theorem is not satisfied unless a large value of P_{time}, the critical time increment divider defined in Eq. (E.4), is selected.

Fig. E.6a depicts the work and kinetic energy summed over the entire domain during a blow of the Disk Shearing Model for $P_{time} = 50$. Fig. E.6b shows the error E between work W and kinetic energy K.

A parametric study on parameter P_{time} yielded the result depicted in Fig E.7. The relationship between P_{time} and the error E is shown to be a log–log relationship. For $P_{time} = 1$, the error between kinetic energy and work is over 7%. For the Disk Shearing Model simulations, a value of $P_{time} = 50$ was selected, unless stated otherwise, which leads to an error $E = 0{\cdot}20\%$.

[1] The shear modulus predicted by the hypoplastic constitutive model depends on stress and strain (see Section 4.2, p. 70). Therefore, the shear modulus G chosen to compute the critical time step is taken as the small strain shear modulus G_0 at the largest stress that the soil can attain during a Disk Shearing Model simulation, *i.e.* p^*_{cs} if the soil is on dry side of critical and p'_e if the soil is on the wet side (p^*_{cs} and p'_e are defined in Fig. 4.1a, p. 67).

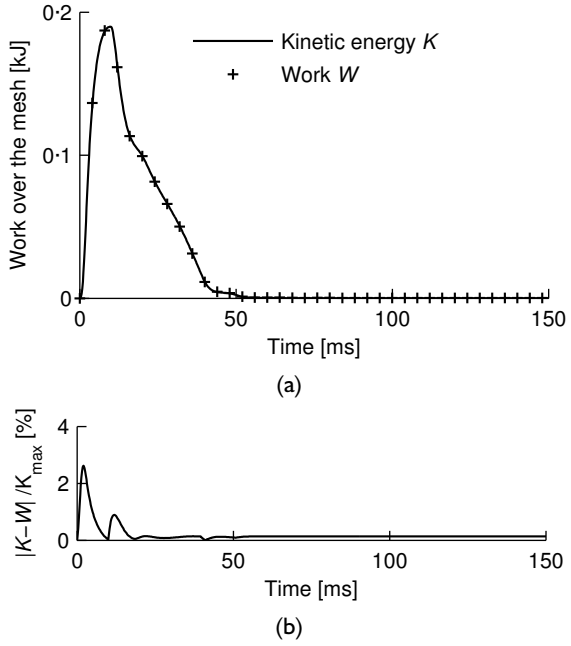

Figure E.6 (a) Work and kinetic energy over the entire domain during a blow for $P_{\text{time}} = 50$ and (b) Error between these two quantities versus time.

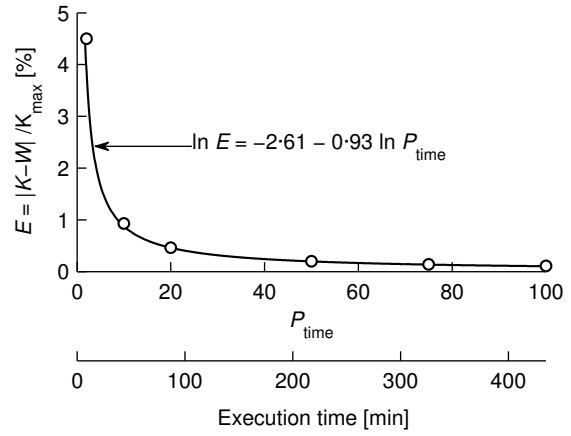

Figure E.7 Error between kinetic energy and work versus the critical time increment parameter P_{time}.

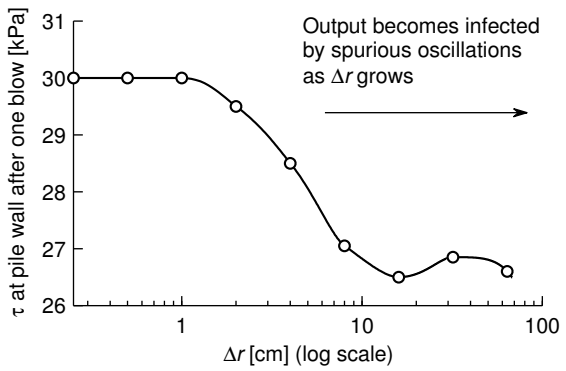

Figure E.8 Shear stress τ at pile wall after a blow for various internodal distances for $P_{\text{time}} = 50$.

Internodal distance The second stability and accuracy condition is related to the wavelength of the signal being transmitted in the soil (Kuhlemeyer and Lysmer, 1973):

$$\Delta r < \frac{\lambda}{10},$$

where λ is the wavelength associated with the highest frequency component that contains appreciable energy (Itasca, n.d.). If not respected, the model exhibits spurious oscillations. The Disk Shearing Model input is analytical (Section 5.2.3a, p. 101) but the non–linear response of the constitutive law implies that the wavelength λ in the soil is not known.

A parametric study on Δr was undertaken, the result of which is depicted in Fig. E.8, which shows the shear stress after one blow of the Disk Shearing Model versus internodal distance Δr. Above $\Delta r = 1\,\text{cm}$, the accuracy of the integration scheme reduces and the solution becomes infected by oscillations. Therefore, selection of the correct internodal distance Δr is paramount. Nonetheless, as long as a relatively small of Δr is chosen, the Shearing Disk Model output is acceptable, as shown by Fig. E.9 which compares the radial effective stress ratio ($\sigma'_{\text{ri}}/\sigma'_{\text{v0}}$) after installation for two radial discretisations.

It should be noted that when Δr is varied, the strain rate at the pile wall varies accordingly, as displayed in Fig. E.10. Therefore, should the constitutive model be rate dependent, the internodal distance should have been chosen so that the rate effects would be realistic.

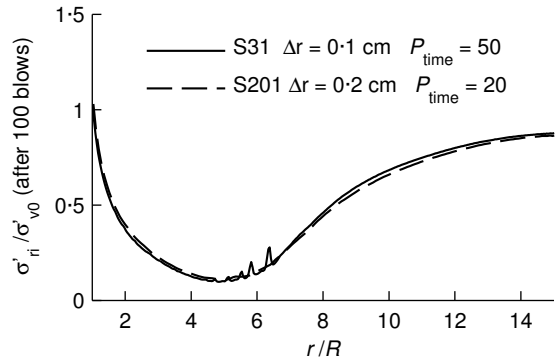

Figure E.9 Comparison of the distribution of radial effective stress after installation for two discretisations.

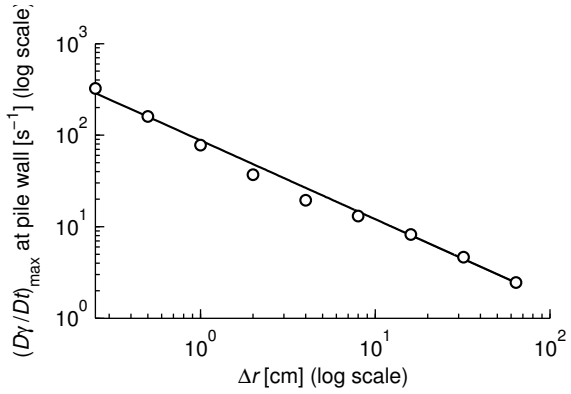

Figure E.10 Maximum shear strain rate $\dot{\gamma}_{\max}$ at pile wall for various internodal distances Δr, for $P_{\text{time}} = 50$.

E.3 Validation of the coupled consolidation analysis

The coupled consolidation analysis developed in Section 5.4 (p. 112) is validated against the results of Randolph, Carter and Wroth (1979), who performed a cylindrical cavity expansion followed by a coupled consolidation analysis using a modified Cam clay constitutive model (with a constant shear modulus G' and the compression plane defined in the conventional $v : \ln p'$ plane). The soil parameters are those of Boston Blue clay and are reproduced in Table E.1. Initial shear strength (s_{u0}) is taken as 33·27 kPa. Randolph, Carter and Wroth (1979) performed the expansion of cavity expansion from radius $R/\sqrt{3}$ to $2R/\sqrt{3} \approx 1{\cdot}15R$, while the present simulation expanded an initially void cavity to radius R.

Fig. E.11a and b depict the radial distribution of stress after cavity expansion and after equalisation, respectively. Results after cavity expansion (Fig. E.11a) are nearly identical. After equalisation (Fig. E.11b), the distribution of stress is very close to the one predicted by Randolph, Carter and Wroth (1979) even though the linear discretisation used in the present simulation did reduce the precision of the result – this is enlarged by the logarithmic scale.

Fig. E.12a and b depict the excess pore pressure and the radial stresses at the pile wall[2] versus normalised time T^* (introduced in Eq. 3.3, p. 61). Again, the three curves are very closely matched.

Table E.1 Modified Cam clay parameters for Boston Blue clay (Randolph, Carter and Wroth, 1979).

M	λ	κ	Γ	G'
1·2	0·15	0·03	2·744	$74\,s_{u0}$

[2] At $r = 1{\cdot}15R$ to be consistent with Randolph, Carter and Wroth (1979).

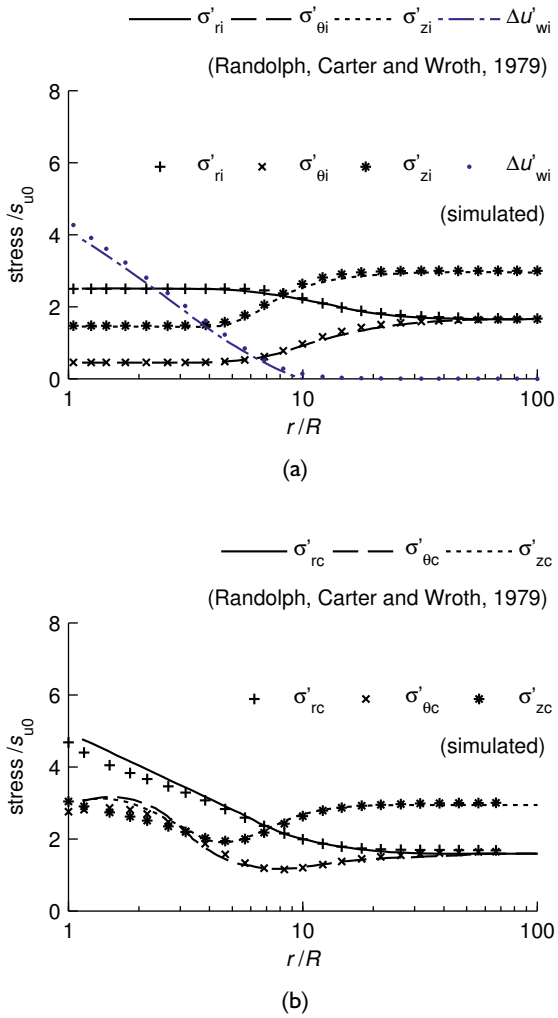

Figure E.11 Distribution of effective stresses (a) after cavity expansion and (b) subsequent consolidation.

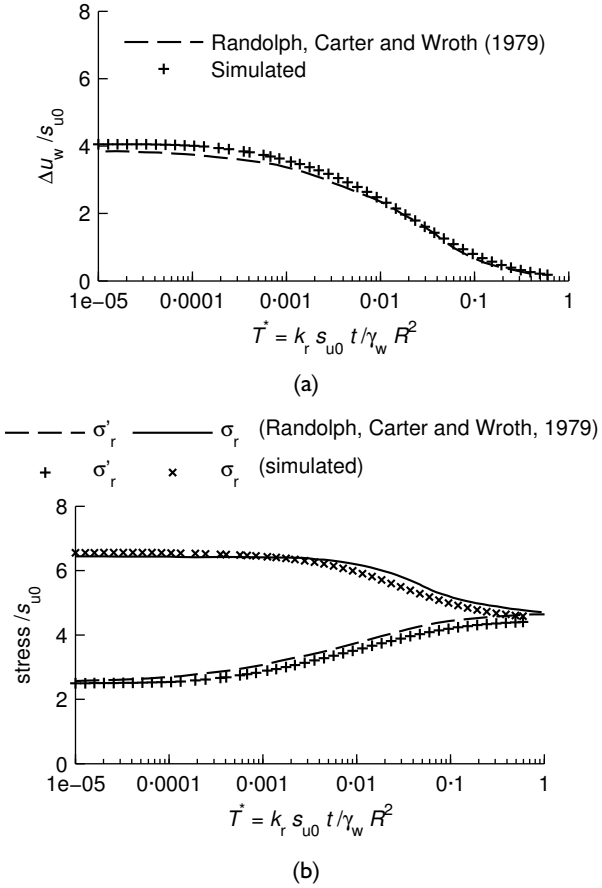

Figure E.12 Values, at pile wall ($r = 1{\cdot}15R$) of (a) excess pore pressure and (b) radial stresses, versus normalised time T^*.

Appendix F

Additional figures of the pile driving model output

Hereunder are reproduced several additional figures from the installation simulated in Section 6.1 (p. 119).

Fig. F.1 presents the shear stress at pile wall versus pile displacement for the last blow of the Disk Shearing Model, for the five investigated initial overconsolidation ratios.

Figs. F.2 to F.6 depict the radial effective stress distribution after the Strain Path Method simulation, after 100 blows of the Disk Shearing Model, and after equalisation, for the five investigated initial overconsolidation ratios.

Figs. F.7 to F.11 present the path followed by the soil adjacent to the pile wall during the pile driving and subsequent equalisation, for the five investigated initial overconsolidation ratios.

Figs. F.12 to F.14 depict the distribution of mean effective stress, undrained shear strength, and water content after equalisation, for the five investigated initial overconsolidation ratios.

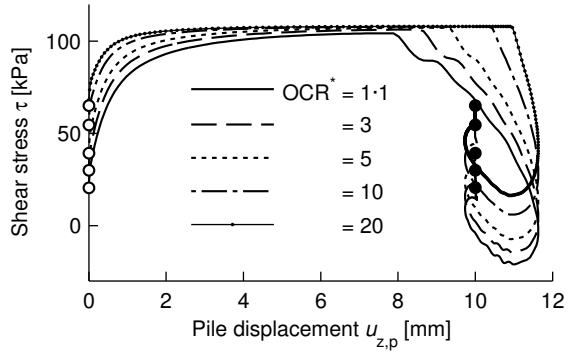

Figure F.1 Shear stress at pile wall versus pile displacement for the last blow.

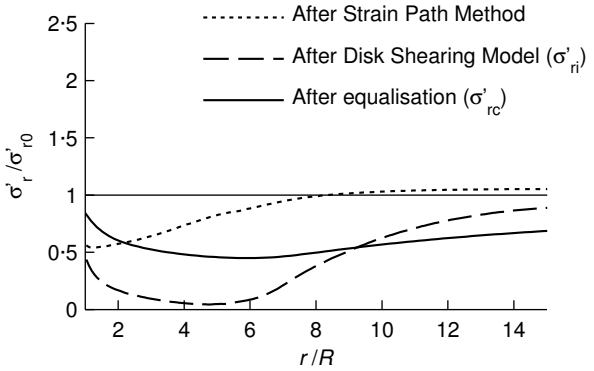

Figure F.2 Distribution of radial effective stress ratio for $OCR^* = 1{\cdot}1$ (OCR = 1).

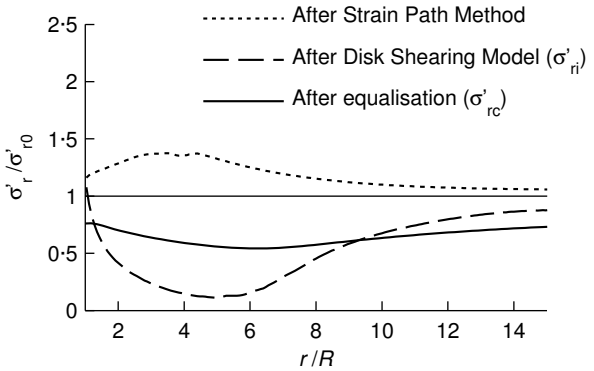

Figure F.3 Distribution of radial effective stress ratio for $OCR^* = 3$ (OCR = 3·4).

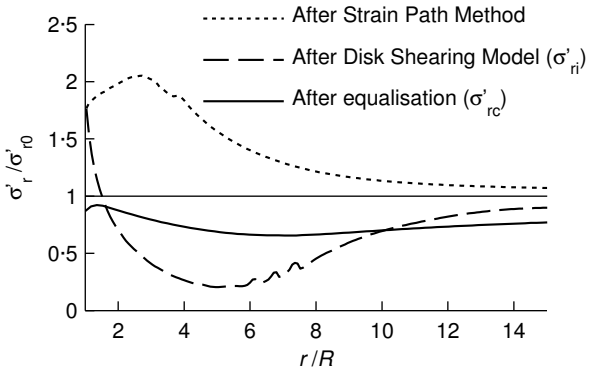

Figure F.4 Distribution of radial effective stress ratio for $OCR^* = 5$ (OCR = 7·1).

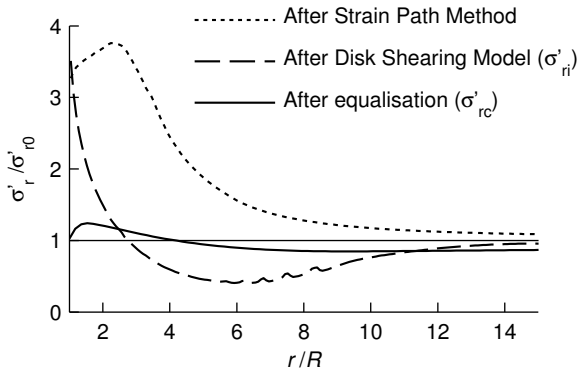

Figure F.5 Distribution of radial effective stress ratio for $OCR^* = 10$ ($OCR = 21{\cdot}1$).

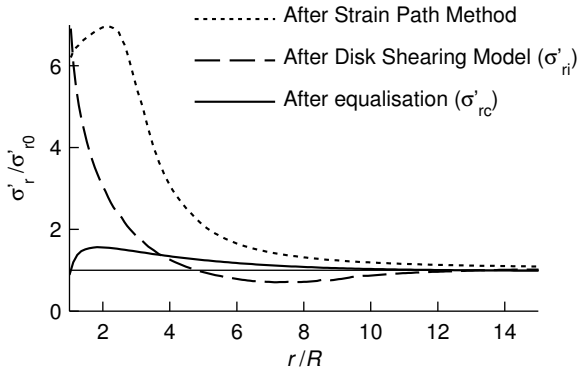

Figure F.6 Distribution of radial effective stress ratio for $OCR^* = 20$ ($OCR = 64{\cdot}1$).

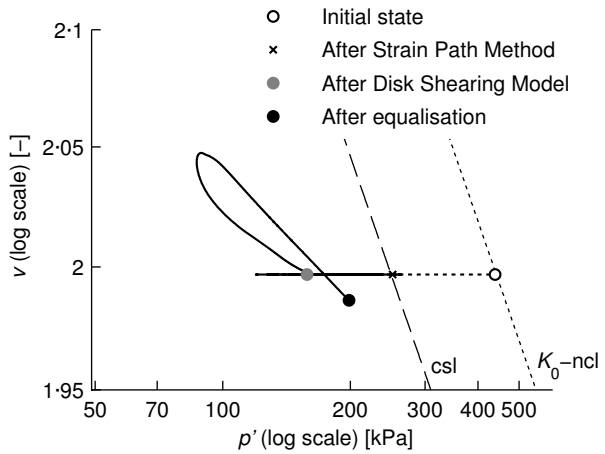

Figure F.7 Stress path at the pile wall in the compression plane for $OCR^* = 1{\cdot}1$ ($OCR = 1$).

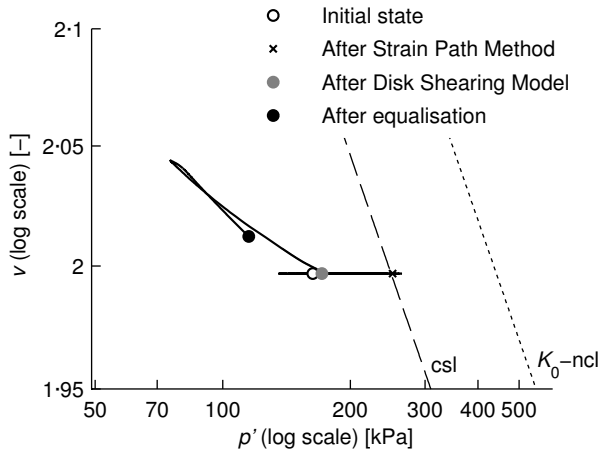

Figure F.8 Stress path at the pile wall in the compression plane for $OCR^* = 3$ ($OCR = 3{\cdot}4$).

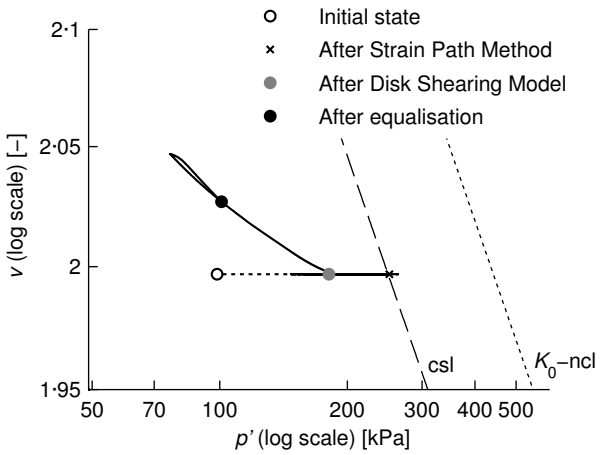

Figure F.9 Stress path at the pile wall in the compression plane for $OCR^* = 5$ (OCR = 7·1).

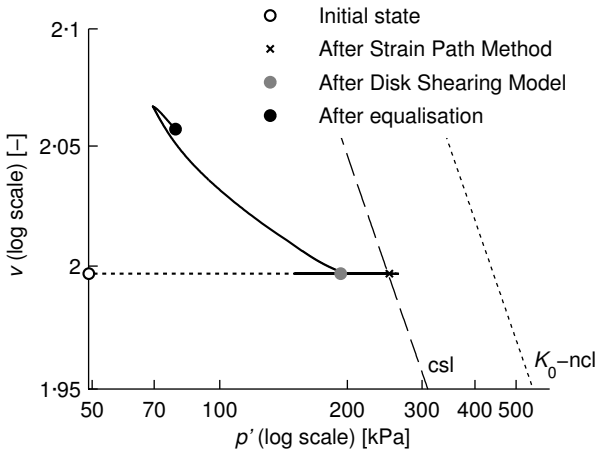

Figure F.10 Stress path at the pile wall in the compression plane for $OCR^* = 10$ (OCR = 21·1).

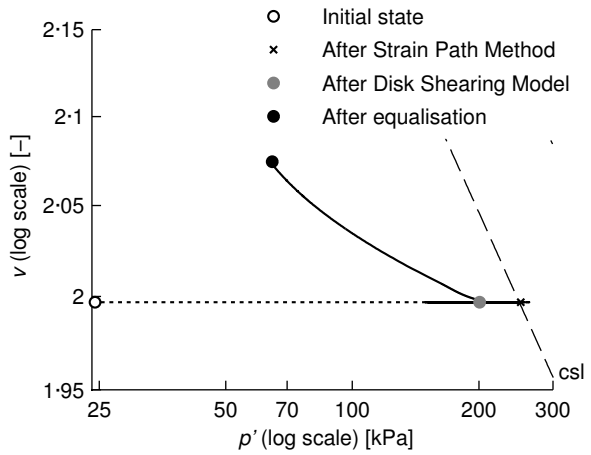

Figure F.11 Stress path at the pile wall in the compression plane for $OCR^* = 20$ ($OCR = 64{\cdot}1$).

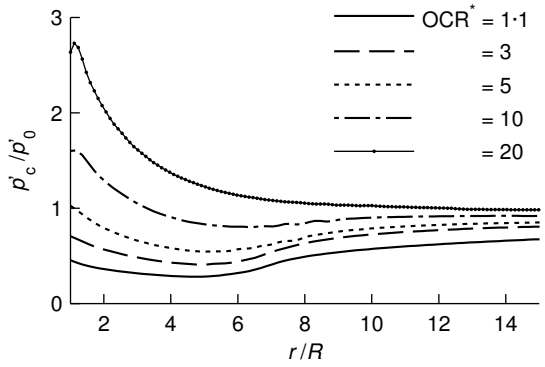

Figure F.12 Distribution of mean effective stress after equalisation.

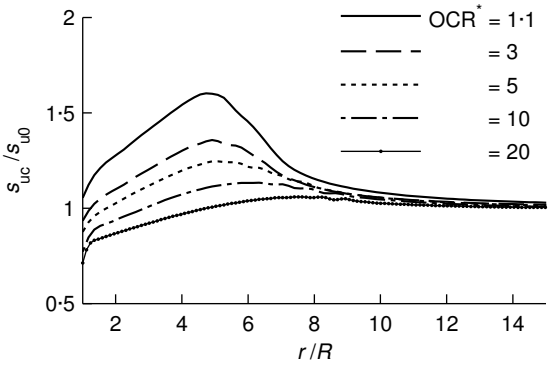

Figure F.13 Distribution of undrained shear strength after equalisation.

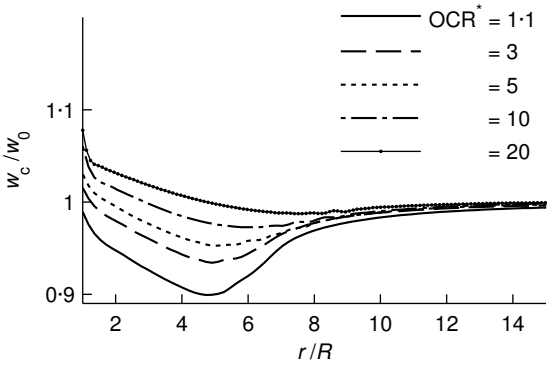

Figure F.14 Distribution of water content after equalisation.